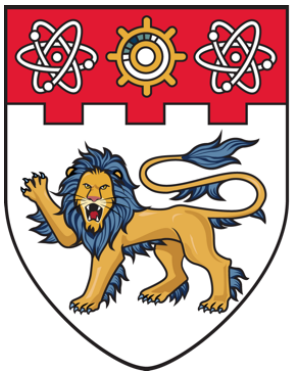

NANYANG TECHNOLOGICAL UNIVERSITY
SINGAPORE

THE DEVELOPMENT OF ORGANIC-BASED SYSTEMS FOR USE IN REDOX FLOW BATTERIES

[RAYMOND SHI RONGSHENG]

SCHOOL OF PHYSICAL AND MATHEMATICAL SCIENCES

[2021]

[THE DEVELOPMENT OF ORGANIC-BASED SYSTEMS FOR USE IN REDOX FLOW BATTERIES]

[RAYMOND SHI RONGSHENG]

SCHOOL OF PHYSICAL AND MATHEMATICAL SCIENCES

A thesis submitted to the Nanyang Technological University in partial fulfilment of the requirement for the degree of Doctor of Philosophy

2021

Statement of Originality

I hereby certify that the work embodied in this thesis is the result of original research done by me except where otherwise stated in this thesis. The thesis work has not been submitted for a degree or professional qualification to any other university or institution. I declare that this thesis is written by myself and is free of plagiarism and of sufficient grammatical clarity to be examined. I confirm that the investigations were conducted in accord with the ethics policies and integrity standards of Nanyang Technological University and that the research data are presented honestly and without prejudice.

07/01/2021

. . . . . .

Date

. . . . . .

Raymond Shi Rong Sheng

Supervisor Declaration Statement

I have reviewed the content and presentation style of this thesis and declare it of sufficient grammatical clarity to be examined. To the best of my knowledge, the thesis is free of plagiarism and the research and writing are those of the candidate's except as acknowledged in the Author Attribution Statement. I confirm that the investigations were conducted in accord with the ethics policies and integrity standards of Nanyang Technological University and that the research data are presented honestly and without prejudice.

07/01/2021

. . . . . .
Date

. . . . . .
Assoc Prof. Richard D. Webster

Authorship Attribution Statement

This thesis contains material from [1] paper published in the following peer-reviewed journals in which I am listed as an author.

A portion of Chapter 4 is published as Shi, R. R. S.; Tessensohn, M. E.; Lauw, S. J. L.; Foo, N. A. B. Y.; Webster, R. D., Tuning the reduction potential of quinones by controlling the effects of hydrogen bonding, protonation and proton-coupled electron transfer reactions. *Chem. Commun*. **2019**, *55*, 2277. DOI: 10.1039/C8CC09188A .

The contributions of the co-authors are as follows:

- A/Prof Richard D. Webster provided the initial project direction and edited the completed manuscript drafts.
- I prepared the manuscript with Dr. Malcolm E. Tessensohn and revised it together with A/Prof Richard D. Webster.
- I designed the study together with A/Prof Richard D. Webster and performed all the laboratory experiments at SPMS.
- I also analysed all the data obtained from the experiments.
- Dr. Sherman Lauw J. L and Miss Nicolette A. Foo B. Y. assisted with voltammetric studies.

07/01/2021

. . . . . .
Date

. . . . . .
Raymond Shi Rong Sheng

Abstract

With the current drive towards environmental sustainability, electrochemical energy storage (EES) systems such as redox flow batteries (RFB) are a promising solution as they can potentially play an important role in balancing energy generation and consumption to ensure power network stability and reliability. Organic compounds possess tremendous promise for energy storage as they are structurally diverse and synthetically tuneable. In addition, organic compounds can be cost-effective and environmentally benign due to the abundance of the required hydrocarbon starting materials from natural sources. However, many organic redox species experienced stability issues in their charged form.

In Chapter 2, voltammetric and spectroscopic experiments were used to identify four organic compounds that were suitable anolytes and catholytes due to their promising electrochemical properties in an organic-based electrolyte system. In Chapter 3, the electrochemical behaviour of quinone and benzidine derivatives were thoroughly investigated. Among the derivatives, anthraquinone (AQ) and *o*-tolidine displayed good chemical reversibility in the presence of trifluoroacetic acid (TFA). In a mixed system, AQ and *o*-tolidine were chemically compatible and showed no sign of deterioration under various conditions. This mixed reactant system also possessed two-electron transfer capability which is useful in designing a high energy battery system.

In Chapter 4, the effects of different additives on the reduction mechanism of a vitamin K analogue (VKA) were examined. In the presence of the weak acid, diethyl malonate (DEM), the electrochemical reduction process of VKA was found to proceed through a “wedge-scheme” mechanism. With controlled amounts of DEM, the reduction potential of VKA could be tuned to achieve a higher cell voltage. The solubility of VKA in CH_3CN was optimized and was found to increase by four-fold upon functionalizing with ethylene glycol ether side chains. The

mixed reactant system comprising the chemically modified VKA (VKA1) and a vitamin E analogue (VEA) exhibited an operational cell voltage of 1.23 V in the presence of DEM. The mixed reactants retain their functionality over a range of expected operational conditions, making them reliable and stable organic-based electrolyte systems that can be utilized in the development of an all-organic battery for RFB applications. In Chapter 5, the benefits of 3D printing technology were illustrated through the design and fabrication of the laboratory test cell prototype. Several 3D printed flow fields and end plates were fabricated with a high level of precision. The rapid prototyping enables quick assessment of the problems associated with the designs for further improvement. As such, 3D printing technology is a very useful tool in RFBs research.

Acknowledgements

First and foremost, Thank you lord for blessing me with strength and wisdom to complete my 4 years of studies. Thank you for bringing me hope through the toughest times and paving the way for me.

I would like to express my sincere thanks to Prof Webster for his guidance and kindness that I have received during these 4 years. He would spend time listening to our new suggestions and help us in achieving our goals. Thank you for placing your trust in us and ensured our well-being.

I would also like to thank my mentor, Dr Sherman; thank you for sharing your knowledge with me and also extending your help to ease my transitioning process as a first year PhD student. I am also very grateful to my other seniors in the lab, Dr Malcolm and Dr Sherli for sharing your valuable knowledge, experiences and providing me with help in your field of expertise. In addition, I would like to express my gratitude to all the seniors and my current lab mates, Dr Xian Liang, Arnold, Si Man, Shafiq and Maja. Thank you for all the help and support during this period of time. I am really grateful for the fun and laughter that we have shared during my PhD journey. I would also like to express appreciation to my buddy, Zhi Zhong for lending me a helping hand in times of need. Moreover, thank you to all my wonderful students for their help and giving me this opportunity to share and learn from one another.

I would like to extend my appreciation to NTU for funding my graduate studies. Special thanks to Prof. Zhao Yan Li and Prof. Lim Teik Thye, for being my thesis advisory committee (TAC) members.

Lastly, I want to express my heartfelt appreciation to my dear parents, thank you for your selfless and unconditional love. Thank you for your endless prayers and giving me the best of

everything. I also thank my family members for their support and understanding. Most importantly, I would like to thank my wife, Shu Hui for showering me with love, care, and concern, for accompanying me to late nights over the past few months. Thank you for being extremely supportive and making countless sacrifices during this entire process. Also, thank you for trusting and believing in me. Without such a family team, I would not have made it this far.

Table of Contents

List of Abbreviations

3D	Three-dimensional
AQ	Anthraquinone
Bu_4NPF_6	Tetrabutylammonium Hexafluorophosphate
CPE	Controlled Potential Electrolysis
CV	Cyclic Voltammetry
DC	Direct Current
DCTC	α,α-dicyano-p-toluoylcyanide
DEM	Diethyl malonate
DISP2	Disproportionation
DMF	Dimethylformamide
DMSO	Dimethyl sulfoxide
Fc/Fc^+	Ferrocene/Ferrocenium Redox Couple
GC	Glassy Carbon
NQ	Naphthoquinone
PCET	Proton-coupled Electron Transfer
PD	*p*-phenylenediamine
PEG	Poly (ethylene glycol)
PLA	Polylactic acid
Pt	Platinum
RFB	Redox Flow Battery
TCNQ	7,7,8,8-tetracyanoquinodimethane
TFA	Trifluoroacetic Acid
TMeQ	2,3,6-trimethylquinoxaline
TMB	3,3’5,5’-tetramethylbenzidine

UV	Ultraviolet
VEA	Vitamin E analogue, pyrano[3,2-*f*]-chromene
VKA	Vitamin K analogue, 2,3-dimethylnaphthoquinone
VKA1	Vitamin K analogue 1, 2,3-di(2-methoxyethoxy)-1,4-naphthoquinone
VKA2	Vitamin K analogue 2, 2,3-bi(2-(2-methoxyethoxy)ethoxy)naphthalene-1,4-dione
VKA3	Vitamin K analogue 3, 2,3-di(2-(2-(2methoxyethoxy)ethoxy)ethoxy)naphthalene-1,4-dione
VRB	Vanadium Redox Flow Battery

Chapter 1

Introduction

1.1 Background Information

Due to the rapid growth of the world's population and economic demand, global energy consumption has been steadily increasing and is believed to be far beyond sustainable. Electricity is one of the world's fastest growing end-use energy consumption and it was reported that the demand for electrical energy has grown over a rate of 3% annually.[1] It is projected that by 2050, the energy consumption of the world will be double the amount of the current energy production rate.[1-3] Other than the concern for the depletion of non-renewable energy resources (such as fossil fuels including coal, oil and natural gas), there is also an increasing awareness of greenhouse effects and climate change caused by the overwhelming emission rate of CO_2 from these intense carbon-based sources. Subsequently, more efforts have been diverted towards greener and more sustainable energy technologies (for example photovoltaic, wind, hydroelectricity and tidal power) over the past decade.[4-6] Many countries have legislatively adopted to incorporate renewable energy sources into their total electrical energy production; for instance, 12% for the United States and 20% for Europe by 2020.[7] Based on the current development in the renewable energy technologies, the World Energy Council predicts that the new wind power capacity will rise to 474 GW globally by the end of 2020. In addition, the use of solar-related energy devices has grown at a rate of 40% annually.[8]

Due to the intermittent nature of the renewable energy sources and the need to cope with the influx of large-scale energy production, energy storage remains a challenge since the current infrastructure lacks sufficient measures to maintain a balance between energy generation and consumption to ensure power network stability and reliability.[9-10] It has been proven that the integration of energy storage systems or devices into the power network can help to better and more effectively manage the utilization of energy during times of peak consumption.[4, 11-12] Generally, energy storage systems have several appealing factors with regards to power management. These include, (i) the ability to store energy surplus during peak

production or overcoming high electrical load demands, (ii) overcoming the temporal deviations in renewable energy, and (iii) improving the reliability and quality of power. Some common forms of energy storage devices are batteries, supercapacitors, compressed air energy storage (CAES) and superconducting magnetic energy storage (SMES) (Figure 1.1a).[1, 7, 9]

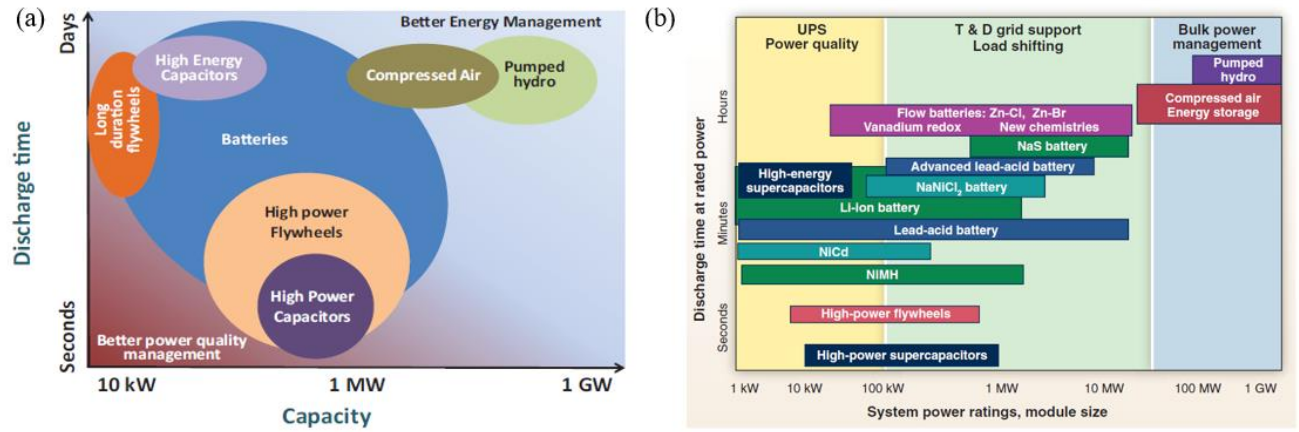

Figure 1.1. (a) Approximate representation of different storage technologies and their respective discharge rate and power capacity. From Ref.[13] (b) Data chart of different EES technologies and their respective discharge rate and power capacity. From Ref.[14]

In general, integration of energy storage systems grants more control over electrical energy transmission to meet demands over time.[8] In this regard, electrochemical energy storage (EES) systems have gained increasing attention as it has proven to be a promising solution for secondary energy containment. According to the global energy storage database, the number of electrochemical storage projects worldwide have grown significantly since the start of this decade from 1 in 2010 to 996 in 2020.[15] EES exhibits a wide range of power ratings (Figure 1.1b) to facilitate the needs of different grid applications.

1.1.1 Redox Flow Batteries

Rechargeable electrochemical energy storage systems such as the redox flow battery (RFB) are gaining particular interest in grid energy storage due to their design simplicity, outstanding operation lifetimes, and high capacitance to deal with power supply fluctuations.[4, 12, 16-17] RFBs are an electrochemical energy conversion device which consist of a flow system facilitated by a pump, electrolyte tank and electrochemical cell as depicted in Figure 1.2.

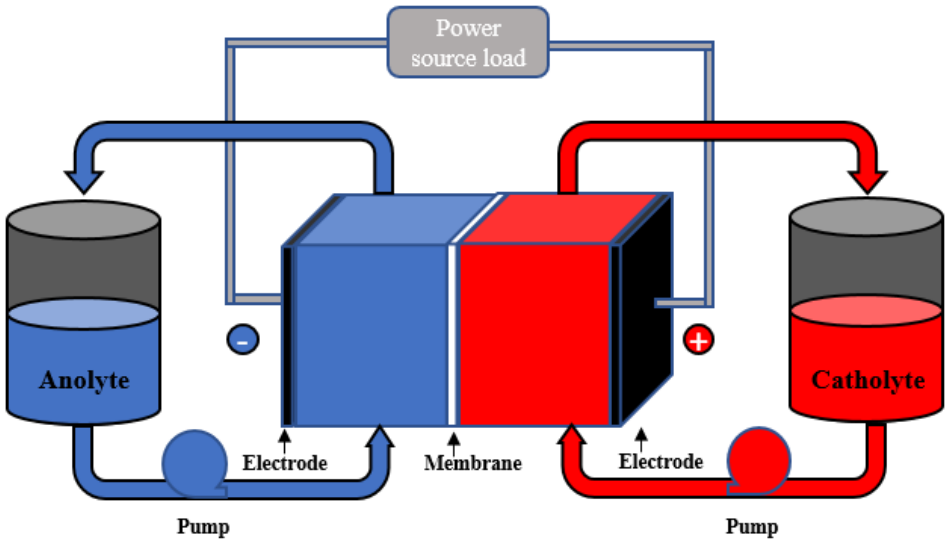

Figure 1.2. Schematic representation of redox flow battery for an electrochemical energy conversion device.

Unlike traditional batteries where the energy is stored within the electrodes, RFBs store the energy in the liquid electrolyte consisting of energy-bearing redox active species, catholyte (positive potential electrolyte) and anolyte (negative potential electrolyte). With the aid of hydraulic pumps, the liquid electrolytes are circulated between the half-cell compartments and the electrolyte tank for power conversion.[8, 16, 18] The pumping energy required is approximately 2-3 % of the total battery energy, which is to account for the pressure losses due to the circulation of the electrolytes (i.e. losses in pipes, flow frames and electrodes) and also to

compensate for the work done to overcome the gravitational energy required to lift the electrolytes.[19-20]

During charging, the catholyte and anolyte undergo oxidation and reduction, respectively, where electrical energy is transformed to chemical potential energy. Spontaneous reverse redox reactions occur during discharging and chemical potential energy is converted back to electrical energy and delivered to the load.[4, 7, 10, 21] The electrodes used in RFBs are chemically inert and the function is solely to provide electrochemically active sites to facilitate charge transfer. This is fundamentally different from a conventional solid-state battery where energy is stored in the energy-bearing electro-active species that are attached or functionalized onto the electrode.[8, 17]

The energy capacity of RFBs is determined by the volume and concentration of electrolytes while the power density depends on the rate that the redox reactions occur at the electrode surface. RFBs possess a unique feature of decoupled power generation and energy storage that allows an independent scaling of the power and energy capacities. This enables RFBs to be used across a wide variety of applications with different energy storage requirements ranging from large-scale (MWh) storage applications in industry or utility settings, to dispatchable residential loads (Wh to kWh).[4, 7-8, 16-18, 22-24]

The redox active species employed in traditional RFBs were traditionally limited within the categories of transition metals, metal complexes and halogen ions.[4, 12, 17] Among all, the vanadium RFB is arguably the most widely used system. The all-vanadium RFB (VRFB) utilizes vanadium redox couples that exist in 4 different oxidation states, namely V^{2+}/V^{3+} and V^{4+}/V^{5+}. Although the VRFB exhibits a long system lifetime[4, 25] and has relatively good reversibility [25-26], it suffers from low volumetric energy capacity due to the constraint in solubility. The practicality of the VRFB is limited by the low energy density [25] compared to Li-ion batteries (>200 Wh L^{-1}). Strong acidic supporting electrolyte (i.e., sulphuric acid, H_2SO_4)

is commonly deployed in the VRFB system to enhance the conductivity of the solution and stability of the electroactive species.[7] However, the use of H_2SO_4 has severely impacted the solubility of vanadium ions, V^{2+}, V^{3+} and V^{4+}.[27] For instance, Skyllas-Kazacos and co-worker have reported that the solubility of $VOSO_4$ decreased tremendously from 3.3 M (in H_2O) to 0.26 M in the presence of 9.0 M H_2SO_4.[28] The vanadium ions precipitated in the form of vanadium sulphate with increasing H_2SO_4 as a result of the common ion effect. On the other hand, the vanadium pentoxide (V_2O_5) is susceptible to precipitation at elevated temperature due to thermal instability.[29]

Other example of traditional metal-based RFBs such as the iron/chromium (ICB) system, experience sluggish electrochemical kinetics of the Cr(II)/Cr(III) couples and low coulombic efficiency due to H_2 evolution since hydrogen ions are more readily reduced than Cr (III) ions.[4, 7, 30-31] In the case of the zinc/bromide (ZBB) system, uneven distribution of the zinc ions and charges at the interface between the anode and electrolyte leads to the formation of zinc dendrites. The residual dendrite on the electrode further aggravates non-uniform dendritic growth, resulting in severe concentration polarization and potentially damaging the membrane and affecting the efficiency of the battery.[32-33] Among various drawbacks, low operating cell voltage remains the key obstacle that limits the energy densities of traditional RFBs. This is attributed to the aqueous system where the narrow electrochemical window of water (1.23 V at 25°C) inherently restricts the operational cell voltage and the choice of redox species available.[4, 34] The utilization of heavy metals in common metal-based RFB (all-vanadium RFB, Fe/Cr and Zn/Br_2) also poses threats to the environment during primary material production, disposal or in the case of damage to the RFB.[16]

Although some of these traditional metal-based RFB systems exhibited power capacities at the megawatt-scale, their prevalent wide market penetration was hampered by the high commodity price of metal-based redox active material, low energy densities and cyclable

efficiencies of the RFBs.[16-17] For instance, the system cost for the VRFB is approximately USD \$320 kWh^{-1} which greatly exceeds the cost target set by the US Department of Energy (DOE) of USD \$100 kWh^{-1} (2018). The cost breakdown in Table 1.1 shows that the metal-based redox-active species contributes to most of the system cost.[35]

Table 1.1. Cost breakdown of the available RFB systems at the 4-MWh scale.[36]

System:	**Vanadium RFB**	**Iron-Vanadium RFB**	**Iron-Chromium RFB**
Redox-active Species	~180	~360	~100
Membrane	~30	~10	~10
Bipolar plates	~10	~50	~60
Felt	~20	~80	~130
Others (e.g. Tank costs, Pumps, maintenance etc.)	~80	~110	~110
Total Cost/USD \$ kWh^{-1}:	~320	~610	~410

In view of the drawbacks encountered by metal-based RFBs, the research direction is gradually shifting towards exploring the use of organic compounds as redox-active materials.[16] Given the scarcity of metallic elements and toxicity concerns related to heavy metals, the transition towards a metal-free battery is undoubtedly beneficial to the development of RFBs. This thesis aims to develop an organic (non-aqueous) based electrolyte system that can

potentially be used in RFB applications. The motivation of using organic compounds stems from several appealing factors which includes the diversity in molecular structure as well as the ability to achieve desirable electrochemical properties through simple chemical modification. The use of organic compounds can also alleviate the environmental impacts that are posed by the inorganic counterparts. As such, different organic redox molecules were studied and evaluated based on their chemical reversibility, stability, and redox potentials.

1.2 Literature Review for Organic Redox Compounds in RFB Applications

1.2.1 Overview

The identity of the redox-active compounds is possibly the most important consideration for the development of a functional battery. In traditional RFBs, the choice of electrochemical materials was mostly limited to heavy metal species. However, their widespread application has been impeded by shortcomings such as high operational costs, sluggish electrochemical kinetics, and environmental toxicity. The pursuit of organic redox compounds seeks to overcome the challenges inherent to the metal species counterparts. Organic redox compounds are greener and less hazardous since they are generally composed of earth abundant elements and environmentally benign.[22, 34] The chemical cost of the organic active materials are generally lower than the vanadium species used for the VRFB electrolyte as shown in Table 1.2.[16] Most importantly, electrochemical and physical properties such as the redox potentials and solubility can be rationally controlled through synthetic means.[17, 21]

Table 1.2. Chemical cost of redox active species for the reported RFB systems.[22, 37-38]

RFB system:	**Chemical Cost/USD $ Kg^{-1}**
All-Vanadium	25 (V_2O_5)

9-Fluorenone (9-FL) /DBMMB	2 (9-FL) 1~5 (Precursors for DBMMB)
Methyl Viologen (MV) / 4-OH-TEMPO	1 (MV) 7 (4-OH-TEMPO)
9-10-anthraquinone-2,7-disulphonic acid (AQDS) / Bromine (Br)	4.74 (AQDS) 1.76 (Br)
Benzophenone (BP) / TEMPO	1-10 (BP) 5-7 (TEMPO)

An ideal organic redox active species should be chemically reversible and possess high chemical stability to achieve a long system lifetime. In addition, redox active species with feasible redox potentials and high solubilities can facilitate the achievement of a RFB system with high energy density. It is also important to ensure that the organic redox compounds are low-cost or relatively easy to synthesize for large scale production.[39]

The state of research pertaining to the use of organic compounds as redox couples is still in its development stage as most of these studies were performed on a small scale in the laboratory. Current literature for aqueous RFBs and non-aqueous (organic) RFB systems revolves around various classes of organic compounds such as aromatic heterocycles, nitroxide radicals, aromatics, and carbonyls (Figure 2.1).[22, 40-42] Capacity decay due to chemical instability encountered by organic redox pairs and cross-over issues are the key challenges that hinders practical applications.[24, 37, 43-44]

Aqueous RFB systems are limited by the inherent properties of water which not only restricts the choice of organic redox active species employed but also the cell potential of the RFB due to their stability within a narrow electrochemical window (1.2 V – 1.6 V) beyond which electrolysis of water occurs.[4, 17] To overcome the various constraints associated with

aqueous systems, organic RFB systems offering expanded operational potential windows (over 2 V) were introduced. In non-aqueous systems, redox couples with elevated voltage can be employed leading to batteries with higher energy densities.[45-47] Moreover, organic solvents broaden the range of electrochemical active species that can be incorporated into RFB.

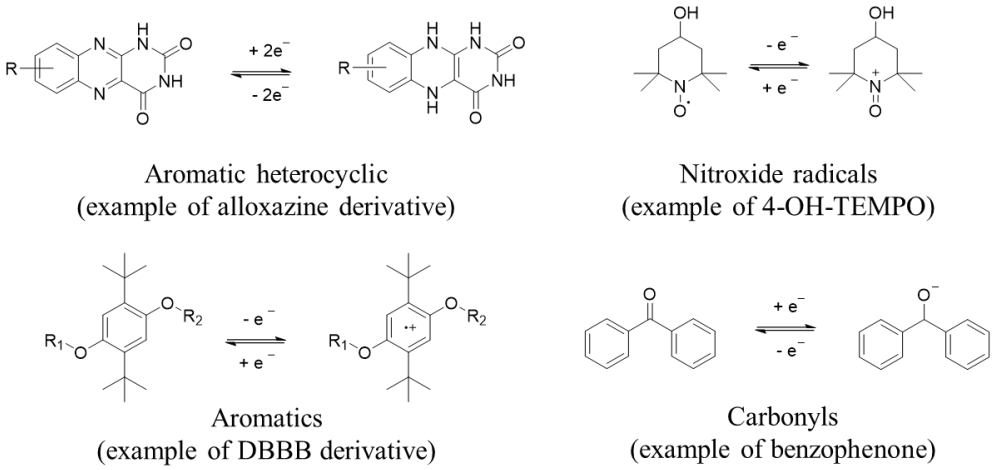

Figure 1.3. Four different classifications of organic compounds used in RFB research studies.

Nevertheless, past research has provided clear insights into the structure-property relationship and some of the important degradation mechanisms associated with different classes of organic compounds. This knowledge has opened up new perspectives in molecular design and provided guidance towards the development of new organic-based system for RFBs. As such, 4 different classifications of organic compounds used in aqueous and organic RFBs will be further discussed in the subsequent sections.

1.2.2 Aromatic Heterocyclic Compounds

Aromatic heterocycles are planar or nearly planar cyclic conjugated heterocycles that possess the aromatic characteristics of (4n+2) delocalized π-electrons.[48] The aromatic heterocycles can be derived from a five-membered or six-membered aromatic ring with at least one CH group replaced by a heteroatom such as nitrogen, oxygen, or sulfur. Different forms of

aromatic heterocyclics have been widely applied in both aqueous and organic RFBs (Figure 1.4).

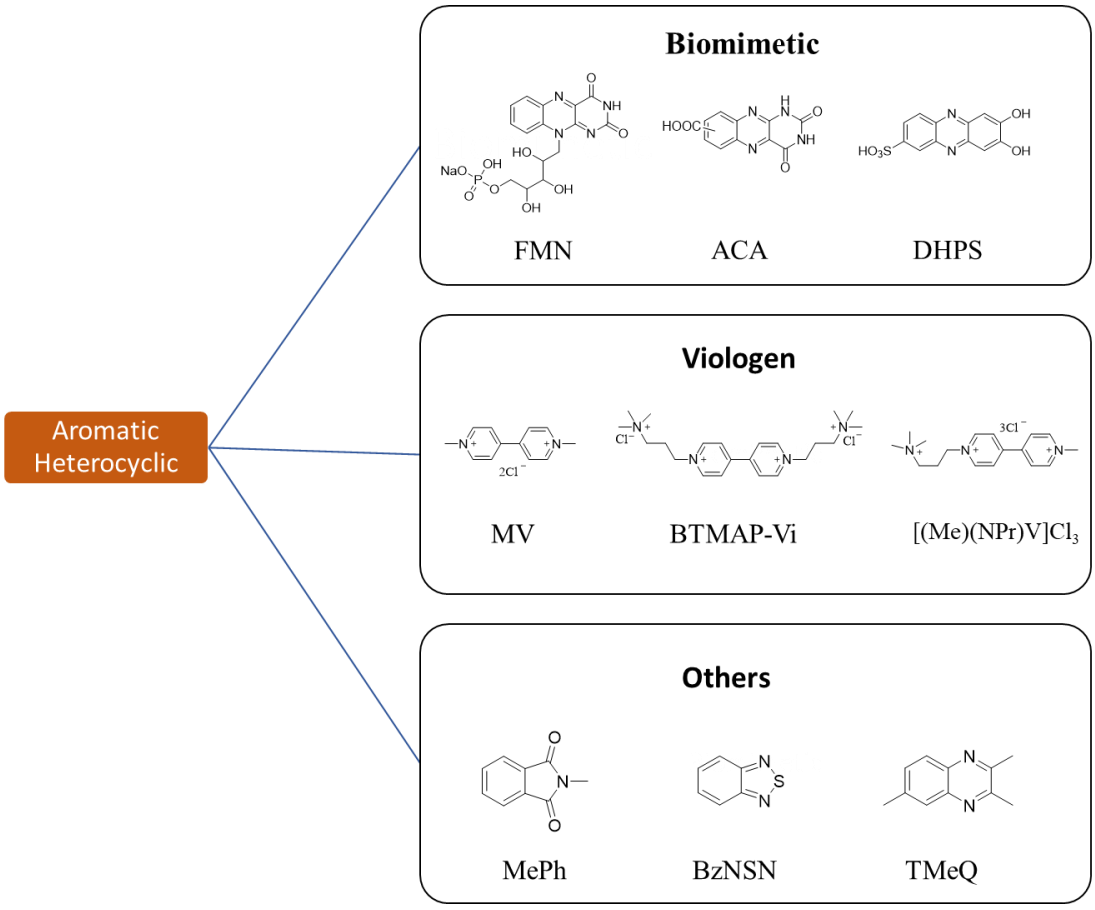

Figure 1.4. Chemical structures of organic compounds classified under aromatic heterocyclics.

Heterocyclic aromatics can potentially offer battery systems with high energy density due to multi-electron transfer capabilities in both aqueous and organic regimes. The aromatic characteristics of the structure also impart increased chemical stability due to charge delocalization. Through rational design and functionalization, heterocyclic aromatics can exhibit remarkable properties and performance.

Taking inspiration from biochemical systems, Meng *et al.*[49] introduced a biomimetic aqueous RFB comprised of the sodium salt of flavin mononucleotide (FMN-Na), a derivative of vitamin B_2 as the anolyte. The core structure of FMN-Na is made up of a similar planar

isoalloxazine ring as the backbone of riboflavin. At high pH (>10.2), the FMN-Na undergoes a 2-electron reduction process at approximately -0.5V vs Ag/AgCl, and the redox potential experienced a cathodic shift beyond pH 10. Under alkaline condition, the FMN-Na undergoes dimerization as evidenced from the UV-vis studies. Despite a side dimerization reaction, the charged form of FMN-Na was chemically stable due to electron delocalization from various resonance forms. In addition, the authors demonstrated the use of additives, such as nicotinamide to improve the solubility of FMN-Na from 100 mM to 1.5 M in an aqueous solution of 1 M KOH. When pairing with $K_4[Fe(CN)_6]$, the cell exhibited high cycling stability with 99% capacity retention after 200 cycles. Similarly, Aziz *et al.*[23] have also reported an alloxazine-based aqueous RFB drawing from the inspiration of vitamin B_2. The alloxazine core was functionalized with an acidic functional group, a carboxylic acid (-COOH), to improve the solubility in alkaline solution. Under prolong storage in alkaline conditions, the synthesized compound, alloxazine 7/8 carboxylic acid (ACA) did not experience dimerization that was known to occur in FMN in aqueous solution.[49-50] ACA undergoes a 2-electron reduction at -0.62V vs SHE and the full-cell testing with ferri/ferrocyanide was able to attain a high-capacity retention of 91% over 400 cycles. Alloxazine is known to undergo an irreversible hydrolysis reaction to produce redox in-active species.[23, 51] The studies have also proposed design strategies to increase the chemical stability of alloxazine by introducing electron-donating groups to reduce the electrophilicity of the carbonyl groups which are prone to attack by water molecules. Prior work on alloxazine-based compounds demonstrated the ability to incorporate acidic functional groups to facilitate the interaction towards the solvent molecules and further enhance the solubility in alkaline electrolyte. However, further work could focus on improving the redox potential of alloxazine-based compounds under alkaline conditions to foster a battery system with higher power density. In another bioinspired work, Wang *et al.*[52] developed an aqueous RFB that is based on the derivatives of the phenazine cofactor as the anolyte material.

Density functional theory (DFT)-based virtual screening was used to determine suitable functional groups to optimize the redox potential and solubility of phenazine. In their study, two different phenazine derivatives, 7,8-dihydroxyphenazine-2-sulfonic acid (DHPS) and 7,8-dihydroxyphenazine-2-carboxylic acid (DHPC) were synthesized. Under alkaline conditions, DHPS and DHPC demonstrated an improved solubility of 1.45 M and 0.95 M respectively, due to the incorporation of an acidic functional group. Compared with pristine phenazine, the presence of the two-hydroxy group on phenazines derivatives (DHPS and DHPC) also leads to a significant cathodic shift in the redox potential of the two-electron reduction process. Flow cell testing comprising DHPS and ferri/ferrocyanide catholyte was performed at a near-saturated concentration of 1.4 M and the capacity retention obtained was 90% over 500 cycles. The slight decrease in the capacity was possibly due to the trapping of DHPS species in the membrane. It is important to understand the electrostatic properties and the compatibility of the functional groups to tailor the redox potential and solubility without affecting the electrochemical behavior of the redox active species.

Viologens (*N*, *N*-disubstituted 4,4-bipyriduium salts) have received increasing interest over the years as potential anolytes for aqueous RFBs due to their superior solubility in water (>3 M). Viologens are widely employed in electrochromic devices and anodic materials in batteries due to their stable $2^{+}/1^{+}$ redox couple.[53-55] Wang *et al.*[37] demonstrated a full organic, neutral pH aqueous RFB comprised of methyl viologen (MV^{2+}) and 4-HO TEMPO as the anolyte and catholyte, respectively. The study showed that the solubility and redox behavior of viologen compounds can be affected by the type of substituent on the nitrogen atoms. Under CV timescales, MV exhibits a reversible 1-electron reduction process at -0.45 V vs NHE. However, the system experienced capacity decay during the full-cell testing after 100 cycles. Aziz *et al.*[56] revealed that the capacity decay is related to the decomposition mechanism of the cation radical, $MV^{\bullet+}$. In aqueous conditions, $MV^{\bullet+}$ undergoes dimerization and the dimer

experienced disproportionation to form MV^{2+} and MV. The neutral form of MV^{0} is poorly soluble in water and can undergo irreversible protonation to form a redox-inactive species. In addition to this, $MV^{\bullet+}$ can also be readily oxidized back to MV^{2+} by molecular oxygen present in the solution. The by-product, hydroxide ions (OH^{-}) of the side oxidation process can eventually results in the demethylation of MV^{2+} to yield 1-methyl-[4,4'-bipyrin]-1-ium chloride which is redox-inactive. The instability of the charged species is detrimental to the battery lifetime due to irreversible capacity loss after every successful charge-discharge cycle. As such, the authors have designed and synthesized a viologen derivative, bis(3-trimethyl-ammonio)propyl viologen tetrachloride (BTMAP-Vi). The two positively charged side "arms" increased the electrostatic repulsion between two viologen molecules to prevent dimerization. In addition, the bulkiness and the enhanced positive charge on BTMAP-Vi reduces the permeability across anion-exchange membranes. To reduce the interference by atmospheric oxygen, the full cell testing with BTMAP-Fc was performed in a nitrogen-filled glovebag and the average capacity retention was 99.998% over 500 cycles.

To further optimize the performance of viologen-based compounds, structural modification was performed to utilize the second electron reduction process. Liu *et al.*[57] proposed replacement of the methyl substituent on the nitrogen atoms of MV with hydrophilic functional groups to resolve the insolubility issue of MV. From the CV experiments, the designed viologen, 1-methyl-1'-[3 (trimethylammonio)propyl]-4.4'bipyridnium trichloride, $[(Me)(NPr)V]Cl_3$ exhibited two successive one-electron reversible reduction processes at -0.39V and -0.78V vs NHE. Although the molecular alteration decreased the solubility of the viologen in aqueous solution (1.8 M in H_2O), the ability to store multi-electrons increased the overall charge capacity. The full cell testing with FcNCl was able to achieve a capacity retention of 91.39% over 50 cycles. However, the cycling stability decreased beyond 50 charge-discharge cycles. Comparison studies between $[(Me)(NPr)V]Cl_3$ and BTMAP-Vi

revealed that the chemical instability of the former was caused by a dimerization degradation process. Overall, viologen-based compounds exhibit a well-define electrochemistry. However, there is a need to balance the use of suitable hydrophilic functional groups that impart solubility to MV^0 and charge repulsion to suppress bimolecular interaction between $MV^{\bullet+}$, in order to achieve two-electron per molecule storage ability and optimum solubility.

Several heterocyclic aromatics were also employed in organic RFBs. These heterocylic aromatics in organic regimes exhibit a very negative redox potential as anolytes, enabling battery systems to reach high cell voltages. Wang *et al.*[44] proposed the use of *N*-methylphthalimide (MePh) as the anolyte to construct a high energy density RFB system. MePh exhibited a reversible one-electron reduction process at a redox potential of -1.79 V vs Ag/Ag^+. Pairing with 2,5-di-*tert*-butyl-1-methoxy-4-[2'-methoxyethoxy]benzene, DBMMB, the battery system was able to achieve a high cell voltage of 2.30 V. However, converting such molecules to their charged state involves the formation of unstable radical ions. The results from the cycling test have shown that the high nucleophilicity of $MePh^{\bullet-}$ enables them to attack solvent molecules (e.g. MeCN and propylene carbonate) and supporting electrolytes (e.g. $TEABF_4$) with electron-deficient functional groups. Therefore, it is important to consider the chemical compatibility between the charged species and other chemical components (i.e. solvent and supporting electrolyte) to ensure the system longevity in organic RFBs.

In another work, Wei *et al.*[46] have reported a new heterocyclic organic anolyte, 2,1,3-benzothiadizole (BzNSN), for an organic RFB. BzNSN exhibits a remarkably solubility of 5.7 M in pure acetonitrile (MeCN). With a redox potential of -1.58 V vs Ag/Ag^+, the RFB system coupled with DBMMB achieved a theoretical cell voltage of 2.36 V. Unlike MePh, the extensive charge delocalization through the conjugated system accounts for the good chemical and cycling stability of the radical anion, $BzNSN^{\bullet-}$ in carbonate and nitrile solvent.

As mentioned above, redox active species with highly negative redox potentials and multi-electron capabilities are favorable as it would likely give rise to large overall cell potential and greater energy density in a non-aqueous battery system. Brushett *et al*.[17] proposed quinoxaline as a potential anolyte for an organic RFB due to its 2-electron transfer capability. The studies revealed that functionalizing quinoxaline with electron-donating alkyl substituents at the 2, 3 and 6 positions further lower its reduction potential from 3.07 V to 2.80 V vs Li/Li^+, and also improves the electron transfer kinetics in propylene carbonate. However, the solubility of 2,3,6-trimethylquinoxaline (TMeQ) decreased significantly from 7.0 M to 0.5 M. As a proof-of-concept, cycling tests were performed on TMeQ coupled with 2,5-di-tert-butyl-1,4-bis(2-methoxyethoxy)benzene (DBBB) in a coin-cell configuration and the result suggest that the proposed system is fairly stable over 30 cycles. The well-defined electrochemistry, flexible synthesis and good electron-transfer kinetics indicates that quinoxaline has great potential for organic RFBs, but further work has to be performed to improve the solubility of TMeQ. Despite the remarkable performance exhibited by these heterocyclic aromatic compounds in organic RFBs, the chemical instability due to the formation of highly charged radical anions is still the main concern. Most of these studies were performed in highly controlled environments (i.e., argon-filled gloveboxes) to eliminate any possible unwanted atmospheric interference. Therefore, more efforts can be directed in this area to encourage the development of organic RFBs that meet practical conditions.

1.2.3 Nitroxide Radicals

Nitroxide radicals are organic compounds that contain the aminoxyl group that is characterized by a $\pi_{N\text{-}O}$ three electron bond (Figure 1.5). The electron density applied to the free radicals is distributed among the nitrogen and oxygen atoms that is dependent by polarity

on the solvent medium and pyramidalization of the nitrogen atom. The stable nitroxide radicals should possess an alkyl or aryl group α to the nitrogen atom.[58]

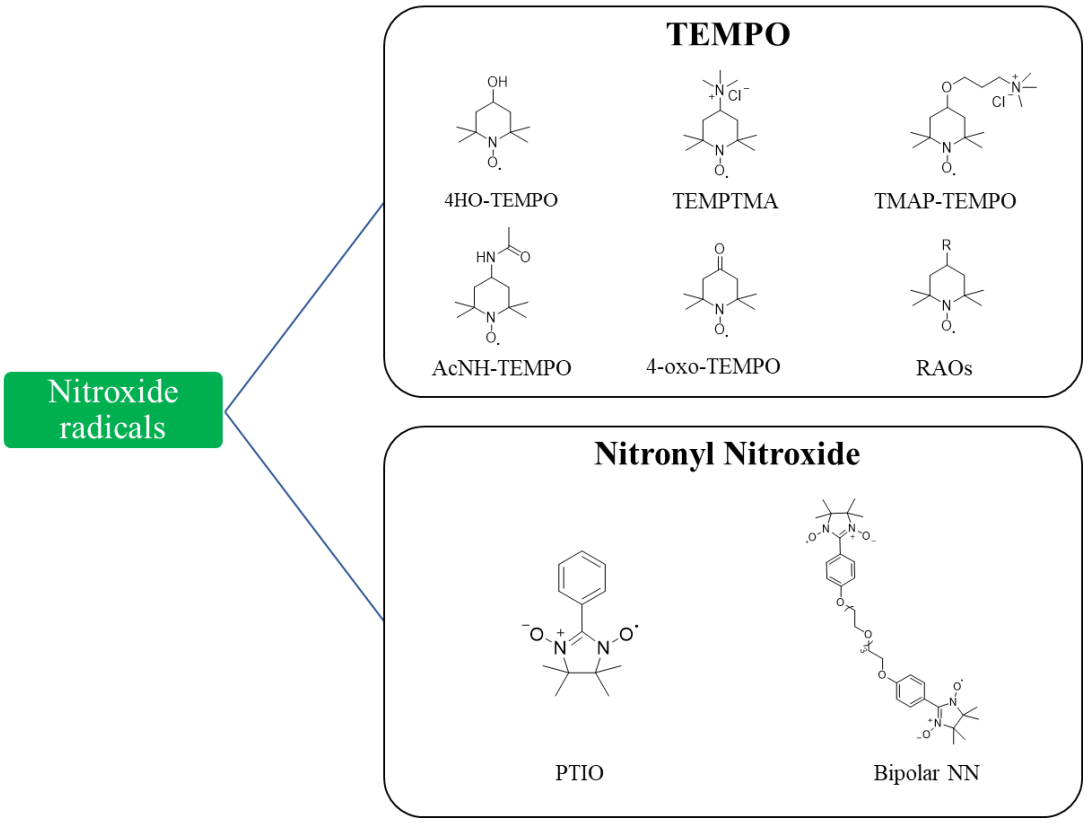

Figure 1.5. Chemical structures of organic compounds classified under nitroxide radicals.

The classic example of a stable nitroxide radical is 2,2,6,6-tetramethylpiperidin-1-yl)oxyl (TEMPO), with four peripheral methyl groups adjacent to the aminoxyl group. In aqueous RFBs, an improved molecular design is required to increase the solubility of TEMPO in aqueous solution. As mentioned previously, Wang *et al.*[37] proposed a MV/4-HO-TEMPO aqueous RFB system with a cell voltage of 1.25 V. The 4-HO-TEMPO exhibited an improved solubility of 2.1 M in H_2O owing to the hydrophilic substitute (-OH) at the para position. However, the energy density of the system was affected by the limited solubility of 4-HO-TEMPO in NaCl solution (0.5 M in 1.5 M NaCl). It is worth noting that the presence of the supporting electrolyte affects the solubility of the redox molecules. Besides organic redox active molecules and solvents, the choice of supporting electrolyte should also be taken into

consideration when developing an effective RFB system. Schubert *et al.*[53] introduced a chemically modified TEMPO with an ionic trimethylammonium chloride group at the para position to improve the solubility in NaCl solution. The modified TEMPO, TEMPTMA exhibited a more positive oxidation potential, 0.79 V vs AgCl/Ag and higher solubility (2.3 M in 1.5 M NaCl) compared to 4-OH TEMPO, 0.64 V vs Ag/AgCl. The proposed TEMPTA/MV system attained a theoretical cell voltage of 1.4 V and the cycling tests performed with a concentration of 2 M showed full capacity retention over 100 cycles. In another work, Xu *et al.*[59] synthesized a highly stable and soluble TEMPO derivative, 3-(trimethylammonium)propyl-functionalized TEMPO chloride, TMAP-TEMPO. TMAP-TEMPO features a solubility of 4.2 M in H_2O and it undergoes a reversible one-electron oxidation at 0.81 V vs SHE. Coupled with BTMAP-Vi, the RFB displayed a cell potential of 1.1 V and the system was able to retain 94% of its initial capacity after 1000 charge-discharge cycles. The authors postulate that the slight capacity loss may be due to chemical degradation of TMAP-TEMPO as a result of parasitic side reactions by water molecules and minor contribution from crossover of active species. Nonetheless, the capacity retention is nearly the same as obtained at different concentrations (0.1, 0.5 and 1.5 M), indicating that the system lifetime is concentration independent. RFB systems with high concentrations can lead to complex side reactions, resulting in capacity losses in subsequent cycling. Therefore, the concentration independent attribute is beneficial for redox active species since higher concentrations are necessary to achieve a high-performance RFBs. Compared to 4OH-TEMPO and TEMPTHA, the key to exceptional stability of TMAP-TEMPO is attributed to a combination of the following factors: (1) suppression of biomolecular degradation by electrostatic repulsion between positively charged TMAP-TEMPO molecules, (2) steric hindrance imposed by four peripheral methyl groups preventing interactions between free

radicals, and (3) incorporation of an aliphatic spacer to reduce the electronic effects of charged substituents.

TEMPO was also widely used in different designs of organic RFBs such as hybrid organic, all-organic and symmetric all-organic systems. Wang *et al.*[60] have introduced a hybrid organic RFB made up of a TEMPO catholyte and Li metal anode. TEMPO undergoes a chemically reversible one-electron oxidation process and exhibits a high solubility of 5.2 M in the proposed solvent mixture (4:1:5) of ethylene carbonate (EC)/propylene carbonate (PC)/ethyl methyl carbonate (EMC). Pairing TEMPO with Li metal, the cell system is able to achieve a high cell voltage of 3.5 V. With 0.1 M of TEMPO in 1.0 M $LiPF_6$, stable cycling performance was observed from the 100 charge-discharge cycles with an average capacity retention of 99.8%. The full cell testing performed with a high concentration of TEMPO of 2.0 M experienced slight capacity fading due to the limitation of the Li metal anode. Nevertheless, the cell system demonstrated the ability to deliver a remarkable energy density of 126 Wh L^{-1}. A similar TEMPO-based hybrid organic RFB with different metal anode, zinc has also been studied.[61]

Apart from the hybrid systems, TEMPO has been employed in studies of all-organic RFBs. Peng *et al.*[62] demonstrated a TEMPO/MePh RFB system in acetonitrile that exhibits a relatively stable charge-discharge cycling over 20 cycles with a cell voltage of 1.60 V. In a similar study, Cook *et al.*[63] discovered that TEMPO is prone to membrane crossover even at low concentration. Irreversible crossover of redox active species can decrease the cyclability of the battery system, leading to capacity fading over time. Therefore, high performance membranes are required to ensure good selectivity but often they have low conductivity and are expensive. To rectify the issue with crossover, Helms *et al.*[64] designed a TEMPO-based redox-active oligomer (RAOs). The oligoethylene oxide motif was functionalized with

TEMPO and the resultant molecules show an increased in redox potential of 56 mV. The TEMPO-based redox-active oligomer has a large molecular size (16Å radii) which limits the crossover by a microporous membrane (PIM-1, 6-8 Å pores). Under bulk electrolysis, the TEMPO-based oligomer maintains a high level of chemical stability with a constant columbic efficiency of 98% over 25 cycles. Different TEMPO derivates such as 4-oxo-TEMPO and AcNH-TEMPO were also investigated in the all-organic system. Jeon *et al.*[65] proposed a cell system featuring 4-oxo-TEMPO and (1S)-(+)camphorquinone as the catholyte and anolyte, respectively. The authors have shown that functionalizing the TEMPO backbone with an electron-donating group increases its oxidation potential. The RFB exhibits a cell voltage of 2.1 V in propylene carbonate but suffered from poor cycling performance due to crossover. Generally, TEMPO demonstrates good chemical stability in organic RFBs except for the issue of crossover in the system. As such, size exclusion approach was implemented to provide better resistance to crossover. In addition, functionalization with electron-withdrawing groups in the TEMPO backbone can further improve the formal redox potential of TEMPO. Ideally, a cross-over free system with stable redox active species enables the RFB to operate with infinite life cycle. In reality, concentration gradient across the membrane is often established when two different redox active species are deployed in a RFB system. This leads to irreversible capacity losses due to crossover by diffusion process. Strategies such as a size exclusion approach and using mixed-reactants can effectively improve the cyclability of the battery system. The design of mixed-reactant electrolytes mitigates the crossover by minimizing the concentration gradient across the membrane. During the charging process, the presence of neutral counterpart does not interact with the charged redox molecules, but as a trade-off, only half of the material concentrations are utilized for energy storage.

TEMPO is an ambipolar organic radical which can undergo one-electron oxidation and reduction to form the oxoammonium cation and aminoxyl anion from the neutral radical,

respectively. TEMPO can potentially act as both catholyte and anolyte in RFB system. However, the aminoxyl anion demonstrates poor chemical stability due to fast proton transfer with the electrolytes. In a recent study, Izgorodina *et al.*[66] have successfully stabilized the aminoxyl anion of TEMPO by suppressing the proton transfer (PT) side reactions with an ionic liquid. The results from their studies have shown that the anion-cation combination of the ionic liquids can influence the reactivity of the aminoxyl anion towards proton transfer reactions. In addition, the ionic liquid, [C_4mpyr][OTf] also helps to stabilize the TEMPO radical which can be seen from the negative shift in the reduction potential from -0.9 V to -1.8 V. In over 200 CV scans, TEMPO exhibited a near identical voltammetric profile, indicating that the reduction process of TEMPO in [C_4mpyr][OTf] is chemically reversible under CV timescales. In this proof-of-concept study, the symmetric cell system with TEMPO species was able to achieve a redox potential of 2.5 V.

Interestingly, Wei *et al.*[34] have demonstrated a nitronyl nitroxide radical-based symmetric all-organic RFB using 2-phenyl-4,4,5,5-tetramethylimidazoline-1-oxyl-3-oxide (PTIO). Similar to TEMPO, PTIO undergoes an ambipolar redox reaction to form an oxoammonium cation ($PTIO^+$) catholyte and an aminoxyl anion ($PTIO^-$) anolyte. The flow cell exhibited a moderately high cell potential of 1.73 V in acetonitrile. Ideally, the crossover of the charged species in a symmetric system should self-discharge back to its original form. However, in the case of PTIO, it experienced a continuous capacity fading which may be due to the poor chemical stability of the aminoxyl anion ($PTIO^-$). In another work, Schubert *et al.*[67] designed and fabricated a bipolar nitronyl nitroxide for a symmetric all-organic RFB. The organic molecule is made up of two nitronyl nitroxide (NN) pendant units connected with a triethylene glycol linker. The presence of the ethylene glycol chain helped to improve the solubility in acetonitrile (3.8 M). The synthesized compound exhibits twice the energy capacity compared to a single NN unit since each molecule comprises two redox active NN units. The

symmetric system offers a cell voltage of 1.62 V. However, during the cycling test, the cell system experienced a drastic capacity decay of nearly 50 %. Similar to PTIO, the chemical degradation may correspond to stability issue arise from the aminoxyl anion (NN^-). Furthermore, at higher concentration, the charged species precipitated during the cycling test. The benefit of symmetric system is the ability to reduce detrimental effects caused by physical crossover. Ideally, there should not be any net loss to the redox active species since the system can be restored through electrolyte mixing. However, the reduction of nitronyl nitroxide-based compounds yields a chemically unstable aminoxyl anion, resulting in continuous capacity losses. As such, the symmetric system is only practically feasible provided the charged and neutral species are chemically stable and soluble in the solvent system.

1.2.4 Aromatics

Generally, an aromatic compound refers to chemical compound that possesses planarity with a cyclic conjugated structure (Figure 1.6). The number of electrons in the delocalized π systems should fulfil the Hückel's rule of [4n+2] π electrons, where n is an integer. The electron that is delocalized by resonance helps to increase the stability in the system.[68]

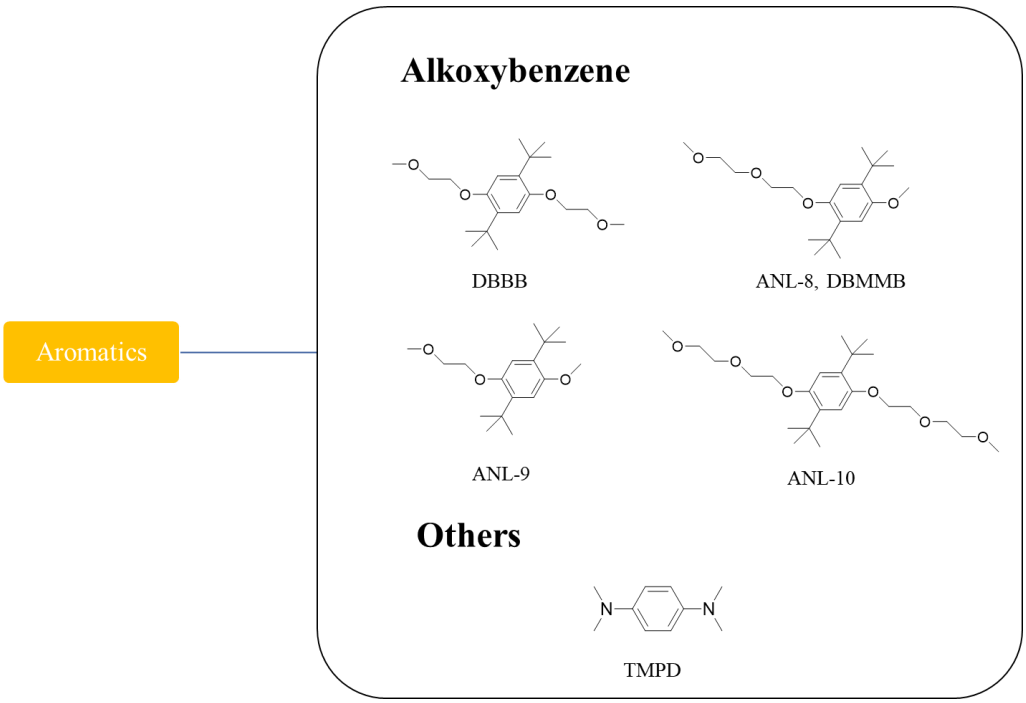

Figure 1.6. Chemical structures of organic compounds classified under aromatics.

Alkoxybenzene redox active species have been widely used as potential catholytes in organic RFBs. The use of DBBB in RFBs was introduced by Jansen *et al.*[17] DBBB undergoes a reversible one-electron oxidation at 4.022 V vs Li/Li^+ to form a stable radical cation, $DBBB^{\bullet+}$. To further improve the solubility of DBBB (~ 0.4 M) in carbonate based electrolyte, Zhang *et al.*[21] adopted two different approaches: (1) incorporating a poly ethylene oxide (PEO) chain into the alkoxybenzene motif, and (2) increasing polarity of alkoxybenzenes by creating an additional intramolecular dipole moment. As such, the authors have synthesized three different analogues of DBBB, namely ANI-8, ANI-9 and ANL-10 (Figure 1.6). Due to the difference in dipole moment, ANI-8 and ANI-9 exist in liquid form while ANL-10 exist in semi-liquid state at room temperature. The chemical modification with a PEO chain shows improvements in solubilities without affecting the electrochemical behavior. As mentioned in section 1.2.2, tailoring compatible functional groups to improve physicochemical properties for redox active molecules is an effective approach to achieve better cell performance. Among the three analogues, ANI-8, DBMMB is well-suited to develop into a high energy density RFB due to

its low viscosity and high miscibility with the solvent system. Generally, organic electrolytes with low viscosity are preferred since viscosity is positively associated with pump performance losses. DBMMB has demonstrated excellent chemical stability under exhaustive electrolysis and also in various all-organic RFB systems such as MePh/DBMMB, FL/DBMMB and BzNSN/DBMMB.[24, 44, 46] The outstanding chemical stability of $DBMMB^{\bullet+}$ is due to the charge stabilization by aromatic resonance and electron-donating effects from the alkoxy substituents, as well as steric protection by bulky substituents (i.e *t*-butyl group) at the 2 and 5 positions.

In a different work, Oh *et al.*[69] proposed phenylenediamine (PD), an aromatic diamine to use for organic RFBs. Unlike DBMMB, PD molecules can potentially deliver higher energy capacity due to their ability to undergo two-electron oxidation. The PD molecule was chemically modified by replacing the hydrogen atoms on the $-NH_2$ with methyl substituents. The resultant molecule, *N,N,N',N'*-tetramethyl-p-phenylenediamine (TMPD) exhibits a ten-fold increase in solubility from <0.5 M to 5.0 M in propylene carbonate and the stability of the dication was enhanced by steric protection. In the proof-of concept study, the cell system coupled with Li metal exhibits stable cycling stability over 450 cycles in a coin-cell configuration.

The benefits of using aromatic compounds in organic RFBs is the exceptional chemical stability of the systems attributed by resonance stabilization through cyclic conjugation. Various design and modifications of aromatic compounds have been proposed to increase the solubility limitations. Further research efforts can be directed towards improving the oxidation potential of these proposed aromatic compounds or focus on discovering new organic aromatic compounds with high oxidation potentials for practical applications.

1.2.5 Carbonyl Compounds

Carbonyl compounds are molecules containing the carbonyl functional group (C=O) and they are susceptible to one-electron transfer to yield either a radical carbon bonded to a negatively charged oxygen (•C-O$^-$) or its mesomeric structure containing a radical oxygen attached to a negatively charged carbon ($^-$C-O•).[70] Converting such molecules to their charged forms will involve the formation of radical ions which are highly unstable. Therefore, the carbonyl functional group is commonly connected to a conjugated system for charge delocalization. Carbonyl compounds such as quinones, benzophenones and fluorenones have been reported in RFB studies (Figure 1.7).

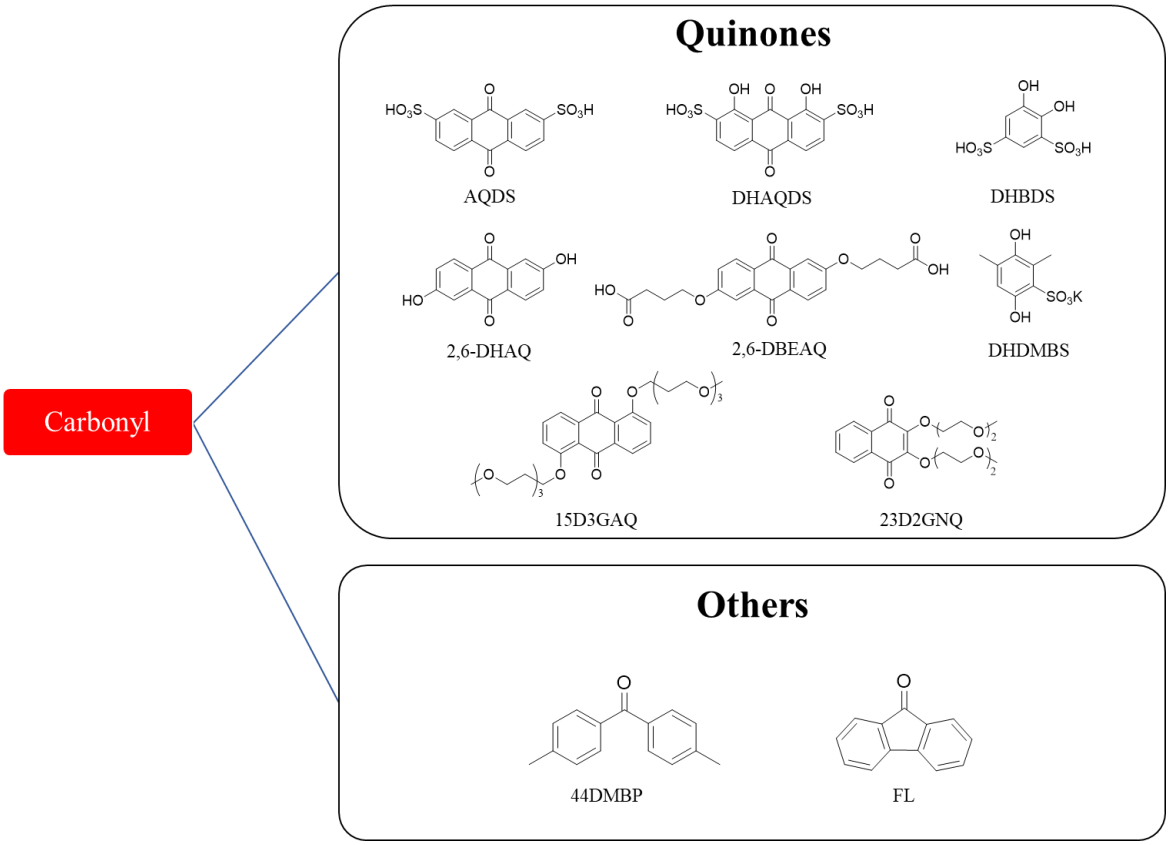

Figure 1.7. Chemical structures of organic compounds classified under carbonyl group.

Quinones have been extensively studied in aqueous RFBs, which have provided important information in relation to their redox mechanism. Under aqueous conditions,

quinones generally exhibits a two-electron per molecular storage capability since they undergo a reversible two-electron reduction. Aziz *et al.*[38] have reported a metal-free RFB based on 9-10-anthraquinone-2,7-disulphonic acid (AQDS) and bromide. Under acidic conditions, AQDS involves a consecutive two-electron and two-proton transfer (PCET) reduction process. The charged form of the AQDS was stabilized via protonation in acidic medium, forming the stable dihydroquinone. Combining with the Br_2/Br^- redox couple, the cell system exhibits a high cycling stability with 99% capacity retention over 15 cycles. To improve on the overall cell performance, understanding the relationship between the chemical structure and specific properties is important for fine-tuning the key properties of organic redox molecules. The study of 1,8-dihydroxy-9,10-anthraquinone-2,7-disulphonic acid (DHAQDS) has shown that increasing number of -OH groups in the anthraquinone (AQ) core structure of AQDS leads to the lowering of reduction potential by approximately -50 mV/OH group. The addition of -OH groups also help to further improve solubility in water due to hydrogen bonding effects. However, the crossover of bromine limits the performance of the battery system. Later, Narayanan *et al.*[12] constructed an all-organic acidic aqueous RFB with anthraquinone-2-6 disulfonic acid (AQDS) as the anolyte and 1,2-dihydrobenzoquinone-3,5-disulfonic acid (DHBDS) as the catholyte. A previous study by the group demonstrated that 1,2-benzoquinone-3,5-disulfonic acid (BQDS) exhibits higher solubility (~1.7 M) as opposed to benzoquinone (0.1 M) due to the incorporation of -OH and sulfonic acid ($-SO_3^-$) functional groups. The incorporation of polar or hydrophilic substituents (e.g. -OH, $-SO_3H$, $-NH_2$ and -COOH) can effectively improve the concentration of quinones in aqueous electrolytes.[71] In this work, the presence of $-SO_3^-$ also increases the formal oxidation potential of DHBDS due to the electron-withdrawing effect. Under extended cycling, DHBDS was found to undergo hydroxylation at the 4- and 6-position due to Michael addition of water, yielding 1,2,4,6-tetrahydroxybenzene-3,5-disulfonic acid.[72] To overcome such a problem, the authors have synthesized a new

analogue of DHBDS, 3,6-dihydroxy-2,4-dimethylbenzenesulfonic (DHDMBS), with only one unsubstituted position on the core structure.[73] As a result, the cell system, DHDMBS/AQDS was able to achieve close to 100 % coulombic efficiency over 25 cycles. The structure-property relationship has provided critical information on the connection between molecular design, redox potential, and degradation mechanisms to guide rational design and optimization of organic redox compounds for RFB applications.

Other than an acidic medium, the use of quinones in RFBs has been extended to alkaline conditions. Aziz *et al.*[74] have proposed the use of 2,6-dihydroxyanthraquinone (2,6-DHAQ) as the anolyte and ferro/ferricyanide as the catholyte to construct a flow cell with a potential of 1.2 V. Under alkaline conditions, 2,6-DHAQ undergoes a reversible two-electron reduction process. The cell exhibits a coulombic efficiency exceeding 99% over 100 cycles, which shows that 2,6-DHAQ has good cycling stability. Results have also suggested that increasing the number of -OH substituents on 2,6-DHAQ can potentially increase the redox potential and solubility in alkaline conditions. To further improve the battery lifetime, the authors have chemically modified 2,6-DHAQ by replacing the -OH group with an ether-linked alkyl chain containing carboxylate functional groups to form 4,4'-((9,10-anthraquinone-2,6-diyl)dioxy)dibutyrate (2,6-DBEAQ).[75] Although 2,6-DBEAQ exhibits a slightly higher redox potential, the reduced form was stabilized by removing the hydroxyl group that is known to cause intramolecular electrostatic repulsion. As such, the symmetric cell testing coupled with ferri/ferrocyanide demonstrate a remarkable battery lifetime with a marginal capacity fading of <0.01 % / day over 26 days.

In contrary to aqueous RFB, anthraquinone (AQ) exhibits low solubility in highly polar organic solvents. To address the concern, Wang *et al.*[76] have reported a chemically modified AQ which shows improved solubility in polar organic solvents. The authors introduced

triethylene glycol chains into the 1 and 5 positions of the AQ core structure. However, results from CV studies and cycling tests showed that the charged species of AQ demonstrates poor chemical stability in carbonate solvents. In another work, Shimizu *et al.*[77] designed and synthesized a liquid quinone for a solvent-free RFB. A diethylene glycol chain was incorporated into benzoquinone and naphthoquinone to liquify them by lowering their melting points. The liquid benzoquinone undergoes a concerted two-electron reduction at -0.64 V vs Fc/Fc^+ while liquid naphthoquinone displayed two closely spaced reduction peaks at -0.85 V and – 0.98 V vs Fc/Fc^+, respectively, in $LiBF_4$/propylene carbonate. Based on the observation from the studies, benzoquinone exhibited a poorer chemical stability compared to naphthoquinone in the carbonate solvent. The high nucleophilicity of the benzoquinone dianion due to its low π conjugation may enable it to attack the solvent molecules. In a solvent-free cycling test, liquid naphthoquinone demonstrates good cycling stability over 10 cycles and exhibits a remarkable discharge energy density of 264 W h L^{-1}. However, due to the high viscosity (179.8 mPa s), the proposed solvent-free system requires a greater pump energy to facilitate the electrolyte flow and also, further optimization is necessary to improve the ionic conductivity. Although quinones are considered promising organic redox molecules for RFB applications, the lack of chemical stability in organic electrolyte impedes its implementation in organic RFBs.

Apart from quinones, other less-investigated carbonyl compounds such as benzophenone (BP) and 9-fluorenone (9-FL) have been reported for organic RFBs. Li *et al.*[43] have introduced BP as anolyte material to develop a high potential organic RFB. The addition of an electron-donating group resulted in an increase in the redox potential of BP. The functionalized BP, 4,4'-dimethylbenzophenone (44DMBP) undergoes a reversible one-electron reduction process at a redox potential of -2.26 V vs Ag/Ag^+ in $TEAPF_6$/MeCN and coupling with DBB yields a cell voltage of 3.08 V. However, the high energy radical species, $44DMBP^{\bullet-}$ was found to

interact with the electron-deficient solvent molecules and supporting electrolytes, resulting in capacity fading over time. Similar phenomena were observed in the case of 9-fluorene (FL). Wang *et al.*[24] reported an all-organic FL/DBMMB RFB system. FL undergoes a reversible one-electron reduction process at a redox potential of -1.64 V vs Ag/Ag^+ with a high solubility of 2.0 M in acetonitrile. The result from ESR suggests that the charged species of FL, $FL^{\bullet-}$, was prone to chemical degradation associated with the interaction with solvents and electrolytes, and also dimerization processes.

1.3 Thesis Objectives

Most organic compounds used in organic (non-aqueous) system are neutral, closed-shell molecules. Converting such molecules into their charged form involves the generation of radicals and other highly reactive charged species that are susceptible to various loss mechanisms. The challenge of stabilizing radical ions is more pronounced for the negative half-cell (i.e. the anolyte).[24] In section 1.2.2 and 1.2.5, the proposed anolyte materials, MePh, 44DMBP and FL were subjected to irreversible degradation that were caused by an incompatible electrolyte system and decomposition due to free radical mechanisms. The poor chemical stability of the charged species reduces the efficiency of the battery as seen from the capacity losses upon each successive charge-discharge cycle. The compatibility between the redox-active species and other chemical components (i.e. solvent and supporting electrolyte) is therefore highly important to sustain chemical stability.

Radical or charge stabilization can also be achieved through electronic resonance, steric effects (e.g. DBMMB and TMPD) and the presence of additives (e.g. quinones). Compounds with extensive conjugated networks (e.g. BzNSN) can help to delocalize charge density and the presence of electron-withdrawing/donating groups can facilitate charge stability via inductive effects, thereby promoting stability of charged species. Although, the

use of bulky functional group provides steric protection, it will ultimately compromise solubility and limit the energy density of the system. As such, the present study does not regard steric crowding as a viable strategy for stabilization. In reality, computational simulation may not be sufficient to rationalize the stability of charged species. Consequently, the search for compatible organic redox couples for organic RFB remains highly elusive.

The objective of this study is to examine new organic redox molecules that exhibit high chemical stability and reversibility in organic system for the development towards the application of RFBs. The present study focuses on the electrochemical aspects of the organic molecules. Battery testing or engineering considerations for flow cell will not be comprehensively included in this study. In chapter 2, preliminary studies were conducted to evaluate the electrochemical behavior of several organic molecules in organic systems. To circumvent the need for expensive membranes, a mixed-reactant system is proposed to reduce material crossover by minimizing the concentration gradient across the membrane. Two new mixed-reactant electrolyte systems will be further discussed and assessed in Chapters 3 and 4.

1.4 Dissertation Overview

This thesis describes the development of new organic-based mixed reactant electrolytes that can be integrated into the design of all-organic battery for RFB applications.

Chapter 1 identifies the problems associated with the traditional RFBs and reviews published work on four main classifications of organic compounds that were implemented in aqueous and organic RFBs, which include (i) aromatic heterocycles, (ii) nitroxide radicals, (iii) aromatic compounds and (iv) carbonyl compounds. This review discusses the common problems associated with organic compounds in organic systems, highlights the objectives of this thesis, and describes the approach to address these problems.

Chapter 2 discusses the electrochemical performances of several organic compounds. Four potential organic compounds were identified based on their chemical reversibility, stability, and redox potentials in organic electrolyte solutions. The studies have also shown that additives can stabilize charged species in organic electrolytes.

Chapter 3 discusses the electrochemical performance of a mixed-reactant electrolyte system that involved the transfer of two-electron per molecule. The electrochemical performance of different quinone and benzidine derivatives were evaluated. The best performing quinone and benzidine derivatives, anthraquinone (AQ) and 3,3′,5,5′-tetramethylbenzidine (TMB), respectively, were subjected to mixed reactant system for evaluation under various conditions.

Chapter 4 discusses the effects that additives impart towards tuning the redox potential of a vitamin K analogue (VKA) by different reduction mechanisms. VKA was chemically modified to improve its solubility in CH_3CN with the incorporation of ethylene glycol ether side chains. The mixed reactant system consisting of the modified VKA and a vitamin E analogue (VEA) were evaluated to determine its practical feasibility.

Chapter 5 demonstrates the use of 3D printing technology to fabricate laboratory test cell components and the benefits of 3D-printing in RFB research were discussed.

Chapter 6 summarizes the findings from each chapter. A thorough overview of new findings in each case was given. This chapter also provides recommendation for further work to optimize the performance of the proposed organic-based electrolyte systems.

1.5 Findings and Outcomes/Originality

This research led to several outcomes by:

1. Screening and identifying new organic compounds that can potentially be used in energy storage applications.
2. Developing a new two-electron storage capable organic electrolyte consisting of anthraquinone and *o*-tolidine in a mixed reactant system with the addition of trifluoroacetic acid.
3. Proposing the use of additives to tune the redox potential of quinone-based organic compounds.
4. Developing a new mixed reactant organic electrolyte system that consists of analogues of vitamin K and vitamin E in the presence of diethyl malonate.

The findings contributed to the search for a reliable and stable organic-based electrolyte system that can be incorporated in the design of an all-organic battery suited for a future electrochemical energy storage system.

References

1. Alotto, P.; Guarnieri, M.; Moro, F. *Renew. Sust. Energ. Rev.* **2014,** *29*, 325-335.

2. Dunn, B.; Kamath, H.; Tarascon, J.-M. *Science.* **2011,** *334*, 928-935.

3. Lewis, N. S.; Nocera, D. G. *Proc. Natl. Acad. Sci. U.S.A.* **2006,** *103*, 15729-15735.

4. Pan, F.; Wang, Q. *Molecules.* **2015,** *20*, 20499-517.

5. Larcher, D.; Tarascon, J. M. *Nat. Chem.* **2015,** *7*, 19-29.

6. Chow, J.; Kopp, R. J.; Portney, P. R. *Science.* **2003,** *302*, 1528-1531.

7. Soloveichik, G. L. *Chem. Rev.* **2015,** *115*, 11533-11558.

8. Wang, W.; Luo, Q.; Li, B.; Wei, X.; Li, L.; Yang, Z. *Adv. Funct. Mater.* **2013,** *23*, 970-986.

9. Luo, X.; Wang, J.; Dooner, M.; Clarke, J. *Appl. Energy.* **2015,** *137*, 511-536.

10. Shin, S.-H.; Yun, S.-H.; Moon, S.-H. *RSC Adv.* **2013,** *3*, 9095-9116.

11. Wedege, K.; Dražević, E.; Konya, D.; Bentien, A. *Sci. Rep.* **2016,** *6*, 39101.

12. Yang, B.; Hoober-Burkhardt, L.; Wang, F.; Surya Prakash, G. K.; Narayanan, S. R. *J. Electrochem. Soc.* **2014,** *161*, A1371-A1380.

13. Badwal, S. P. S.; Giddey, S. S.; Munnings, C.; Bhatt, A. I.; Hollenkamp, A. F. *Front. Chem.* **2014,** *2*.

14. *Electrical energy storage technology options*; 1020676; Electric Power Research Institute: Palo Alto, CA, December, 2010.

15. US Department of Energy, O. o. E. D. E. R. Global Energy Storage Database. https://www.sandia.gov/ess-ssl/global-energy-storage-database-home/ (accessed December 26th, 2020).

16. Winsberg, J.; Hagemann, T.; Janoschka, T.; Hager, M. D.; Schubert, U. S. *Angew. Chem. Int. Ed.* **2017,** *56*, 686-711.

17. Brushett, F. R.; Vaughey, J. T.; Jansen, A. N. *Adv. Energy Mater.* **2012,** *2*, 1390-1396.

18. Divya, K. C.; Østergaard, J. *Electr. Power Syst. Res.* **2009,** *79*, 511-520.

19. Tang, A.; Bao, J.; Skyllas-Kazacos, M. *J. Power Sources.* **2014,** *248*, 154-162.

20. Largent, R. L.; Skylas-Kazacos, M.; Chieng, J. *Improved PV system performance using vanadium batteries*, Conference Record of the Twenty Third IEEE Photovoltaic Specialists Conference - 1993 (Cat. No.93CH3283-9), 10-14 May; 1993; pp 1119-1124.

21. Huang, J.; Cheng, L.; Assary, R. S.; Wang, P.; Xue, Z.; Burrell, A. K.; Curtiss, L. A.; Zhang, L. *Adv. Energy Mater.* **2015,** *5*, 1401782.

22. Wei, X.; Pan, W.; Duan, W.; Hollas, A.; Yang, Z.; Li, B.; Nie, Z.; Liu, J.; Reed, D.; Wang, W.; Sprenkle, V. *ACS Energy Lett.* **2017,** *2*, 2187-2204.

23. Lin, K.; Gómez-Bombarelli, R.; Beh, E. S.; Tong, L.; Chen, Q.; Valle, A.; Aspuru-Guzik, A.; Aziz, M. J.; Gordon, R. G. *Nat. Energy.* **2016,** *1*, 16102.

24. Wei, X.; Xu, W.; Huang, J.; Zhang, L.; Walter, E.; Lawrence , C.; Vijayakumar, M.; Henderson, W. A.; Liu, T.; Cosimbescu, L.; Li, B.; Sprenkle, V.; Wang, W. *Angew. Chem. Int. Ed.* **2015,** *54*, 8684-8687.

25. Li, L.; Kim, S.; Wang, W.; Vijayakumar, M.; Nie, Z.; Chen, B.; Zhang, J.; Xia, G.; Hu, J.; Graff, G.; Liu, J.; Yang, Z. *Adv. Energy Mater.* **2011,** *1*, 394-400.

26. Leung, P.; Shah, A. A.; Sanz, L.; Flox, C.; Morante, J. R.; Xu, Q.; Mohamed, M. R.; Ponce de León, C.; Walsh, F. C. *J. Power Sources.* **2017,** *360*, 243-283.

27. Skyllas-Kazacos, M.; Cao, L.; Kazacos, M.; Kausar, N.; Mousa, A. *ChemSusChem.* **2016,** *9*, 1521-1543.

28. Rahman, F.; Skyllas-Kazacos, M. *J. Power Sources.* **1998,** *72*, 105-110.

29. Vijayakumar, M.; Li, L.; Graff, G.; Liu, J.; Zhang, H.; Yang, Z.; Hu, J. Z. *J. Power Sources.* **2011,** *196*, 3669-3672.

30. Zeng, Y. K.; Zhao, T. S.; An, L.; Zhou, X. L.; Wei, L. *J. Power Sources.* **2015,** *300*, 438-443.

31. Bae, C. H.; Roberts, E. P. L.; Dryfe, R. A. W. *Electrochim. Acta.* **2002,** *48*, 279-287.

32. Xu, Z.; Fan, Q.; Li, Y.; Wang, J.; Lund, P. D. *Renew. Sust. Energ. Rev.* **2020,** *127*, 109838.

33. Guo, L.; Guo, H.; Huang, H.; Tao, S.; Cheng, Y. *Front. Chem.* **2020,** *8*.

34. Duan, W.; Vemuri, R. S.; Milshtein, J. D.; Laramie, S.; Dmello, R. D.; Huang, J.; Zhang, L.; Hu, D.; Vijayakumar, M.; Wang, W.; Liu, J.; Darling, R. M.; Thompson, L.; Smith, K.; Moore, J. S.; Brushett, F. R.; Wei, X. *J. Mater. Chem. A.* **2016,** *4*, 5448-5456.

35. Chiang, Y.-M. *Science.* **2010,** *330*, 1485-1486.

36. Crawford, A.; Viswanathan, V.; Stephenson, D.; Wang, W.; Thomsen, E.; Reed, D.; Li, B.; Balducci, P.; Kintner-Meyer, M.; Sprenkle, V. *J. Power Sources.* **2015,** *293*, 388-399.

37. Liu, T.; Wei, X.; Nie, Z.; Sprenkle, V.; Wang, W. *Adv. Energy Mater.* **2016,** *6*, 1501449.

38. Huskinson, B.; Marshak, M. P.; Suh, C.; Er, S.; Gerhardt, M. R.; Galvin, C. J.; Chen, X.; Aspuru-Guzik, A.; Gordon, R. G.; Aziz, M. J. *Nature.* **2014,** *505*, 195-198.

39. Zhang, C.; Zhang, L.; Ding, Y.; Peng, S.; Guo, X.; Zhao, Y.; He, G.; Yu, G. *Energy Storage Mater.* **2018,** *15*, 324-350.

40. Singh, V.; Kim, S.; Kang, J.; Byon, H. R. *Nano Res.* **2019,** *12*, 1988-2001.

41. Armstrong, C. G.; Toghill, K. E. *Electrochem. Commun.* **2018,** *91*, 19-24.

42. Kaur, A. P.; Holubowitch, N. E.; Ergun, S.; Elliott, C. F.; Odom, S. A. *Energy Technol.* **2015,** *3*, 476-480.

43. Huo, Y.; Xing, X.; Zhang, C.; Wang, X.; Li, Y. *RSC Adv.* **2019,** *9*, 13128-13132.

44. Wei, X.; Duan, W.; Huang, J.; Zhang, L.; Li, B.; Reed, D.; Xu, W.; Sprenkle, V.; Wang, W. *ACS Energy Lett.* **2016,** *1*, 705-711.

45. Xing, X.; Huo, Y.; Wang, X.; Zhao, Y.; Li, Y. *Int. J. Hydrogen Energy.* **2017,** *42*, 17488-17494.

46. Duan, W.; Huang, J.; Kowalski, J. A.; Shkrob, I. A.; Vijayakumar, M.; Walter, E.; Pan, B.; Yang, Z.; Milshtein, J. D.; Li, B.; Liao, C.; Zhang, Z.; Wang, W.; Liu, J.; Moore, J. S.; Brushett, F. R.; Zhang, L.; Wei, X. *ACS Energy Lett.* **2017,** *2*, 1156-1161.

47. Gong, K.; Fang, Q.; Gu, S.; Li, S. F. Y.; Yan, Y. *Energy Environ. Sci.* **2015,** *8*, 3515-3530.

48. Gupta, R. R.; Kumar, M.; Gupta, V. *Heterocyclic chemistry*; Springer: New York, 1998.

49. Orita, A.; Verde, M. G.; Sakai, M.; Meng, Y. S. *Nat. Commun.* **2016,** *7*, 13230.

50. Grajek, H. *J. Mol. Liq.* **2015,** *209*, 169-186.

51. Koziol, J.; Metzler, D. E. *Z. Naturforsch. B.* **1972,** *27*, 1027-1029.

52. Hollas, A.; Wei, X.; Murugesan, V.; Nie, Z.; Li, B.; Reed, D.; Liu, J.; Sprenkle, V.; Wang, W. *Nat. Energy.* **2018,** *3*, 508-514.

53. Janoschka, T.; Martin, N.; Hager, M. D.; Schubert, U. S. *Angew. Chem. Int. Ed.* **2016,** *55*, 14427-14430.

54. Madasamy, K.; Velayutham, D.; Suryanarayanan, V.; Kathiresan, M.; Ho, K.-C. *J. Mater. Chem. C.* **2019,** *7*, 4622-4637.

55. Sen, S.; Saraidaridis, J.; Kim, S. Y.; Palmore, G. T. R. *ACS Appl. Mater. Interfaces.* **2013,** *5*, 7825-7830.

56. Beh, E. S.; De Porcellinis, D.; Gracia, R. L.; Xia, K. T.; Gordon, R. G.; Aziz, M. J. *ACS Energy Lett.* **2017,** *2*, 639-644.

57. DeBruler, C.; Hu, B.; Moss, J.; Liu, X.; Luo, J.; Sun, Y.; Liu, T. L. *Chem.* **2017,** *3*, 961-978.

58. Hicks, R. G. *Stable Radicals: Fundamentals and Applied Aspects of Odd-Electron Compounds*; John Wiley & Sons: United Kingdom, 2010.

59. Liu, Y.; Goulet, M.-A.; Tong, L.; Liu, Y.; Ji, Y.; Wu, L.; Gordon, R. G.; Aziz, M. J.; Yang, Z.; Xu, T. *Chem.* **2019,** *5*, 1861-1870.

60. Wei, X.; Xu, W.; Vijayakumar, M.; Cosimbescu, L.; Liu, T.; Sprenkle, V.; Wang, W. *Adv. Mater.* **2014,** *26*, 7649-7653.

61. Yu, X.; Yu, W. A.; Manthiram, A. *ACS Appl. Mater. Interfaces.* **2020,** *12*, 48654-48661.

62. Li, Z.; Li, S.; Liu, S.; Huang, K.; Fang, D.; Wang, F.; Peng, S. *Electrochem. Solid-State Lett.* **2011,** *14*, A171.

63. Kosswattaarachchi, A. M.; Cook, T. R. *Electrochim. Acta.* **2018,** *261*, 296-306.

64. Baran, M. J.; Braten, M. N.; Montoto, E. C.; Gossage, Z. T.; Ma, L.; Chénard, E.; Moore, J. S.; Rodríguez-López, J.; Helms, B. A. *Chem. Mater.* **2018,** *30*, 3861-3866.

65. Park, S.-K.; Shim, J.; Yang, J.; Shin, K.-H.; Jin, C.-S.; Lee, B. S.; Lee, Y.-S.; Jeon, J.-D. *Electrochem. Commun.* **2015,** *59*, 68-71.

66. Wylie, L.; Blesch, T.; Freeman, R.; Hatakeyama-Sato, K.; Oyaizu, K.; Yoshizawa-Fujita, M.; Izgorodina, E. I. *ACS Sustainable Chem. Eng.* **2020,** *8*, 17988-17996.

67. Hagemann, T.; Winsberg, J.; Häupler, B.; Janoschka, T.; Gruber, J. J.; Wild, A.; Schubert, U. S. *NPG Asia Mater.* **2017,** *9*, e340-e340.

68. Ouellette, R. J.; Rawn, J. D., In *Principles of Organic Chemistry*, Ouellette, R. J.; Rawn, J. D., Eds. Elsevier: Boston, 2015; pp 133-162.

69. Kim, H.-s.; Lee, K.-J.; Han, Y.-K.; Ryu, J. H.; Oh, S. M. *J. Power Sources.* **2017,** *348*, 264-269.

70. Lee, K. N.; Ngai, M.-Y. *Chem. Commun.* **2017,** *53*, 13093-13112.

71. Er, S.; Suh, C.; Marshak, M. P.; Aspuru-Guzik, A. *Chem. Sci.* **2015,** *6*, 885-893.

72. Yang, B.; Hoober-Burkhardt, L.; Krishnamoorthy, S.; Murali, A.; Prakash, G. K. S.; Narayanan, S. R. *J. Electrochem. Soc.* **2016,** *163*, A1442-A1449.

73. Hoober-Burkhardt, L.; Krishnamoorthy, S.; Yang, B.; Murali, A.; Nirmalchandar, A.; Prakash, G. K. S.; Narayanan, S. R. *J. Electrochem. Soc.* **2017,** *164*, A600-A607.

74. Lin, K.; Chen, Q.; Gerhardt, M. R.; Tong, L.; Kim, S. B.; Eisenach, L.; Valle, A. W.; Hardee, D.; Gordon, R. G.; Aziz, M. J.; Marshak, M. P. *Science.* **2015,** *349*, 1529-1532.

75. Kwabi, D. G.; Lin, K.; Ji, Y.; Kerr, E. F.; Goulet, M.-A.; De Porcellinis, D.; Tabor, D. P.; Pollack, D. A.; Aspuru-Guzik, A.; Gordon, R. G.; Aziz, M. J. *Joule.* **2018,** *2*, 1894-1906.

76. Wang, W.; Xu, W.; Cosimbescu, L.; Choi, D.; Li, L.; Yang, Z. *Chem. Commun.* **2012,** *48*, 6669-6671.

77. Shimizu, A.; Takenaka, K.; Handa, N.; Nokami, T.; Itoh, T.; Yoshida, J.-I. *Adv. Mater.* **2017,** *29*, 1606592.

Chapter 2

Electrochemical Studies of Potential Anolytes and Catholytes for Organic-based Redox Flow Battery

---

2.1 Introduction

The most important consideration to develop a functional redox flow battery is determined by the selection of the redox active species. The current stage of research pertaining to the use of organic redox couples revolves around various classes of organic compounds such as heterocyclic aromatics, nitroxide radicals and aromatics and carbonyls. Capacity decay due to chemical instability remains the key challenge that hinders the practicality of organic redox species in redox flow battery applications. As discussed in section 1.2.2 and 1.2.5, many of the organic species in the reported studies are subject to irreversible degradation such as decomposition (e.g. *N*-Methylphthalimide, MePh) or parasitic side reactions (e.g. 9-fluorenone, FL) that were caused by an incompatible electrolyte system or other interferences, resulting in material losses.[1-3] For example, the high energy radical species, $FL^{\bullet-}$ was prone to dimerization and also susceptible to interaction with solvent molecules and supporting electrolyte. Unlike the metal-based redox couples, most of the neutral organic compounds involves formation of radical ions through gaining or losing electrons during charging. The chemical instability or reactivity of many radical ions reduces the efficiency of the battery due to capacity losses upon each successive charge-discharge cycle. Radical anions can be air sensitive and can possibly undergo irreversible hydrolysis reactions in the presence of trace water. As such, most of the previous studies are conducted in highly controlled environments such as argon-filled gloveboxes to rule out any unwanted atmospheric interference. In general, the stabilization of radical ions can be achieved through electronic resonance (e.g. extensive conjugated networks), steric effects (e.g. bulky substituent), or the addition of additives (e.g. Bronsted acid).[4-6] However, the strategy to impart radical stability via steric effects was not considered viable in the redox flow battery context because introducing very bulky substituents or using bulky molecules would compromise solubility and limit the energy density of the system.

In this chapter, preliminary studies were conducted on several organic compounds as sources for suitable anolytes and catholytes for the organic-based electrolyte system. The selected organic compounds should possess high chemical stability and reversibility under robust environments. The electrochemical properties of the compounds were evaluated with a set of tests consisting of CV analysis, controlled potential electrolysis (CPE) and UV-vis spectroscopy.

2.2 Experimental and Methods

2.2.1 *Chemicals and reagents*

Most chemical and reagents were purchased from chemicals company and used as received unless otherwise stated. N,N'-di-2-naphthyl-1,4-phenylenediamine (> 96%), 7,7,8,8-tetracyanoquinodimethane (TCNQ) (> 98%) and 2,1,3-benzothiadiazole (> 99%) were obtained from Tokyo Chemical Industry Co., Ltd., *p*-Phenylenediamine (> 99%), N,N'-diphenyl-1,4-phenylenediamine (98%), 2,3,5,6-tetramethyl-1,4-phenylenediamine (electronic grade, 99% trace metal analysis), 3,3'5,5'-tetramethylbenzidine (> 99%), 4-nitrobenzene (> 99%), octafluoronapthalene (> 96%), 4-nitrophenol (> 99%), phenyl-2-pyridinylmethanone (> 99%), 4,4-dipyridyl (> 98%), and quinoxaline (99%) were bought from Sigma-Aldrich. 2,3,6-trimethylquinoxaline (97%) was bought from Alfa-Aesar. Acetonitrile (CH_3CN) used was HPLC grade and was purchased from Anhui Fulltime Solvents & Reagents Co., Ltd. VEA was synthesized based on a previous reported procedure.[7] VKA was synthesized based on a modified procedure (Chapter 4.7). The supporting electrolyte, tetrabutylammonium hexafluorophosphate (*n*-Bu_4NPF_6), was synthesized by mixing equivalent molarity of 40% tetrabutylammonium hydroxide (*n*-Bu_4NOH) solution (Alfa-Aesar) with 60% hexafluorophosphoric acid (HPF_6) acid solution (Alfa-Aesar). The precipitate was washed with deionized water repeatedly until the pH of the filtrate was above pH 5, and subsequently

purifying the crude product via recrystallization for three times from hot ethanol before drying under vacuum at 433 K for 6 hours.

2.2.2 *Voltammetry*

CV experiments were performed in a three-electrode cell system with the aid of computer-controlled Eco Chemie Metrohm Autolab PGSTAT302N potentiostat. The three-electrode cell system consists of a 1-mm diameter planar glassy carbon disk (GC) working electrode (eDAQ Pty Ltd) which was used in conjunction with a Pt auxiliary/counter electrode (Metrohm) and a silver wire miniature reference electrode (eDAQ Pty Ltd) isolated via a salt bridge containing 0.5 M *n*-Bu_4NPF_6 in CH_3CN.[8] Most of the voltammetric experiments were conducted at 25±2 °C and with a Faraday cage to prevent any external electrical field interference.

The concentration used in all the experiments were standardized with 2 mM analyte in 0.2 M *n*-Bu_4NPF_6/CH_3CN and unless otherwise stated, all test solutions were deaerated with argon gas for approximately 5 minutes prior to any voltammetric scans. The surface of the working electrode was cleaned through polishing with alumina oxide (grain size 0.3 µm) slurry on a Buehler Ultra-pad polishing cloth and then, rinsed with ultrapure water followed by acetone and dried with a lint free tissue prior to each use.[9]

The redox potentials obtained at the end of experiment were corrected with reference to the oxidation potential of the ferrocene/ferrocenium redox couple (Fc/Fc^+). Ferrocene is often added in the test solutions as an internal reference due to its chemical and electrochemical reversible electrochemical behaviour via a one-electron transfer process regardless the nature of the organic solvent.[10]

2.2.3 *Controlled Potential Electrolysis*

Controlled potential electrolysis (CPE) experiments were conducted in a two-compartment electrolysis cell separated by a sintered glass frit with porosity no. 5 (1.0 – 1.7 μm). Two identical GC cylindrical electrodes were used as working and counter electrodes.[11] Each electrode has a total surface area of 34.4 cm^2 and were positioned in separate compartments (working & counter) with respect to each other. The silver wire reference electrode isolated by a salt bridge containing 0.2 M Bu_4NPF_6 in CH_3CN was positioned near (~2 mm) the surface of the working electrode.[11] For the working electrode compartment, 2 mM analyte with *n*-Bu_4NPF_6 in CH_3CN was used, while the auxiliary electrode compartment consisted of 0.2 M *n*-Bu_4NPF_6 in CH_3CN. The total volume of the solution in each compartment was approximate 25 mL and they were deaerated and stirred by constant bubbling of the argon gas to ensure homogeneous distribution. The number of electrons involved in the bulk electrolysis can be determined using the Faraday's equation.

In CPE experiments, the current flowing through the WE and CE is measured as a function of time.[12-13] The charge, *Q* can be determined via the integration of the current, *I*, over the time, *t*, from the reaction as expressed in Equation 1:

$$Q = \int_0^t I\, dt = F.N \tag{1}$$

According to Faraday's law of electrolysis, it states that the number of moles of the reactant that underwent a chemical reaction during electrolysis is proportional to the amount of charge passed. Thus, the Faraday's equation can be derived from the Equation 2 to give:

$$N_A = \frac{Q}{nF} \tag{2}$$

where N_A is the number of moles of reactant, Q is the amount of charge produced in Coulombs, n is number of electrons transferred per molecule during the bulk conversion process, and F is the Faraday's constant (96 485 C mol^{-1}).[13]

2.2.4 *In-situ* Electrochemical UV-visible Spectroscopy

The *in-situ* electrochemical UV-visible (UV-vis) spectroscopic experiments were performed in an optically semi-transparent thin-layer electrochemical (OSTLE) cell at 25±2 °C. *In-situ* electrolysis of the sample solutions was carried out under constant potential controlled by an Eco Chemie Metrohm Autolab PGSTAT302N potentiostat. The electrode system consisted of a Pt wire mesh working electrode used in conjunction with a Pt wire reference electrode and a Pt wire mesh counter electrode which were separated from the test solution by miniature glass cells with sintered frits.[14] The UV-vis spectra of the redox couple were recorded with a Perkin Elmer Model Lambda 750 UV/Vis-NIR spectrophotometer.

2.2.5 Choice of Solvent/Supporting Electrolyte/Electrode

In this study, acetonitrile (CH_3CN) was selected as the solvent for screening the organic redox couples. CH_3CN is a polar aprotic solvent that exhibits several good physical and electrochemical properties and is proven to be compatible with a wide variety of organic compounds and inorganic salts. Supporting electrolytes in CH_3CN also exhibit reasonably high conductivity due to its moderately high dielectric constant ($\varepsilon = 37$).[15-16] In addition, CH_3CN provides an electrochemical potential window of 6.1 V (depending on the nature of the supporting electrolyte and water content) which allows a wide range of organic redox species to be studied within an effective potential range in both the anodic and cathodic directions without causing solvent breakdown. Apart from the good electrochemical properties, CH_3CN is also a good choice of solvent for UV spectroscopy because of its optical transparency over

a range of wavelengths until 190 nm. The solvent system will not interfere with the characterization of the analyte within the range of 190 to 750 nm. The wide liquid temperature range of CH_3CN (–45 to 82 °C) also helps to facilitate the electrochemical studies of the organic redox active species under specific operating temperature conditions (0 to 50°C). DMSO and DMF have similar dielectric constants and excellent dissolving power, however they are not suitable for this study due to the low oxidation potential windows.[16] The aim of the study is to develop a robust redox system that can operate effectively, therefore, the solvent that was used was not pre-dried. Due to the fluctuating natural humidity levels, the water content in the solvent under ambient condition changes over time. Typically, the trace water content presence in the solvent varies between 0.001 – 0.1 M.[17]

Typically, pure organic solvents have extremely low conductivity, hence supporting electrolytes are important to provide adequate ionic conductivity to minimize solution resistance and facilitate the flow of current.[16] The supporting electrolyte used in the study was tetrabutylammonium hexafluorophosphate (*n*-Bu_4NPF_6). The inorganic salt has excellent solubility in organic solvents and relative ease of synthesis for large scale production. Following Stoke's law, the cation (*n*-Bu_4^+) and anion (PF_6^-) of the inorganic salt also experienced lesser viscous drag due to their small ionic radii which give rise to higher limiting molar conductivity.[18] In addition, Bu_4NPF_6 does not interfere with the analyte profile signal due to the potential window of the cation (*n*-Bu_4^+) and anion (PF_6^-).[16, 18] Therefore, tetrabutylammonium hexafluorophosphate (Bu_4NPF_6) is considered the most suitable supporting electrolyte to be used in the study.

Some of the commonly used materials for electrodes are glassy carbon (GC), platinum, carbon felt and gold.[16] GC electrodes was suitable for the studies mainly because of the wide operating voltage range and high chemical tolerance in harsh conditions (in the presence of

acid and base). In addition, GC electrodes have higher overpotentials for oxygen and hydrogen evolution compared to platinum electrodes. This helps to mitigate the interference caused by the reduction of the hydronium ion (H_3O^+) in an acidic medium or any possible side reaction that are caused by the presence of atmospheric oxygen or water that enter the system over the time.[16] Therefore, GC electrodes were chosen for the study in the majority of the experiments unless otherwise stated.

2.3 Anolyte

In this study, several candidates for anolyte were evaluated via a set of preliminary tests (Table 2.1). Each redox species was pre-examined by CV to evaluate its electrochemical profile. After the chemical reversibility was established, CPE was carried out to determine the redox species stability over an extended timescale (> minutes). Lastly, UV-vis spectroscopy was performed to characterize the redox species and ascertain the chemical stability under ambient conditions.

During the screening process, most of the compounds displayed good chemical reversibility under the timescale of CV (e.g., quinoxaline, 2,1,3-Benzothiadiazole and 4-Nitrobenzene etc.) . However, their respective reduced forms were found to be unstable over an extended period (> minutes) during CPE. Out of the eleven compounds that were evaluated, only two compounds, TCNQ and the vitamin K analogue (VKA) had the potential to be used as the anolyte candidates in the organic-based system. A summary of the results from the eleven compounds are included in Table 2.1. The electrochemical behaviours of TCNQ and VKA will be discussed in detail in this chapter.

Table 2.1. List of compounds screened for suitable anolyte used in organic-based battery.

Chemicals	Structure	Remarks
2,3,6-trimethylquinoxaline (TMeQ)	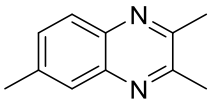	Chemically irreversible (Figure A.1)
Quinoxaline	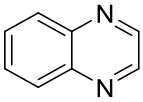	Chemically irreversible during CPE (Figure 2.1)
2,1,3-Benzothiadiazole	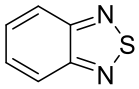	Unrecoverable charge during re-oxidation CPE (Figure 2.2)
4-Nitrobenzene	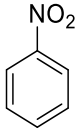	Capacity loss during CPE (Figure 2.3).
4,4-dipyridyl	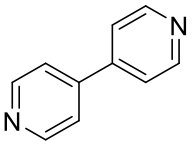	Spontaneous decomposition during CPE (Figure A.2).
4-Nitrophenol	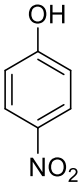	Complicated voltammetric profile (Figure A.3a).
Octafluoronapthalene (OFN)	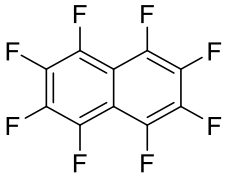	Complicated voltammetric profile and chemically irreversible (Figure A.3b).
Phenyl-2-pyridinylmethanone	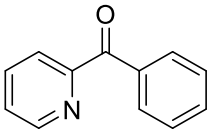	Spontaneous decomposition during CPE. (Figure A.3c)

7,7,8,8-tetracyanoquinodimethane (TCNQ)	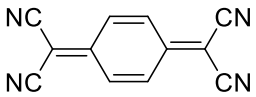	Chemically reversible. $TCNQ^{2-}$ decomposed in the presence of atmospheric oxygen. (This compound will be further discussed in this Chapter).
2,3-dimethylnapthoquinone, vitamin K analogue (VKA)	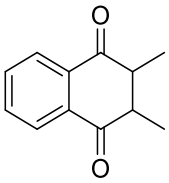	Chemically reversibile in the presence of Bronsted acid and Malonic ester. (This compound will be further discussed in Chapter 5)

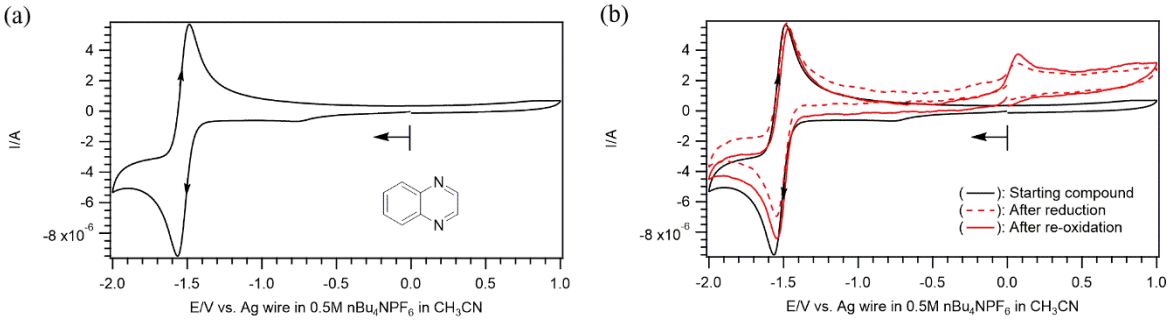

Figure 2.1. Cyclic voltammograms of 1 mM QUI in 0.1 M *n*-Bu_4NPF_6/CH_3CN recorded using a 1-mm diameter planar GC disk electrode at 0.1 V s^{-1} (a) QUI, (b) QUI before and after exhaustive CPE.

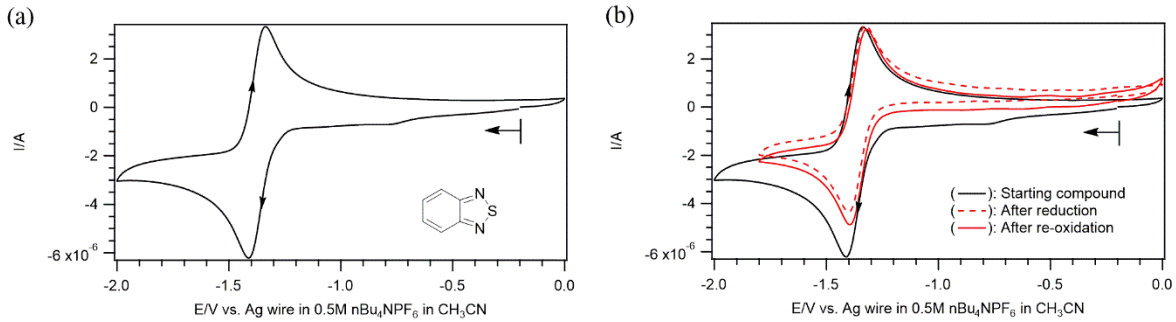

Figure 2.2. Cyclic voltammograms of 2,1,3-Benzothiadiazole in 0.1 M *n*-Bu_4NPF_6/CH_3CN recorded using a 1-mm diameter planar GC disk electrode at 0.1 V s^{-1} (a) 5 mM of 2,1,3-Benzothiadiazole, (b) 1 mM of 2,1,3-benzothiadiazole before and after exhaustive CPE.

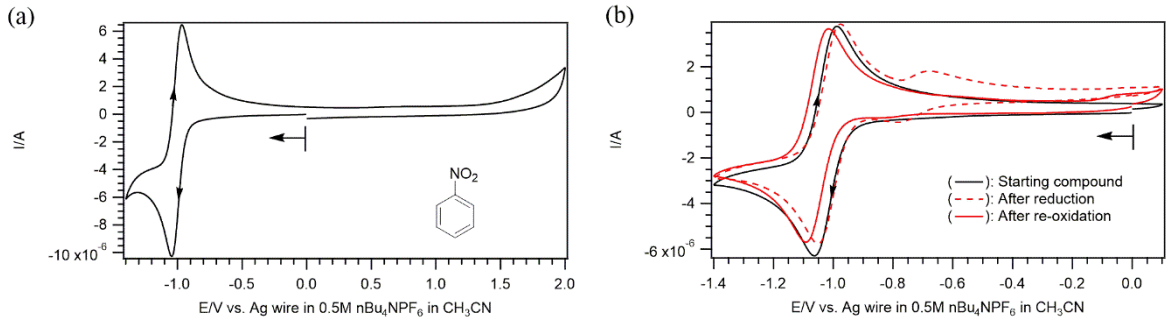

Figure 2.3. Cyclic voltammograms of 1 mM 4-nitrobenzene in 0.1 M *n*-Bu_4NPF_6/CH_3CN recorded using a 1-mm diameter planar GC disk electrode at 0.1 V s^{-1} (a) 4-nitrobenzene, (b) 4-nitrobenzene before and after exhaustive CPE.

2.3.1 *Electrochemical Studies of TCNQ*

From the CV study, the electrochemical reduction of TCNQ in CH_3CN occurs in two successive one-electron reduction processes forming the radical anion ($TCNQ^{\bullet-}$) followed by the dianion ($TCNQ^{2-}$) at a more negative applied potentials as shown in Figure 2.4.

TCNQ has a strong electron accepting ability because the two-electron reduction allows the planar TCNQ ring to achieve complete aromatization with a decreasing quinoidal characteristic.[19-20] In the doubly charged state, the additional electrons are delocalized to the peripheral dicyanomethylene groups.[21]

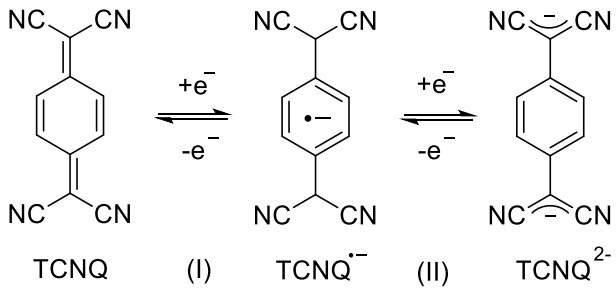

Scheme 2.1. Electrochemical reduction process of TCNQ.

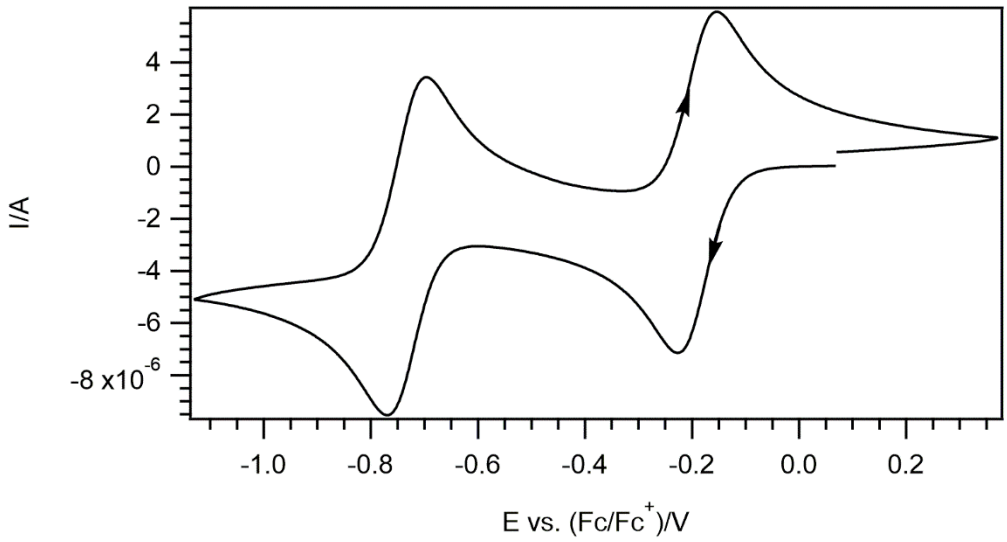

Figure 2.4. Cyclic Voltammetry of 2 mM TCNQ in 0.2 M *n*-Bu_4NPF_6/CH_3CN recorded using a 1-mm diameter planar GC disk electrode at 0.1 V s^{-1}.

Table 2.2. Half-wave potentials ($E_{½}$) and peak-to-peak separation (ΔE_p) of 2 mM TCNQ in 0.2 M *n*-Bu_4NPF_6/CH_3CN.

Step	$E_{½}$ vs (Fc/Fc$^+$)/V	ΔE_p/mV
I	– 0.200	69.4
II	– 0.744	69.4

The ratio of anodic peak current (i_p^{ox}) to cathodic peak current (i_p^{red}) were close to unity for both one-electron reduction processes, thus implying that TCNQ exhibits high chemical reversibility on the CV time scale (≤ seconds) at the given experimental setting. Considering the above factors and in conjunction with the reasonably negative second reduction potential (–0.744 vs (Fc/Fc$^+$)/V, Table 2.2), TCNQ has the potential to be used for anolyte in this study.

To gain more information on the redox processes of TCNQ, CPE was conducted to confirm the number of electrons involved in each reduction step. In addition, CPE also provides information on the stability of the reduced species ($TCNQ^{\bullet-}$ and $TCNQ^{2-}$) over extended timescales (> minutes). Based on the coulometric data obtained (Figures 2.5a and 2.5c) during the first reduction process at –0.345 vs (Fc/Fc$^+$)/V and the second reduction process at –0.916 vs (Fc/Fc$^+$)/V, approximately 1.03 electrons and 2.04 electrons (total) were experimentally calculated to be transferred to TCNQ, respectively. The results obtained are in good agreement with the reported redox behaviour of TCNQ (Scheme 2.1) which involves two successive one-electron transfer steps.[22] Based on the observation made during the CPE, the colour of the solution changed from yellow to dark green after the first-electron reduction and to light yellowish green for the second-electron reduction process.

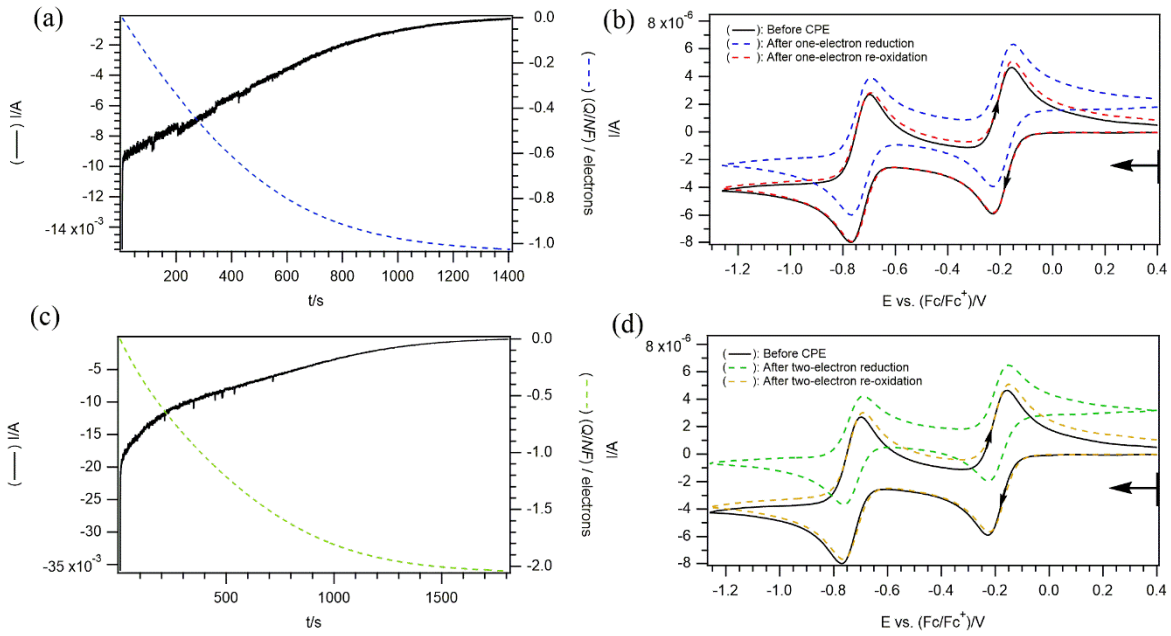

Figure 2.5. Coulometric data (current against time) and CV response for the reductive electrolysis of 2 mM TCNQ in 0.2 M *n*-Bu_4NPF_6/CH_3CN using a 1-mm diameter planar GC disk electrode at 0.1 V s^{-1} (a) Coulometric data for the reductive CPE for the first reduction process at -0.345 vs (Fc/Fc^+)/V. (b) CV response before and after reductive and oxidative CPE for first reduction process. (Black solid line) Original voltammetric profile of TCNQ (Blue dashed line) After one-electron reductive CPE (Red dashed line) After one-electron oxidative CPE back to starting material. (c) Coulometric data for the reductive CPE for the second reduction process at -0.916 vs (Fc/Fc^+)/V. (d) CV response before and after reductive and oxidative CPE for second reduction process. (Black solid line) Original voltammetric profile of TCNQ (Green dashed line) After two-electron reductive CPE of TCNQ (Orange dashed line) After exhaustive two-electron oxidation back to starting material.

It is important to note that CV studies performed for post-electrolysis only provides information on the chemical stability of the candidate molecules and it does not hold evidence to substantiate a complete conversion, which instead comes from the coulometric data.

The CV responses (Figure 2.5b) recorded after CPE (red solid line) coincides well with that of the starting material (black solid line) after bulk conversion. The peak current is nearly identical with no additional peaks observed. Due to the change in oxidation state of TCNQ species present in the bulk solution after reductive CPE, positive current was flowing at the beginning of the CV scan, resulting to the upward shift in the voltammetric profile. Similar electrochemical behaviour was also observed in the CV response for the second reduction step (Figure 2.5d). This implies that both the reduced species ($TCNQ^{\bullet-}$ and $TCNQ^{2-}$) are stable and chemically reversible during exhaustive electrolysis.

Based on the initial results obtained from the CPE experiment, TCNQ is likely to achieve a good cycle life. The decrease in current close to zero as the electrolysis progresses suggests complete conversion of the charged species. Therefore, TCNQ could be a potential candidate for the anolyte in the organic-based battery system. *In-situ* electrochemical UV-vis spectroscopy was conducted to characterize the redox couple of TCNQ ($TCNQ^{\bullet-}$ and $TCNQ^{2-}$) as well as to further determine the chemical stability of the reduced states.

The *in-situ* electrolysis was conducted using a Pt mesh working electrode inside an OSTLE cell. Simultaneous UV-vis measurements were recorded during exhaustive reduction of TCNQ to provide precise and real-time monitoring of the redox species behaviour. Unlike CV, the test solution for the *in-situ* electrochemical UV-vis spectroscopy was deliberately not deaerated in order to test the effect of trace or background oxygen on the long-term stability of the system. Hence, the analysis was taken place with the presence of dissolved atmospheric gases.

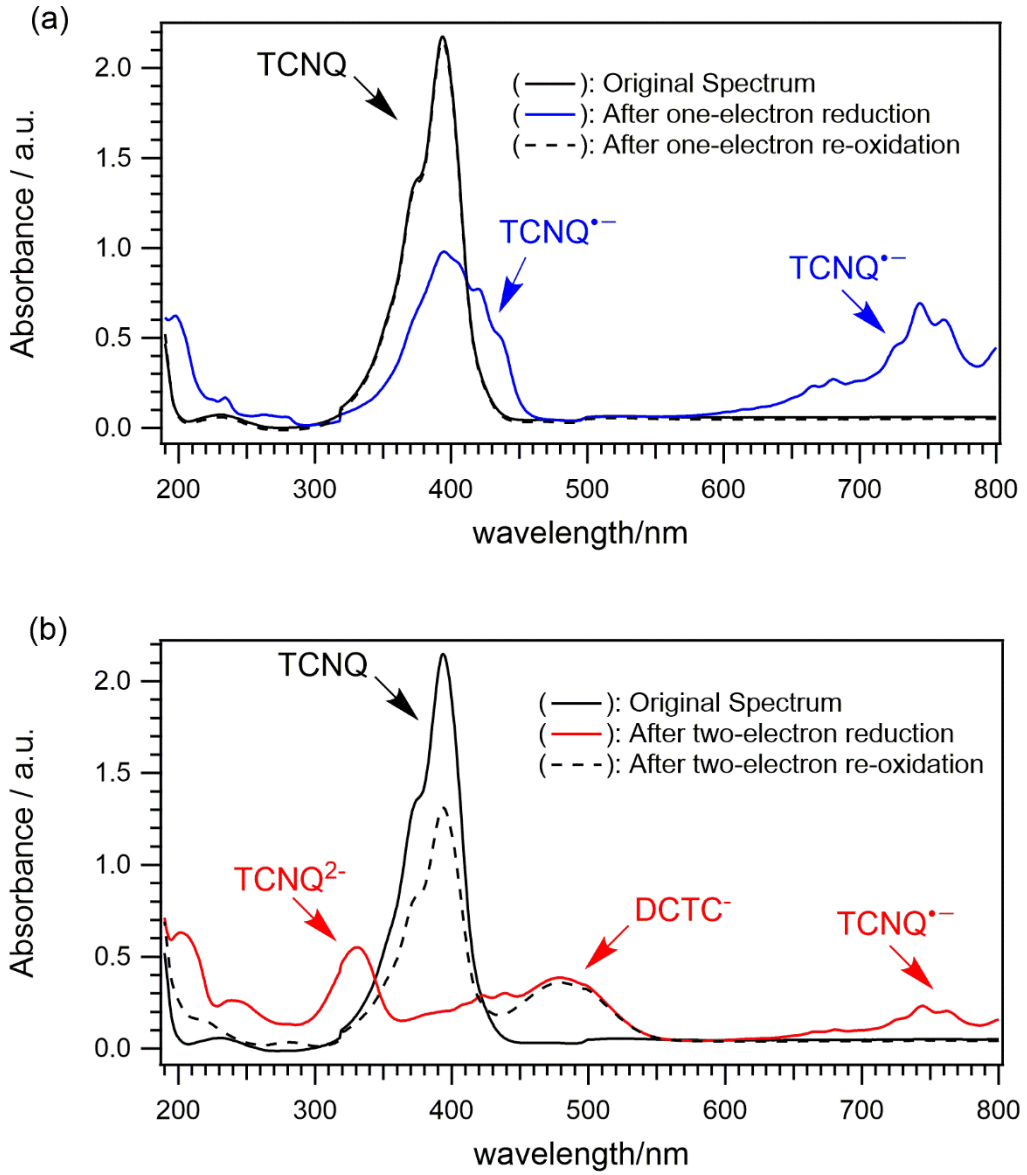

Figure 2.6. Background-subtracted *in-situ* electrochemical UV-vis spectra of 0.5 mM TCNQ in 0.1 M *n*-Bu_4NPF_6/CH_3CN containing Pt mesh electrode (a) one-electron reduction process and (b) two-electron reduction process. (Black solid line) Original spectrum. (Blue solid line) Spectra after one-electron reduction. (Red solid line) Spectra after two-electron reduction. (Black dashed line) Spectra back to starting material.

Based on the UV-vis spectra recorded from the *in-situ* one electron reductive CPE (Figure 2.6a), the $TCNQ^{\bullet-}$ radical anion (blue solid line) exhibits two distinct bands in the 350 to 900 nm region. The absorption spectrum of the one-electron reduction of TCNQ was in close

agreement with the reported spectrum.[23] After converting back to the starting material (TCNQ), the spectra collected (black dashed line) was almost indistinguishable from the original spectrum (black solid line). Quantitative recovery of the starting compound was achieved from the one-electron reduction process. One can conclude that the $TCNQ^{\bullet-}$ radical anion was chemically stable in the presence of atmospheric gases.

On the other hand, such comparable spectra were not obtained in an attempt for *in-situ* two-electron reductive CPE (Figure 2.6b). There was a drastic decrease in the intensity of the two distinct bands in the 350 to 900 nm region that represents TCNQ and a new band emerged at 490 nm (black dashed line). In addition, the solution turned orange. The results suggested that the degradation product of $TCNQ^{2-}$ was formed during the reductive CPE. Based on the spectra recorded during the two-electron reduction process (red solid line), the newly emerged band at 490 nm could possibly be the degradation product. The orange solution obtained was likely to be the degradation product α,α-dicyano-p-toluoylcyanide anion ($DCTC^-$) that was formed during the exhaustive two-electron reduction (Scheme 3.2).[24]

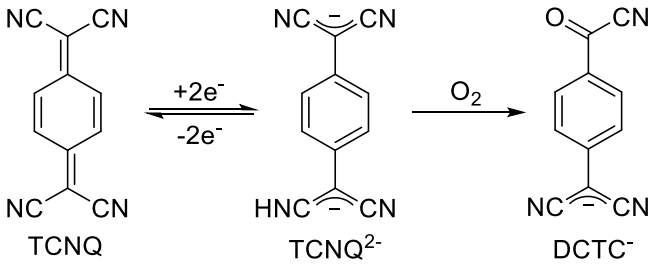

Scheme 2.2. Decomposition pathway of TCNQ to $DCTC^-$

The proposed decomposition pathway suggests that the $TCNQ^{2-}$ dianion reacted with the atmospheric oxygen, which depletes the effective concentration of TCNQ. This phenomenon is likely to occur if TCNQ undergoes an exhaustive two-electron reduction in the presence of atmospheric oxygen. This was not observed in the earlier test because the test

solution in CV analysis and CPE experiment was deaerated to remove any dissolved gases (such as oxygen).

Water (0.1 M) was intentionally introduced into the *in-situ* electrochemical UV-vis spectroscopy experiment to stabilize the $TCNQ^{2-}$ dianion via hydrogen bonding. However, such an effect was not effective in preventing the decomposition (Figure 2.7). Another attempt to stabilize the $TCNQ^{2-}$ dianion was performed by changing the supporting electrolyte to lithium perchlorate, $LiClO_4$. Unfortunately, the stabilization effect by Li^+ cation has little to no effect since a similar orange solution was obtained.

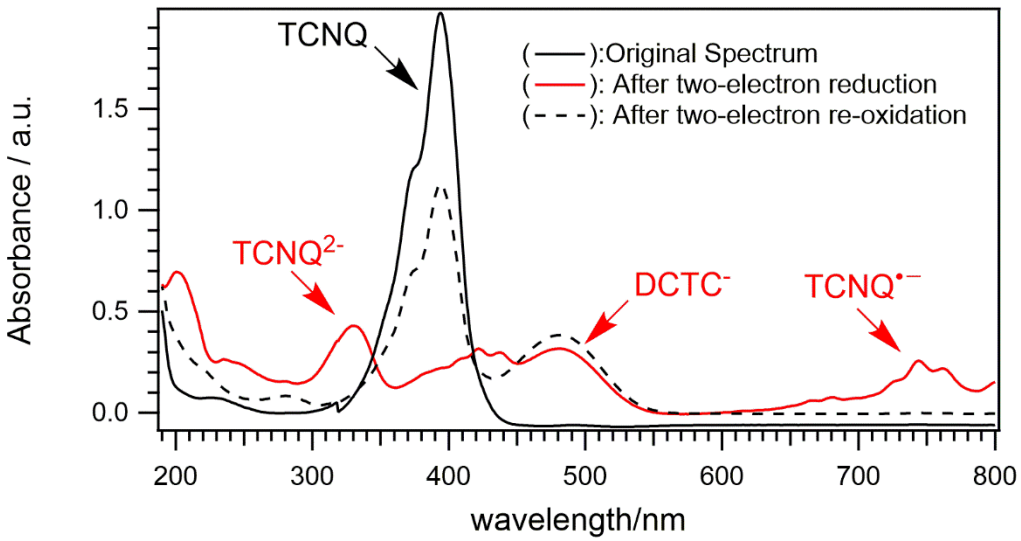

Figure 2.7. Background-subtracted in-*situ* electrochemical UV-vis spectra of 0.5 mM TCNQ in 0.1 M of water and 0.1 M *n*-Bu_4NPF_6/CH_3CN containing Pt mesh electrode. (Black solid line) Original spectrum before two-electron reduction process (Red solid line) Spectra after two-electron reduction process (Black dashed line) Spectra after re-oxidation back to starting compound.

In conclusion, electrochemical studies have shown that TCNQ exhibits good chemical stability and reversibility under oxygen-free conditions. However, the results from the *in-situ* electrochemical UV-vis spectroscopy experiments have shown that $TCNQ^{2-}$ was prone to

decomposition in the presence of atmospheric oxygen. Therefore, a TCNQ-based battery would require a more stringent cell design to eliminate the presence of atmospheric oxygen to prevent capacity fading over time.

2.3.2 *Electrochemical Studies of VKA*

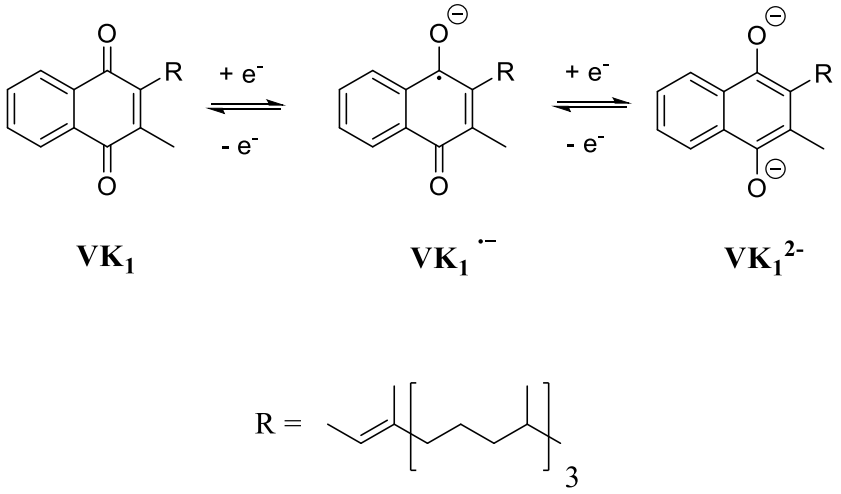

Scheme 2.3. Electrochemical reduction process of VK_1.

Vitamin K_1 (VK_1; also known as phylloquinone) is a natural occurring compound that exhibits similar electrochemical behavior to other para-quinones. In the presence of aprotic organic solvents (such as CH_3CN) at low water concentrations, it undergoes two successive chemically reversible one-electron reduction processes, forming the semiquinone ($VK_1^{\bullet-}$) and followed by the dianion (VK_1^{2-}) at a more negative applied potential as shown in Figure 2.8.[16, 25]

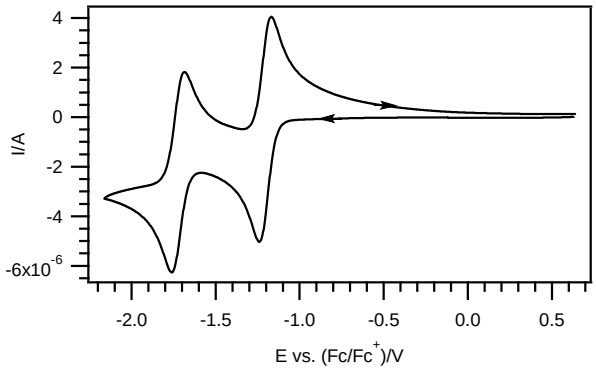

Figure 2.8. Cyclic Voltammetry of 2 mM VK_1 in 0.2 M *n*-Bu_4NPF_6/CH_3CN recorded using a 1-mm diameter planar GC disk electrode at 0.1 V s^{-1}.

Due to the lipophilic nature of VK_1, it is postulated that the solubility of the VK_1 is likely to be poor in polar aprotic solvent such as CH_3CN. From a biological viewpoint, the phytyl side chain improves the compatibility of VK_1 in the hydrophobic environment while the naphthoquinone functional group is responsible for the transfer of protons and electrons.[25] Hence, a vitamin K analogue (VKA) was synthesized by replacing the hydrophobic phytyl side chain with a methyl group, which theoretically helps to improve the solubility of vitamin K_1 in polar organic solvents without affecting the redox behaviour. CV experiments conducted on VKA did show similar electrochemical behaviour as VK_1, with chemically reversible two successive one-electron reduction processes as shown in Scheme 2.4 and Figure 2.9.

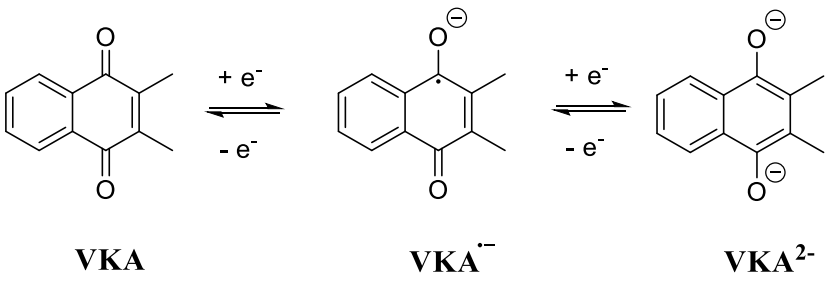

Scheme 2.4. Electrochemical reduction process of VKA.

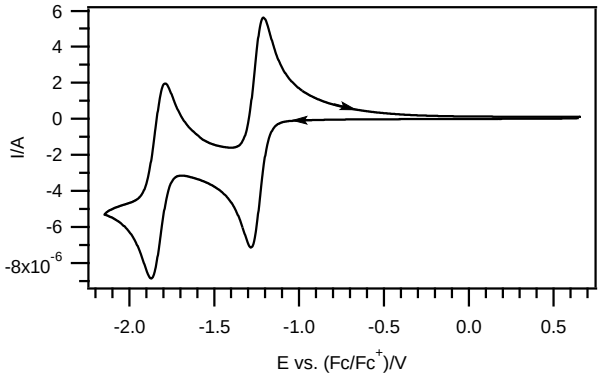

Figure 2.9. Cyclic voltammetry of 2 mM VKA in 0.2 M *n*-Bu_4NPF_6/CH_3CN recorded using a 1-mm diameter planar GC disk electrode at 0.1 V s^{-1}.

In general, the dianions of quinones, Q^{2-} are relatively reactive in aprotic solvents and are likely to undergo side reactions such as comproportionation, irreversible dimerization or nucleophilic attack on solvent molecules with electron deficient function groups.[26-27] This prevents the electrochemical process from being chemically reversible. However, the addition of a Bronsted acid helps to stabilize the dianion, Q^{2-} to form a stable dihydroquinone species. In acidic medium, quinones demonstrate a classical two electrons and two protons ($2e^-/2H^+$) mechanism.[27] Previous studies have shown that VK_1 undergoes a chemically reversible $2e^-/2H^+$ reduction process to form a stable dihydroquinone VK_1H_2 in the presence of strong non-aqueous acid, CF_3SO_3H.[25]

Therefore, in order to improve the stability of the reduced species, an acidic addictive in the form of trifluoroacetic acid (TFA) was introduced into the system to facilitate the $2e^-/2H^+$ reduction of VKA. In the CV analysis, the electrochemical behavior of VKA was studied in the presence of TFA from 0 to 100 equivalents (Figure 2.10). As the concentration of the acid increased, a new reduction wave appeared at more positive potential and the peak current was approximately doubled the size, this suggest a $2e^-/2H^+$ reduction process leading to the formation of $VKAH_2$. It was postulated that VKA undergoes a concerted electron-proton

transfer reduction process (PCET) involving an ECEC mechanism (Scheme 2.5). In addition, the intensity of the cathodic peak current (i_p^{red}) and the shift in reduction peak potential (E_p^{red}) was affected by the amount of acid added to the system. Therefore, 50 equivalents of TFA were sufficient to optimize the system while still maintaining a reasonably high reduction potential of VKA.

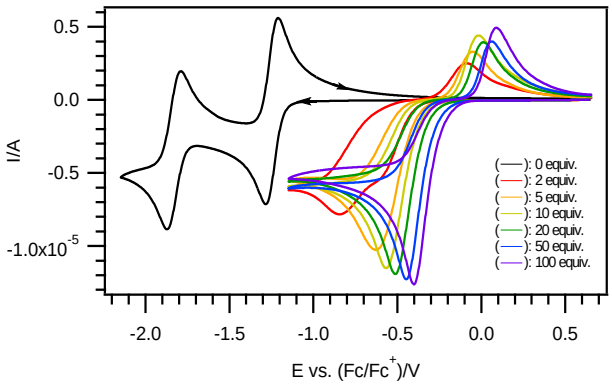

Figure 2.10. Cyclic voltammograms of 2 mM VKA in 0.2 M *n*-Bu_4NPF_6/CH_3CN and the addition of 0 to 100 equiv. TFA recorded at a scan rate of 0.1 V s^{-1}, with a 1-mm diameter planar GC electrode.

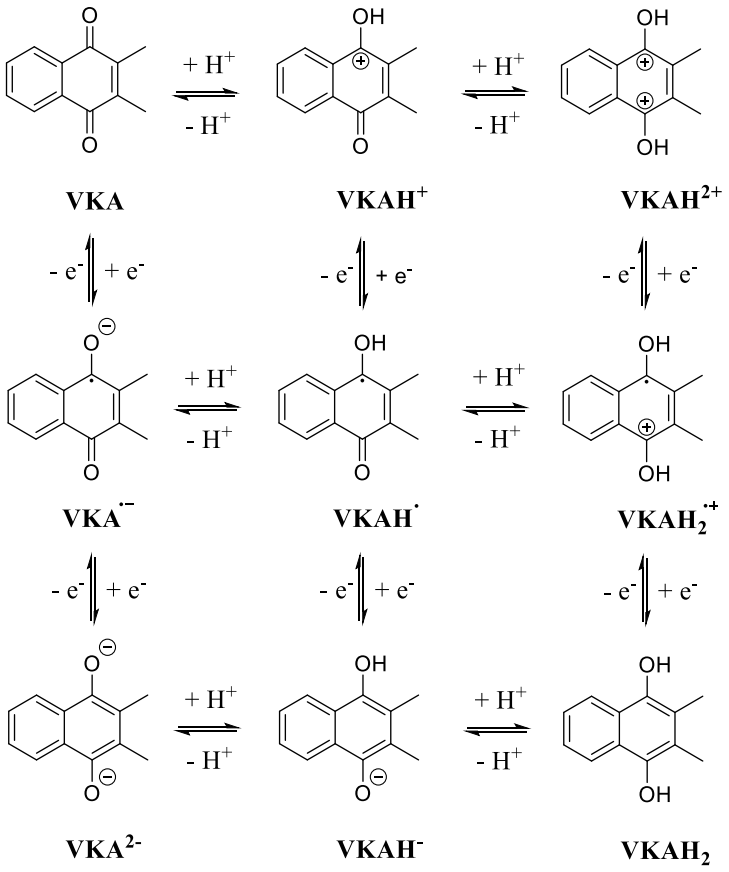

Scheme 2.5. Proposed electrochemical square-scheme mechanism of VKA in CH_3CN with the presence of TFA.[28]

Based on the CV analysis, VKA exhibits a quasi-reversible electrochemical profile in the presence of TFA. The reverse oxidation of the dihydroquinone was more complicated than the forward reduction process. It was proposed that a second order disproportionation mechanism (DISP2) may occur during the reverse oxidation (Scheme 2.6).[29] The other possible explanation for the wide peak-to-peak separation in the presence of acid is that the quinone may also undergo an ECEC process (Scheme 2.5) converting to the hydroquinone and then back to its initial form. However, the forward and reverse pathways are unlikely to occur by the same route since the equilibrium for the homogeneous proton transfers favor one particular direction depending on the pH. Thus, the wide peak separation between the cathodic and anodic peaks may be due to a combination of redox processes with different reaction pathways.[28]

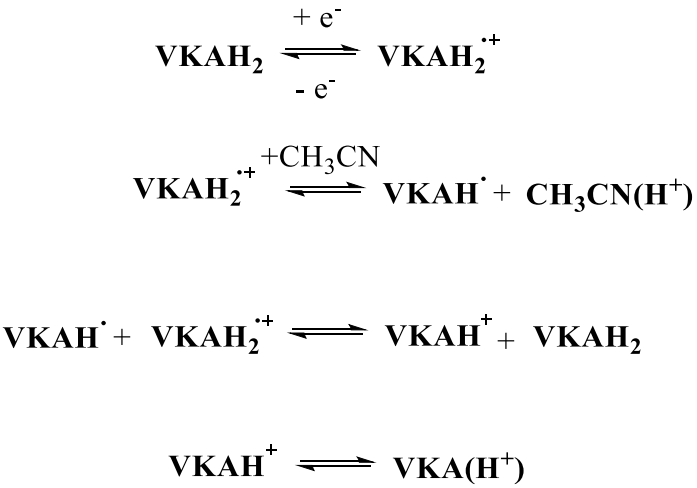

Scheme 2.6. Proposed DISP2 mechanism for reversed oxidation of $VKAH_2$

Next, CPE experiments were carried out attain more information on the stability of VKA in the presence of TFA. The applied potential for the reductive CPE was set at 0.15 V more negative than the reductive peak potential (E_p^{red}) of VKA to ensure complete reduction in the bulk solution. Based on the coulometric data obtained (Figures 2.11a and 2.11b), approximately 2 electrons were calculated to be transferred and recovered during the whole CPE experiment.

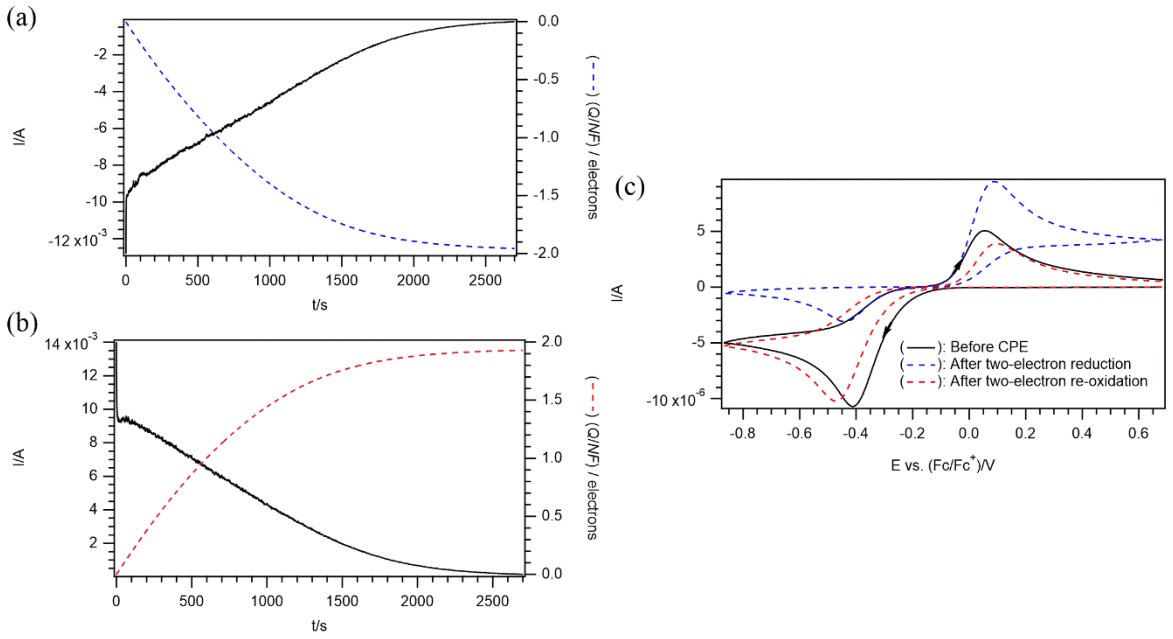

Figure 2.11. Coulometric data (current against time) and CV response for the reductive electrolysis of 2 mM VKA in 0.2 M *n*-Bu_4NPF_6/CH_3CN and 50 equiv. of TFA using a 1-mm diameter planar GC disk electrode at 0.1 V s^{-1} (a) Coulometric data for the reductive CPE at –0.56 vs (Fc/Fc^+)/V. (b) Coulometric data for the oxidative CPE at 0.25 vs (Fc/Fc^+)/V. (c) CV response before and after reductive and oxidative CPE. (Black solid line) Original voltammetric profile of VKA (Blue dashed line) After two-electron reductive CPE (Red dashed line) After two-electron oxidative CPE back to starting material.

As shown in Figure 2.11c, a comparable CV response were obtained before (black solid line) and after (red dashed line) exhaustive electrolysis revealed that quantitative recovery of VKA was achieved. Despite having a complicated re-oxidation pathway, VKA has proven to be chemically reversible in the presence of TFA.

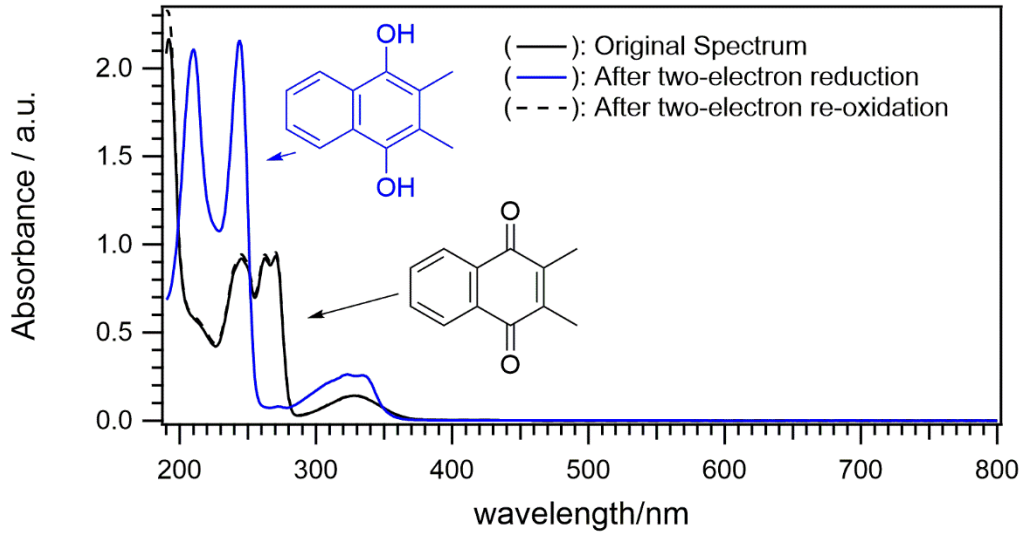

Figure 2.12. Background-subtracted UV-vis spectra of 1 mM VKA in 0.1 M *n*-Bu_4NPF_6/CH_3CN and 50 equiv. TFA. (Black solid line) Original spectrum. (Blue solid line) Spectra after two-electron reduction. (Black dashed line) Spectra after two-electron re-oxidation.

Initial findings obtained from the preceding section have revealed that the reduced form of VKA survived over extended time scales (> minutes) under exhaustive electrolysis. To corroborate the validity of the results, the stability of VKA in the presence of TFA was further examined spectroscopically via UV-vis spectroscopy. *Ex-situ* electrolysis was performed before introducing the converted species into the OSTLE cell for real-time monitoring.

The UV-vis absorption spectra of VKA are presented in Figure 2.12. Two characteristic bands between 260-272 nm were observed from the original spectrum of VKA (black solid line). The absorption spectrum (blue solid line) of the reduced species, $VKAH_2$ showed two distinctive bands at 210 nm and 244 nm. The absorption spectrum of VKA (black solid line) completely overlapped with that of the re-oxidized form (black dashed line). No additional absorption band was observed. This implies that VKA can be quantitatively recovered from its reduced form and ruled out the possibility of unwanted side products.

Overall, VKA is a better candidate to use as the anolyte since it demonstrates good chemical stability and reversibility under ambient conditions which fits the aim of the research to design a robust battery system.

2.4 Catholyte

Similar screening procedures were conducted to find suitable catholytes for the organic-based redox flow battery. During CV analysis, all the test compounds displayed good electrochemical reversibility (Table 2.3). However, the oxidation potential of 2,3,5,6-Tetramethyl-p-phenylenediamine was considered too low and would compromise the cell voltage of the battery. Similarly, the PD derivatives, N,N'-diphenyl-p-phenylenediamine and N,N'-di-2-naphthyl-1,4-phenylenediamine had low oxidation potentials and displayed poor solubility in CH_3CN. Therefore, only two compounds, 3,3',5,5'-tetramethylbenzidine (TMB) and a vitamin E analogue (VEA) qualified as suitable anolyte candidates. In-depth studies for TMB and VEA were carried out and described in the following sections.

Table 2.3. List of compounds screened for suitable catholyte used in organic-based battery.

Chemicals	Structure	Remarks
2,3,5,6-Tetramethyl-p-phenylenediamine	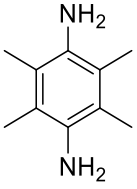	Chemically reversible, low oxidation potential (Figure 2.13, red solid line).
***N*,*N*'-diphenyl-*p*-phenylenediamine**	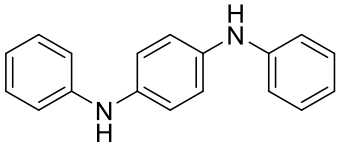	Chemically reversible, poorly soluble in CH_3CN (Figure 2.13, blue solid line).

***N,N'*-di-2-naphthyl-1,4-phenylenediamine**	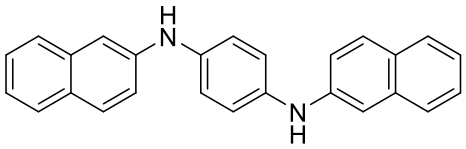	Chemically reversible, poorly soluble in CH_3CN (Figure 2.13, black solid line).
3,3',5,5'-tetramethylbenzidine (TMB)	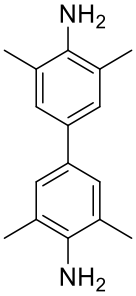	Chemically reversible, good chemical stability. (Further discussed in this Chapter).
Vitamin E analogue (VEA)	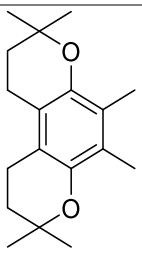	Chemically reversible, good chemical stability. (Further discussed in this Chapter).

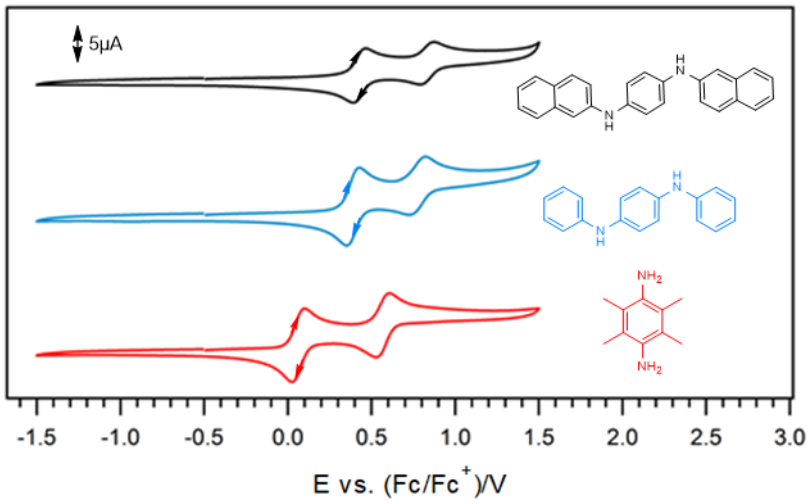

Figure 2.13. Cyclic voltammograms of 2 mM (each) *N,N'*-di-2-naphthyl-1,4-phenylenediamine, *N,N'*-diphenyl-*p*-phenylenediamine and 2,3,5,6-Tetramethyl-p-phenylenediamine (in descending order) in 0.2 M *n*-Bu_4NPF_6/CH_3CN recorded using a 1-mm diameter planar GC disk electrode at 0.1 V s^{-1}.

2.4.1 *Electrochemical Studies of TMB*

Stabilization of radical cations can be achieved via the resonance effect. Phenylenediamine (PD) exhibits good chemical reversibility and has proven to be long-lived in its radical cationic form due to the conjugated structure that enables the delocalization of the electrons.[14] With this in mind, a chemical structure with an extended conjugation system could further enhanced the stability of the radical cation. Therefore, the derivatives of benzidine, 3,3',5,5'-tetramethylbenzidine (TMB) were considered for the study because of their similarity in chemical structure to *p*-phenylenediamine and also with two additional phenyl rings which provides an extended conjugated network.

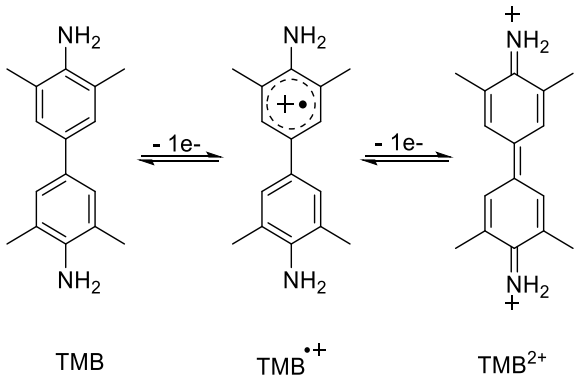

Scheme 2.7. Two successive one-electron oxidations of TMB.

Based on the CV analysis, the electrochemical behaviour of TMB in CH_3CN occurs in two successive one-electron oxidation processes (Scheme 2.7) forming the radical cation ($TMB^{\bullet+}$) followed by the dication (TMB^{2+}) at a more positive potential as shown in Figure 2.14.

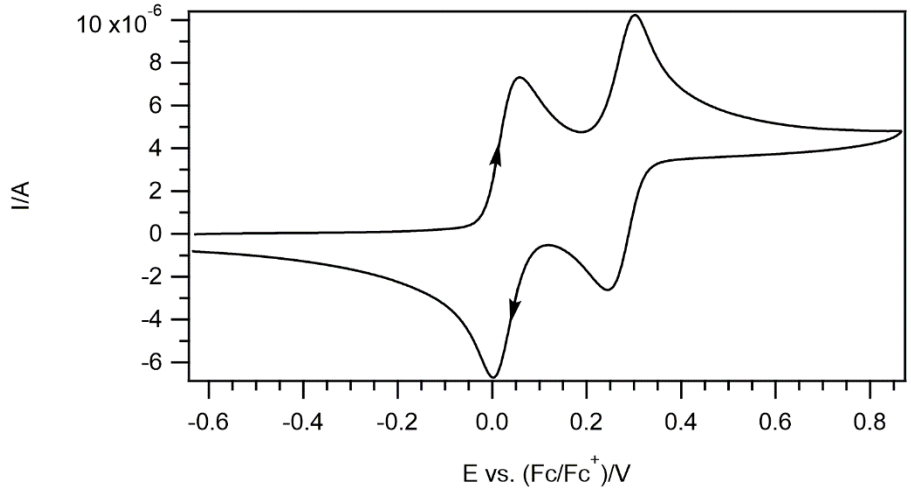

Figure 2.14. Cyclic voltammogram of 2 mM TMB in 0.2 M *n*-Bu_4NPF_6/CH_3CN recorded using a 1-mm diameter planar GC disk electrode at 0.1 V s^{-1}.

The current ratio of i_p^{ox} and i_p^{red} were close to unity for both oxidation processes, providing evidence that TMB exhibits high electrochemical reversibility on CV time scale (≤ seconds).

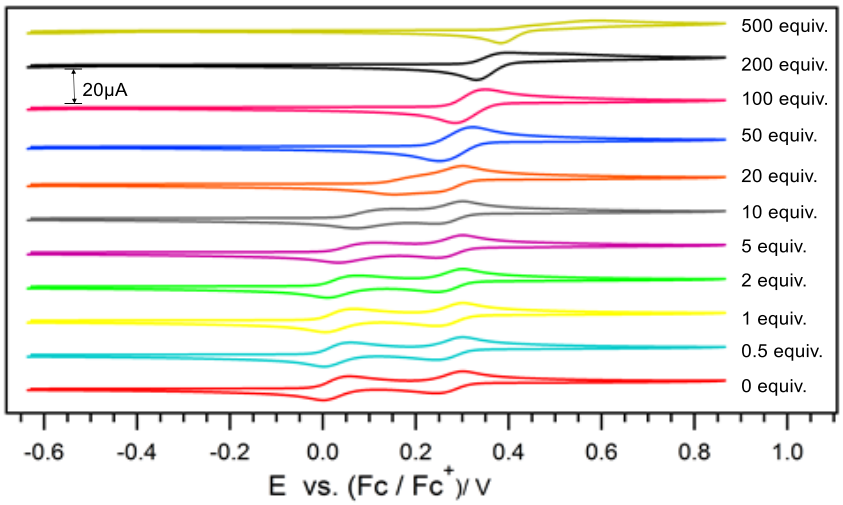

Figure 2.15. Cyclic voltammograms of 2 mM TMB in 0.2 M *n*-Bu_4NPF_6/CH_3CN and the addition of 0 to 500 equiv. TFA recorded at a scan rate of 0.1 V s^{-1}, with a 1-mm diameter planar GC electrode.

Studies have shown that the stability of the benzidine dication, BZN^{2+} is influenced by the pH of the solution.[30] At higher pH (> 3), the diimines can be easily hydrolyzed to quinones or undergo side reactions such as polymerization or substitution reactions. Previously, CPE experiments were carried out on TMB in CH3CN containing *n*-Bu_4NPF_6. However, a green crystalline solid was observed at the working electrode compartment after the oxidative CPE. The solid remained in the solution despite attempts to convert it back to the original state. Therefore, an acidic environment was proposed in the study of TMB.

The electrochemical behavior of TMB was studied in the presence of trifluoroacetic acid (TFA) from 0 to 500 equivalents (Figure 2.15). The increase in the acid concentration result in a positive shift of the oxidative potential (E_p^{ox}) for the first oxidation process, while the E_p^{ox} of the second oxidation process remain unchanged. It was postulated that the neutral TMB undergoes protonation in the presence of acid leading to the formation of the protonated TMB ($TMBH^+$). A greater oxidative potential is required to oxidize the $TMBH^+$ cation to $TMBH^{\bullet 2+}$ radical cation since the $TMBH^+$ cation is more electron deficient than its neutral form, this would explain the shift in the peak potential of the first oxidation state. With sufficient acid concentration, the first E_p^{ox} would eventually come close and merge with the E_p^{ox} of the second oxidation process.

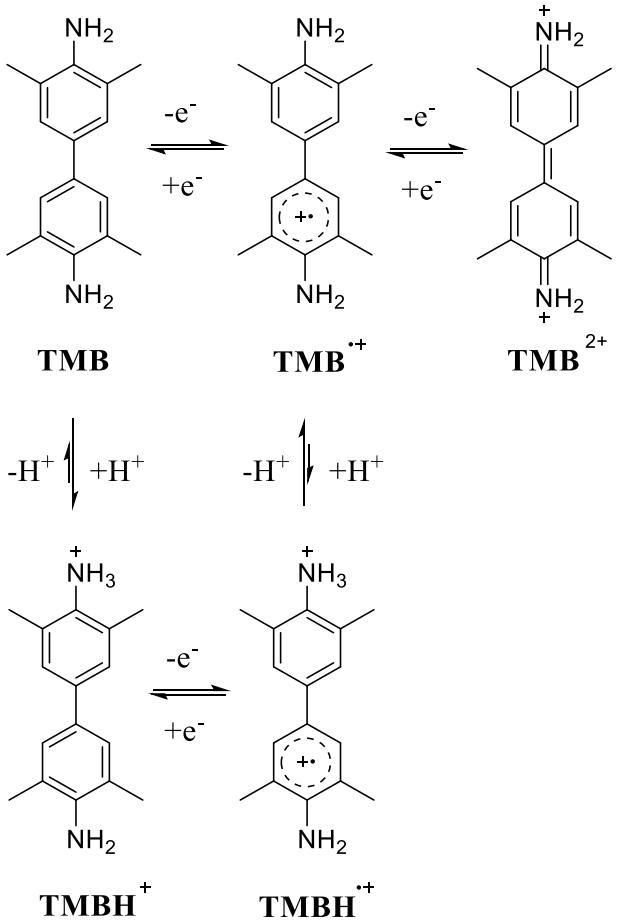

Scheme 2.8. Proposed electrochemical mechanism of TMB in TFA.

After losing one electron, the radical cation, $TMBH^{\bullet 2+}$ becomes much more acidic and it is unlikely to undergo another protonation process due to electrostatic repulsion. Hence, deprotonation will take place follow by the second electron oxidation at the same potential (Scheme 2.8). This ECE mechanism occurs in quick succession such that it appears concerted on the CV time scale. (Figure 2.15). Therefore, the oxidation process of the $TMBH^+$ cation involves a two–electron and one–proton ($-2e^-/-1H^+$) mechanism.

Beyond 50 equivalents of TFA, TMB experienced a decrease in the anodic peak current that signaled the loss of chemical reversibility. Hence, 50 equivalents of TFA were determined to be the optimum concentration for TMB to impart stability while retaining its chemical reversibility.

CPE experiments were conducted to determine the number of electrons involved in the oxidation process of TMB in the presence of TFA. It also provides more information on the stability of the oxidized species (TMB^{2+}) over extended timescales (> minutes). Here, a total of two electrons were calculated to be transferred in the bulk oxidation of TMB at +0.44 vs (Fc/Fc^{+})/V. The coulometric data (Figures 2.16a and 2.16b) are in good agreement with the postulated mechanism that involves two electrons in the oxidation process of TMB. The voltammograms (Figure 2.16c) recorded before CPE (black solid line) and after the oxidative CPE (red dashed line) displayed similar electrochemical profiles. This implies that the oxidized species (TMB^{2+}) is stable in the presence of TFA. The slight discrepancy of the CV profile before CPE (black solid line) and after reductive CPE (blue dashed line) was due to the change in the environmental condition after electrolysis. On top of that, no precipitate was observed during and after the CPE experiment.

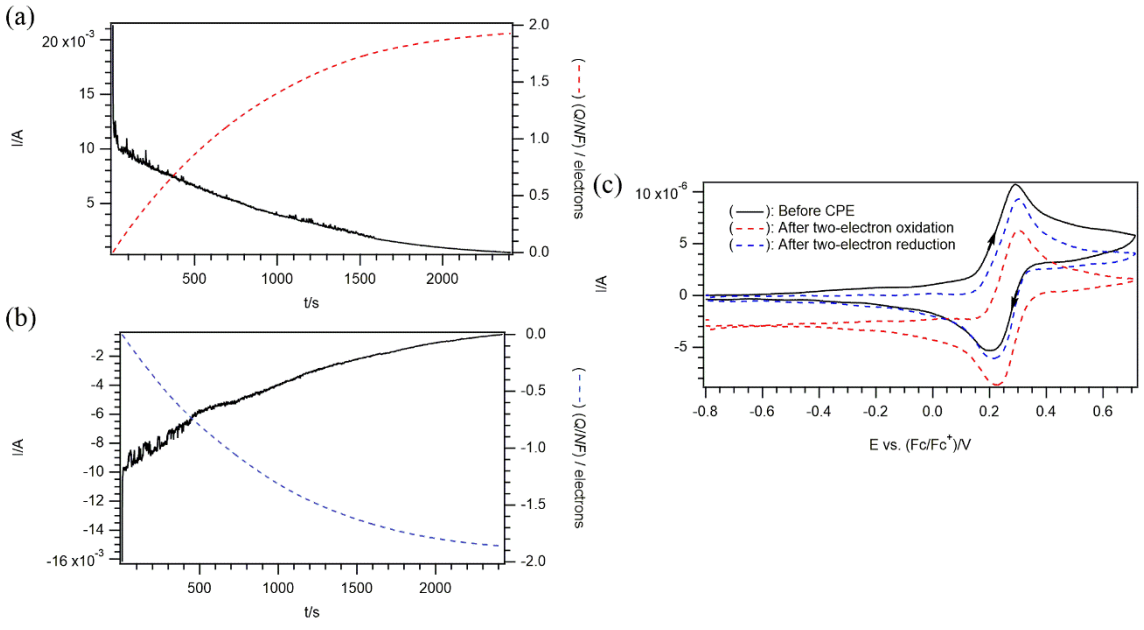

Figure 2.16. Coulometric data (current against time) and CV response for the oxidative electrolysis of 2 mM TMB in 0.2 M *n*-Bu_4NPF_6/CH_3CN and 50 equiv. of TFA using a 1-mm diameter planar GC disk electrode at 0.1 V s^{-1} (a) Coulometric data for the oxidative CPE for the oxidation process at 0.62 vs (Fc/Fc^{+})/V. (b) Coulometric data for the reductive CPE for the

reduction process at 0.05 vs (Fc/Fc^{+})/V. (c) CV response before and after oxidative and reductive CPE for the oxidation process. (Black solid line) Original voltammetric profile of TMB (Red dashed line) After two-electron oxidative CPE (Blue dashed line) After two-electron reductive CPE back to starting material.

In-situ electrochemical UV-vis spectroscopy was performed to characterize the oxidized species of TMB in the presence of TFA.

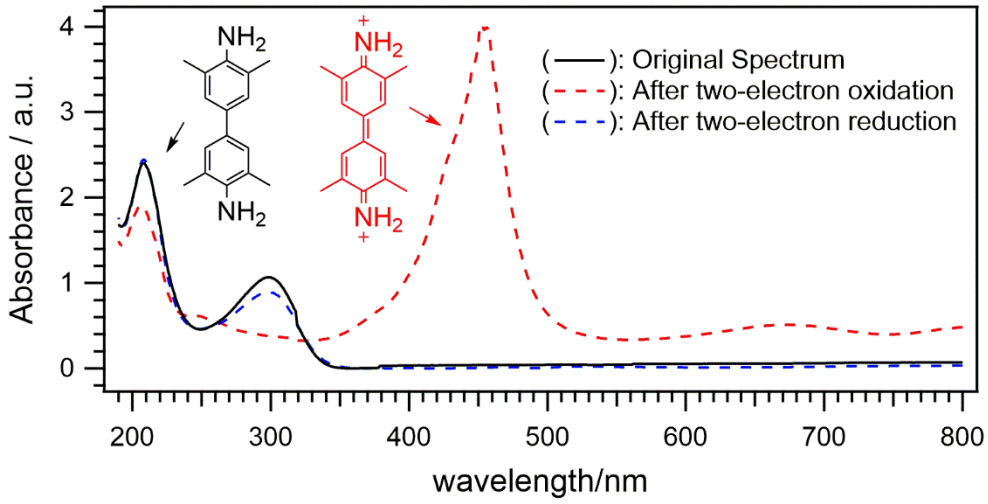

Figure 2.17. Background subtracted *In-situ* electrochemical UV-vis spectra of 1 mM TMB in 0.1 M *n*-Bu_4NPF_6/CH_3CN and 50 equiv. of TFA (Black solid line) original spectrum. (Red dashed line) After two-electron oxidation. (Blue dashed line) After two-electron reduction.

The starting material display a distinct band at 300 nm (Figure 2.17, black solid line). After electrolysis (red dashed line), a broad absorption peak appears at 450 nm and this value is in good agreement with the reported value of the TMB^{2+} dication.[31] The test solution was then subjected to bulk reduction. The resulting UV-vis absorption spectrum (blue dashed line) is almost identical to the original spectrum (black solid line). As such, the chemical stability of the dication, TMB^{2+} can be attained in the presence of TFA.

In conclusion, electrochemical studies on TMB have shown good chemical reversibility in the presence of TFA. In addition, TMB has shown promising stability (> minutes) during CPE. *In-situ* electrochemical UV-vis spectroscopy experiments have also ascertained the stability of the oxidized species of TMB with the presence of TFA. Therefore, the use TMB as catholyte for RFB would require the presence of acidic additives such as TFA to ensure the system remains functional.

2.4.2 *Electrochemical Studies of VEA*

The electrochemistry of vitamin E, particularly α-tocopherol (α-TOH) has been studied extensively for many years. Like most of the lipid soluble compounds, α-TOH has a saturated phytyl side chain, which provides compatibility in a hydrophobic environment. It is known that vitamin E can be electrochemical oxidized to form a long-lived diamagnetic cation (α-TO^+) in dry organic solvents via a two-electron and one-proton process (Scheme 2.9).[32]

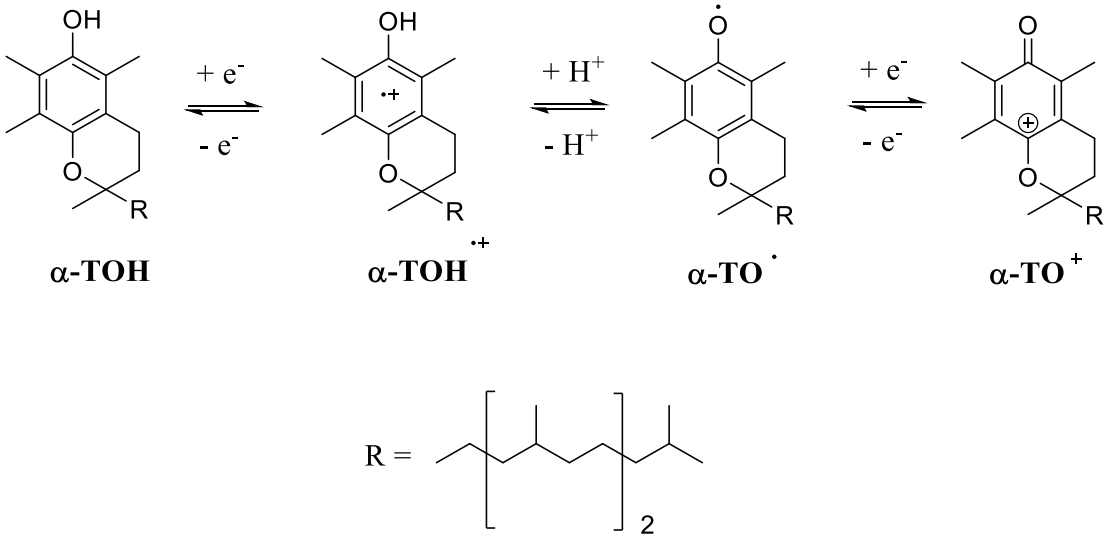

Scheme 2.9. Electrochemical oxidation process of α-TOH in CH_3CN.[7]

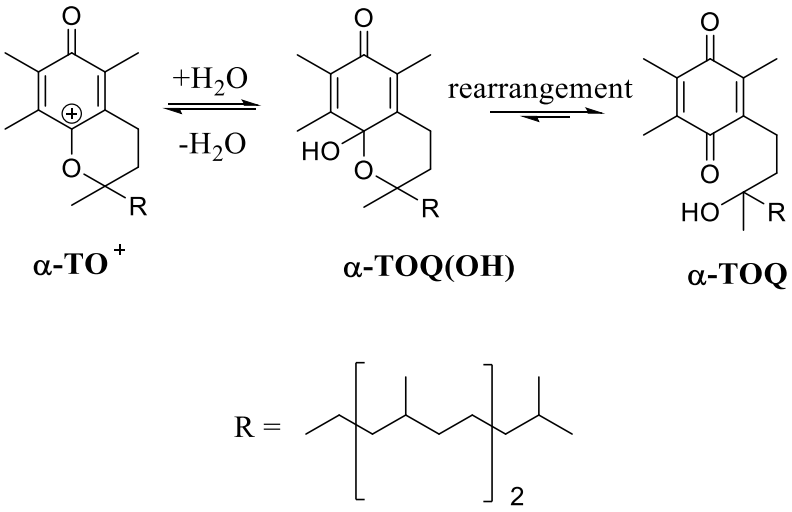

Scheme 2.10. Irreversible chemical reaction of α-TO^+ in the presence of water.

However, the product of the second oxidation process, α-TO^+ is very sensitive to trace water. In the presence of water, α-TO^+ will undergo an irreversible chemical reaction (Scheme 2.10) to form a hemiketal, α-TOQ(OH) follow by rearrangement to form the *para*-quinone, (α-TOQ).[32] Hence, a vitamin E analogue (VEA) was designed to remove phenolic hydrogen atom to prevent the second oxidation process from taking place.[7] In addition, the phytyl side chain was also removed to improve the solubility of VEA in acetonitrile.

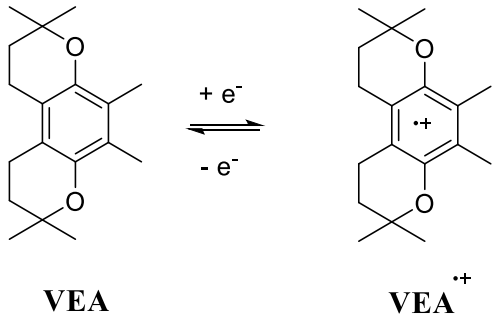

Scheme 2.11. Electrochemical oxidation process of VEA.[7]

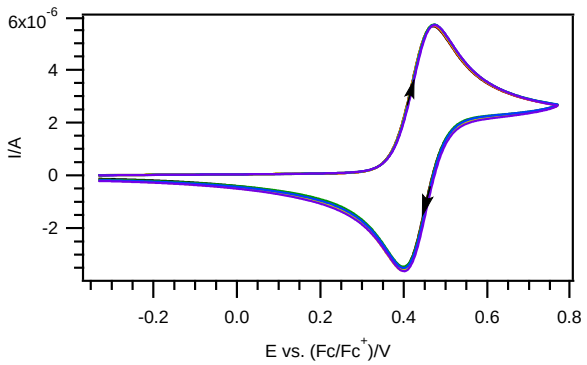

Figure 2.18. Cyclic voltammetry of 2 mM VEA in 0.2 M *n*-Bu_4NPF_6/CH_3CN recorded using a 1-mm diameter planar GC disk electrode at 0.1 V s^{-1}.

Table 2.4. Half-wave potentials ($E_{½}$) and peak-to-peak separation (ΔE_p) of 2 mM VEA in 0.2 M *n*-Bu_4NPF_6/CH_3CN.

Step	$E_{½}$ **vs (Fc/Fc$^+$)/V**	ΔE_p**/mV**
I	+0.44	77.0

The electrochemistry of VEA involves a one-electron chemically (Scheme 2.11) and electrochemically reversible oxidation process (Figure 2.18). Based on the voltammetric profile, the current ratio of i_p^{ox} and i_p^{red} was close to unity. Therefore, VEA exhibited good chemical and electrochemical reversibility on the CV time scale (≤ seconds). In addition, the oxidation potential ($E^r_{½}$ = +0.44 vs (Fc/Fc$^+$)/V) of VEA is reasonably positive to achieve a decent cell voltage for the organic-based battery.

In the mixed reactant electrolyte system, the catholyte and anolyte must be compatible under the same experimental condition. Based on the studies in the previous section, VKA was overall a better anolyte candidate for the organic-based battery. However, acid addictive is required to ensure system longevity for VKA. Therefore, there is a need to investigate the electrochemical performance of the selected catholyte in the presence of TFA. In the CV

analysis, the electrochemical behavior of VEA was studied in the presence of TFA from 0 to 100 equivalents (Figure 2.19). Based on the CV response, there was no change to the profile signal as the acid concentration increased. This shows that VEA has excellent acid tolerance, as expected for a radical cation.

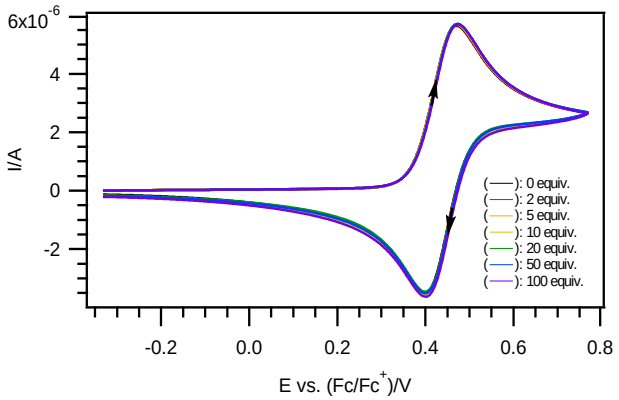

Figure 2.19. Cyclic voltammograms of 2 mM of VEA in 0.2 M *n*-Bu_4NPF_6/CH_3CN and the addition of 0 to 100 equiv. TFA recorded at a scan rate of 0.1 V s^{-1}, with a 1-mm diameter planar GC electrode.

CPE experiments were performed to evaluate the chemical reversibility of VEA in the presence of 50 equivalence of TFA. VEA was electrochemically oxidized at a constant potential of +0.62 vs $(Fc/Fc^+)/V$. Based on the coulometric data obtained (Figures 2.20a and 2.20b), one electron was calculated to be transferred and recovered during the exhaustive electrolysis. The CV recorded at the completion of the oxidative CPE (Figure 2.20c, red dashed line) was offset in the negative current direction due to the change in the oxidation state of VEA species present in the bulk solution. The oxidized solution was reduced back at 0.25 vs $(Fc/Fc^+)/V$. The resulting profile signal fitted perfectly with the CV of the starting material (black solid line), implying that VEA is chemically reversible in the presence of TFA.

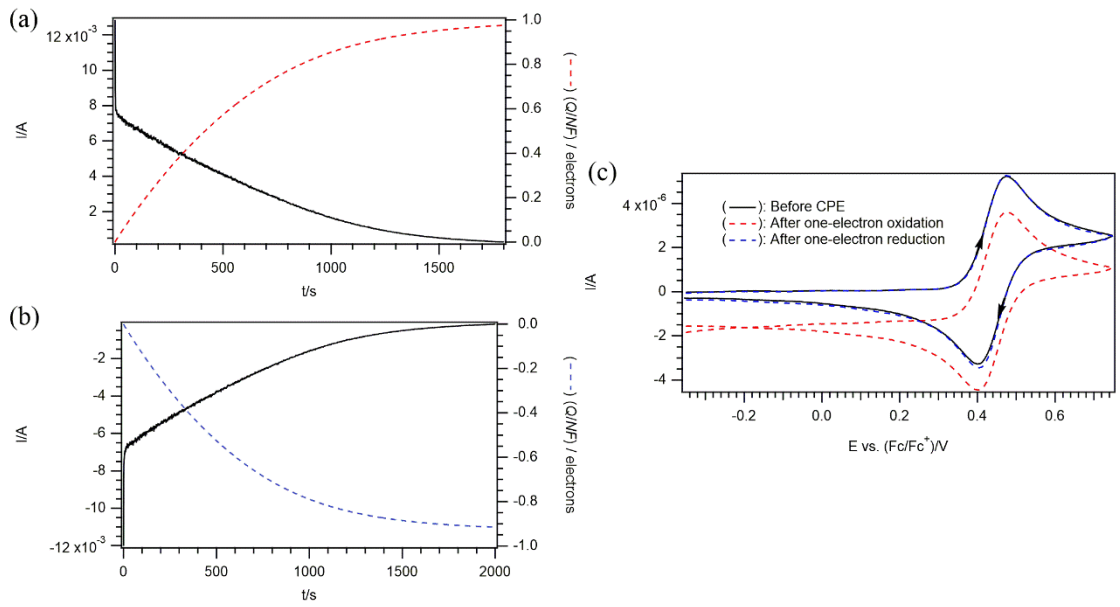

Figure 2.20. Coulometric data (current against time) and CV response for the oxidative electrolysis of 1 mM VE_A in 0.1 M *n*-Bu_4NPF_6/CH_3CN and 50 equiv. of TFA using a 1-mm diameter planar GC disk electrode at 0.1 V s^{-1} (a) Coulometric data for the oxidative CPE at 0.62 vs (Fc/Fc^+)/V. (b) Coulometric data for the reductive CPE at 0.25 vs (Fc/Fc^+)/V. (c) CV response before and after oxidative and reductive CPE. (Black line) Original voltammetric profile of VEA (Red line) After one-electron oxidative CPE (Blue line) After one-electron reductive CPE back to starting material.

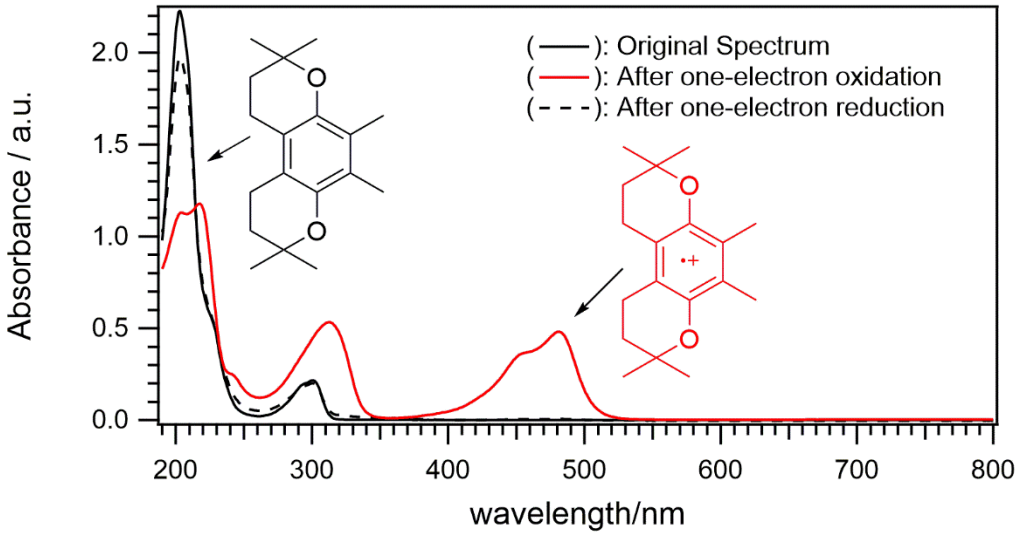

Figure 2.21. Background-subtracted UV-vis spectra of 1 mM VEA in 0.1 M *n*-Bu_4NPF_6/CH_3CN and 50 equiv. TFA. (Black solid line) Original spectrum. (Red solid line) Spectra after one-electron oxidation. (Black dashed line) Spectra back to starting compound after approximately 20 hours.

Ex-situ electrochemical UV-vis spectroscopy was performed to characterize the oxidized form of VEA and to further verify the chemical reversibility. The absorption spectrum obtained from the oxidized solution (Figure 2.21, red solid line) shows two main bands at 313 nm and 482 nm (with a shoulder at 456 nm). The obtained values were in good agreement with the reported spectrum of $VEA^{\bullet+}$ radical cation.[7] The oxidized solution was then subjected to bulk reduction. From the almost indistinguishable UV-vis spectra of VEA before (black solid line) and after (black-dashed line) electrolysis, quantitative recovery of the VEA was achieved.

In conclusion, VEA demonstrated good chemical stability and reversibility in the presence of TFA. In combination with its good oxidation potential ($E½$ = +0.44 vs (Fc/Fc^+)/V), this makes VEA is an ideal catholyte for the organic-based battery.

3.5 Summary

In this study, four different organic compounds have demonstrated their ability to be used for constructing the organic-based redox flow battery. Acid additives are required to impart chemical stability to VKA and TMB systems. In the presence of 50 equivalence of TFA, VKA undergoes a $2e^-/2H^+$ reversible reduction process while TMB undergoes a $2e^-/H^+$ reversible oxidation process. The ability to store multiply electrons favors the development of high energy density RFBs. The use of 2-electron systems can offer twice the energy density compared to a single electron system. Studies have revealed that TCNQ would require a more stringent cell design to prevent parasitic side reactions caused by the presence of oxygen. On the other hand, results have shown that the electrochemical performance of VEA is not affected by the presence of acid. VEA undergoes a reversible one-electron oxidation process at a moderately high oxidative potential ($E_{½}$ = +0.44 vs (Fc/Fc^+)/V) which enables the proposed organic-based redox flow battery to operate at higher cell voltage.

References

1. Wei, X.; Xu, W.; Huang, J.; Zhang, L.; Walter, E.; Lawrence , C.; Vijayakumar, M.; Henderson, W. A.; Liu, T.; Cosimbescu, L.; Li, B.; Sprenkle, V.; Wang, W. *Angew. Chem. Int. Ed.* **2015,** *54*, 8684-8687.

2. Wei, X.; Duan, W.; Huang, J.; Zhang, L.; Li, B.; Reed, D.; Xu, W.; Sprenkle, V.; Wang, W. *ACS Energy Lett.* **2016,** *1*, 705-711.

3. Huo, Y.; Xing, X.; Zhang, C.; Wang, X.; Li, Y. *RSC Adv.* **2019,** *9*, 13128-13132.

4. Huskinson, B.; Marshak, M. P.; Suh, C.; Er, S.; Gerhardt, M. R.; Galvin, C. J.; Chen, X.; Aspuru-Guzik, A.; Gordon, R. G.; Aziz, M. J. *Nature.* **2014,** *505*, 195-198.

5. Duan, W.; Huang, J.; Kowalski, J. A.; Shkrob, I. A.; Vijayakumar, M.; Walter, E.; Pan, B.; Yang, Z.; Milshtein, J. D.; Li, B.; Liao, C.; Zhang, Z.; Wang, W.; Liu, J.; Moore, J. S.; Brushett, F. R.; Zhang, L.; Wei, X. *ACS Energy Lett.* **2017,** *2*, 1156-1161.

6. Liu, Y.; Goulet, M.-A.; Tong, L.; Liu, Y.; Ji, Y.; Wu, L.; Gordon, R. G.; Aziz, M. J.; Yang, Z.; Xu, T. *Chem.* **2019,** *5*, 1861-1870.

7. Peng, H. M.; Choules, B. F.; Yao, W. W.; Zhang, Z.; Webster, R. D.; Gill, P. M. W. *J. Phys. Chem. B.* **2008,** *112*, 10367-10374.

8. Xu, X.; Webster, R. D. *RSC Adv.* **2014,** *4*, 18100-18107.

9. Chan, K. K.; Webster, R. D. *Electroanalysis.* **2016,** *28*, 516-522.

10. Gritzner, G.; Kuta, J. *Pure Appl. Chem.* **1984,** *56*, 461-466.

11. Lee, J. H. Q.; Koh, Y. R.; Webster, R. D. *J. Electroanal. Chem.* **2017,** *799*, 92-101.

12. Harris, D. C. *Quantitative chemical analysis*; seventh ed.; W.H. Freeman: New York, 2007.

13. Skoog, D. A.; West, D. M.; Holler, F. J.; Crouch, S. R. *Fundamentals of analytical chemistry*; eighth ed.; Brooks/Cole: Belmont, Calif., 2004.

14. Lauw, S. J. L.; Xu, X.; Webster, R. D. *ChemPlusChem.* **2015,** *80*, 1288-1297.

15. Kissinger, P. T. E.; Heineman, W. R. E. *Laboratory Techniques in Electroanalytical Chemistry*; Marcel Dekker: New York, 1984.

16. Lund, H.; Hammerich, O. *Organic electrochemistry: revised and expanded*; fourth ed.; Marcel Dekker: New York, 2001.

17. Tessensohn, M. E.; Hirao, H.; Webster, R. D. *J. Phys. Chem. C.* **2013,** *117*, 1081-1090.

18. Gong, K.; Fang, Q.; Gu, S.; Li, S. F. Y.; Yan, Y. *Energy Environ. Sci.* **2015,** *8*, 3515-3530.

19. Martín, N.; Segura, J. L.; Seoane, C. *J. Mater. Chem.* **1997,** *7*, 1661-1676.

20. Tseng, T.-C.; Urban, C.; Wang, Y.; Otero, R.; Tait, S. L.; Alcamí, M.; Écija, D.; Trelka, M.; Gallego, J. M.; Lin, N.; Konuma, M.; Starke, U.; Nefedov, A.; Langner, A.; Wöll, C.; Herranz, M. Á.; Martín, F.; Martín, N.; Kern, K.; Miranda, R. *Nat. Chem.* **2010,** *2*, 374-379.

21. Otero, R.; Vázquez de Parga, A. L.; Gallego, J. M. *Surf. Sci. Rep.* **2017,** *72*, 105-145.

22. Oyama, M.; Webster, R. D.; Suárez, M.; Marken, F.; Compton, R. G.; Okazaki, S. *J. Phys. Chem. B.* **1998,** *102*, 6588-6595.

23. Jeanmaire, D. L.; Van Duyne, R. P. *J. Am. Chem. Soc.* **1976,** *98*, 4029-4033.

24. Grossel, M. C.; Duke, A. J.; Hibbert, D. B.; Lewis, I. K.; Seddon, E. A.; Horton, P. N.; Weston, S. C. *Chem. Mater.* **2000,** *12*, 2319-2323.

25. Hui, Y.; Chng, E. L. K.; Chng, C. Y. L.; Poh, H. L.; Webster, R. D. *J. Am. Chem. Soc.* **2009,** *131*, 1523-1534.

26. Pekmez, K.; Can, M.; Yildiz, A. *Electrochim. Acta.* **1993,** *38*, 607-611.

27. Guin, P. S.; Das, S.; Mandal, P. C. *Int. J. Electrochem.* **2011,** *2011*, 816202.

28. Webster, R. D. *Chem. Rec.* **2012,** *12*, 188-200.

29. Astudillo, P. D.; Tiburcio, J.; González, F. J. *J. Electroanal. Chem.* **2007,** *604*, 57-64.

30. Rifi, M. R. *Tetrahedron Lett.* **1969,** *10*, 5089-5092.

31. Bally, R. W.; Gribnau, T. C. *J Clin Chem Clin Biochem.* **1989,** *27*, 791-6.

32. Tan, Y. S.; Chen, S.; Hong, W. M.; Kan, J. M.; Kwek, E. S. H.; Lim, S. Y.; Lim, Z. H.; Tessensohn, M. E.; Zhang, Y.; Webster, R. D. *PCCP*. **2011,** *13*, 12745-12754.

Chapter 3

Organic-based Battery Powered by Anthraquinone and *o*-Tolidine

---

3.1 Introduction

Organic compounds have shown tremendous potential in the development of RFBs. The advantage for using organic compounds comes from the diversity of molecular structures and the flexibility to achieve desired electrochemical properties by structural modifications via synthetic means. For example: structure-activity studies have shown that the functionalization of quinoxaline with methyl substitution on the 2,3,6 position led to a negative shift in the reduction potential. A more negative reduction potential is favorable for the anolyte component as it would give rise to a higher energy density in the battery system.[1-3] This illustrates the ability of organic compounds undergoing structural tailoring to achieve a desirable redox potential. In addition, organic compounds can be potentially cost-effective and environmentally benign due to their abundance in nature.[4-5]

The redox-active organic materials are the key components that determine the energy density and cyclability of the RFB. The energy density of the RFB can be improved in three different aspects: the cell potential, number of electron-transfer involved, and solubility.[6-7] In addition, the overall cost of the electrolyte can also be further lowered with the selection of the redox-active species based on their cell voltage and/or multi-electron transfer properties.[8] To develop promising battery performance in the non-aqueous regimes, the organic redox pairs should possess desirable redox potentials and have high chemical stability in their reduced and oxidized states.[9] Among various organic compounds screened in Chapter 3, VKA and TMB demonstrated their ability to undergo multi-electron transfer redox processes. The use of two-electron from a single redox molecule can directly increase the molar energy density of the RFB system. In the presence of TFA, the reduction process of VKA involves a $2e^-/2H^+$ mechanism while TMB undergoes a $2e^-/H^+$ chemically reversible oxidation process. Furthermore, the two redox pair have also shown high chemical stability. However, the pairing

of both half-cells resulted in a low theoretical cell voltage of 0.47 V (Figure 3.1). The application of quinones in RFB studies are mostly limited to aqueous-based system where their redox mechanism is better understood and the research on benzidine-related compounds in RFB are not well-established.[10-13] To optimize the cell voltage of a quinone-benzidine based battery system, the electrochemical performance of quinones and benzidines derivatives were investigated in this chapter.

In this study, anthraquinone (section 3.3.1) and *o*-Tolidine (section 3.4.1) were selected as the anolyte and catholyte respectively among other eligible derivatives. Electrochemical studies were first performed on each half cell in isolation (section 3.3.2 and 3.4.2) After which, the redox pairs were subjected to the mixed-reactant system and a series of tests were conducted to evaluate their overall performance under practical conditions.

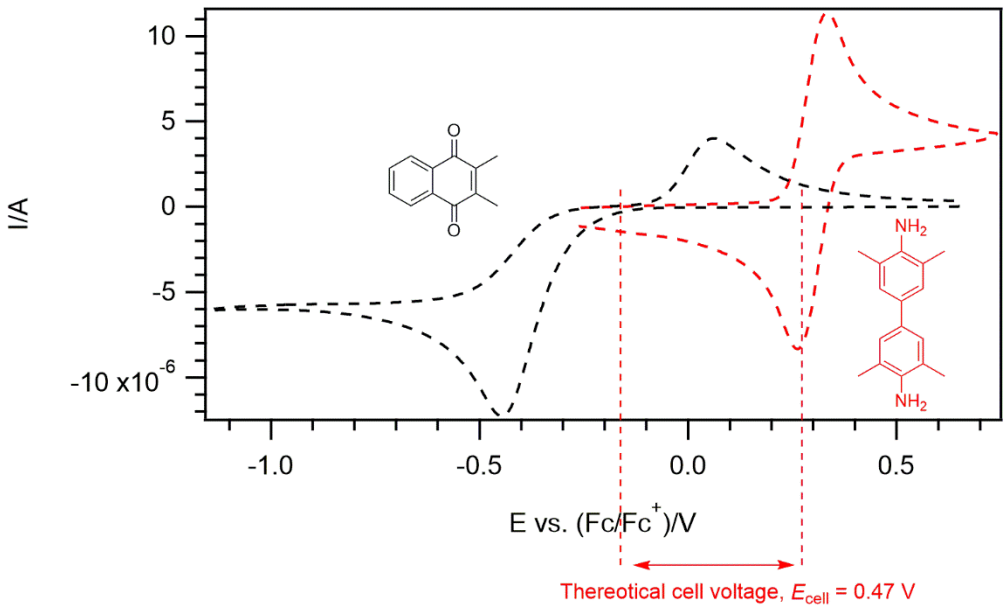

Figure 3.1. Cyclic voltammograms of 1 mM VKA/TMB in 0.1 M *n*-Bu_4NPF_6/CH_3CN and 50 equiv. TFA recorded using a 1-mm diameter planar GC disk electrode at 0.1 V s^{-1}.

3.2 Experimental and Methods

3.2.1 *Chemicals and reagents*

Most chemical and reagents were purchased from chemicals company and used as received unless otherwise stated. Anthraquinone (97%), duroquinone (97%), 9-10-phenanthrenequinone (≥ 99%), tetrachloro-1,4-benzoquinone (99%) and 3,3'5,5'-tetramethylbenzidine (> 99%) were obtained from Sigma-Aldrich. 2,2'-Bis(trifluoromethyl)benzidine (> 98%), *o*-tolidine (> 98%) and trifluoroacetic acid (> 99%) were obtained from Tokyo Chemical Industry Co., Ltd. Acetonitrile (CH_3CN) used was HPLC grade and was purchased from Anhui Fulltime Solvents & Reagents Co., Ltd. The supporting electrolyte, tetrabutylammonium hexafluorophosphate (*n*-Bu_4NPF_6), was synthesized by mixing equivalent molarity of 40% tetrabutylammonium hydroxide (*n*-Bu_4NOH) solution (Alfa-Aesar) with 60% hexafluorophosphoric acid (HPF_6) acid solution (Alfa-Aesar). The precipitate was washed with deionized water repeatedly until the pH of the filtrate was above pH 5, and subsequently purifying the crude product via recrystallization for three times from hot ethanol before drying under vacuum at 433 K for 6 hours.

3.2.2 *Voltammetry*

Variable temperature cyclic voltammetry experiments were performed in a Metrohm jacketed glass cell using a Julabo FP89-HL ultraflow refrigerated ethanol circulator bath to regulate the temperature of the working solution during CV measurement.[14] In the experiment, the temperature of the working solution varied from 0 to 50°C, where CV measurement were taken at each interval of 10°C.

For the ambient stability test, the mixed-reactant samples were dissolved in a 0.1 M *n*-Bu_4NPF_6/CH_3CN with 50 molar equivalents of TFA. The solution was left to stand under

ambient conditions and stored away from light sources. An aliquot (5 mL) was retrieved from the bulk solution on days 0, 3, 5 and 7 for CV measurement to study the chemical stability of the system. The voltammetric profile recorded over 7 days were compared to identify any sign of degradation.

The sensitivity of the mixed reactant system to water was investigated by spiking the working solution with increasing amounts of water. CV analysis was performed after each addition of water to study for the change in electrochemical behaviour. The maximum threshold concentration of water was set at 10 M due to the fixed volume constraint of the cell.

The concentration used in all the experiments were standardized with 1 mM analyte in 0.1 M *n*-Bu_4NPF_6/CH_3CN and unless otherwise stated, all test solutions were deaerated with argon gas for approximately 5 minutes prior to any voltammetric scans. The surface of the working electrode was cleaned through polishing with alumina oxide (grain size 0.3 μm) slurry on a Buehler Ultra-pad polishing cloth and then, rinsed with ultrapure water followed by acetone and dried with a lint free tissue prior to each use.[15]

The redox potentials obtained at the end of experiment were corrected with reference to the oxidation potential of the ferrocene/ferrocenium redox couple (Fc/Fc^+). Ferrocene is often added in the test solutions as an internal reference due to its chemical and electrochemical reversible behaviour via a one-electron transfer process regardless the nature of the organic solvent.[16]

3.2.3 UV-visible Spectroscopy

The UV-visible (UV-vis) spectroscopic experiments were performed in an optically semi-transparent thin-layer electrochemical (OSTLE) cell at 25±2 °C. UV-vis spectroscopy was performed in conjugation with *ex-situ* electrolysis to characterize the identities of the

reduced and oxidized forms of the compound of interest. The UV-vis spectra of the redox couple were recorded with a Perkin Elmer Model Lambda 750 UV/Vis-NIR spectrophotometer.

24-hour UV-vis spectroscopic studies were also conducted to monitor the stability of the reduced / oxidized forms of compound of interest over a longer time scale and to detect for the possibility of side product formation, if any.

3.3 Electrochemical Behaviour of Quinone Derivatives

3.3.1 Cyclic voltammetry of Quinone Derivatives in the presence of TFA

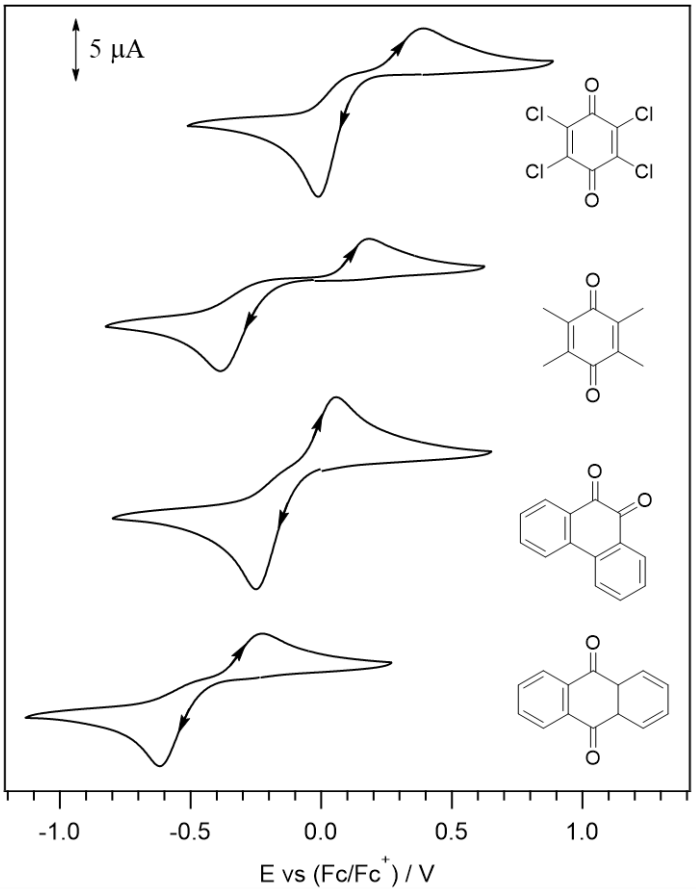

Figure 3.2. Cyclic voltammograms of 1 mM (each) Chloranil, Phenanthrenequinone, Duroquinone and Anthraquinone (in descending order) in 0.1 M *n*-Bu_4NPF_6/CH_3CN and 50 equiv. of TFA recorded using a 1-mm diameter planar GC disk electrode at 0.1 V s^{-1}.

Table 3.1: Half-wave potentials ($E_{½}$) of quinones in 0.1 M *n*-Bu_4NPF_6/CH_3CN and 50 equiv. of TFA

Type of Quinone	***E*½ vs (Fc/Fc$^+$)/V**
Chloranil	+ 0.20
Duroquinone	– 0.10
Phenanthrenequinone	– 0.11
Anthraquinone	– 0.42
VKA	– 0.18

As mentioned in the preceding Chapter 2.3.2, quinones are known to undergo a chemically reversible $2e^-/2H^+$ reduction process to form a stable hydroquinone in the presence of a Bronsted acid.[17-18] The formal reduction potential of quinones is affected by a combination of factors such as the basicity of the quinone, the strength of the acid and the type of solvent used. In this study, CV was carried out to analyse the electrochemical behaviours for a set of substituted quinones, namely, tetrachloro-1,4-benzoquinone (chloranil), 2,3,5,6-tetramethyl-1,4-benzoquinone (duroquinone), 9,10-phenanthrenequinone and anthraquinone as shown in Figure 3.2. The same experimental conditions used for VKA analysis (Chapter 2.3.2) were applied to this study to ensure fair comparison between the results.

Table 3.1 summarises the half-wave potential ($E_{½}$) for the quinone derivatives with respect to Fc/Fc$^+$. The $E_{½}$ lies midway between the E_p^{ox} and E_p^{red} peaks and is only an

approximate estimate of the formal reduction potential due to the complication that the redox processes involve the transfer of two-electron and two protons in likely consecutive individual electron transfer and proton transfer steps.[19] Among the quinone derivatives which includes VKA, AQ has the most negative $E_{½}$ (-0.42 vs (Fc/Fc^{+})/V) in the presence of 50 equivalence of TFA. A more negative reduction potential is favourable since it widens the redox potential gaps between anolyte and catholyte, yielding a higher cell voltage. Therefore, AQ is the best anolyte candidate to use for the later part of the study.

3.3.2 Electrochemical studies of Anthraquinone

In the neutral aprotic organic solvent, anthraquinone (AQ) undergoes two successive one-electron reduction processes (Scheme 3.1), forming the semiquinone ($AQ^{\bullet-}$, wave I) and followed by the dianion (AQ^{2-}, wave II) at a more negative applied potential as shown in Figure 3.3.

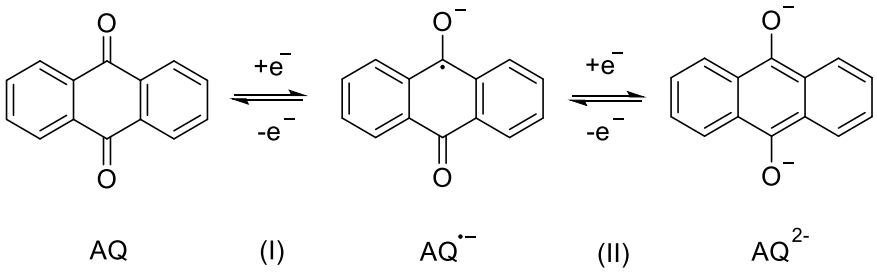

Scheme 3.1. Electrochemical reduction process of AQ.

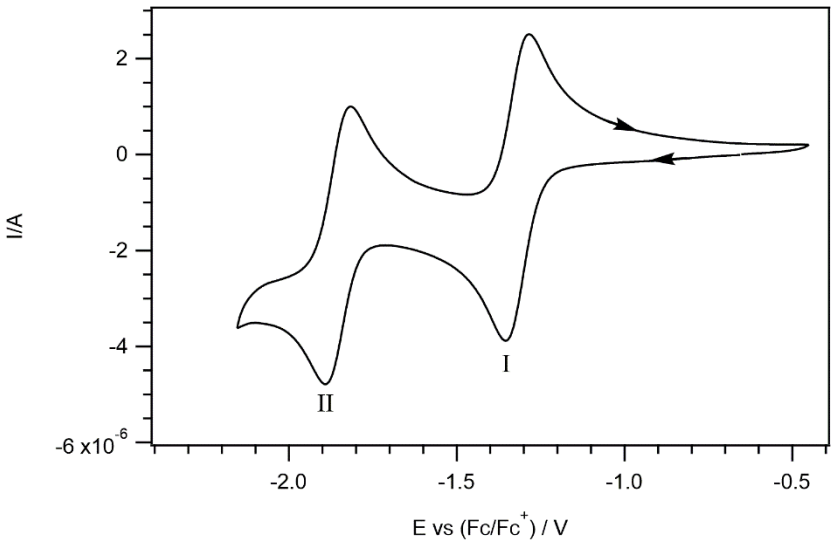

Figure 3.3. Cyclic voltammogram of 1 mM AQ in 0.1 M *n*-Bu_4NPF_6/CH_3CN recorded using a 1-mm diameter planar GC disk electrode at 0.1 V s–1.

From the CV profile, the first reduction process (wave I) is electrochemically reversible while the second reduction process (wave II) is regarded as quasi-reversible.[17, 20] The dianion species, AQ^{2-} are relatively reactive and short-lived in aprotic solvents, this prevents the electrochemical process from being chemically reversible, particularly over electrolysis timescales (≥ minutes). Similar to VKA, TFA was added as the proton source to impart stability to AQ^{2-} in the form of dihydroquinone (AQH_2). The addition of the Bronsted acid induced a change in the reduction mechanism of AQ as shown in Scheme 3.2.[21]

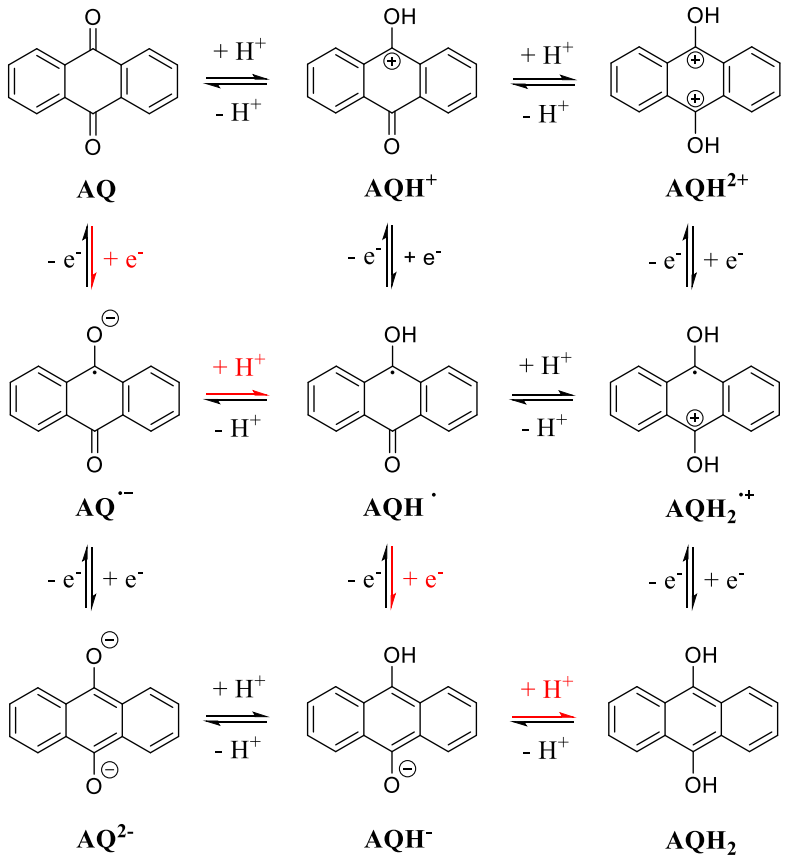

Scheme 3.2. Proposed electrochemical square-scheme mechanism of AQ in ACN with the presence of TFA.[21]

In the presence of TFA, the electrochemical reduction of AQ proceeds through an ECEC mechanism denoted by the red arrows in Scheme 3.2.[22] After gaining an electron, fast protonation of $AQ^{\bullet-}$ takes place and the neutral radical intermediate, $AQH^{\cdot}$, can be readily reduced again at the same potential to form the anion, AQH^{-}.[23] This is followed by another subsequent protonation to form the neutral and stable anthrahydroquinone, AQH_2.

Similar to VKA, the re-oxidation pathway of AQH_2 may proceed via similar or different ECEC mechanism back to the starting material. It was postulated that the re-oxidation of AQH_2 may also take place in another reaction pathway by a second order disproportionation mechanism (DISP2) that was previously mentioned in Chapter 2.3.2.[23]

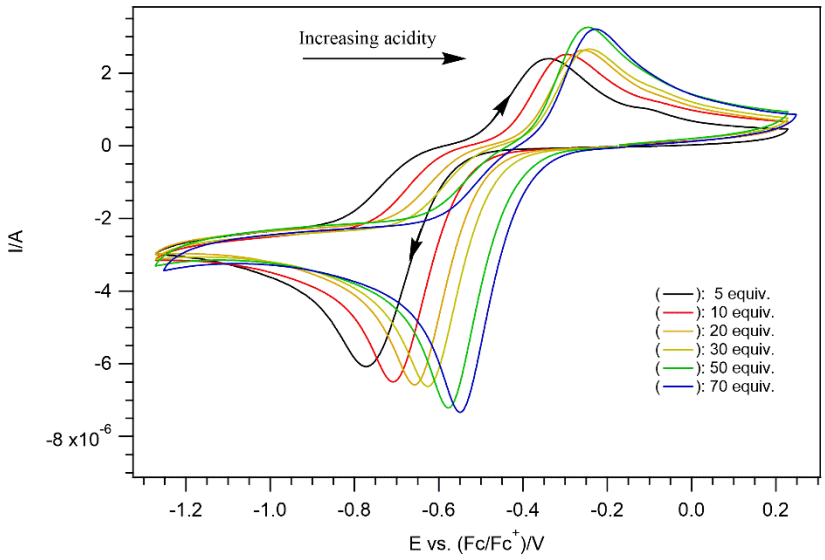

Figure 3.4. Cyclic voltammograms of 1 mM AQ in 0.1 M *n*-Bu_4NPF_6/CH_3CN with the addition of 5 to 70 equiv. TFA recorded at a scan rate of 0.1 V s–1, with a 1-mm diameter planar GC electrode.

With the addition of TFA (Figure 3.4), the initial reduction wave shifts to a more positive potential and the magnitude of the cathodic peak current is approximately doubled the size of the individual cathodic peaks (wave I and II) in Figure 3.2. This suggest that the second electron transfer step (reduction of $AQH^{\cdot}$) occurs at a similar or even lower potential that the first electron transfer step (reduction of AQ), with the coupled proton transfer steps occurring relatively quickly so as not to be outrun on CV time scale (Scheme 3.1). In the reverse scan, the re-oxidation process of the AQH_2 give rise to an anodic peak with a smaller magnitude. This is because the deprotonation processes are thermodynamically less favorable in an acidic environment, and the reverse oxidation reaction occurs through a different order of steps than the forward process shown in Scheme 3.1.[22] The ratio of the peak currents in this study is therefore not a good indication of the system's reversibility and a CPE experiment was then conducted for further verification.

Over the course of TFA addition, the magnitude of the cathodic peak current also increased with rising acid concentration. This is because the PCET process has gradually become the dominate reduction pathway with increasing availability of protons. However, the magnitude of the cathodic peak current does not show any further increment beyond 50 equivalents of TFA. To maintain a reasonably high reduction potential, 50 equivalents of TFA was determined to be the optimum acid concentration.

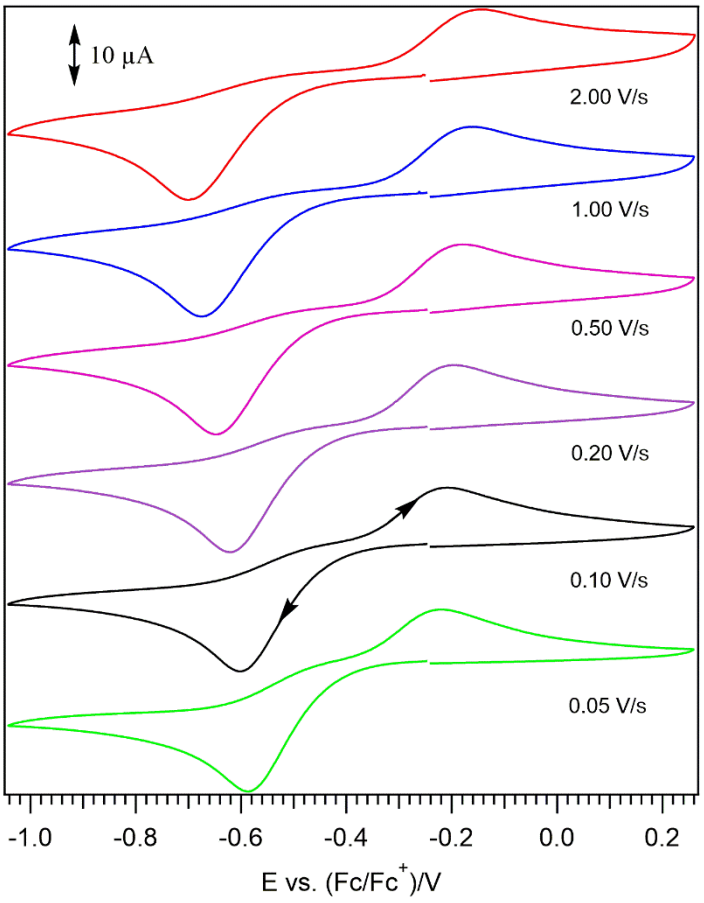

Figure 3.5. Cyclic voltammograms of 1 mM AQ in 0.1 M *n*-Bu_4NPF_6/CH_3CN and 50 equiv. of TFA recorded using a 1-mm diameter planar GC disk electrode at different scan rates. Normalisation of the current data have been carried out via division by (scan rate, $\nu)^{½}$.

CV was performed at different scan rates ranging from 0.05 Vs^{-1} to 2.00 Vs^{-1} to detect possible side reactions that may have been outrun at the usual scan rate (0.10 Vs^{-1}) In addition, the relationship between the cathodic peak current and scan rate can be used to determine the nature of the electron transfer process. From the normalized data obtained in Figure 3.5, the ratio of the anodic peak current (i_p^{ox}) to cathodic peak current (i_p^{red}) remain relatively constant across various scan rate, while the anodic (E_p^{ox}) to cathodic (E_p^{red}) peak-to-peak separation increased with increasing scan rate. This suggests slow electron transfer kinetic between the electrode and AQ in the acidic aprotic solvent. Nonetheless, AQ exhibits good chemical reversibility in the presence of TFA due to the absence of unexpected peaks which suggest that no secondary products were generated across different scan rates.

Table 3.2. Cathodic (E_p^{red}), anodic (E_p^{ox}) peak potentials, half-wave potentials ($E_{½}$) and cathodic peak current (i_p^{red}) for 1 mM AQ in 0.1 M *n*-Bu_4NPF_6/CH_3CN and 50 equiv. of TFA at different scan rates.

Scan rate/Vs^{-1}	E_p^{red}/V	E_p^{ox}/V	$E_{½}$/V	$\sqrt{v/Vs^{-1}}$	i_p^{red}/μA
0.05	-0.596	-0.238	-0.417	0.224	-3.998
0.10	-0.607	-0.226	-0.417	0.316	-5.524
0.20	-0.627	-0.208	-0.418	0.447	-7.648
0.50	-0.653	-0.195	-0.424	0.707	-11.851
1.00	-0.680	-0.175	-0.428	1.000	-16.334
2.00	-0.706	-0.167	-0.436	1.414	-22.614

The apparent diffusion coefficient of AQ was calculated to be 6.8 x 10^{-6} cm^2 s^{-1} by substituting the values (Table 3.2) into the Randles-Sevcik expression[24]:

$$i_p = (2.69 \times 10^5)n^{3/2}ACD^{1/2}\nu^{1/2}$$

where n = number of electrons involved in the charge transfer, A = electrode surface area (cm^2), C = concentration of analyte in bulk solution (mol cm^{-3}), D = diffusion coefficient (cm^2 s^{-1})

and ν = scan rate (Vs^{-1}). However, this equation applies to simple fast one-electron transfer processes and not reactions involving coupled chemical processes.

As illustrated in Figure 3.6, the plot of cathodic peak currents (i_p^{red}) against square root of scan rate ($\nu^{½}$) demonstrated a linear relationship. Therefore, it can be established the nature of the electrochemical reduction process of AQ is primarily diffusion-controlled under the experimental conditions, although again this plot applies to fast (electrochemically reversible) electron transfer processes.

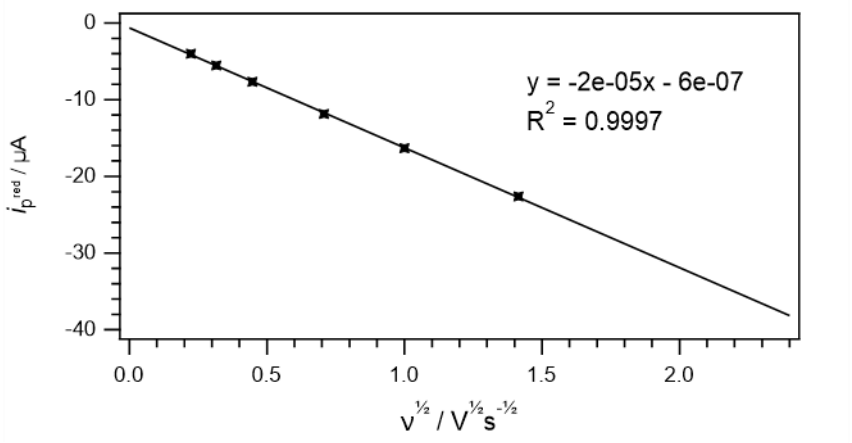

Figure 3.6. Plots of cathodic peak (i_p^{red}) current against square root of scan rate ($\nu^{½}$) for cyclic voltammograms of 1 mM AQ in 0.1 M *n*-Bu_4NPF_6/CH_3CN with 50 equiv. of TFA recorded using 1-mm diameter planar GC disk electrode at different scan rates (0.05, 0.10, 0.20, 0.50, 1.00, 2.00 Vs^{-1}).

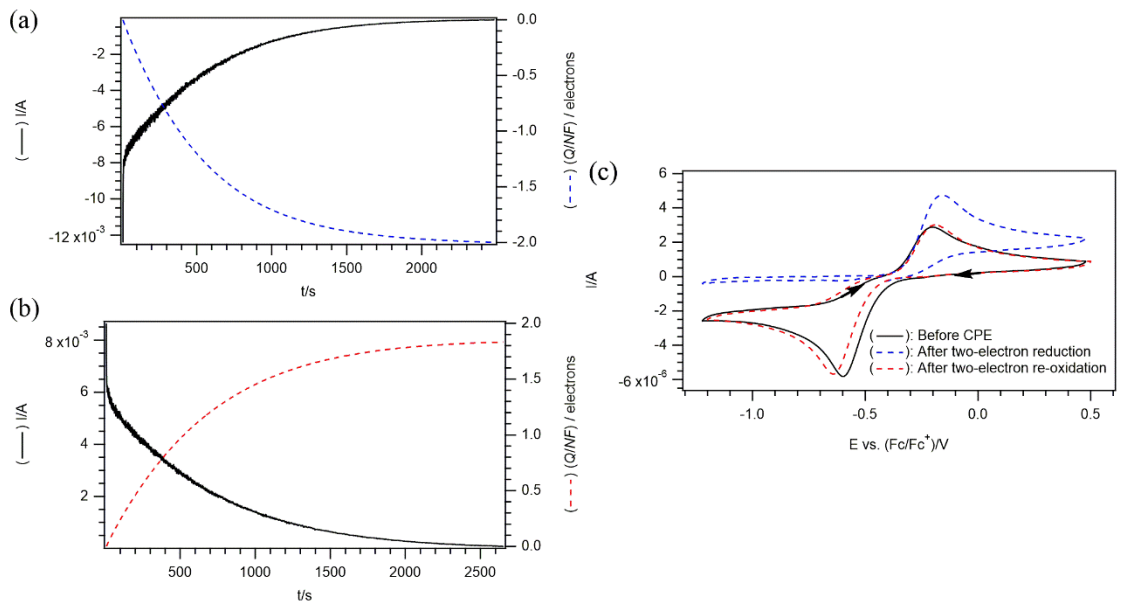

Figure 3.7. Coulometric data (current against time) and CV response for the reductive electrolysis of 1 mM AQ in 0.1 M *n*-Bu_4NPF_6/CH_3CN and 50 equiv. of TFA using a 1-mm diameter planar GC disk electrode at 0.1 V s–1 (a) Coulometric data for the reductive CPE at –0.75 vs (Fc/Fc+)/V. (b) Coulometric data for the oxidative CPE at -0.07 vs (Fc/Fc+)/V. (c) CV response before and after reductive and oxidative CPE. (Black solid line) Original voltammetric profile of AQ (Blue dashed line) After two-electron reductive CPE (Red solid line) After two-electron oxidative CPE back to starting material.

The chemical reversibility of the redox process cannot be established solely by the CV experiments. CV is considered a microanalysis technique where only a small fraction of the analyte on the surface of the electrode is electrochemically modified. Therefore, CPE experiments were carried out to determine the chemical reversibility and stability of the reduced species, AQH_2 under bulk conversion over extended timescales (>minutes). The applied potential for the reductive CPE was set at 0.15 V more negative than the reductive peak potential (E_p^{red}) of AQ to ensure complete reduction in the bulk solution. Based on the coulometric data obtained (Figures 3.7a and 3.7b), approximately 2 electrons were calculated to be transferred and recovered during the whole CPE experiment. The slight shortage of $2e^-$

in the oxidative charge may due to spontaneous re-oxidation which take place at the interface of the working and auxiliary electrode compartments of the H-cell and the possibility of cross-compartment diffusion of the reduced species.[25-26]

Nonetheless, comparable CV responses were obtained before (black solid line) and after (red dashed line) exhaustive electrolysis as shown in Figure 3.7c, this revealed that quantitative recovery of AQ was achieved. As such, AQ has proven to be chemically reversible in the presence of TFA.

Ex-situ electrochemical UV-vis spectroscopy was performed to characterize the reduced form of AQ and to further examined the chemical reversibility of AQ.

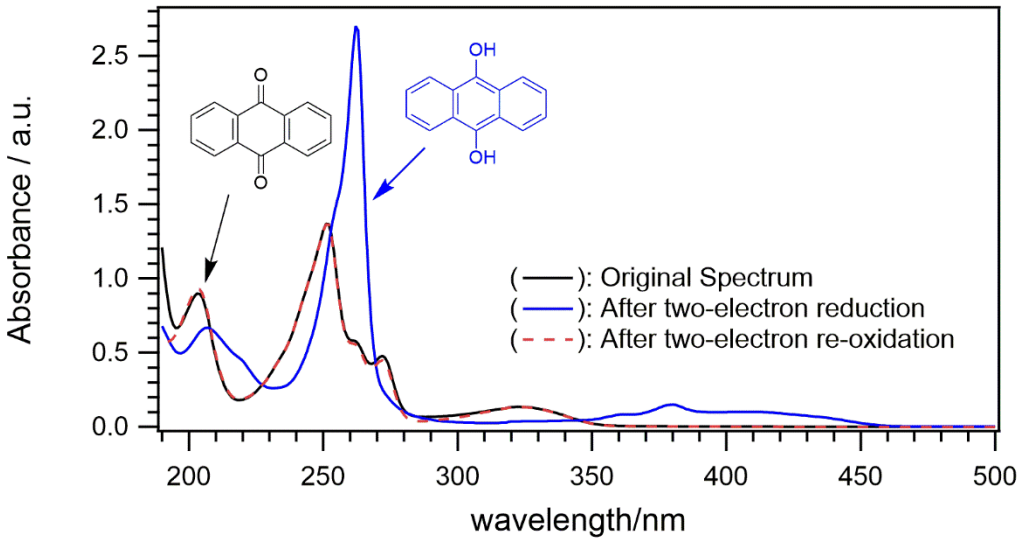

Figure 3.8. Background-subtracted UV-vis spectra of 0.25 mM AQ in 25 mM *n*-Bu_4NPF_6/CH_3CN and 50 equiv. TFA. (Black solid line) Original spectrum. (Blue solid line) Spectra after two-electron reduction. (Red dashed line) Spectra back to starting compound.

The UV-vis absorption spectra of AQ presented in Figure 3.8 shows two characteristic bands at 204 nm and 251 nm (with a shoulder peak at 272 nm) in the original spectrum (black solid line) while the reduced species, AQH_2 has a distinctive band at 262 nm (blue solid line).

The values obtained were in close agreement with the reported spectrum in different solvents.[27-28] As shown in Figure 3.8, the spectra collected (red dashed line) after re-oxidation was almost indistinguishable from the original spectrum (black solid line), this shows that a quantitative recovery of the starting compound was achieved.

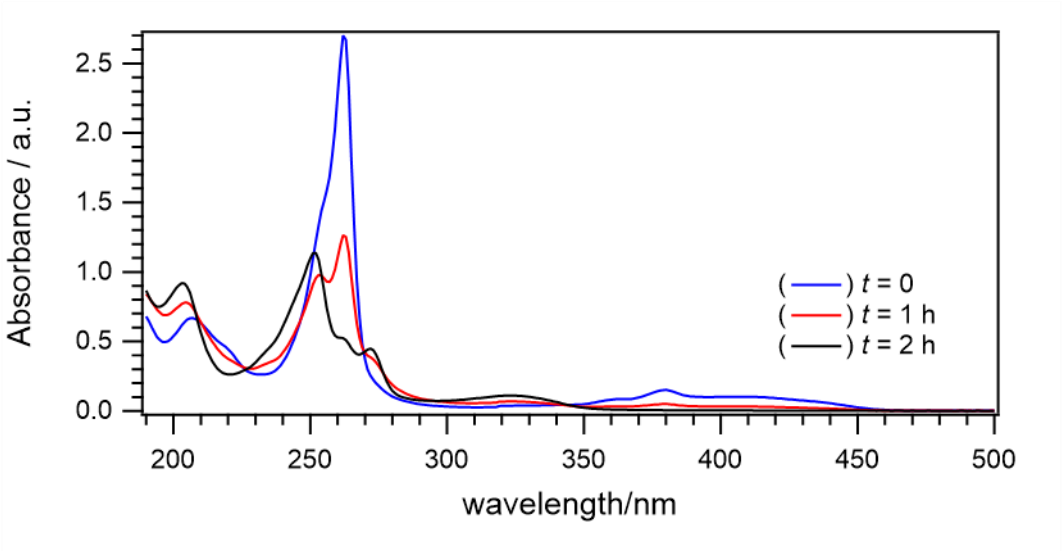

Figure 3.9. Background-subtracted UV-vis spectra of 0.25 mM AQ in 25 mM *n*-Bu_4NPF_6/CH_3CN and 50 equiv. TFA recorded over time. (Black solid line) Initial scan at 0 h. (Red solid line) After 1 h. (Black solid line) Final scan after 2 h.

However, results from the time-based study over 2 hours have revealed that the reduced species, AQH_2 undergo spontaneous oxidation under ambient condition. The absorption maxima at 262 nm are observed to decrease after 1 hour (Figure 3.9, red solid line), while a distinct band at 251 nm (characteristic absorption bands of AQ) has re-emerged. Based on the observation, the reduced species were converted back to the starting material. The spontaneous oxidation is likely caused by the presence of atmospheric oxygen in the solution. The reduced species mediates one-electron reduction of oxygen to form the superoxide anion radical which leads to the self-discharge.[18] Nevertheless, the functionality of system is still preserved since the presence of oxygen does not appear to incur any loss to the AQ.

3.4 Electrochemical Behaviour of Benzidine Derivatives

To construct an ideal organic based RFB, the selected catholyte should undergo oxidation at a reasonably positive potential to maximize the potential difference upon pairing of both half-cells. As such, CV was carried out to analyse the electrochemical behaviour of a series of benzidine analogues, namely 2,2′-bis(trifluoromethyl)benzidine, 3,3′-dimethylbenzidine (*o*-tolidine) and 3,3′,5,5′-tetramethylbenzidine (TMB) as shown in Figure 3.10.

3.4.1 Cyclic voltammetry of Benzidine Derivatives in the presence of TFA

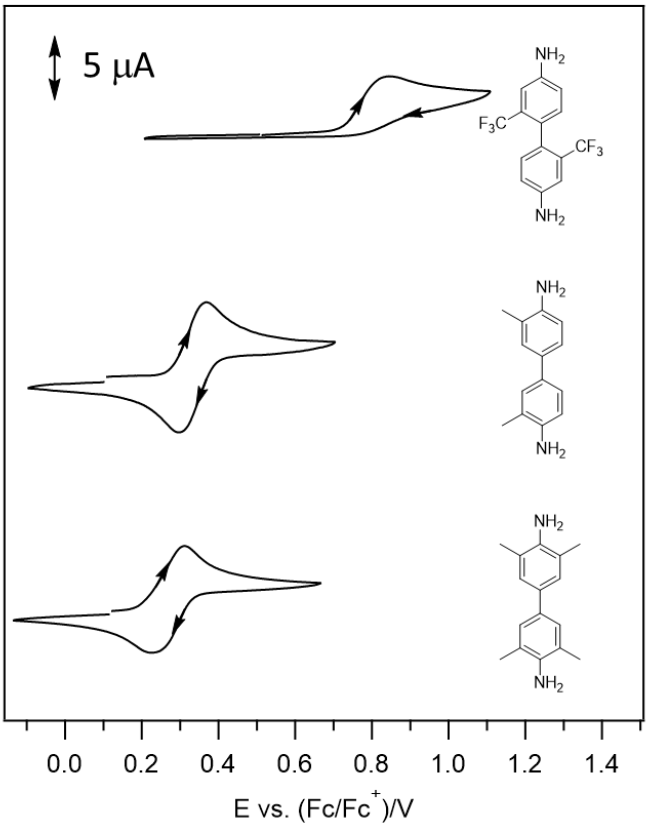

Figure 3.10. Cyclic voltammograms of 1 mM (each) 2,2'-bis(trifluoromethyl)benzidine, *o*-tolidine, and TMB (in descending order) in 0.1 M *n*-Bu_4NPF_6/CH_3CN and 50 equiv. of TFA recorded using a 1-mm diameter planar GC disk electrode at 0.1 V s–1.

Benzidines are aromatic diamine compounds which are made up of 2 phenyl rings. Generally, benzidine compounds are known to undergoes sequential one-electron oxidation processes as shown in Scheme 3.3.[29]

Table 3.3. Half-wave potentials ($E_{½}$) of benzidine analogues in 0.1 M *n*-Bu_4NPF_6/CH_3CN and 50 equiv. of TFA.

Type of Quinone	$E_{½}$ vs (Fc/Fc^+)/V
2,2′-bis(trifluoromethyl)benzidine	-
***o*-tolidine**	+ 0.33
TMB	+ 0.27

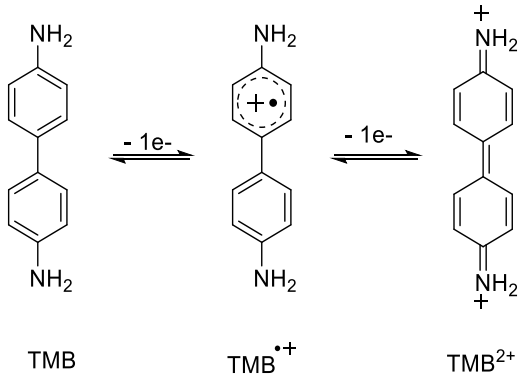

Scheme 3.3. Sequential one-electron oxidation of benzidine.

In this study, CV experiments were performed in the presence of 50 equivalents of TFA as shown in Figure 3.10. The amount of acid added to the system was determined based on the optimum acid concentration that was concluded previously for the quinones (section 3.3.2). To operate under mixed-reactant conditions, the electrochemical performance of the catholyte and anolyte should be evaluated under the same experimental conditions. Under the influence of TFA, the oxidation process of the benzidine involves a two–electron and one–proton ($–2e^–/–1H^+$) mechanism which will be further discussed in this section.

Table 3.3 summarises the half-wave potential ($E_{½}$) for the benzidine analogues with respect to Fc/Fc^{+}. The substituent effects can be clearly seen from the change in the oxidation potentials of the benzidine analogues. Aromatic compounds with electron donating functional group such as *o*-tolidine and TMB exhibit lower oxidation potentials because excess electron density is supplied to an area in the aromatic ring where the electron is removed. As a result, the oxidation processes becomes energetically favored.[30] In contrast, the presence of an electron-withdrawing group leads to an electron deficiency aromatic ring from which electrons cannot be easily removed, thus a higher oxidation potential is required. 2,2′-Bis(trifluoromethyl)benzidine has the highest oxidative potential owing to the strong electron-withdrawing trifluoromethyl substituents. However, the oxidation process is chemically irreversible since no peak was observed on the reverse scan.

Among the feasible benzidine analogues, *o*-tolidine exhibits good chemical reversibility and a slightly more positive $E_{½}$ (+0.33 vs $(Fc/Fc^{+})/V$) in the presence of TFA. In addition, the cost of *o*-tolidine (1.28 USD/g) is significantly lower than TMB (15.92 USD/g).[31] Therefore, *o*-tolidine is the best catholyte to be used for the later part of the study.

3.4.2 Electrochemical studies of *o*-Tolidine

In pure acetonitrile, o-*t*olidine undergoes two sequential one-electron oxidation processes, forming the radical cation and followed by the dication at a more positive applied potentials as shown in Figure 3.11 (black solid line).

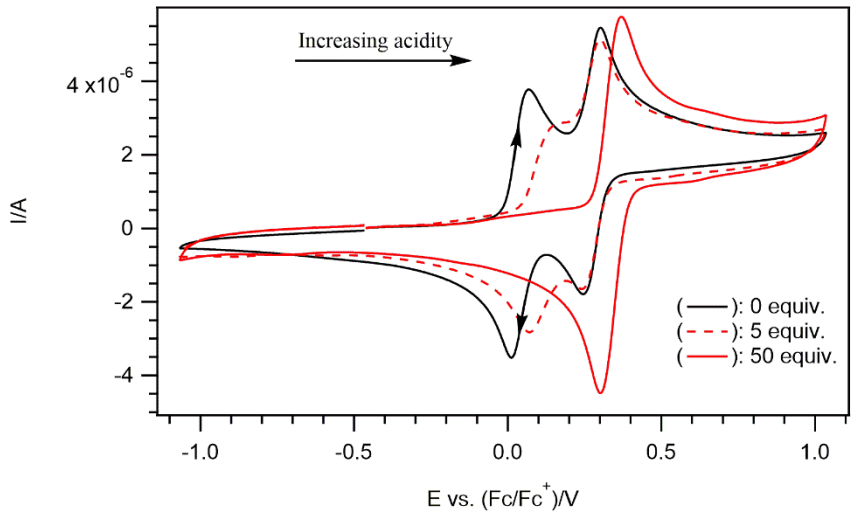

Figure 3.11. Cyclic voltammograms of 1 mM *o*-Tolidine in 0.1 M *n*-Bu_4NPF_6/CH_3CN with the addition of 0 to 50 equiv. TFA recorded at a scan rate of 0.1 V s–1, with a 1-mm diameter planar GC electrode. (Black solid line) 0 equiv. (Red dashed line) 5 equiv. (Red solid line) 50 equiv. of TFA.

Due to structural similarity, the electrochemical behaviour of *o*-tolidine in the presence of TFA is similar to TMB. With sufficient acid concentration (50 equivalents of TFA), the first E_p^{ox} shifts towards and merges with the E_p^{ox} of the second oxidation process to form a single peak, at a slightly more positive potential than observed for the second oxidation process in the absence of TFA.

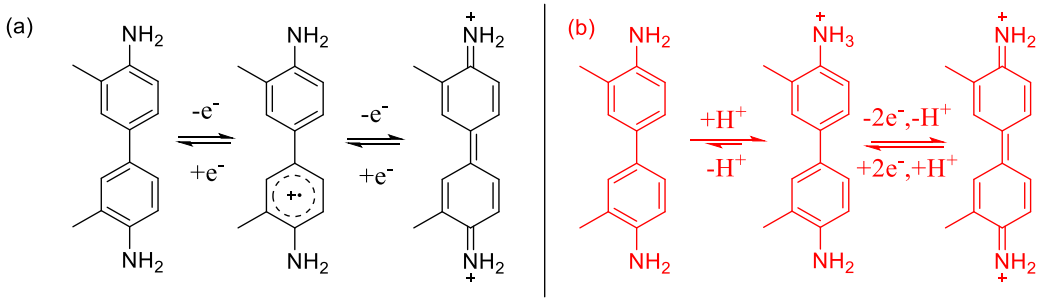

Scheme 3.4. Proposed electrochemical mechanism of *o*-Tolidine in (a) Pure ACN (b) With TFA.

In the absence of acid additive, the oxidation process of *o*-tolidine proceeds via an EE mechanism (Scheme 3.4a). However, with the addition of TFA, the first step of the proposed reaction pathway involves the protonation of the neutral *o*-tolidine (Scheme 3.4b).[32] The following ECE mechanism is proposed to occur in quick succession such that it appears concerted on the CV time scale as shown in Figure 3.11 (red solid line).

In the case of *o*-tolidine, only a marginal increase was observed in the anodic (E_p^{ox}) to cathodic (E_p^{red}) peak-to-peak separation with increasing scan rate. This suggests moderate electron transfer kinetic between the electrode and *o*-tolidine in the presence of TFA. Nonetheless, the absence of anomalous peaks suggests that the oxidation of *o*-tolidine is chemically reversible since no side reaction was outrun on the CV time scale.

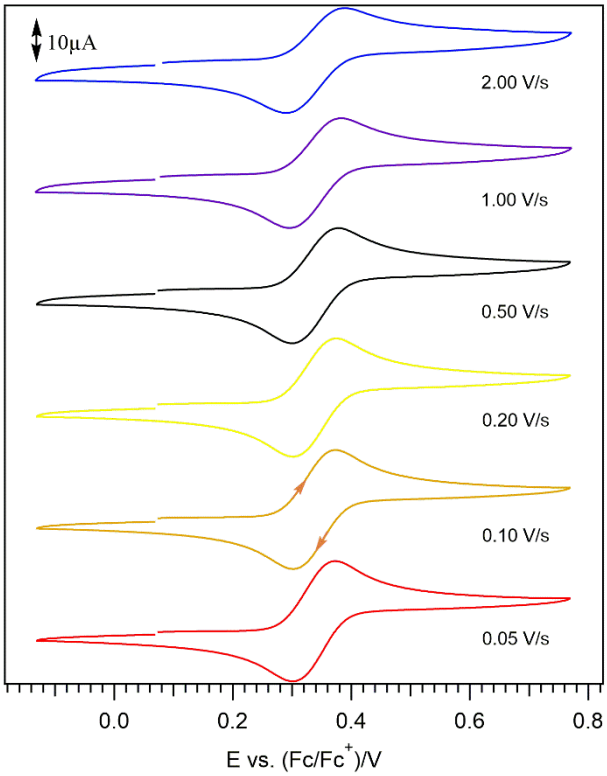

Figure 3.12. Cyclic voltammograms of 1 mM *o*-Tolidine in 0.1 M *n*-Bu_4NPF_6/CH_3CN and 50 equiv. of TFA recorded using a 1-mm diameter planar GC disk electrode at different scan rates. Normalisation of the current data have been carried out via division by (scan rate, $\nu)^{½}$.

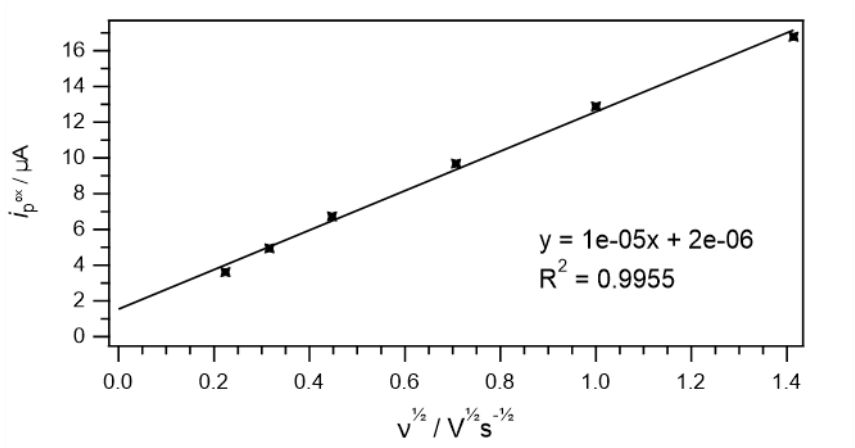

Figure 3.13. Randles-Sevcik plots of cathodic peak (i_p^{red}) current against square root of scan rate ($\nu^{½}$) for cyclic voltammograms of 1 mM *o*-tolidine in 0.1 M *n*-Bu_4NPF_6/CH_3CN with 50

equiv. of TFA recorded using 1-mm diameter planar GC disk electrode at different scan rates (0.05, 0.10, 0.20, 0.50, 1.00, 2.00 Vs^{-1}).

By applying the values (Table 3.4) to the Randles-Sevcik equation, the apparent diffusion coefficient of *o*-Tolidine was calculated to be 3.4 x 10^{-6} cm^2 s^{-1}. The linear relationship between anodic peak currents (i_p^{ox}) and the square root of scan rate ($\nu^{½}$) indicates that the nature of the electrochemical oxidation process of *o*-tolidine is primarily diffusion-controlled (Figure 3.13), although again this equation applies predominately to simple electron transfer not involving coupled chemical reactions.

Table 3.4. Anodic (E_p^{ox}), cathodic (E_p^{red}) peak potentials, half-wave potentials ($E_{½}$) and anodic peak current (i_p^{ox}) for 1 mM *o*-tolidine in 0.1 M *n*-Bu_4NPF_6/CH_3CN and 50 equiv. of TFA at different scan rates.

Scan rate/Vs^{-1}	E_p^{ox}/V	E_p^{red}/V	$E_{½}$/V	$\sqrt{v/Vs^{-1}}$	i_p^{ox}/μA
0.05	0.368	0.301	0.334	0.224	3.609
0.10	0.370	0.303	0.336	0.316	4.934
0.20	0.370	0.303	0.336	0.447	6.726
0.50	0.374	0.301	0.337	0.707	9.681
1.00	0.376	0.297	0.336	1.000	12.881
2.00	0.382	0.287	0.334	1.414	16.782

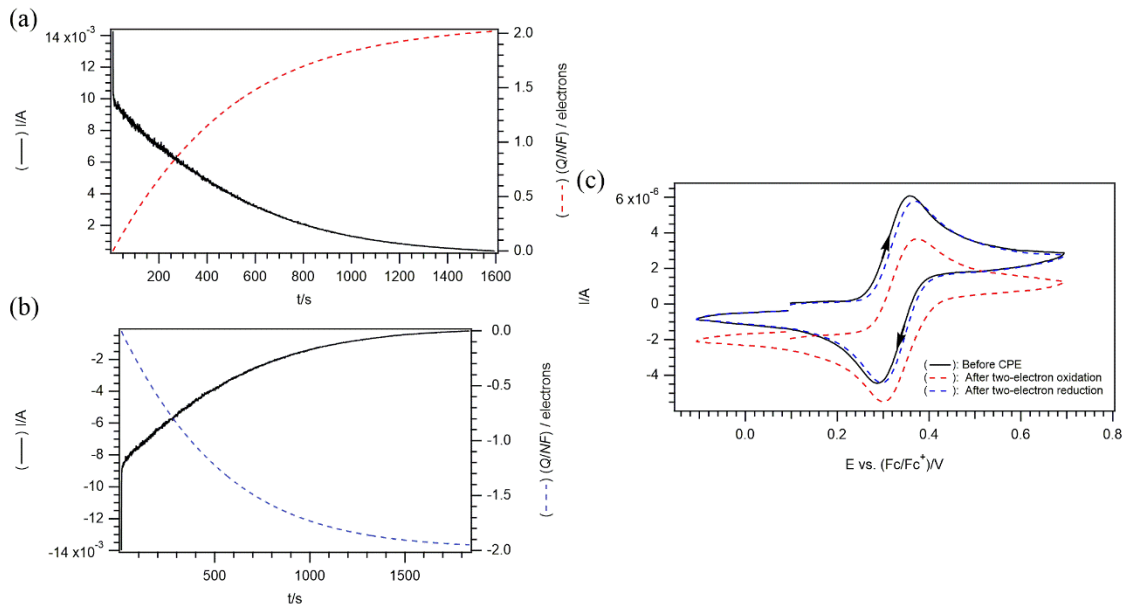

Figure 3.14. Coulometric data (current against time) and CV response for the oxidative electrolysis of 1 mM *o*-tolidine in 0.1 M *n*-Bu_4NPF_6/CH_3CN and 50 equiv. of TFA using a 1-mm diameter planar GC disk electrode at 0.1 V s^{-1} (a) Coulometric data for the oxidative CPE at 0.50 *vs* (Fc/Fc^+)/V. (b) Coulometric data for the reductive CPE at 0.10 *vs* (Fc/Fc^+)/V. (c) CV response before and after oxidative and reductive CPE. (Black solid line) Original voltammetric profile of *o*-tolidine. (Red dashed line) After two-electron oxidative CPE. (Blue dashed line) After two-electron reductive CPE back to starting material.

A CPE experiment was carried out to determine the chemical reversibility and to quantify the number of electrons involved in the redox process of *o*-tolidine. The applied potential for the oxidative CPE was set at 0.15 V more positive than the oxidative peak potential (E_p^{ox}) of *o*-tolidine. The CV recorded at the completion of the oxidative CPE (Figure 3.14c, red dashed line) was offset in the negative current direction. Approximately 2 electrons were calculated to be transferred and recovered during the CPE experiment. In addition, well-overlapped CV responses were obtained before (black solid line) and after (blue dashed line) exhaustive electrolysis as shown in Figure 3.14c, thus confirming the chemical reversibility of *o*-tolidine in the presence of TFA.

UV-vis spectroscopy was performed in conjugation with *ex-situ* electrolysis to characterize the identity of the oxidized form of *o*-tolidine and to further examined the chemical reversibility.

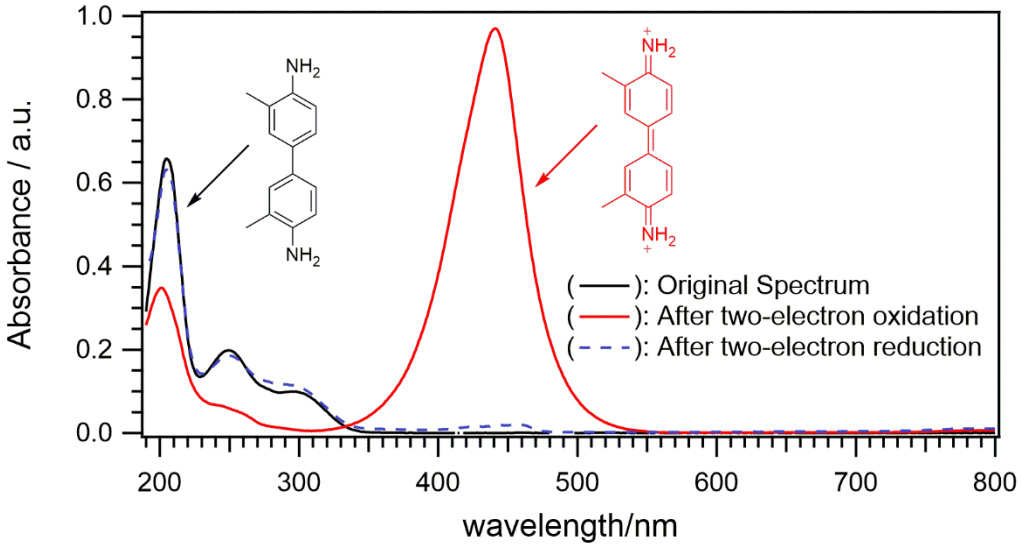

Figure 3.15. Background-subtracted UV-vis spectra of 0.25 mM *o*-tolidine in 25 mM *n*-Bu_4NPF_6/CH_3CN and 50 equiv. TFA. (Black solid line) Original spectrum. (Red solid line) Spectra after two-electron oxidation. (Blue dashed line) Spectra back to starting compound.

The UV-vis absorption spectra of *o*-tolidine presented in Figure 3.15 show a characteristic peak at 250 nm in the original spectrum (black solid line). After oxidative CPE, a broad absorption peak emerged at 443 nm and this value is in good agreement with the reported value of the o-*t*olidine dication.[33] Despite having a trace amount of unconverted oxidized species, the magnitude of the absorption spectra after CPE (blue dashed line) was well-maintained and quantitatively comparable to the starting material (black solid line).

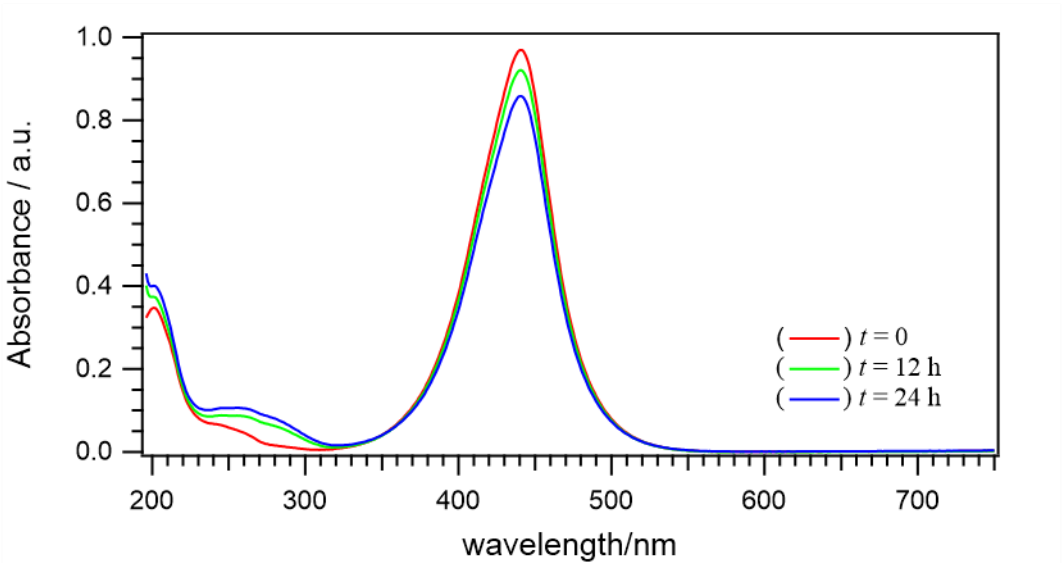

Figure 3.16. Background-subtracted UV-vis spectra of 0.25 mM *o*-tolidine in 25 mM *n*-Bu_4NPF_6/CH_3CN and 50 equiv. TFA recorded over time. (Red solid line) Initial scan at 0 h. (Green solid line) After 12 h. (Blue solid line) Final scan after 24 h.

A time-based study was performed in order to further examine the stability of the oxidized form spectroscopically over 24 hours (Figure 3.16). The intensity of the absorption band corresponding to the radical dication at 443 nm decreased gradually over time. The self-discharging phenomena can be induced by trace impurities that were present in the acetonitrile or by contamination from reduced species produced in the counter electrode compartment during the exhaustive electrolysis. Nevertheless, no anomalous peaks were observed from the final scan after 24 hours (blue solid line). Therefore, the studies by UV-vis spectroscopy strongly suggests that *o*-tolidine is chemically reversible and stable in the proposed experimental conditions.

3.5 Mixed Reactant System for Anthraquinone and *o*-Tolidine in the presence of TFA

Generally, irreversible crossover is one of the main issues that leads to unrecoverable capacity loss in the tradition RFBs.[10, 34-35] As such, the mixed-reactant electrolyte system was proposed in this study to minimize the crossover by reducing the concentration gradients across the membrane. To implement such a concept, both compounds (catholyte and anolyte) should be chemically compatible such that their charged forms can co-exist with the neutral form of the opposite half-cell. In the fully charged state, each of the half-cell in the mixed reactant system will consist of its oxidized/reduced species along with the neutral form of the redox species from the opposite half-cell (Figure 3.17). The advantage of this approach is that the slow concentration dependent diffusion that will invariably occur when the solutions in the two compartments are different, will not occur when the compositions are essentially identical, thereby improving the long-term stability of the entire system.

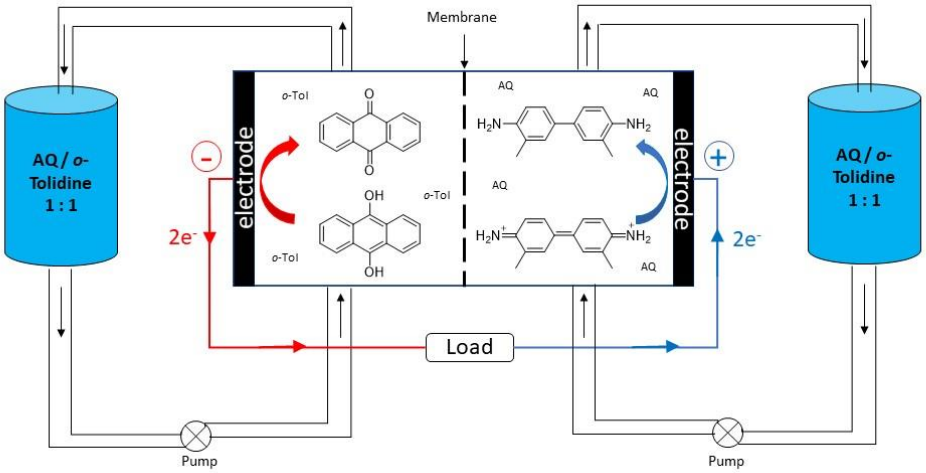

Figure 3.17. Schematic diagram of the proposed mixed-reactant system based on AQ and *o*-tolidine in discharge mode.

In this study, AQ and *o*-tolidine were paired up to construct a mixed reactant organic-based RFB with a theoretical cell voltage of 0.75 vs (Fc/Fc^+). The value was estimated based on the potential difference between the approximate $E_{½}$ of AQ and *o*-tolidine as illustrated in Figure 3.18.

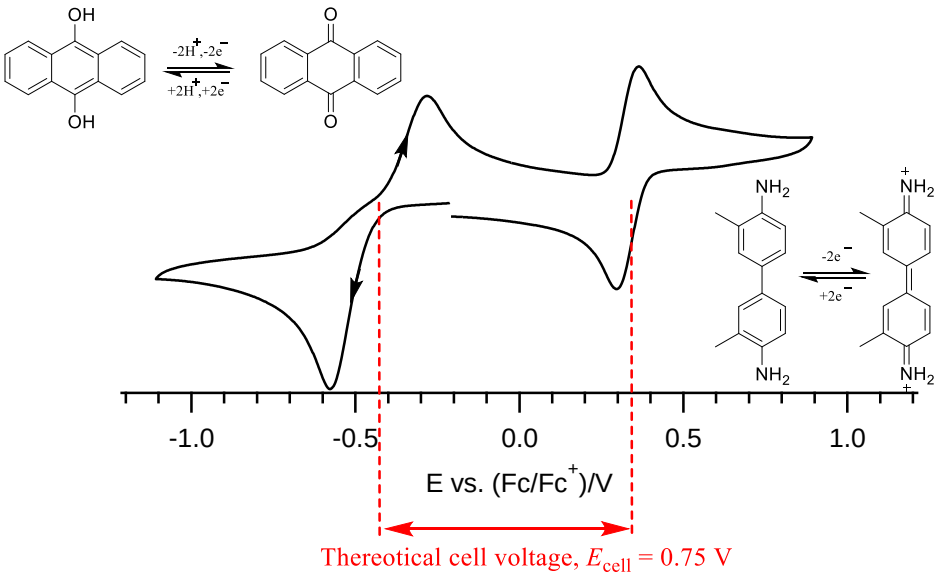

Figure 3.18. Conceptual illustration of the mixed-reactant system.

The functionality of the mixed reactant system was evaluated by a series of tests performed under practical conditions.

3.5.1 Mixed Reactants Electrolysis

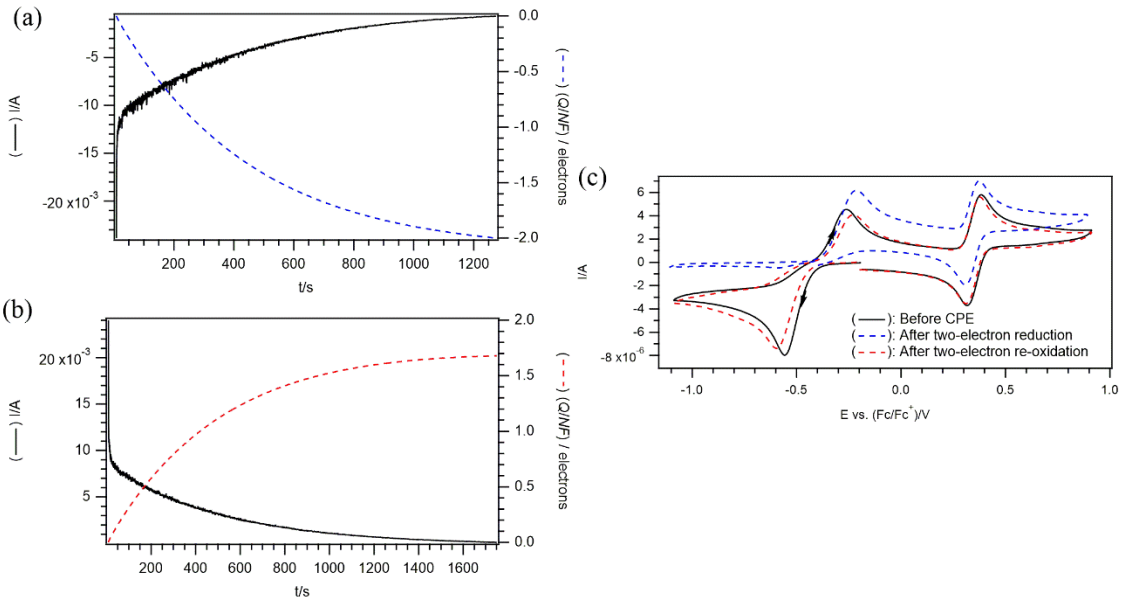

Figure 3.19. Coulometric data (current against time) and CV response for the reductive electrolysis of 1 mM AQ/*o*-tolidine in 0.1 M *n*-Bu_4NPF_6/CH_3CN and 50 equiv. of TFA using a 1-mm diameter planar GC disk electrode at 0.1 V s^{-1} (a) Coulometric data for the reductive CPE at -0.70 vs (Fc/Fc^+)/V. (b) Coulometric data for the oxidative CPE at -0.10 vs (Fc/Fc^+)/V. (c) CV response before and after reductive and oxidative CPE. (Black solid line) Original voltammetric profile, (Blue dashed line) After two-electron reductive CPE, (Red dashed line) After two-electron oxidative CPE back to starting material.

Previously, the results from the individual CPE experiments have shown that AQ and *o*-tolidine demonstrated good chemical reversibility under bulk conversion. To further affirm the chemical stability of each individual redox species in a mixed system, similar exhaustive electrolysis experiments were carried out.

An exhaustive two–electrons reduction was performed on AQ at a constant potential of -0.70 vs (Fc/Fc+)/V. Figure 3.19 illustrates similar voltammetric behaviour as the previous CPE study of AQ in isolation (Figure 3.7). As shown in Figure 3.19c, the CVs recorded before

(black solid line) and after (blue dashed line) electrolysis closely overlapped. Apart from the slight shortage of charge (less than $2e^-$) recovered from the re-oxidation process (possibly from some spontaneous discharge that was previously discussed), there was clearly no sign of interference by the presence of *o*-tolidine during the exhaustive electrolysis. Nonetheless, the near quantitative charge recovery and the close resemblance in CV profiles after CPE show that the reduced species of AQ is chemically reversible and compatible in the mixed reactant system.

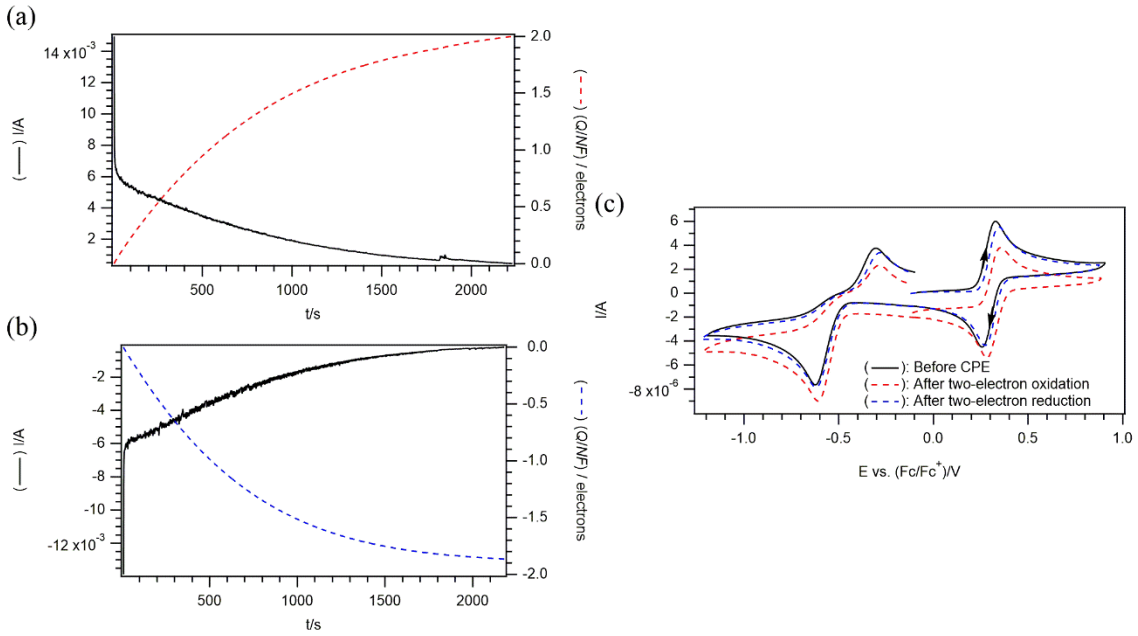

Figure 3.20. Coulometric data (current against time) and CV response for the oxidative electrolysis of 1 mM AQ/*o*-tolidine in 0.1 M *n*-Bu_4NPF_6/CH_3CN and 50 equiv. of TFA using a 1-mm diameter planar GC disk electrode at 0.1 V s^{-1} (a) Coulometric data for the oxidative CPE at 0.50 vs (Fc/Fc^+)/V. (b) Coulometric data for the reductive CPE at 0.10 vs (Fc/Fc^+)/V. (c) CV response before and after oxidative and reductive CPE. (Black solid line) Original voltammetric profile, (Red dashed line) After two-electron oxidative CPE, (Blue dashed line) After two-electron reductive CPE back to starting material.

CPE was also performed on *o*-tolidine in the presence of AQ to determine the chemical compatibility in the mixed-reactant system. The absence of unexpected changes to the CV waves strongly suggests that the oxidized form of *o*-tolidine is chemically compatible with AQ (Figure 3.20c).

3.5.2 Cycling Test

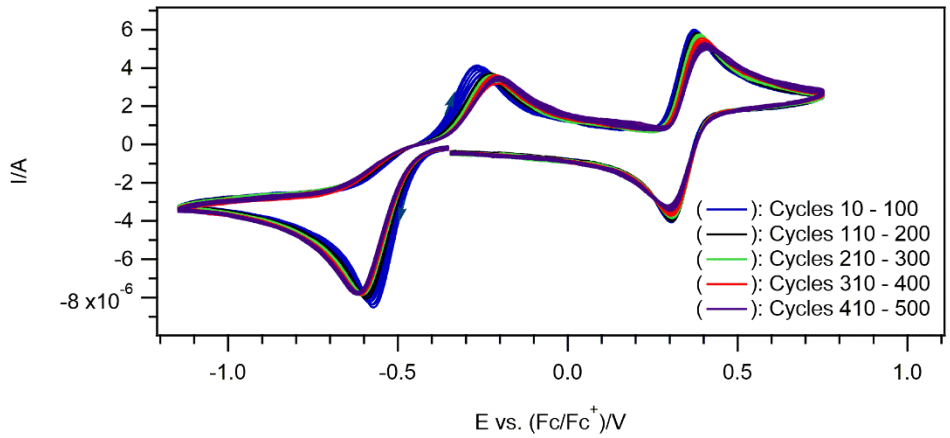

Figure 3.21. Cyclic voltammograms for extended cycling of 1 mM of AQ/*o*-tolidine in 0.1 M *n*-Bu_4NPF_6/CH_3CN and 50 equiv. TFA up to 500 cycles recorded using 1-mm GC disk electrode at 0.5 V s^{-1}.

Multi-cycle successive CV scanning was performed to evaluate the long-term stability of the mixed reactant system. Upon extending cycling, the electrode may experience surface fouling over time which might affect the performance and reliability of the battery system.[36] The purpose of the extended cycling test is to simulate the process of frequent charging and discharging processes occurring in energy storage devices at microscale.

Based on the results obtained from the 500 CV cycles, there were negligible difference upon stacking of the voltammetric profiles except the slight shifts in potential owing to minor changes in possibly the electrode surface over time. (Figure 3.21). The redox behaviour shown

by both redox couples remains highly consistent throughout the extended cycling, demonstrating high electrochemical stability of the mixed reactant system.

3.5.3 Ambient Stability Test

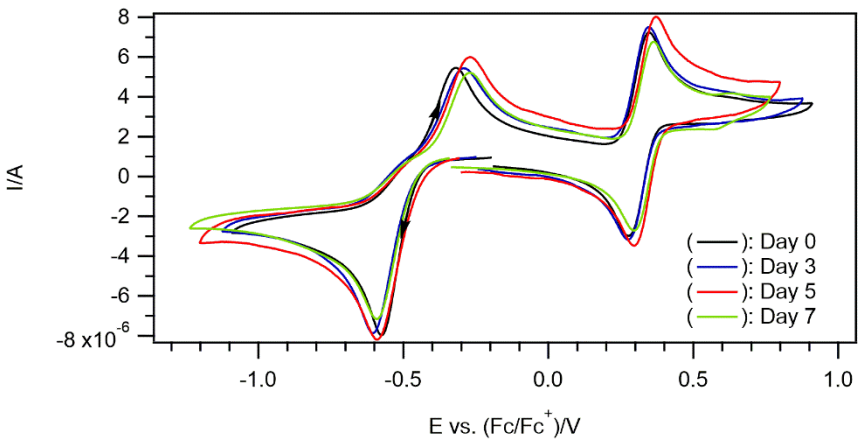

Figure 3.22. Cyclic voltammograms of 1 mM AQ/*o*-tolidine in 0.1 M *n*-Bu_4NPF_6/CH_3CN and 50 equiv. TFA recorded using a 1-mm diameter planar GC disk electrode at 0.1 V s^{-1} conducted over 7 days.

Studies have revealed that organic compounds can degrade over time upon prolonged storage in solvents.[37-38] In view of this, 1 mM AQ and *o*-tolidine in 0.1 M *n*Bu_4NPF_6/CH_3CN and 50 equivalents of TFA were prepared and stored in sample vials to study the chemical stability of the mixed reactant on storage in the electrolyte solution over extended periods. To determine the ruggedness of the system, no pre-treatment was carried out to remove any moisture or oxygen presence in the solvent that are known to cause degradation of redox active species. The sample vials were stored under ambient condition for over a period of 7 days.

The stability of the mixed reactant was evaluated periodically by CV experiments. Over the 7 days, there was no visible change to the colour intensity of the test solutions. The voltammetric profiles of the mixed reactant were well-retained throughout the period of

analysis (Figure 3.22). The slight inconsistency in the profile signal on day 5 might be due to poor storage condition which caused a change in concentration due to solvent evaporation. Nonetheless, the relative peak potential and the ratio of the i_p^{ox} to i_p^{red} remained constant at different time intervals of the experiment. It can be inferred that the mixed reactants AQ and *o*-tolidine possess good ambient stability in the supporting electrolyte solution for at least a week. This property is valuable in the development of durable battery system since the mixed reactant can be stored with negligible degradation in the fully discharged mode.

3.5.4 Thermal Stability Test

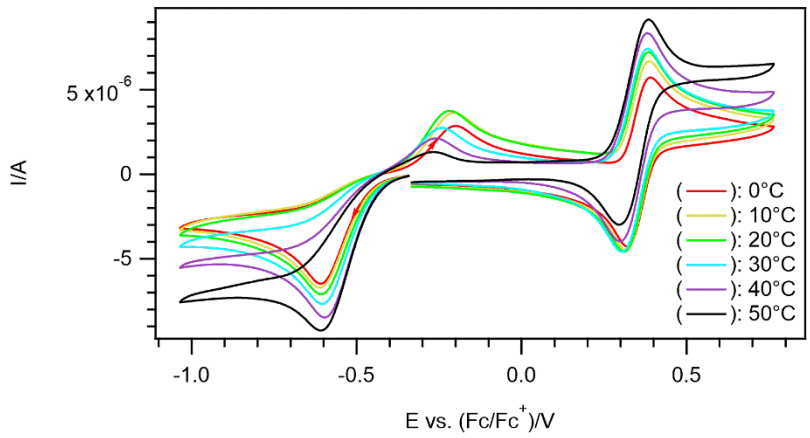

Figure 3.23. Cyclic voltammograms of 1 mM AQ/*o*-tolidine in 0.1 M *n*-Bu_4NPF_6/CH_3CN and 50 equiv. TFA recorded using a 1-mm diameter planar GC disk electrode at different temperatures.

Variable temperature CV was used to evaluate the thermal stability of the mixed reactant system under the operating temperature range of a typical RFB. The operating temperature can potentially affect the physical and chemical properties of the organic compounds and the electrochemical performance of the redox process.[39] On this basis, the CV experiments were carried out at a temperature range from 0 to 50°C.

From the voltammetric profiles shown in Figure 3.23, the magnitude of the i_p^{red} for AQ shows an increasing trend from 0 to 50°C. This implies that the extent of reduction for AQ is greater at a higher temperature. Studies have shown that diffusion coefficients increased with temperature due to the diminishing solvent viscosity at elevated temperature.[40] Therefore, more AQ can be rapidly replenished to the surface of the electrode for reduction.

In contrast, the i_p^{ox} of AQ decreased significantly with rising temperature. Along with the slow re-oxidation kinetics of AQ, the rate at which the reduced species diffuses away from the surface of the electrode was much faster than the applied scan rate, especially at higher temperatures (due to faster diffusion). As such, lesser AQH_2 was able to undergo re-oxidation, which accounts for the decreased i_p^{ox} observed at elevated temperatures. This affords the impression of compromising the chemical reversibility of AQ at higher operating temperatures. However, the data obtained only suggests that re-oxidation of AQH_2 occurs at a longer time scale relative to the process of diffusion. In addition, no sign of thermal decomposition or unexpected peak distortions were observed during the experiment.

Table 3.5. Approximate difference in half-wave potentials ($E_{½}$) of 1 mM AQ/*o*-tolidine in 0.1 M *n*-Bu_4NPF_6/CH_3CN and 50 equiv. of TFA at the temperature range from 0 to 50°C.

Temperature/°C	$E_{½}$ **vs (Fc/Fc$^+$)/V**
0	0.760
10	0.758
20	0.761
30	0.768
40	0.766
50	0.778

In the case of *o*-tolidine, the decrease in i_p^{red} on the reverse scan was not observed since the ratio of i_p^{ox} and i_p^{red} for *o*-tolidine were relatively constant. This is because the anodic to cathodic peak-to-peak separation was much smaller for *o*-tolidine than for AQ, thus there was less time for the oxidised form to diffuse away from the electrode surface. Similarly, *o*-tolidine did not show any thermal decomposition or any abnormal profile signal on rising temperatures.

Across the temperature range, the theoretical cell voltage of the mixed-reactant system was well-maintained with an average value of approximately ~0.76 vs (Fc/Fc$^+$) with a negligible difference of less than 2% (Table 3.5). Therefore, it is reasonable to consider that the mixed-reactant system of AQ and *o*-tolidine were thermally stable.

3.5.5 Water Tolerance Test

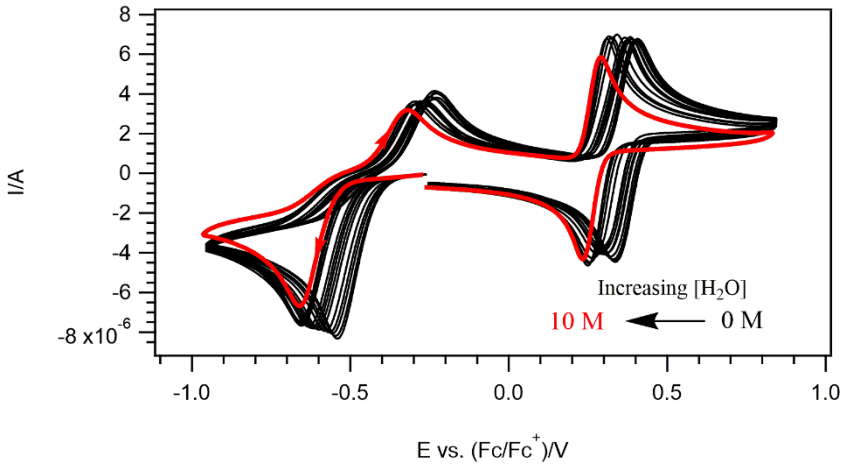

Figure 3.24. Cyclic voltammograms of 1 mM of AQ/*o*-tolidine in 0.1 M *n*-Bu_4NPF_6/CH_3CN and 50 equiv. TFA with increasing concentrations of water, recorded using a 1-mm diameter planar GC disk electrode. (Red line) After 10 M of water was added.

It is challenging to eliminate the presence of water completely in practical scenarios, especially for large-scale battery storage applications. In non-aqueous regimes, oxygen and water can have a negative impact on the performance of the RFB.[1] Therefore, CV analysis was carried out to study the influence of water on the electrochemistry of the mixed reactant system. A known amount of water was carefully introduced into the system. As shown in Figure 3.24, the addition of water dilutes the analyte concentration resulting in the declining of the peak current magnitudes. With increasing water concentration, a notable shift in the negative direction was observed on the profile signal of the mixed reactants. This is because the dilution of the electrolyte lowers the acidity of the solution, hence it decreased the extent of protonation. As such, it would require a more negative potential to complete the redox process for AQ and *o*-tolidine.

Regardless, the voltammetric profiles of the mixed reactants were well preserved despite the inclusion of up to 10 M of water. Therefore, it can be concluded that the mixed reactant system has high tolerance to water.

3.6 Summary

The electrochemical behavior of AQ and *o*-tolidine were thoroughly investigated in the single and mixed-reactant system by voltammetric and spectroscopic methods. With the addition of 50 equivalents of TFA, AQ proceeded with a chemically reversible $2e^-/-2H^+$ reduction process while *o*-tolidine undergoes a chemically reversible $2e^-/H^+$ oxidation process. In the mixed reactant system, the pairing of both half-cells provides a theoretical cell potential of 0.750 V while the experimental measured value (with a voltmeter) amounts to 0.916 V. The feasibility of the mixed-reactant system was further evaluated under practical conditions. The proposed system demonstrates good cyclability and stability under ambient conditions. Furthermore, the electrochemical performance was consistent in the presence of water and over the typical operating temperature of a RFB. Such qualities are useful in designing a robust organic-based battery system without having to be concerned about temperature fluctuations and water penetration. However, two main limitations were encountered by the proposed system. The negative half-cell was susceptible to self-discharge when exposed to oxygen. Although the AQ system remains chemically reversible, further work is required to explore ways to decrease the reactivity of reduced anthrahydroquinone towards oxygen. The other limitation faced by the system was the solubility issues. The solubility of AQ in acetonitrile was found to be approximately 0.007 M while the *o*-tolidine was 0.400 M. The low solubility of AQ would severely limit the energy density of the battery system. Further studies could involve the functionalization of the aromatic rings to enhance the solubility.

References

1. Gong, K.; Fang, Q.; Gu, S.; Li, S. F. Y.; Yan, Y. *Energy Environ. Sci.* **2015,** *8*, 3515-3530.

2. Xing, X.; Huo, Y.; Wang, X.; Zhao, Y.; Li, Y. *Int. J. Hydrogen Energy.* **2017,** *42*, 17488-17494.

3. Wei, X.; Duan, W.; Huang, J.; Zhang, L.; Li, B.; Reed, D.; Xu, W.; Sprenkle, V.; Wang, W. *ACS Energy Lett.* **2016,** *1*, 705-711.

4. Luo, J.; Hu, B.; Hu, M.; Zhao, Y.; Liu, T. L. *ACS Energy Lett.* **2019,** *4*, 2220-2240.

5. Zhong, F.; Yang, M.; Ding, M.; Jia, C. *Front. Chem.* **2020,** *8*.

6. Wei, X.; Pan, W.; Duan, W.; Hollas, A.; Yang, Z.; Li, B.; Nie, Z.; Liu, J.; Reed, D.; Wang, W.; Sprenkle, V. *ACS Energy Lett.* **2017,** *2*, 2187-2204.

7. Chen, H.; Cong, G.; Lu, Y.-C. *J. Energy Chem.* **2018,** *27*, 1304-1325.

8. Leung, P.; Shah, A. A.; Sanz, L.; Flox, C.; Morante, J. R.; Xu, Q.; Mohamed, M. R.; Ponce de León, C.; Walsh, F. C. *J. Power Sources.* **2017,** *360*, 243-283.

9. Duan, W.; Huang, J.; Kowalski, J. A.; Shkrob, I. A.; Vijayakumar, M.; Walter, E.; Pan, B.; Yang, Z.; Milshtein, J. D.; Li, B.; Liao, C.; Zhang, Z.; Wang, W.; Liu, J.; Moore, J. S.; Brushett, F. R.; Zhang, L.; Wei, X. *ACS Energy Lett.* **2017,** *2*, 1156-1161.

10. Huskinson, B.; Marshak, M. P.; Suh, C.; Er, S.; Gerhardt, M. R.; Galvin, C. J.; Chen, X.; Aspuru-Guzik, A.; Gordon, R. G.; Aziz, M. J. *Nature.* **2014,** *505*, 195-198.

11. Lin, K.; Chen, Q.; Gerhardt, M. R.; Tong, L.; Kim, S. B.; Eisenach, L.; Valle, A. W.; Hardee, D.; Gordon, R. G.; Aziz, M. J.; Marshak, M. P. *Science.* **2015,** *349*, 1529-1532.

12. Kwabi, D. G.; Lin, K.; Ji, Y.; Kerr, E. F.; Goulet, M.-A.; De Porcellinis, D.; Tabor, D. P.; Pollack, D. A.; Aspuru-Guzik, A.; Gordon, R. G.; Aziz, M. J. *Joule.* **2018,** *2*, 1894-1906.

13. Hu, B.; Luo, J.; Hu, M.; Yuan, B.; Liu, T. L. *Angew. Chem. Int. Ed.* **2019,** *58*, 16629-16636.

14. Xu, X.; Webster, R. D. *RSC Adv.* **2014,** *4*, 18100-18107.

15. Chan, K. K.; Webster, R. D. *Electroanalysis.* **2016,** *28*, 516-522.

16. Gritzner, G.; Kuta, J. *Pure Appl. Chem.* **1984,** *56*, 461-466.

17. Gupta, N.; Linschitz, H. *J. Am. Chem. Soc.* **1997,** *119*, 6384-6391.

18. Guin, P. S.; Das, S.; Mandal, P. C. *Int. J. Electrochem.* **2011,** *2011*, 816202.

19. Elgrishi, N.; Rountree, K. J.; McCarthy, B. D.; Rountree, E. S.; Eisenhart, T. T.; Dempsey, J. L. *J. Chem. Educ.* **2018,** *95*, 197-206.

20. Lund, H.; Hammerich, O. *Organic electrochemistry: revised and expanded*; fourth ed.; Marcel Dekker: New York, 2001.

21. Webster, R. D. *Chem. Rec.* **2012,** *12*, 188-200.

22. Costentin, C. *Chem. Rev.* **2008,** *108*, 2145-2179.

23. Astudillo, P. D.; Tiburcio, J.; González, F. J. *J. Electroanal. Chem.* **2007,** *604*, 57-64.

24. Wang, J. *Analytical Electrochemistry*; Third ed.; Wiley-VCH: New Jersey, 2006.

25. Williams, L. L.; Webster, R. D. *J. Am. Chem. Soc.* **2004,** *126*, 12441-12450.

26. Tan, S. L. J.; Webster, R. D. *J. Am. Chem. Soc.* **2012,** *134*, 5954-5964.

27. Hill, R. R.; Mitchell, G. H. *J. Chem. Soc. B.* **1969**, 61-64.

28. Tickle, K.; Wilkinson, F. *Trans. Faraday Soc.* **1965,** *61*, 1981-1990.

29. Dvořák, V.; Němec, I.; Zýka, J. *Microchem. J.* **1967,** *12*, 324-349.

30. Pelzer, K. M.; Cheng, L.; Curtiss, L. A. *J. Phys. Chem. C.* **2017,** *121*, 237-245.

31. Tokyo Chemical Industry. https://www.tcichemicals.com/SG/en/ (accessed December 10), 2020.

32. Ditzler, M. A.; Gutknecht, W. F. *Anal. Chem.* **1978,** *50*, 1883-1886.

33. Lewis, G. P. *J Clin Pathol.* **1965,** *18*, 235-239.

34. Kosswattaarachchi, A. M.; Cook, T. R. *Electrochim. Acta.* **2018,** *261*, 296-306.

35. Zhao, P.; Zhang, H.; Zhou, H.; Yi, B. *Electrochim. Acta.* **2005,** *51*, 1091-1098.

36. Hanssen, B. L.; Siraj, S.; Wong, D. K. Y. *Rev. Anal. Chem.* **2016,** *35*, 1-28.

37. Kozikowski, B. A.; Burt, T. M.; Tirey, D. A.; Williams, L. E.; Kuzmak, B. R.; Stanton, D. T.; Morand, K. L.; Nelson, S. L. *J. Biomol. Screen.* **2003,** *8*, 205-209.

38. Kozikowski, B. A.; Burt, T. M.; Tirey, D. A.; Williams, L. E.; Kuzmak, B. R.; Stanton, D. T.; Morand, K. L.; Nelson, S. L. *J. Biomol. Screen.* **2003,** *8*, 210-215.

39. Zhang, C.; Zhao, T. S.; Xu, Q.; An, L.; Zhao, G. *Appl. Energy.* **2015,** *155*, 349-353.

40. Jacob, S. R.; Hong, Q.; Coles, B. A.; Compton, R. G. *J. Phys. Chem. B.* **1999,** *103*, 2963-2969.

Chapter 4

Vitamin-based Electrolytes for All-Organic Battery

4.1 Introduction

Organic compounds are useful in providing a large range of cell voltages because their chemical and redox properties can be modified via functionalization. A fully organic RFB can thus be prepared together with an organic solvent, organic supporting electrolyte, and non-metallic electrodes. The major drawbacks of molecularly based RFBs, however, are the generation of radicals and other highly reactive charged species that may compromise the stability and, consequently, lifetime of the battery. The energy density of the battery is also compromised by the poor solubility of redox-active organic compounds in organic solvents.[1-3] Few organic compounds proposed for organic-based system currently possess comparable properties to the benchmark VRB system in terms of redox potential, solubility, and chemical stability.[4-5] Quinones and pyranochromene compounds are useful for this purpose due to the simplicity of their electrochemical behaviour. The structural-activity studies of quinones in aqueous systems have been extensively established theoretically and experimentally.[6-7] In these studies, quinones offer design flexibility in order to improve the solubility and redox potentials in aqueous RFBs, via chemical modification of their side groups. However, to date there has been no study on the actual change in redox potential and stability of quinones induced by the effects of additives in organic-based RFBs. In addition, the use of pyranochromene compounds for organic-based RFBs have not been established.

In this chapter, we describe optimization in the performance of an all-organic battery comprised of 2,3-dimethyl-1,4-naphthoquinone (VKA), an analogue of vitamin K_1, and pyrano[3,2-*f*]-chromene, an analogue of vitamin E (VEA), by exploring the effects of different additives such as diethyl malonate (a weak organic acid), trifluoroethanol (a strong hydrogen-bonding reagent) and trifluoroacetic acid (a strong organic acid). We also attempted to improve the solubility of the VKA by incorporating a polar functional group to increase its solubility in organic solvents. The modified form of VKA and VEA were utilised in a mixed reactant system

and electrochemical performance assessed through a series of voltammetric, coulometric and spectroscopic experiments.

4.2 Effects of Additives on the Electrochemical Behaviour of VKA

Among the compounds screened in the preliminary study conducted in Chapter 2, quinone and pyranochromene compounds were found to be well-suited for the design of a fully functional organic-based RFB. Both organic compounds exhibit chemically reversible electrochemical behaviour in organic solvents but involving the transfer of different numbers of electrons. In an organic aprotic solvent like CH_3CN, the analogue of vitamin K_1, 2,3-dimethyl-1,4-napthoquinone (VKA), undergoes two one-electron reduction reactions (i.e. an EE mechanism where E represents an electron-transfer step) to first give the radical anion ($VKA^{\bullet-}$) at -1.22 V vs. Fc/Fc^+ ($E^{red(1)}$) and subsequently the aromatic dianion (VKA^{2-}) at -1.76 V vs. Fc/Fc^+ ($E^{red(2)}$) (Figure 4.1a, red solid line).[8-14] The analogue of vitamin E, pyrano[3,2-f]chromene (VEA), on the other hand, undergoes a one-electron oxidation reaction to its radical cation ($VEA^{\bullet+}$) at +0.45 V vs. Fc/Fc^+ (E^{ox}) (Figure 4.1a, blue solid line).[15] The chemical structures of both compounds are shown in Scheme 4.1.

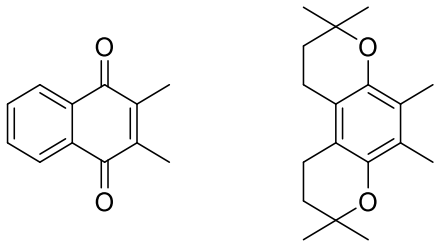

VKA VEA

Scheme 4.1. Chemical structure of vitamin K analogue (VKA) and vitamin E analogue (VEA)

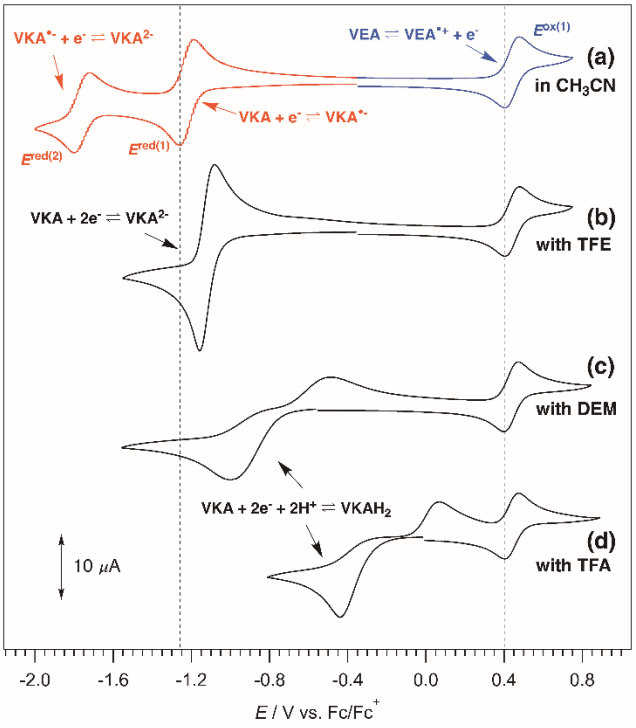

Figure 4.1. Cyclic voltammograms of 2 mM VKA and VEA with 0.2 M *n*-Bu_4NPF_6/CH_3CN (a) only, and with (b) 200 mM TFE, (c) 400 mM DEM and (d) 100 mM TFA. The voltammograms were recorded on a 1 mm diameter planar disk glassy carbon working electrode at a scan rate of 0.1 V s^{-1} at 25±2 °C.

The electron-transfer processes of both compounds show good chemical reversibility on the timescale of CVs (seconds) and so enables them to potentially serve as electroactive compounds in batteries, with a theoretical maximum cell voltage of 2.21 V ($E_{cell} = E_{cathode} - E_{anode} = E_{½}^{ox} - E_{½}^{red(2)}$). However, the stability of the cell in pure CH_3CN is quite poor owing to the high reactivity of the dianion, VKA^{2-} (likely due to reactions with trace oxygen or electrophiles). Nevertheless, the cell stability under electrolysis timescales (>minutes) can be improved through stabilization of $VKA^{\bullet-}$ and VKA^{2-}. The use of trifluoroethanol (TFE), trifluoroacetic acid (TFA) or diethyl malonate (DEM) can improve the stability of the reduced species of VKA through different interaction mechanisms such as hydrogen bonding (Figure 4.1b), protonation (Figure 4.1d) or possibly a combination of both (hydrogen bonding and

proton transfer) (Figure 4.1c). The presence of additives facilitates the reduction of VKA and shifts the reduction potentials to less negative values. The oxidation of VEA appears to be unaffected by the addition of TFE, DEM and TFA (i.e. no change in E^{ox}); this indicates that VEA and $VEA^{\bullet+}$ are less affected by hydrogen-bonding and proton-transfer reactions. In the presence of TFE, DEM and TFA, the approximate E_{cell} values of 1.56, 1.18 and 0.61 V were obtained respectively, from the CVs in Figure 4.1. The results suggest that hydrogen bonding between VKA and TFE gives a larger half-cell potential (~950 mV) compared to the value obtained through protonation by TFA.

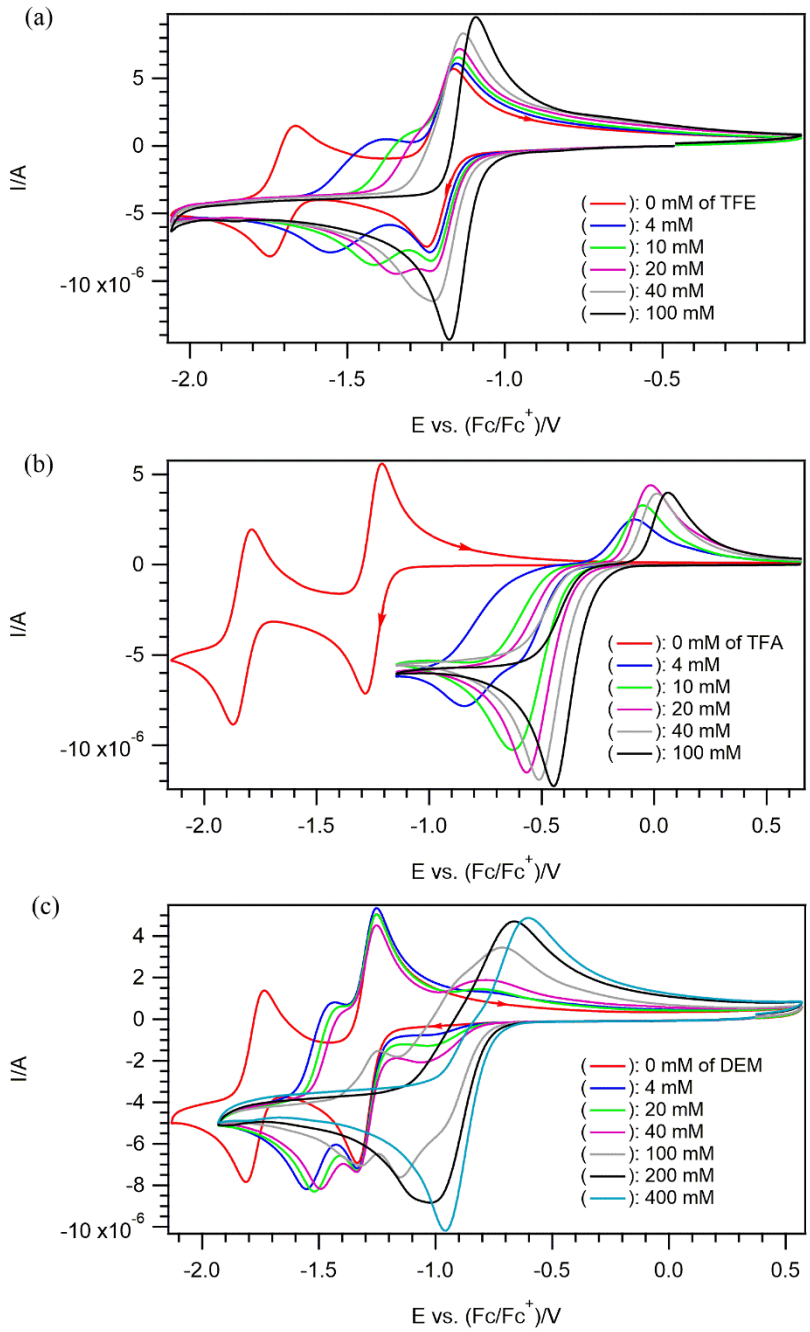

Figure 4.2. Cyclic voltammograms of 2 mM VKA with 0.2 M *n*-Bu_4NPF_6/CH_3CN recorded with a 1 mm diameter planar disk glassy carbon working electrode at 0.1 V s^{-1} at 25±2 °C at different concentrations of (a) TFE, (b) TFA and (c) DEM.

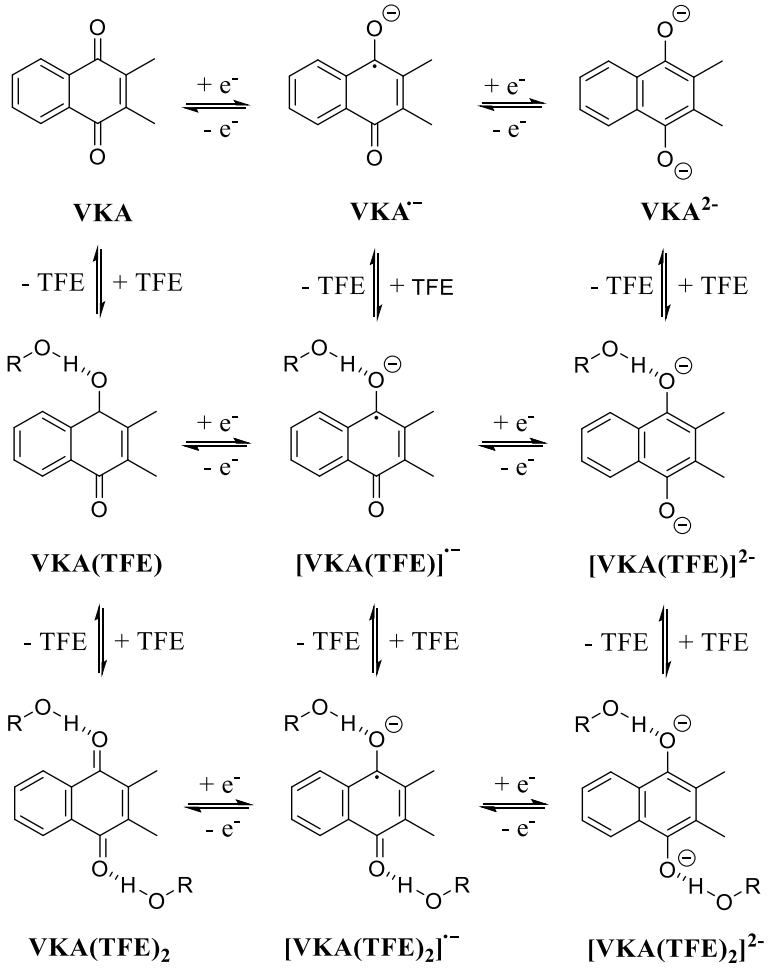

Scheme 4.2. Electrochemical "square-scheme" mechanism for the reduction of VKA with hydrogen bonding to TFE. R = CH_2CF_3.

Hydrogen bonding between VKA and TFE results in the gradual shifting of the reduction processes $E^{red(1)}$ and $E^{red(2)}$ towards more positive values; this occurs over a wide concentration range and is dependent on the extent of the interaction (see Figure 4.2a).[16-20] The shifts in $E^{red(2)}$ are greater than those of $E^{red(1)}$ which result in the formation of a single two-electron reduction process when sufficient amounts of TFE are present (50 equivalents), through the merger of the individual one-electron reduction reactions, that converts VKA directly into VKA^{2-}. Despite the noticeable changes in the CV, the two-electrons chemical reversible reduction process remains unaffected by hydrogen bonding other than the shifts in potential. These shifts in reduction potential of quinones in organic solvents have been studied

extensively during the addition of water, which also undergoes relatively strong hydrogen-bonding interactions with the semiquinones and especially dianions.[17-19] The series of possible consecutive electron-transfer and hydrogen-bonding reactions associated with the chemically reversible transformation between VKA and its hydrogen-bonded dianion, $[VKA(TFE)_2]^{2-}$, can be more accurately described by the electrochemical "square-scheme" mechanism shown in Scheme 4.2, where the electron-transfer reactions are drawn horizontally and the hydrogen-bonding reactions are given vertically.

Protonation can be viewed as an extreme case of hydrogen bonding where the interaction between the hydrogen donor and hydrogen acceptor is so strong that the hydrogen nucleus is completely transferred. The addition of small amounts of TFA resulted in an immediate large shift in the $E^{red(1)}$ and $E^{red(2)}$ processes (Figure 4.2b) of VKA, which may be due to strong hydrogen bonding and/or protonation of the neutral quinone. The dihydroquinone $VKAH_2$ is also obtained as the final product because of the greater basicity of VKA^{2-}, to which the overall two-electron two-proton reduction may proceed through the ECEC or ECCE pathway. The other distinct difference of protonation compared to hydrogen bonding (where there is no transfer of protons to the reduced quinone) are the occurrence of the reduction of VKA at potentials that are significantly more positive (cf. Figures 4.1b and 4.1d), with lower concentrations of the acid, a marked increase in the E^{red} to E^{ox} separation as well as slowed heterogeneous electron-transfer rates (see Figure 4.2b).[21-22] The electrochemical "square-scheme" in Chapter 2 (Scheme 2.5) which is analogous to Scheme 4.2, shows the sequence of electron-transfer (drawn vertically) and proton-transfer (given horizontally) reactions that VKA can undergo during its chemically reversible transformation into $VKAH_2$ in the presence of high amounts of TFA. No change in the UV-vis spectra of the starting material was observed in the absence and presence of low amounts of TFA (< 0.5 M), suggesting that the VKA does not undergo immediate protonation (Figure 4.3).

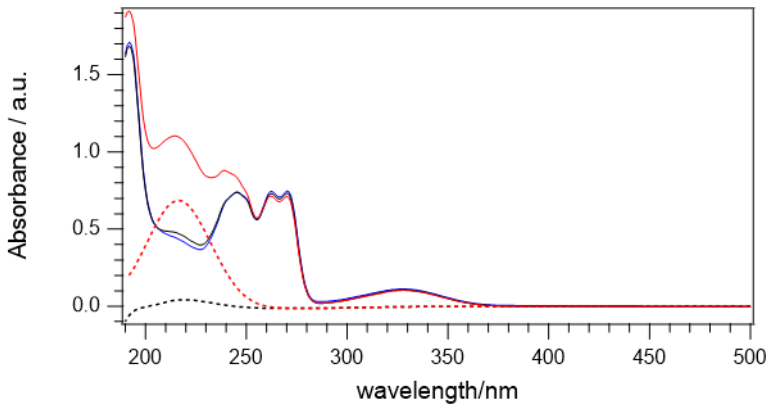

Figure 4.3. UV-vis spectra of VKA in the absence and presence of TFA. Legend: blue solid line – 1 mM VKA only, black solid line – 1 mM VKA with 0.5 M (50 equivalents) TFA, black dashed line – 0.5 M TFA only, red solid line – 1 mM VKA with 5 M (500 equivalents) TFA, red dashed line – 5 M TFA only.

For the experiments with DEM, the electrochemical reduction of VKA appears to show features of hydrogen bonding at low (<10 mM) concentrations of DEM (i.e. two one-electron reduction behaviour with $E^{red(2)}$ shifted, yet no change in the chemical reversibility of both processes) as well as protonation at high (>20 mM) concentrations of DEM (i.e. a single reduction process accompanied by a broad reverse oxidation peak) (Figure 4.2c). Since DEM is a weak acid and does not fully dissociate in CH_3CN, it is likely that the reduction of VKA in the presence of DEM involves a combination of proton-coupled electron transfer (PCET)[23-29] and hydrogen bonding through a "wedge-scheme" type (Scheme 4.3) mechanism.[30] In the PCET pathway, the proton and electron transfers may be concerted (that would be represented in Chapter 2 (Scheme 2.5) by a series of diagonal arrows) or stepwise. The "wedge-scheme" mechanism in Scheme 4.3 may be viewed as an intermediate scenario lying between Scheme 4.2 and Chapter 2 (Scheme 2.5) where both hydrogen bonding (blue reaction arrows) and protonation (red reaction arrows) occur simultaneously, with hydrogen bonding favoured at lower concentrations of DEM and with the neutral VKA, while protonation supersedes at

higher concentrations of DEM and preferentially involves the dianion VKA^{2-}. A direct transformation between the protonated and hydrogen-bonded states may also occur via equilibrium proton-transfer reactions (represented by the green reaction arrows). The exact pathway undertaken in the "wedge-scheme" mechanism is highly dependent on the combination of the basicity of the quinone, acidity of the hydrogen donor, their concentrations as well as type of solvent used.

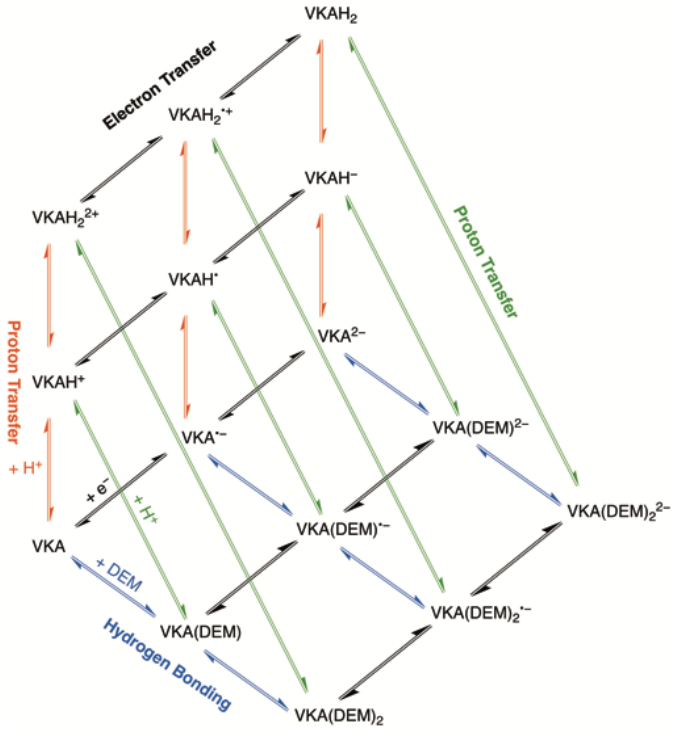

Scheme 4.3. Electrochemical "wedge-scheme" mechanism for the reduction of VKA with hydrogen bonding and proton-transfer reactions with DEM.

Based on the results obtained from the CPE experiments, the hydrogen-bonded dianion $[VKA(TFE)_2]^{2-}$ was however found to be less stable than $VKAH_2$, and so undermines the applicability of TFE for use in an all-organic battery. The stabilities of VKA and its reduced products, $[VKA(TFE)_2]^{2-}$ and $VKAH_2$, were determined through a comparison of the peak reduction currents from the CVs (Figure 4.4) as well as UV-vis spectra (Figure 4.5a and 4.5b) recorded at the start and upon completion of the CPE experiments. The voltammetric peak

currents for $[VKA(TFE)_2]^{2-}$ recorded immediately after the electrolysis were noticeably smaller than prior to electrolysis as shown in Figure 4.4d. However, for $VKAH_2$, the voltammetric peak currents showed a negligible change over the course of the electrolysis experiments (Figure 4.4e and 4.4f). The applied potential needed for exhaustive reduction of VKA decreased in the presence of the additives in the order TFA < DEM < TFE, and this potential decrease can be correlated to improving the stability of the reduced quinone via the lowered reactivity of the product.

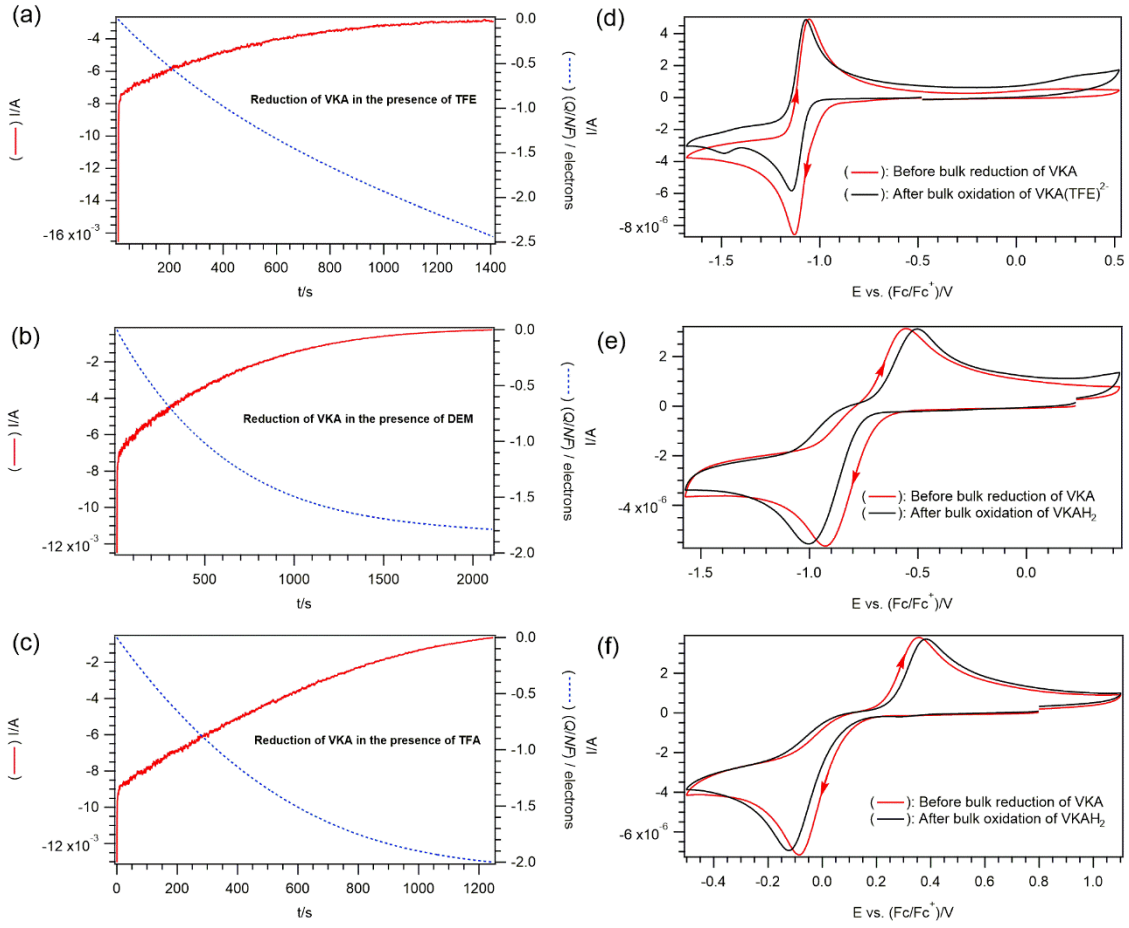

Figure 4.4. (a-c) Coulometric data for the reductive controlled potential electrolysis of 2 mM VKA/0.2 M nBu$_4$NPF$_6$ in CH_3CN in the presence of (a) 200 mM TFE, (b) 100 mM TFA and (c) and 400 mM DEM. The i vs. t and no. of electrons transferred vs. t plots are shown in red and blue, respectively. (d-f) Corresponding cyclic voltammograms recorded with a 1 mm

diameter planar disk glassy carbon working electrode at 0.1 V s^{-1} at 25±2 °C before the bulk reduction of VKA (red) and after the bulk oxidation of reduced VKA (i.e. hydrogen-bonded VKA^{2-} or $VKAH_2$) (black) in the presence of (d) 200 mM TFE, (e) 100 mM TFA and (f) and 400 mM DEM.

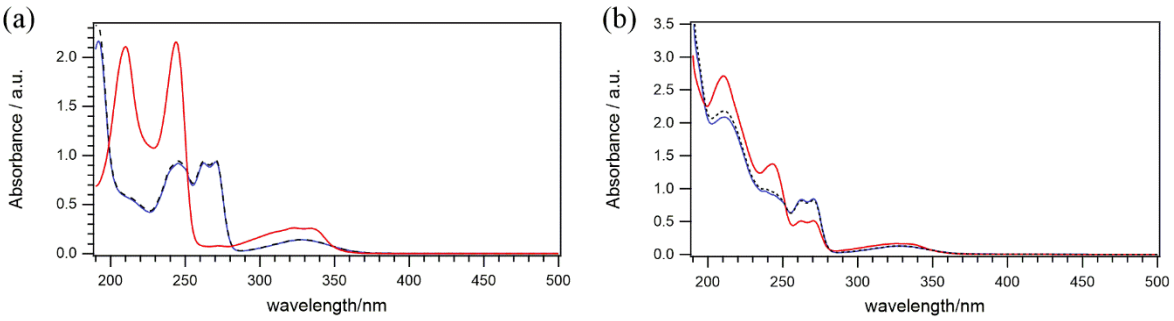

Figure 4.5. UV-vis spectra of 1 mM VKA/0.1 M *n*Bu_4NPF_6 in CH_3CN with (a) 50 mM of TFA and (b) 200 mM of DEM. Legend: blue solid line – at the start of the experiment before bulk electrolysis, red solid line – after 2-electron bulk reduction, black dashed line – after 2-electron bulk re-oxidation.

Most importantly, the addition of easily controlled amounts of DEM allowed the potential of the two-electron reduction of the quinone to be optimised, so that a larger E_{cell} value (i.e. about two times that obtained with TFA) and excellent compound stability (voltammograms and UV-vis spectra recorded before bulk electrolysis and after complete discharge did not show any unexpected changes over a 24-hour period, Figure 4.6) were achieved.

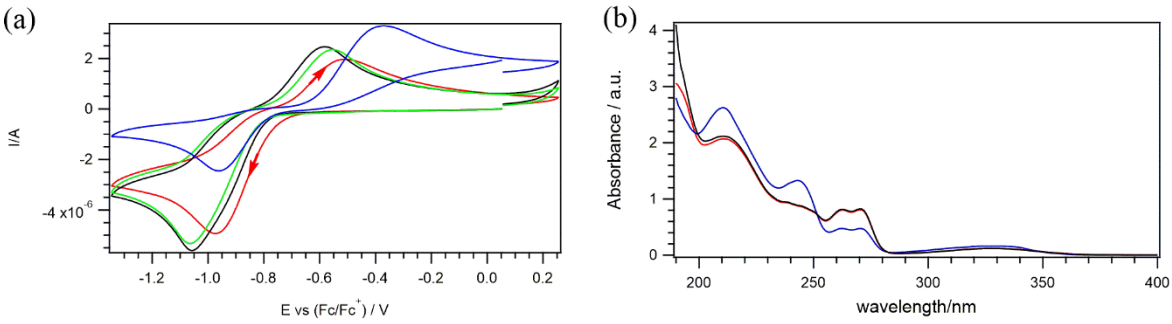

Figure 4.6. Cyclic voltammograms (a) and UV-vis spectra (b) of 1 mM VKA/0.1 M *n*Bu_4NPF_6 in CH_3CN with 200 mM of DEM. Voltammograms were recorded with a 1 mm diameter planar glassy carbon working electrode at 0.1 V s^{-1} at 25±2 °C. Legend: red solid line – at the start of the experiment before bulk electrolysis, blue solid line – at t = 0 after 2-electron bulk reduction, black line – at t = 24 h after 2-electron bulk reduction, green solid line – after t = 24 h after 2-electron bulk re-oxidation.

The results of this study show that the nature and amount of the additive is critical in determining the reduction mechanism as well as for achieving a combination of good stability and large cell potential for organic solvent based RFBs that utilize quinones as the anolyte.

4.3 Mixed Reactant System for VKA and VEA

To establish the effectiveness of the additives, further investigations were conducted to evaluate the electrochemical performance of the mixed-reactant system under the influence of TFA and DEM.

4.3.1 Electrochemical Studies in presence of TFA and DEM

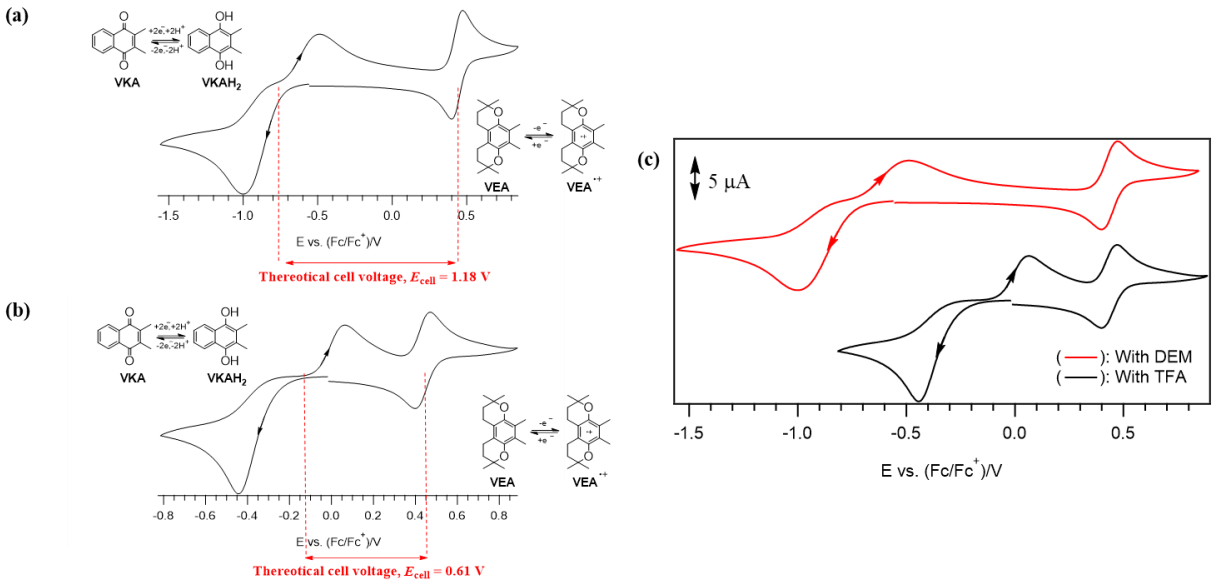

Figure 4.7. Conceptual illustration of the mixed-reactant system. (a) with DEM. (b) with TFA. (c) Cyclic voltammograms of 1 mM VEA/VKA in 0.1 M *n*-Bu_4NPF_6/CH_3CN (Red solid line) 200 equiv. DEM (Black solid line) 50 equiv. TFA recorded using a 1-mm diameter planar GC disk electrode at 0.1 V s^{-1}.

CV was performed on the mixed-reactant system containing equimolar amounts of VKA (1 mM) and VEA (1 mM). From the conceptual illustration shown in Figure 4.7, the pairing of VKA and VEA in the presence of DEM yielded a theoretical cell voltage of 1.18 V which is almost double that of 0.61 V obtained with TFA. The approximate formal redox potential of VKA in the presence TFA and DEM are tabulated in Table 4.1.

Table 4.1. Half-wave potentials ($E_{½}$) of 1 mM VKA in 0.1 M *n*-Bu_4NPF_6/CH_3CN with TFA and DEM.

Type of additives	$E_{½}$ **vs** (Fc/Fc^+)**/V)**
TFA	-0.16
DEM	-0.73

a

In the previous study, the individual CPE performance of VKA was found to exhibit good chemical reversibility in the presence of TFA and DEM. The advantage of the additives is only feasible provided the redox reactions of both compounds are chemically reversible when placed in the mixed reactant systems. Therefore, electrolysis was performed on the mixed-reactant electrolyte of VKA and VEA with the presence of TFA and DEM to simulate the charging and discharging process of the RFB.

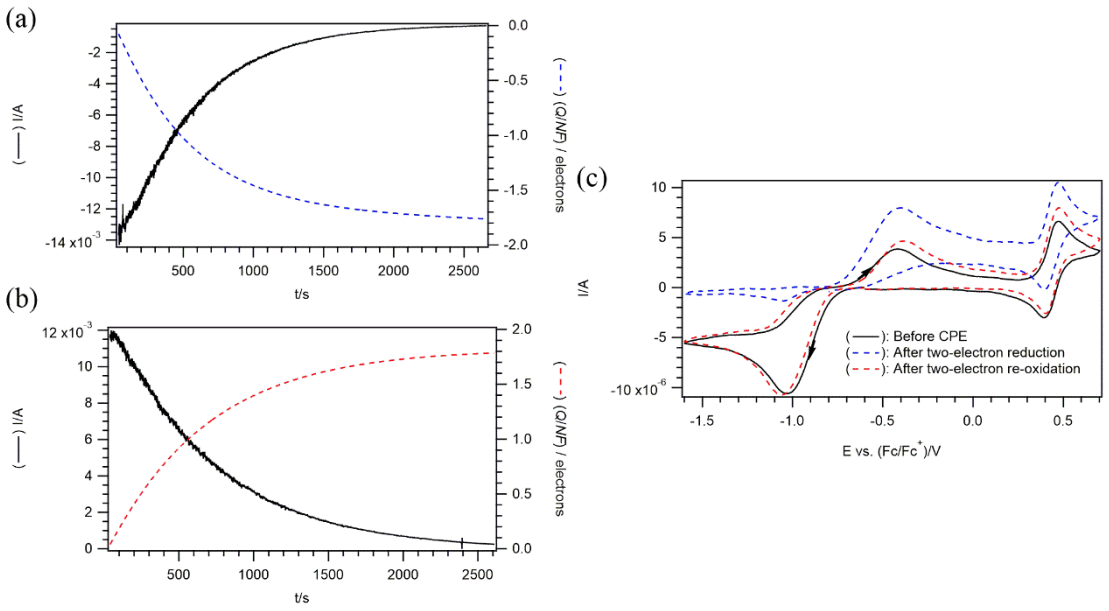

Figure 4.8. Coulometric data (current against time) and CV response for the reductive electrolysis of 2 mM VKA/VEA in 0.2 M *n*-Bu_4NPF_6/CH_3CN and 200 equiv. of DEM using a 1-mm diameter planar GC disk electrode at 0.1 V s^{-1} (a) Coulometric data for the reductive CPE at -1.18 vs (Fc/Fc+)/V. (b) Coulometric data for the oxidative CPE at -0.10 vs (Fc/Fc+)/V. (c) CV response before and after reductive and oxidative CPE. (Black solid line) Original voltammetric profile (Blue dashed line) After two-electrons reductive CPE (Red dashed line) After two-electrons oxidative CPE back to starting material.

The initial voltammogram shows two sets of redox peaks corresponding to VKA and VEA (Figure 4.8c, black solid line). In the presence 200 equivalents of DEM, VKA was electrochemically reduced at -1.18 V vs (Fc/Fc^+)/V. After the exhaustive reduction, the cathodic peak at -1.05 V was nearly consumed (Figure 4.8c, blue dashed line). This indicates that most of the VKA species were reduced. The voltammetric peak characteristics of VEA remains unaffected during the electrolysis.

After the reverse electrolysis, the voltammogram (Figure 4.8c, red dashed line) obtained is nearly superimposable with that of the starting mixture and no sign of a side reaction

was observed. The charge transfer efficiency was nearly 100 % since the number of electrons transferred (Figure 4.8a) and recovered (Figure 4.8b) during the electrolysis is almost equal. A similar electrochemical behaviour was observed from the electrolysis experiment with the presence of TFA (Figure A.4).

CPE was also conducted on the positive half-cell to investigate the effects of the additives during the bulk oxidation of VEA (Figure 4.9). The electrochemical behaviours of VKA and VEA remain chemically unchanged (other than the offset in current) as evident by the similar voltammetric profiles displayed before and after oxidative CPE. This is a good indication that VEA does not undergo decomposition or any side reaction in the presence of VKA and DEM. A comparable result was also obtained from the electrolysis experiment of VEA conducted in the presence of TFA (Figure A.5).

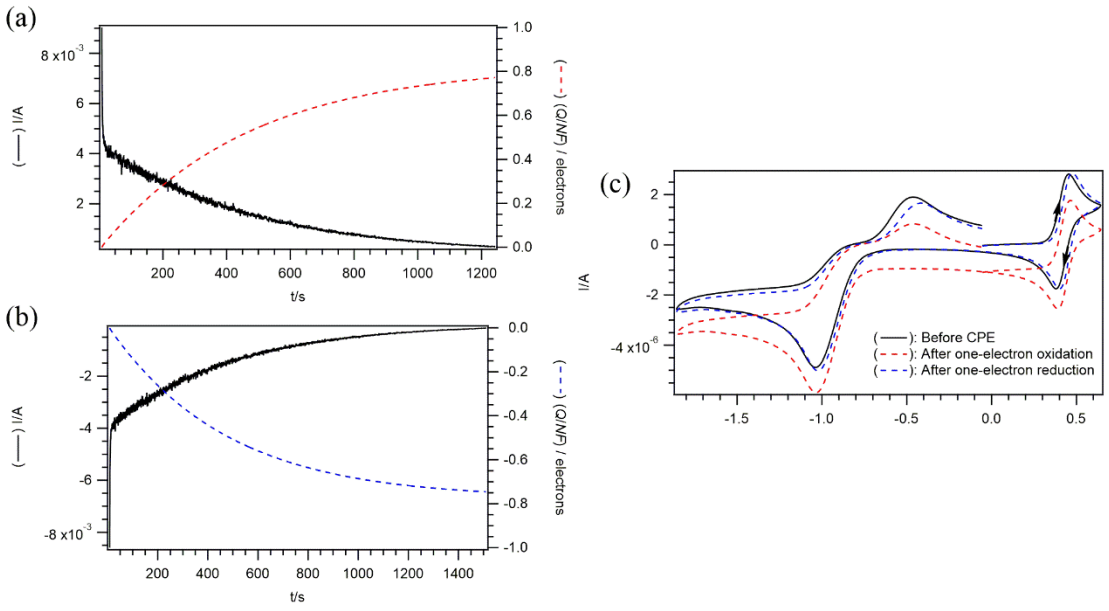

Figure 4.9. Coulometric data (current against time) and CV response for the oxidative electrolysis of 1 mM VKA/VEA in 0.1 M *n*-Bu_4NPF_6/CH_3CN and 200 equiv. of DEM using a 1-mm diameter planar GC disk electrode at 0.1 V s^{-1} (a) Coulometric data for the oxidative CPE at 0.58 vs (Fc/Fc^+)/V. (b) Coulometric data for the reductive CPE at 0.25 vs (Fc/Fc^+)/V.

(c) CV response before and after oxidative and reductive CPE. (Black solid line) Original voltammetric profile (Red dashed line) After one-electron oxidative CPE (Blue solid line) After one-electron reductive CPE back to starting material.

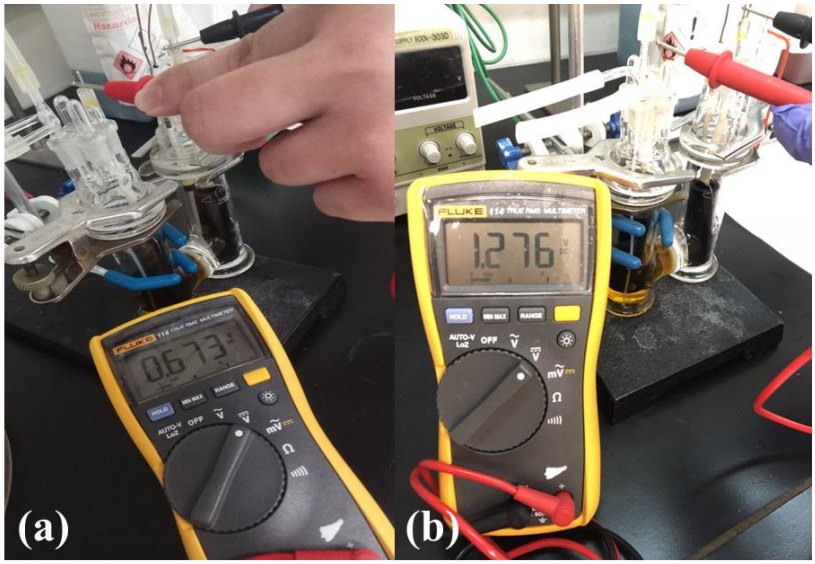

Figure 4.10. Measurement of experimental cell voltage of the mixed reactants in the presence of (a) TFA, (b) DEM using a multimeter in DC mode.

To illustrate the practicality of the proposed mixed-reactant system, the electromotive force was measured using a multimeter by pairing the two half-cells in the charged mode. In the presence of additives, the proposed battery with TFA yield an experimental cell voltage of 0.673 V (Figure 4.10) while the system with DEM offers an experimental cell voltage of 1.276 V. The slight discrepancy between the theoretical and experimental cell voltage is attributed to the inaccuracy associated with the use of $E_{½}$ of VKA involving coupled chemical processes as an approximation for the formal reduction potential.

Nevertheless, the results from the CPE experiments show that the addition of the TFA and DEM can effectively stabilize the reduced species of VKA without affecting the electrochemical performance of VEA in the mixed-reactant system. With the use of DEM (200

equiv.), the reduction potential of VKA was further optimized, resulting in a high experimental cell voltage of 1.276 V which is almost double that obtained with TFA.

4.4 Structural Optimization for VKA

Redox active organic materials often exhibit low solubility in polar organic solvents which limits the energy density of organic-based RFBs. One of the effective strategies adopted is to incorporate polar functional groups to improve the interaction between the solute and solvent molecules.[2, 31-33] In this study, we attempt to improve the solubility of VKA (<0.2 M in pure CH_3CN) by introducing poly (ethylene glycol, PEG) chains into the naphthoquinone (NQ) molecular structure.

4.4.1 Synthesis of VKA Derivatives with Improved Solubility

VKA was structurally modified by replacing the methyl group with ethylene glycol ether side chains. Three VKA derivatives (VKA1, VKA2 and VKA3) with a different number of repeating ethylene oxide units in the side chain were synthesized via a similar synthetic route (Scheme 4.4) but with different corresponding alcohols. The ^{1}H NMR characterization of the three VKA derivatives can be found in Appendix (Figure A.9 to A.11). The physical properties of VKA and its derivatives are summarized in Table 4.2.

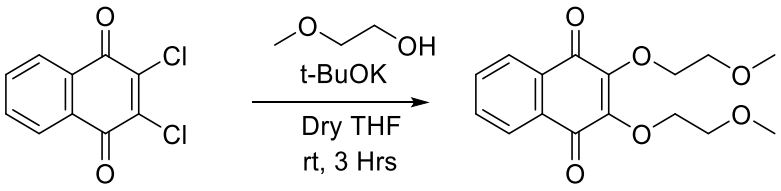

Scheme 4.4. Synthetic route of mono-ethylene glycol substituted VKA derivative.[31]

VKA1 exhibits a high solubility of 2.0 M in pure CH_3CN which is 4 times more than VKA. This value is comparable to, and even higher than some of those reported organic redox

active materials used in the organic-based RFB.[1, 34-35] In the case of VKA2 and VKA3, they exist in liquid state at room temperature and are completely miscible with CH_3CN.

Table 4.2. Physical properties of VKA and its derivatives at 25±2 °C.

Name	**VKA**	**VKA1**	**VKA2**	**VKA3**
Functional Group	Methyl Substituted	Mono-ethylene Glycol Substituted	Di-ethylene Glycol Substituted	Tri-ethylene Glycol Substituted
Chemical Structure	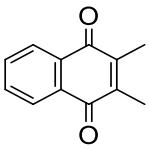	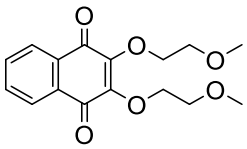	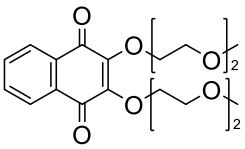	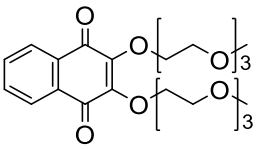
Physical State	Solid	Solid	Liquid	Liquid
Solubility (in CH_3CN)	0.5 M	~2.0 M	Miscible	Miscible

Among the three VKA derivatives, VKA1 has the potential for large scale production due to the simplicity of the synthesis process. For VKA2 and VKA3, an additional purification step was required to remove the remaining unreacted starting material from the final product.

The alcohol reactants for VKA2 and VKA3 have similar polarity to the products which increases the difficulty of the separation during column chromatography. Therefore, the

isolated products were then subjected to heating under vacuum to remove any excess alcohol. In the case of VKA3, a highly polar solvent system is required to run the column chromatography due to the strong interaction between the compound and the silica gel.

4.4.2 Electrochemical Behaviour of VKA Derivatives in the presence of DEM

CV experiments were performed on each of the VKA derivatives as shown in Figure 4.11. Similar to VKA, the derivatives were reduced in two consecutive one electron steps to form a radical anion followed by a dianion. For VKA3, an anomalous peak was detected at -1.67 V vs (Fc/Fc^+)/V, which could be due to the presence of trace impurities.

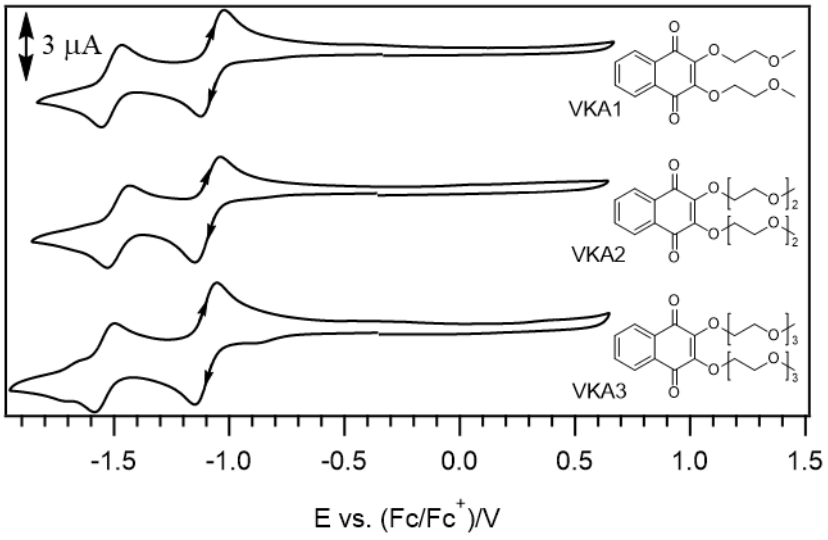

Figure 4.11. Cyclic voltammograms of 1 mM (each) VKA1, VKA2 and VKA3 (in descending order) in 0.1 M *n*-Bu_4NPF_6/CH_3CN recorded using a 1-mm diameter planar GC disk electrode at 0.1 V s^{-1}.

CPE was conducted on the VKA derivatives in the presence of 200 equivalents of DEM. A potential of -1.10 V vs (Fc/Fc^+)/V was applied to reduce VKA1. After the completion of the 1st cycle of CPE (Figure 4.12a), the voltammetric profile of VKA1 obtained (red dashed line)

was similar to the starting material (black solid line) except for the positive shift in the E^{ox}. No further changes to the peak characteristic of VKA1 were detected for the subsequent cycle.

The CV response for the 2 CPE cycles closely overlapped and the charged transfer efficiency obtained was up to 97 % (Table 4.3). Similar performance was observed for both VKA2 and VKA3 (Figure A.6 and A.7) except that the charge transfer efficiency of VKA3 was only up to 87 %. The decrease in the charge transfer efficiency is attributed to the presence of trace impurities that induces the self-discharge. The wide peak-to-peak separation after CPE suggests that the electrode surface might experience some minor changes over time, resulting in slow electron transfer kinetics. The system's utility is nonetheless preserved since the electrochemical behaviour of VKA1 was restored after polishing the working electrode and there is no net loss of redox-active species based on the voltammetric profiles observed from the CPE experiment.

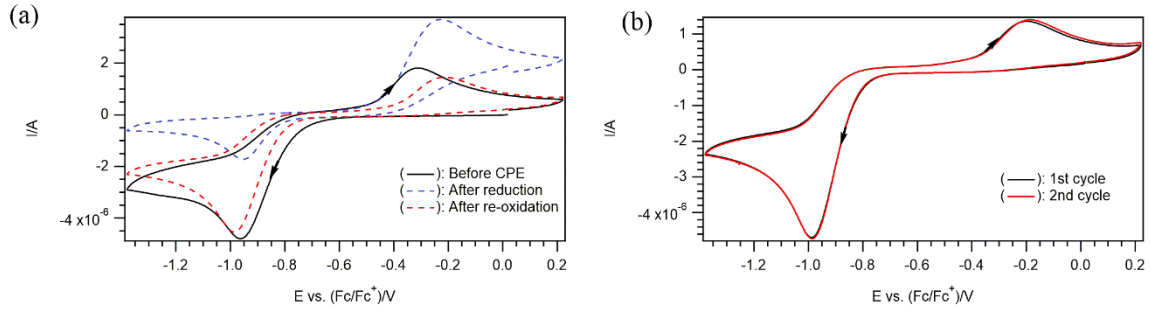

Figure 4.12. CV responses for the exhaustive electrolysis of 1 mM VKA1 in 0.1 M *n*-Bu_4NPF_6/CH_3CN and 200 equiv. of DEM performed using a 1-mm diameter planar GC disk electrode at 0.1 V s^{-1} (a) CV response before and after reductive and oxidative CPE. (Black solid line) Original voltammetric profile (Red dashed line) After reductive CPE (Blue solid line) After oxidative CPE back to starting material. (b) CV response of VKA1 after exhaustive CPE for cycle 1 and 2.

Table 4.3. Charge transfer efficiency for CPE of 1 mM (each) VKA1, VKA2 and VKA3 with 200 equiv. of DEM in 0.1 M *n*-Bu_4NPF_6/CH_3CN.

Compound	1st Cycle	2nd Cycle
VKA1	97.92 %	94.30 %
VKA2	94.41 %	97.60 %
VKA3	81.86 %	86.92 %

The UV-vis absorption spectra of VKA1 presented in Figure 4.13 shows two characteristic bands at 213 nm and 281 nm (with a shoulder peak at 255 nm) in the original spectrum (Figure 4.13, black solid line) while the reduced species, $VKA1H_2$ have two distinctive bands at 214 and 249 nm (Figure 4.13, blue solid line). The spectra obtained after re-oxidation (red solid line) was comparable to the original spectrum (black solid line). The slight increase in the peak magnitudes at 214 and 249 nm indicates that trace amount of reduced species, $VKA1H_2$ were present. Nevertheless, VKA1 can be regenerated from its reduced form without forming side products, as suggested by the absence of additional anomalous peaks. As such, the chemical reversibility of VKA1 was spectroscopically established.

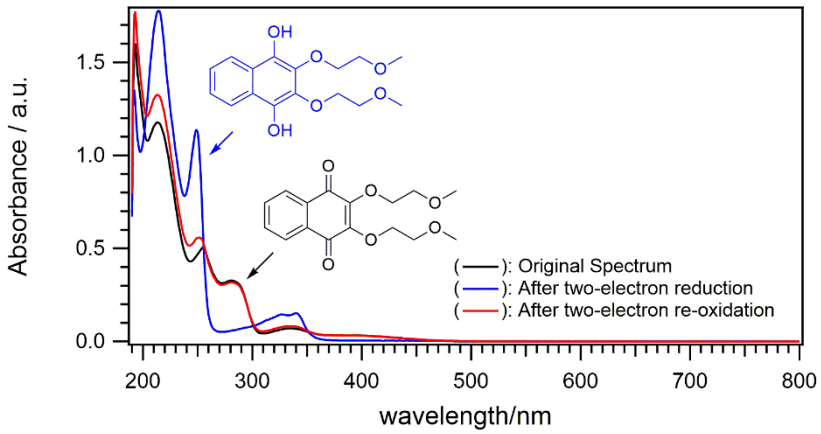

Figure 4.13. Background-subtracted UV-vis spectra of 0.5 mM VKA1 in 50 mM *n*-Bu_4NPF_6/CH_3CN and 200 equiv. DEM. (Black solid line) Original spectrum. (Blue solid line) Spectra after two-electrons reduction. (Red solid line) Spectra back to starting compound.

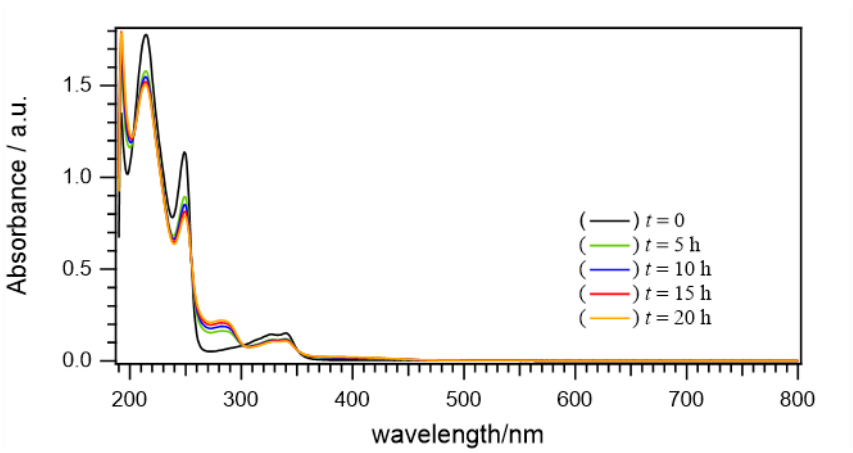

Figure 4.14. Background-subtracted UV-vis spectra of 0.5 mM VKA1 in 50 mM *n*-Bu_4NPF_6/CH_3CN and 200 equiv. DEM recorded over time. (Black solid line) Initial scan at 0 h. (Green solid line) After 5 h. (Blue solid line) After 10 h. (Red solid line) After 15 h. (Orange solid line) Final scan after 20 h.

Results from the time-based study over 20 hours have revealed that the reduced species, $VKA1H_2$ undergo spontaneous oxidation under ambient conditions. The absorption maxima at 249 nm are observed to decrease gradually over time (Figure 4.14, black solid line), while a

distinct band at 281 nm (characteristic absorption bands of VKA1) re-emerged. After 5 hours, the change in absorption bands becomes marginal. Based on the observation, the reduced species of VKA1 were converted back to the starting material. The self-discharge phenomena are likely caused by the presence of atmospheric oxygen in the solution. The reduced species initiate the reduction of oxygen in the solution resulting in oxidation to the neutral form. However, the presence of oxygen does not appear to incur any chemical loss to VKA1 through side reactions, and the functionality of the system is still well-maintained.

VKA1 is a good choice of redox active organic material for the organic-based RFB since it possesses high solubility in CH_3CN (~2.0 M), it also exhibits decent reduction potential (-0.62 V vs. Fc/Fc^+) and high chemical stability in the presence of DEM. Most importantly, VKA1 can be synthesize easily for large-scale production. Hence, VKA1 was subjected to the mixed-reactant system with VEA for further investigation.

4.5 Mixed Reactant System for VKA1 and VEA

4.5.1 Electrochemical Studies in presence of DEM

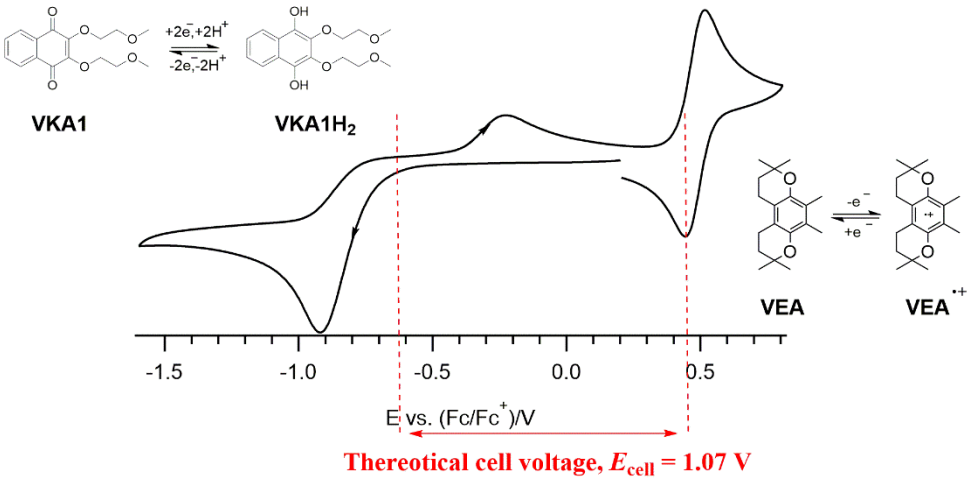

Figure 4.15. Conceptual illustration of the mixed reactant system of VKA1 and VEA with DEM.

In this section, VKA1 and VEA were paired up to construct a mixed reactant organic-based electrolyte system in CH_3CN in the presence of 200 equivalents of DEM with a theoretical cell voltage of 1.07 vs (Fc/Fc^+) as shown in Figure 4.15. The feasibility of the mixed reactant system was further accessed by a series of tests performed under realistic conditions.

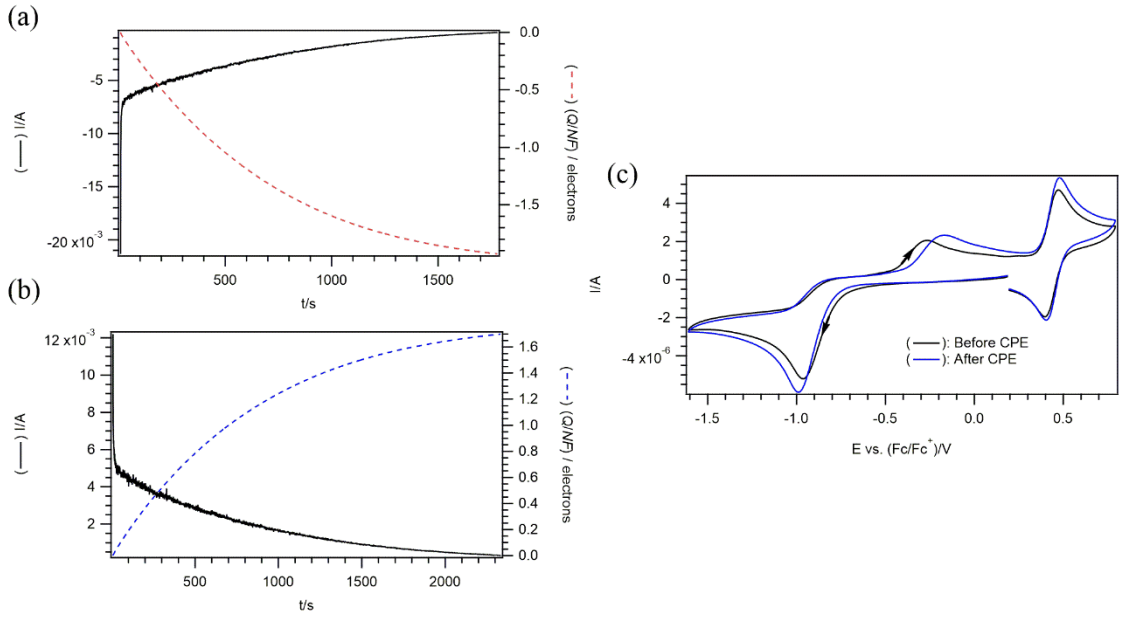

Figure 4.16. Coulometric data (current against time) and CV response for the reductive electrolysis of 1 mM VKA1/VEA in 0.1 M *n*-Bu_4NPF_6/CH_3CN and 200 equiv. of DEM using a 1-mm diameter planar GC disk electrode at 0.1 V s^{-1} (a) Coulometric data for the reductive CPE at -1.11 vs (Fc/Fc+)/V. (b) Coulometric data for the oxidative CPE at -0.13 vs (Fc/Fc^+)/V. (c) CV response before and after reductive and oxidative CPE. (Black solid line) Before CPE (Blue solid line) After CPE.

In Figure 4.16c, the CV scans before (black solid line) and after (blue dashed line) the exhaustive electrolysis were comparable but there was a slight increase in the magnitude of the profile signal for the mixed reactants. This can relate to the solvent evaporation during the electrolysis, leading to an increase of electrolyte concentration over time. As aforementioned, the anodic peak shift can be restored via electrode polishing. (Figure 4.17)

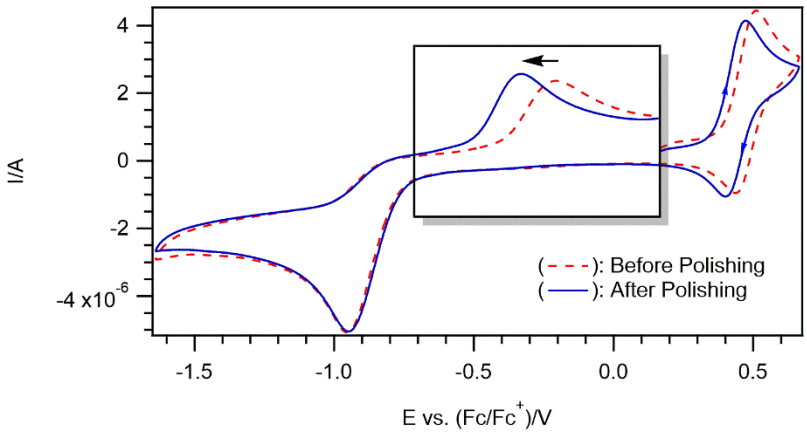

Figure 4.17. CV response after the exhaustive electrolysis of 1 mM VKA1 in 0.1 M *n*-Bu_4NPF_6/CH_3CN and 200 equiv. of DEM performed using a 1-mm diameter planar GC disk electrode at 0.1 V s^{-1} (Blue solid line) Before electrode polishing (Red dashed line) After electrode polishing.

The shortage of charge recovered from the re-oxidation process was possibly due to a similar discharge phenomenon experienced by AQ that was previously discussed in Chapter 3. The closely resembled CV profiles after CPE clearly show that the reduced species of VKA1 is chemically reversible and there was no sign of interference by the presence of VEA or any form of secondary reaction during the exhaustive electrolysis.

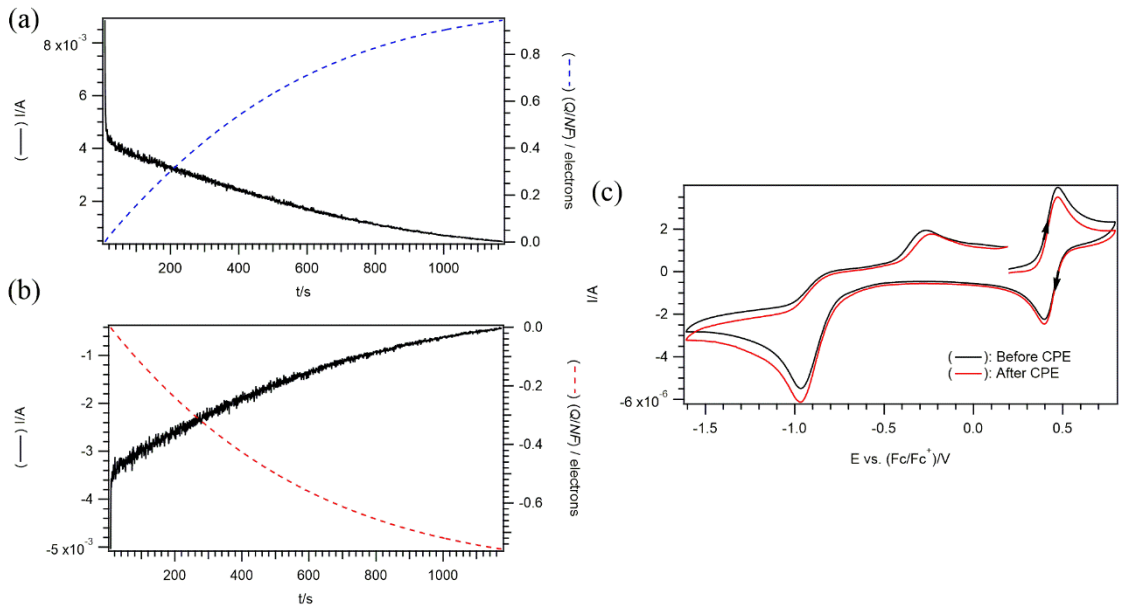

Figure 4.18. Coulometric data (current against time) and CV response for the oxidative electrolysis of 1 mM VKA1/VEA in 0.1 M *n*-Bu_4NPF_6/CH_3CN and 200 equiv. of DEM using a 1-mm diameter planar GC disk electrode at 0.1 V s^{-1} (a) Coulometric data for the oxidative CPE at 0.61 vs (Fc/Fc+)/V. (b) Coulometric data for the reductive CPE at 0.25 vs (Fc/Fc^+)/V. (c) CV response before and after oxidative and reductive CPE. (Black solid line) Before CPE (Red solid line) After CPE.

The absence of change to the CV waves after CPE strongly suggests that the oxidized form of VEA is chemically compatible with VKA1 (Figure 4.18c). The shortage of charge during the reverse reductive CPE of VEA was possibly due to the spontaneous discharge by the unwanted crossover of charged species. Nonetheless, the initial state of the system is restored after one complete CPE cycle, confirming that VEA is chemically reversibly oxidised in the mixed reactant system.

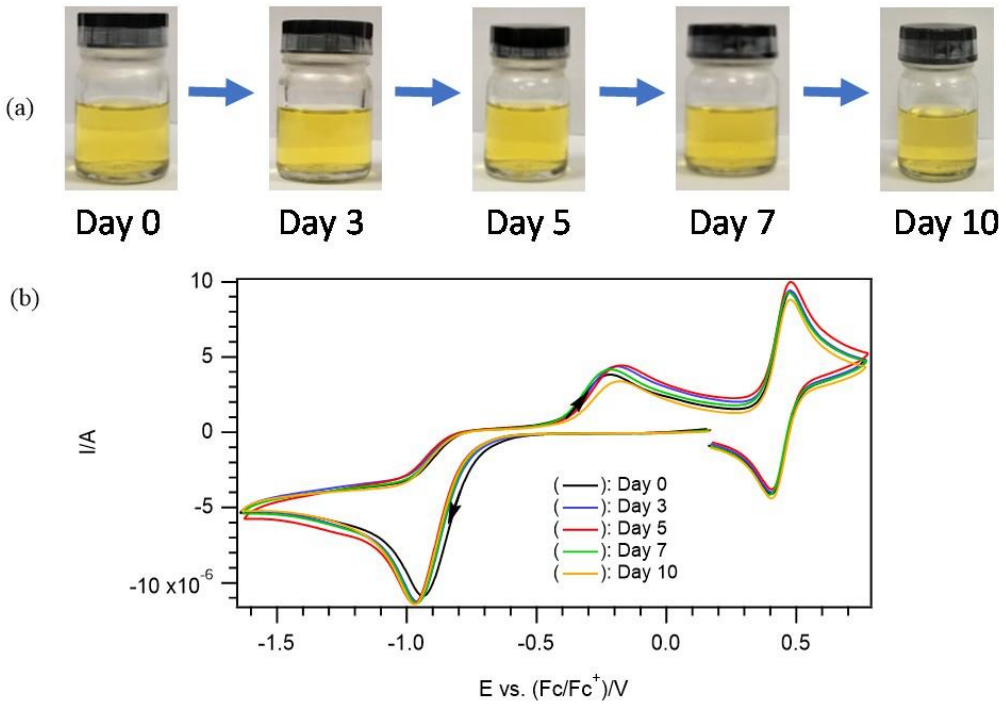

Figure 4.19. (a) 1 mM VKA1/VEA stored in 0.1 M *n*-Bu_4NPF_6/CH_3CN and 200 equiv. DEM over 10 days (b) Cyclic voltammograms of 1 mM VKA1/VEA in 0.1 M *n*-Bu_4NPF_6/CH_3CN and 200 equiv. DEM recorded using a 1-mm diameter planar GC disk electrode at 0.1 V s^{-1} conducted over 10 days.

To evaluate the ambient stability of the mixed-reactant system, 1 mM VKA1 and VEA in 0.1 M *n*-Bu_4NPF_6/CH_3CN with 200 equivalents of DEM were prepared and stored in the sample vials for over a period of 10 days. The sample vials were kept under ambient conditions without exclusion of water and oxygen present in the atmosphere that are known to cause degradation of some redox active species.[17, 36-37] The chemical stability of the mixed reactants was evaluated periodically by CV experiments. From the pictorial evidence shown in Figure 4.19a, there was no visible change to the colour intensity of the electrolyte solutions over the 10 days. The relative peak potential and the ratio of the i_p^{ox} to i_p^{red} for VKA1 and VEA remained constant at different time intervals of the experiment (Figure 4.19b). In addition, no appreciable degradation was detected in the mixed reactants from the voltammetric profiles obtained

throughout the period of analysis. This implies that the mixed reactants of VKA1 and VEA are chemically stable upon prolonged storage in the supporting electrolyte solution under ambient condition.

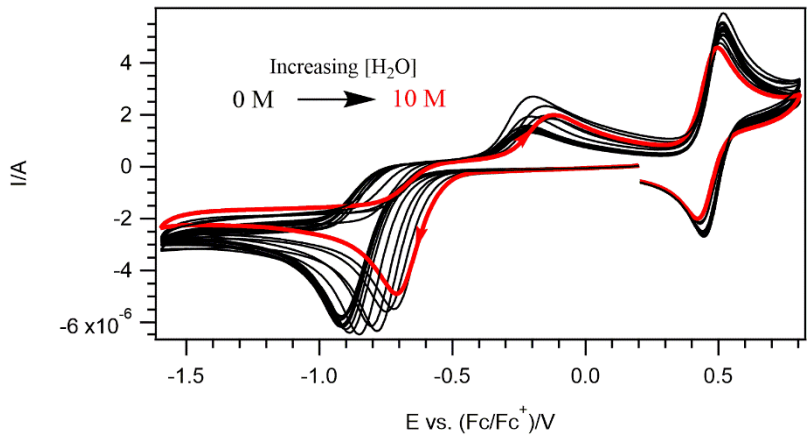

Figure 4.20. Cyclic voltammograms of 1 mM of VKA1/VKE in 0.1 M *n*-Bu_4NPF_6/CH_3CN and 200 equiv. DEM with increasing concentrations of water, recorded using a 1-mm diameter planar GC disk electrode at 0.1 V s^{-1}. (Red solid line) After 10 M of water was added.

The presence of water can sometimes be detrimental to a non-aqueous battery system as water can be correlated to side reactions that affect the electrochemical behaviour of the redox species.[38] Therefore, the water tolerance test was performed to study the influence of water on the electrochemistry of the mixed reactants. As shown in Figure 4.20, increasing water concentration results in a small decline in the peak current magnitudes. This is likely caused by the decrease in the analyte concentration as the result of the dilution and possibly a lowering of the diffusion coefficients of the molecules (*D*-values are usually substantially lower in aqueous compared to non-aqueous solutions). With increasing water concentration, a notable shift in the positive direction was observed for the profile signal of the VKA1. The addition of water allows DEM to dissociate into more free protons into the solution, therefore it increases the extent of protonation for the reduction process of VKA1. As such, the redox process of

VKA1 occurs at a less negative potential. The chemical reversibility of the mixed reactants was maintained in spite of the 10 M of water added to the system.

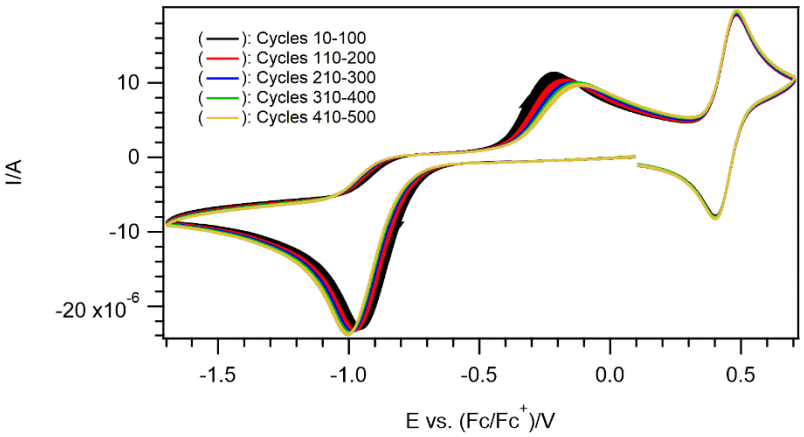

Figure 4.21. Cyclic voltammograms for extended cycling of 1 mM of VKA1/VEA in 0.1 M *n*-Bu_4NPF_6/CH_3CN and 200 equiv. DEM up to 500 cycles recorded using 1-mm GC disk electrode at 0.5 V s–1.

Multi-cycle successive CV scanning was performed to evaluate the redox reversibility of the mixed reactant system on a microscale through prolonged cycling. As shown in Figure 4.21, the CV scans from 500 cycles overlap considerably well apart from the slight shifts in the E^{ox} experienced by VKA1, possibly due to some changes on the electrode surface over time. The change in the E^{ox} was also observed in the previous CPE experiment performed on VKA1 in the presence of DEM (Figure 4.12). Nonetheless, there is no sign of chemical degradation as each cycle proceeds with consistency. The reproducible electrochemical behaviour of both redox species is a good indication of high electrochemical stability of the mixed reactant system.

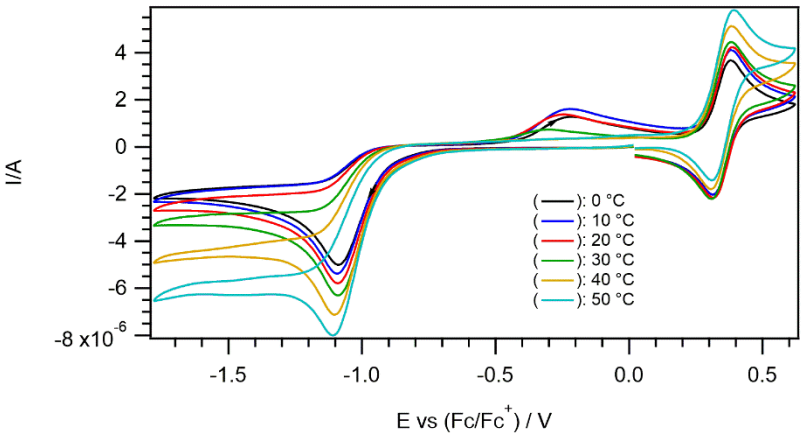

Figure 4.22. Cyclic voltammograms of 1 mM VKA1/VEA in 0.1 M *n*-Bu_4NPF_6/CH_3CN and 200 equiv. DEM recorded using a 1-mm diameter planar GC disk electrode at different temperatures.

The thermal stability of the mixed reactant system was assessed over a temperature range of 0 to 50°C.[39] Studies at variable temperature are important for RFBs since the electrolyte/analyte are prone to side reaction or decomposition at high temperature.[40] The voltammetric profile from Figure 4.22 shows that the magnitude of the i_p^{red} for VKA1 increased with increasing temperature, which is associated with the diminishing of the solvent viscosity at elevated temperature. The lowering of the solvent viscosity increases the rate of diffusion by allowing more VKA1 to undergo reduction at the surface of the electrode.[39, 41] However, the i_p^{ox} that was observed on the reverse scan after first reducing the VKA1 began to diminish at temperatures ≥ 40°C. This may be due to the higher temperature favouring faster diffusion, thus the reduced species have sufficient time to diffuse away from the electrode surface before the can be oxidised back to the starting material. This is particularly notable for the VKA1 system because of the wide separation between the reduction and oxidation peaks obtained during CV measurements. As such, lesser reduced species of VKA1 were able to re-oxidize back to its neutral state, which accounts for the decreased i_p^{ox} observed at elevated temperatures.

Table 4.4. Peak current ratios for VEA at operating temperature of 0-50°C

Temperature (°C)	0	10	20	30	40	50
VEA ($\|i_p^{ox}/i_p^{red}\|$)	0.974	0.989	0.980	0.978	0.954	0.975

In the case of VEA, the anodic and cathodic peak-to-peak separation was much smaller than VKA1, hence the oxidized form of VEA has lesser time to diffuse away from the electrode surface. This can be further supported by the close to unity anodic (i_p^{ox}) and cathodic (i_p^{red}) peak current ratios in the oxidation step of VEA (Table 4.4). The electrochemical profile of the mixed reactants obtained at room temperature (25±2 °C) after the study were similar to that obtained before the experiment (Figure 4.23). Except for the slight shift in the overall redox potential due to the change to the electrode surface, the increase in the magnitude of the profile signal can be correlated to the solvent evaporation which leads to an increase of electrolyte concentration over time. No peak distortion due to thermal decomposition was observed, therefore it is reasonable to assume that both VKA1 and VEA are thermally stable.

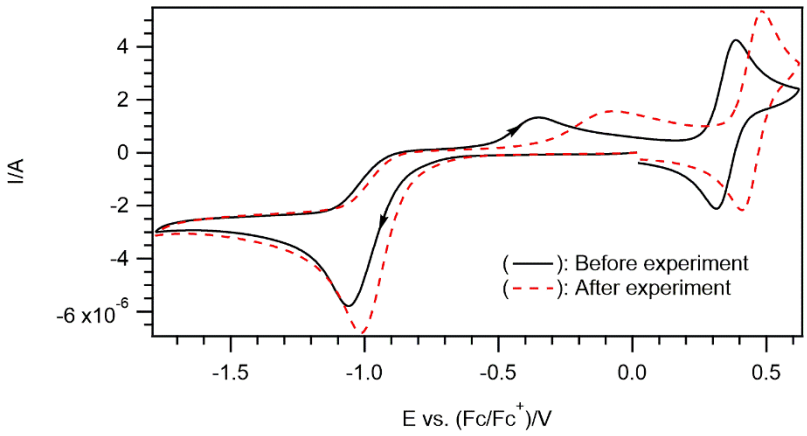

Figure 4.23. Comparison between CVs before and after variable temperature experiments at 25±2 °C.

4.6 Summary

The proposal of malonic ester (weak acid) incorporated into the quinone system has allowed for an improvement in the redox potential for the two-electron reduction process as well as its chemical stability. The result from the study shows that the reduction mechanism of VKA with DEM proceeds through a "wedge-scheme" mechanism which is highly dependent on the concentration of the DEM. The functionalization of VKA with the incorporation of ethylene glycol ether side chains has effectively increased the solubility in CH_3CN from 0.5 M (VKA) to 2.0 M (VKA1). The electrochemical tests have revealed that the VKA1 demonstrates good electrochemical reversibility and stability in the presence of 200 equivalents of DEM. The pairing of both half-cells provides a theoretical cell potential of 1.07 V (based on estimations of $E^r_{1/2}$ values) while the experimental measured value (with a voltmeter) amounts to 1.23 V. The proposed mixed reactants in the presence of DEM displayed good stability and chemical reversibility in their redox active states in the presence of water as well as over the typical operating temperature of RFBs. The system also showed high durability under prolonged storage in the supporting electrolyte solution. Most importantly, electrochemical solutions containing the mixed reactants VKA1 and VEA were proved to be chemically compatible and reversible since the individual charged species did not interact with the neutral counterpart. To further enhance the energy density of the proposed mix reactant system, future studies can be directed to improve the solubility of VEA which was reported to be 0.12 M in CH_3CN. In conclusion, the present study has fulfilled its objective to develop a new organic based electrolyte system the with potential to serve as an all-organic battery suited for the electrochemical energy storage system.

4.7 Experimental Section

Materials and Methods Most chemicals and reagents were purchased from standard commercial suppliers and used as received unless otherwise stated. 2, -Dichloro-1,4-napththoquinone (95%), potassium *tert*-butoxide (97%), 2-methoxyethanol (99%), 2-(2-methoxyethoxy)ethanol (99%) and triethylene glycol monomethyl ether (98%) were obtained from Tokyo Chemical Industry Co., Ltd. 2,3-Dimethylbenzene-1,4-diol (97%), *p*-toluenesulfonic acid monohydrate (≥98.5 %) and 2-methyl-but-3-en-2-ol (98%) were obtained from Sigma-Aldrich. Acetonitrile (CH_3CN) was HPLC grade and was purchased from Anhui Fulltime Solvents & Reagents Co., Ltd. The supporting electrolyte, tetrabutylammonium hexafluorophosphate (*n*-Bu_4NPF_6), was synthesized according to a literature procedure.[42] ^1H NMR spectroscopy was performed at room temperature on a Bruker AV 300MHz NMR (BBO probe) spectrometer. Chemical shifts are reported in parts per million (ppm) with reference to residual solvent peaks in the ^1H NMR spectrum. UV-visible spectroscopy was conducted using a PerkinElmer Model LAMBDA 750 UV/Vis spectrophotometer.

Cyclic Voltammetry For the ambient stability test, the mixed-reactant samples were dissolved in 0.1 M *n*-Bu_4NPF_6/CH_3CN with 200 molar equivalents of DEM. The solution was left to stand under ambient conditions and stored away from light sources. An aliquot (5 mL) was retrieved from the bulk solution on days 0, 3, 5, 7 and 10 for CV measurement to study the chemical stability of the system.

Solubility Measurement The solubility test of VKA and VKA1 was performed at room temperature (25±2 °C). 10 μL of pure CH_3CN was added per interval to a fixed amount of compound. After each addition, the mixture was subjected to sonication for 5 minutes. The process was repeated until no solid was visually detected.

Synthesis of Compound

Compound pyrano[3,2-f]chromene (VEA)

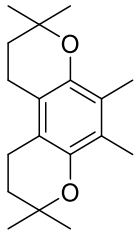

The synthesis of compound VEA was adopted from a literature procedure.[15] 2,3-Dimethylbenzene-1,4-diol (0.276 g, 2.00 mmol) and *p*-toluenesulfonic acid, TsOH (0.038 g, 0.2 mmol) were added to a 25 mL round bottom flask, followed by the addition of 5 mL of dry toluene under argon. 2-Methyl-but-3-en-2-ol (0.189 g, 4.10 mmol) was added dropwise into the mixture and was refluxed for 18 hours at 100 ^{o}C. The solution was cooled to room temperature and diluted with ethyl acetate. 5 mL of water was added to the mixture for extraction. The organic layer collected was washed with 5 mL of brine, dried over Na_2SO_4 and filtered. The solvent was removed in vacuo and purified by column chromatography over silica gel. (hexane: ethyl acetate = 1000:1). VEA was obtained as a white solid.^{1}H NMR (CDCl3, 300 MHz) δ: 3.40 (s, 3H), 3.71-3.74 (m, 2H), 4.49-4.52 (m, 2H), 7.67-7.70 (m, 2H) and 8.03-8.05 (m, 2H).

Compound 2,3-dimethyl-1,4-naphthoquinone (VKA)

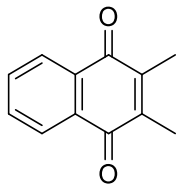

The current procedure was adapted from previous published method.[43] 1,4-naphthoquinone (1.08 g, 6.30 mmol), silver nitrate (0.64 g, 3.77 mmol) and 0.5 mL of acetic acid were dissolved in the mixture of 40 mL of acetonitrile and 20 mL of water. Ammonium persulfate (1.90 g, 8.33 mmol) was dissolved in 20 mL of water and added gradually to the mixture. The resulted mixture was first incubated at 80^{o}C for 5 hours, followed by over the night at room temperature. 100 mL of water was added to the mixture and was extracted twice

with 25 mL of CH_2Cl_2. The organic layer was washed twice with 50 mL of water. dried over Na_2SO_4 and filtered. The solvent was removed in vacuo. The crude product was purified by sublimation at 80°C. VKA (2.34 g, 56%) was obtained as a yellow solid. ^{1}H NMR ($CDCl_3$, 300 MHz) δ: 2.17 (s, 6H), 7.69 (m, 2H), 8.08 (m, 2H).

Compound 2,3-bis(2-methoxyethoxy)-1,4-naphthalenedione (VKA1)

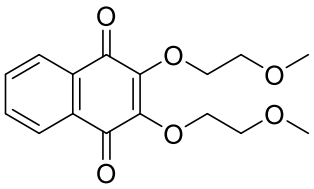

The synthesis of compound VKA1 was adopted from a literature procedure.[31] 2,3- dichloro-1,4-naphthoquinone (1.00 g, 4.4 mmol) in 60 mL of dry THF were added to a 100 mL round-bottom flask. A mixture of 2-methoxyethanol (10 mL, 127 mmol) and potassium *tert*-butoxide (1.032 g, 9.2 mmol) in 4 mL of dry THF was added. The mixture was stirred at room temperature for 3 hours. The mixture was filtered, and the filtrate was dried in vacuum. 40 mL of water was added into the compound and the mixture was extracted three times with 40 mL of CH_2Cl_2. The combined organic layer collected was washed with 40 mL of brine, dried over $MgSO_4$, and filtered. The solvent was removed in vacuo to afford a dark orange viscous oil. The residue was purified by column chromatography over silica gel (hexane: ethyl acetate = 1:1). VKA1 was obtained as yellowish-orange solid. ^{1}H NMR (CDCl3, 300 MHz) δ: 3.40 (s, 3H), 3.71-3.74 (m, 2H), 4.49-4.52 (m, 2H), 7.67-7.70 (m, 2H) and 8.03-8.05 (m, 2H).

Compound 2,3-bis(2-(2-methoxyethoxy)ethoxy)naphthalene-1,4-dione (VKA2)

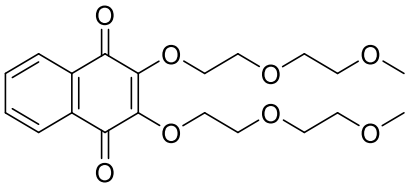

The synthesis of compound VKA2 was adopted from a literature procedure.[31] 2,3-dichloro-1,4-naphthoquinone (0.50 g, 2.2 mmol) in 30 mL of dry

THF were added to a 100 mL round-bottom flask. A mixture of 2-(2-methoxyethoxy)ethanol (4 mL, 34 mmol) and potassium *tert*-butoxide (0.52 g, 4.6 mmol) in 2 mL of dry THF was added. The mixture was stirred at room temperature for 5 hours. The mixture was filtered, and the filtrate was dried in vacuum. 20 mL of water was added into the compound and the mixture was extracted three times with 20 mL of CH_2Cl_2. The combined organic layer collected was washed with 20 mL of brine, dried over $MgSO_4$, and filtered. The solvent was removed in vacuo to afford a dark orange viscous oil. The residue was purified by column chromatography over silica gel (hexane: ethyl acetate = 7:3) and the product was dried under vacuum at 90°C, VKA2 was obtained as orange viscous oil. ^{1}H NMR (CDCl3, 300 MHz) δ: 3.30 (s, 6H), 3.47-3.50 (m, 4H), 3.66-3.68 (m, 4H), 3.81-3.84 (m, 4H), 4.51-4.54 (m, 4H), 7.66-7.69 (m, 2H) and 8.02-8.05 (m, 2H).

Compound 2,3-bis(2-(2-(2-methoxyethoxy)ethoxy)ethoxy)naphthalene-1,4-dione (VKA3)

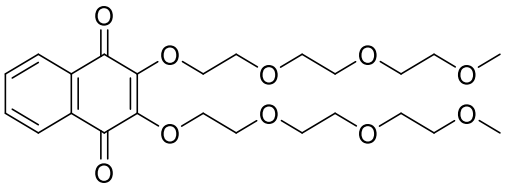

The current procedure was adapted from previous published method.[33] 2,3-dichloro-1,4-naphthoquinone (0.50 g, 2.2 mmol) were mixed with KOH (0.308 g, 5.5 mmol) and triethylene glycol monomethyl ether (15 mL, 93.7 mmol). The resulting thick slurry was warmed to dissolve. The solution was heated at 100°C for 3 hours. The mixture was cooled to room temperature and quenched with HCl (25 mL, 0.5 M). The resulting mixture was extracted five times with 25 mL of CH_2Cl_2 and washed five times with 1 M $NaHCO_3$. The organic layer collected was washed with 25 mL of water to a neutral pH, dried over Na_2SO_4 and filtered. The solvent was removed in vacuo to afford a dark orange viscous oil. The residue was purified by column chromatography over silica gel (100% ethyl acetate) and the product was dried under vacuum at 90°C, VKA3 (0.034 g, 6.8 %) was obtained as orange viscous oil.^{1}H NMR (CDCl3, 300 MHz) δ: 3.35 (s, 6H), 3.48-3.52 (m, 4H), 3.56-

3.62 (m, 8H), 3.66-3.70 (m, 4H), 3.80-3.83 (m, 4H), 4.51-4.54 (m, 4H), 7.67-7.70 (m, 2H) and 8.03-8.06 (m, 2H).

References

1. Huo, Y.; Xing, X.; Zhang, C.; Wang, X.; Li, Y. *RSC Adv.* **2019,** *9*, 13128-13132.

2. Zhang, J.; Yang, Z.; Shkrob, I. A.; Assary, R. S.; Tung, S. o.; Silcox, B.; Duan, W.; Zhang, J.; Su, C. C.; Hu, B.; Pan, B.; Liao, C.; Zhang, Z.; Wang, W.; Curtiss, L. A.; Thompson, L. T.; Wei, X.; Zhang, L. *Adv. Energy Mater.* **2017,** *7*, 1701272.

3. Su, L.; Ferrandon, M.; Kowalski, J. A.; Vaughey, J. T.; Brushett, F. R. *J. Electrochem. Soc.* **2014,** *161*, A1905-A1914.

4. Duan, W.; Huang, J.; Kowalski, J. A.; Shkrob, I. A.; Vijayakumar, M.; Walter, E.; Pan, B.; Yang, Z.; Milshtein, J. D.; Li, B.; Liao, C.; Zhang, Z.; Wang, W.; Liu, J.; Moore, J. S.; Brushett, F. R.; Zhang, L.; Wei, X. *ACS Energy Lett.* **2017,** *2*, 1156-1161.

5. Wei, X.; Xu, W.; Vijayakumar, M.; Cosimbescu, L.; Liu, T.; Sprenkle, V.; Wang, W. *Adv. Mater.* **2014,** *26*, 7649-7653.

6. Wedege, K.; Dražević, E.; Konya, D.; Bentien, A. *Sci. Rep.* **2016,** *6*, 39101.

7. Er, S.; Suh, C.; Marshak, M. P.; Aspuru-Guzik, A. *Chem. Sci.* **2015,** *6*, 885-893.

8. Bunji, U.; Atsushi, K.; Kenji, K. *Chem. Lett.* **1992,** *21*, 1017-1020.

9. Gupta, N.; Linschitz, H. *J. Am. Chem. Soc.* **1997,** *119*, 6384-6391.

10. Aguilar-Martínez, M.; Gonzalez, I.; Ruvalcaba, N. *J. Mex. Chem. Soc.* **2000,** *44*, 74.

11. Gómez, M.; González, F. J.; González, I. *Electroanalysis.* **2003,** *15*, 635-645.

12. Aguilar-Martinez, M.; Macias-Ruvalcaba, N. A.; Bautista-Martinez, J. A.; Gomez, M.; Gonzalez, F. J.; Gonzalez, I. *Curr. Org. Chem.* **2004,** *8*, 1721-1738.

13. Katsumi, J.; Nakayama, T.; Esaka, Y.; Uno, B. *Anal. Sci.* **2012,** *28*, 257-257.

14. Jin, B.; Huang, J.; Zhao, A.; Zhang, S.; Tian, Y.; Yang, J. *J. Electroanal. Chem.* **2010,** *650*, 116-126.

15. Peng, H. M.; Choules, B. F.; Yao, W. W.; Zhang, Z.; Webster, R. D.; Gill, P. M. W. *J. Phys. Chem. B.* **2008,** *112*, 10367-10374.

16. Tessensohn, M. E.; Lee, M.; Hirao, H.; Webster, R. D. *ChemPhysChem.* **2015,** *16*, 160-168.

17. Tessensohn, M. E.; Hirao, H.; Webster, R. D. *J. Phys. Chem. C.* **2013,** *117*, 1081-1090.

18. Hui, Y.; Chng, E. L. K.; Chua, L. P.-L.; Liu, W. Z.; Webster, R. D. *Anal. Chem.* **2010,** *82*, 1928-1934.

19. Hui, Y.; Chng, E. L. K.; Chng, C. Y. L.; Poh, H. L.; Webster, R. D. *J. Am. Chem. Soc.* **2009,** *131*, 1523-1534.

20. Shigeo, H.; Masamichi, F. *Bull. Chem. Soc. Jpn.* **1971,** *44*, 2051-2055.

21. Kim, H. S.; Chung, T. D.; Kim, H. *J. Electroanal. Chem.* **2001,** *498*, 209-215.

22. Kim, J.; Chung, T. D.; Kim, H. *J. Electroanal. Chem.* **2001,** *499*, 78-84.

23. Costentin, C.; Robert, M.; Savéant, J.-M. *J. Am. Chem. Soc.* **2006,** *128*, 8726-8727.

24. Costentin, C.; Robert, M.; Savéant, J.-M. *J. Am. Chem. Soc.* **2006,** *128*, 4552-4553.

25. Costentin, C. *Chem. Rev.* **2008,** *108*, 2145-2179.

26. Costentin, C.; Robert, M.; Savéant, J.-M. *Acc. Chem. Res.* **2010,** *43*, 1019-1029.

27. Costentin, C.; Robert, M.; Savéant, J.-M. *PCCP.* **2010,** *12*, 11179-11190.

28. Costentin, C.; Robert, M.; Savéant, J.-M.; Tard, C. *Angew. Chem. Int. Ed.* **2010,** *49*, 3803-3806.

29. Savéant, J.-M.; Tard, C. *J. Am. Chem. Soc.* **2014,** *136*, 8907-8910.

30. Tamashiro, B. T.; Cedano, M. R.; Pham, A. T.; Smith, D. K. *J. Phys. Chem. C.* **2015,** *119*, 12865-12874.

31. Shimizu, A.; Takenaka, K.; Handa, N.; Nokami, T.; Itoh, T.; Yoshida, J.-I. *Adv. Mater.* **2017,** *29*, 1606592.

32. Milshtein, J. D.; Kaur, A. P.; Casselman, M. D.; Kowalski, J. A.; Modekrutti, S.; Zhang, P. L.; Harsha Attanayake, N.; Elliott, C. F.; Parkin, S. R.; Risko, C.; Brushett, F. R.; Odom, S. A. *Energy Environ. Sci.* **2016,** *9*, 3531-3543.

33. Wang, W.; Xu, W.; Cosimbescu, L.; Choi, D.; Li, L.; Yang, Z. *Chem. Commun.* **2012,** *48*, 6669-6671.

34. Wei, X.; Duan, W.; Huang, J.; Zhang, L.; Li, B.; Reed, D.; Xu, W.; Sprenkle, V.; Wang, W. *ACS Energy Lett.* **2016,** *1*, 705-711.

35. Brushett, F. R.; Vaughey, J. T.; Jansen, A. N. *Adv. Energy Mater.* **2012,** *2*, 1390-1396.

36. Beh, E. S.; De Porcellinis, D.; Gracia, R. L.; Xia, K. T.; Gordon, R. G.; Aziz, M. J. *ACS Energy Lett.* **2017,** *2*, 639-644.

37. Zotti, G.; Schiavon, G.; Zecchin, S.; Favretto, D. *J. Electroanal. Chem.* **1998,** *456*, 217-221.

38. Shinkle, A. A.; Sleightholme, A. E. S.; Griffith, L. D.; Thompson, L. T.; Monroe, C. W. *J. Power Sources.* **2012,** *206*, 490-496.

39. Li, L.; Kim, S.; Wang, W.; Vijayakumar, M.; Nie, Z.; Chen, B.; Zhang, J.; Xia, G.; Hu, J.; Graff, G.; Liu, J.; Yang, Z. *Adv. Energy Mater.* **2011,** *1*, 394-400.

40. Winsberg, J.; Hagemann, T.; Janoschka, T.; Hager, M. D.; Schubert, U. S. *Angew. Chem. Int. Ed.* **2017,** *56*, 686-711.

41. Zhang, D.; Lan, H.; Li, Y. *J. Power Sources.* **2012,** *217*, 199-203.

42. Kissinger, P. T. E.; Heineman, W. R. E. *Laboratory Techniques in Electroanalytical Chemistry*; Marcel Dekker: New York, 1984.

43. Wang, Y.; Liu, Z. *J. Org. Chem.* **2002,** *67*, 8507-8512.

Chapter 5

Exploring the Benefits of 3D-printing in the Development for Laboratory Scale Test Cell

---

5.1 Cell Architecture of Redox Flow Battery

A typical cell assembly for the RFB consists of six main components including the end plate, current collector, bipolar plate, felt electrode, flow frame and membrane (Figure 5.1).[1]

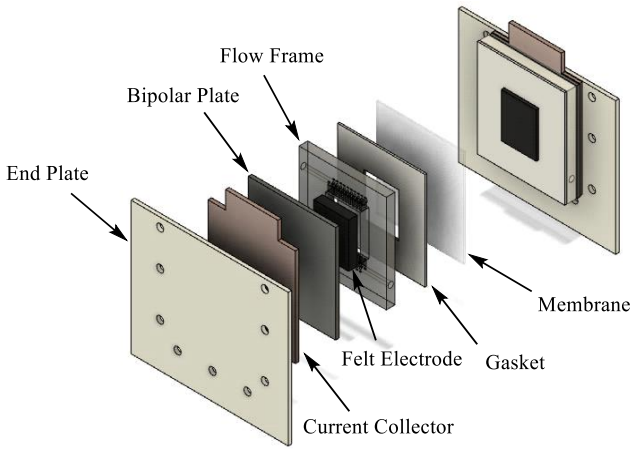

Figure 5.1: Exploded view of a typical RFB cell assembly.

In the RFB systems, the catholyte and anolyte are respectively stored in two separate tanks. With the aid of pumps, the electrolytes are directed to the electrode surface to undergo electrochemical reactions (Figure 5.2a). The electrodes used are chemically inert and only provide an active surface to facilitate charge transfer. The membrane serves to segregate the half-cell compartments to minimize crossover of redox-active species[2] and the end plates are positioned at both sides of the stack body to provide uniform compression to the cell assembly. During operation, the electrolytes are circulated between their respective half-cell compartment and the tanks (Figure 5.2b). Upon discharging, chemical potential energy is converted to electrical energy as the redox active materials undergo electrochemical reaction at the electrodes. The negatively charged active materials are oxidized at the anode and the released electrons pass through the bipolar plate and the current collector to the external load. Thereafter, the cathode receives the electrons from the external load to reduce the positively charge active species. As such, this process generates electricity.

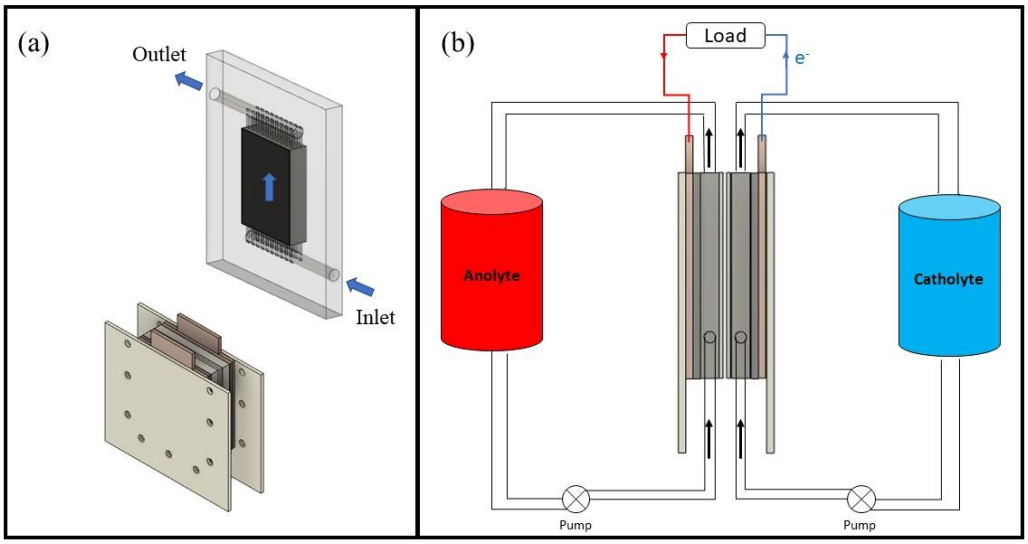

Figure 5.2. *Flow-through configuration* RFB (a) RFB stack and flow frame (b) RFB setup during charging (cross sectional view).

5.2 Design and Fabrication of Test Cell Prototype

The development of RFBs often begins with the laboratory research, where a test cell is used to evaluate the electrochemical performance of the electrolytes as well as being used to optimize the engineering aspects of the system before proceeding towards large scale operations.[3] As such, low-cost rapid prototyping is important in the design process of the laboratory test cell. The ability to translate a design idea into a physical 3D prototype is especially important in the study of critical components of the test cell such as flow frame. In this study, we will demonstrate the use of 3D printing to design and fabricate the cell components that can be used as part of the assembly for a laboratory test cell prototype. 3D-printed Fused Deposit Modelling (FDM) was used to fabricate two of the main RFB components; the flow frame, and the end plates. The 3D sketches of the cell components were designed by using the CAD software (Autodesk Fusion 360). Fusion 360 is a useful design tools for 3D modelling and enabled us to create several types of design for the flow field as illustrated in Table 5.1. The use of 3D printing technology is a fast and cost-effective way to implement innovative ideas and new concepts to the cell design.

Table 5.1. 3D illustration for different type of flow fields.

Type of flow field	3D illustration
Flow-through configuration	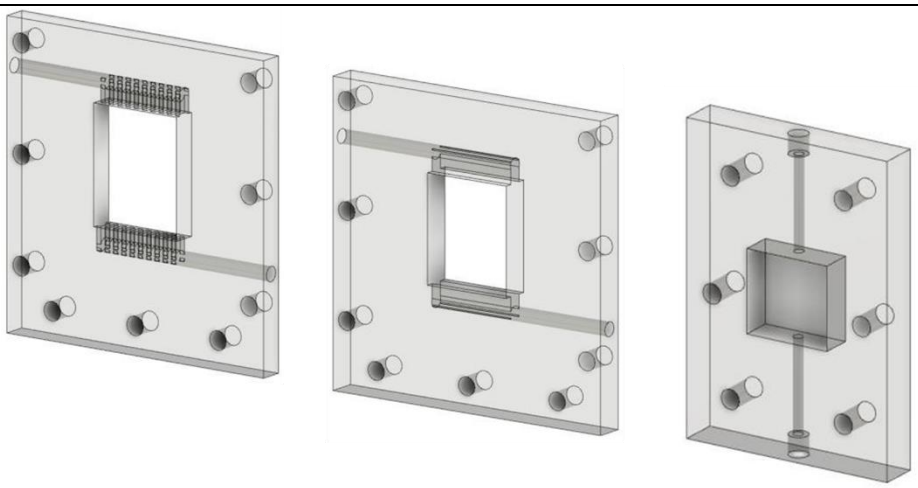
Flow-by configuration (Serpentine and Interdigitated)	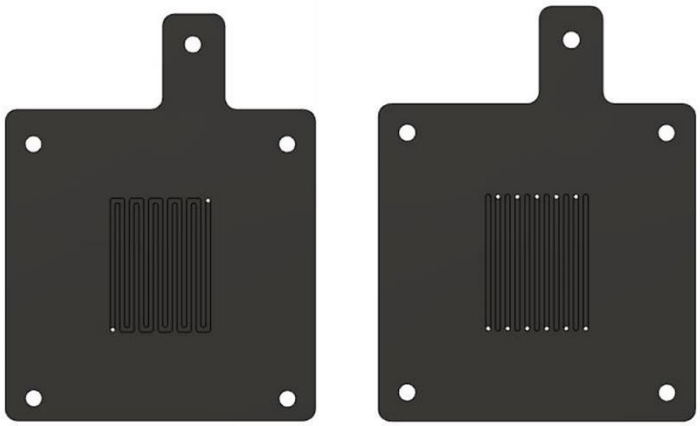
Flow-by configuration (Interdigitated with ramps)[4]	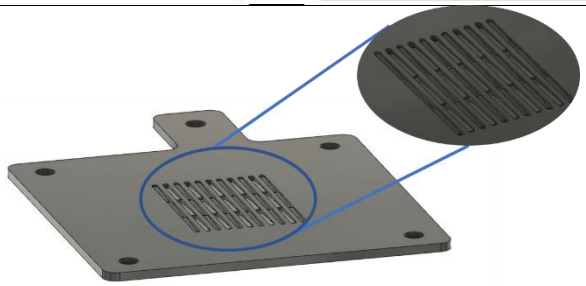
Flow-by configuration (Interdigitated with tapered channel)	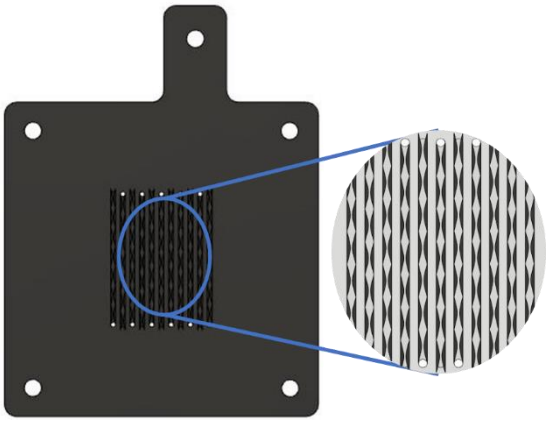

The 3D sketches were translated to the standard tessellation language (.STL) file and the data was processed by the slicer program to generate the multiple slices 2D object. Thereafter, the 3D printer coordinates with the slicer program to fabricate the cell component through a layer-by-layer deposition based on the generated 2D object.[5-6] Figure 6.4 shows the 3D-printed flow frame fabricated in this study. The overall dimensions of the 3D-printed objects were closely resembled to the original sketches with an error of ($\pm$ 0.1 mm). The high level of precision in 3D printing technology can easily reproduce similar 3D printed parts for multiple testing.

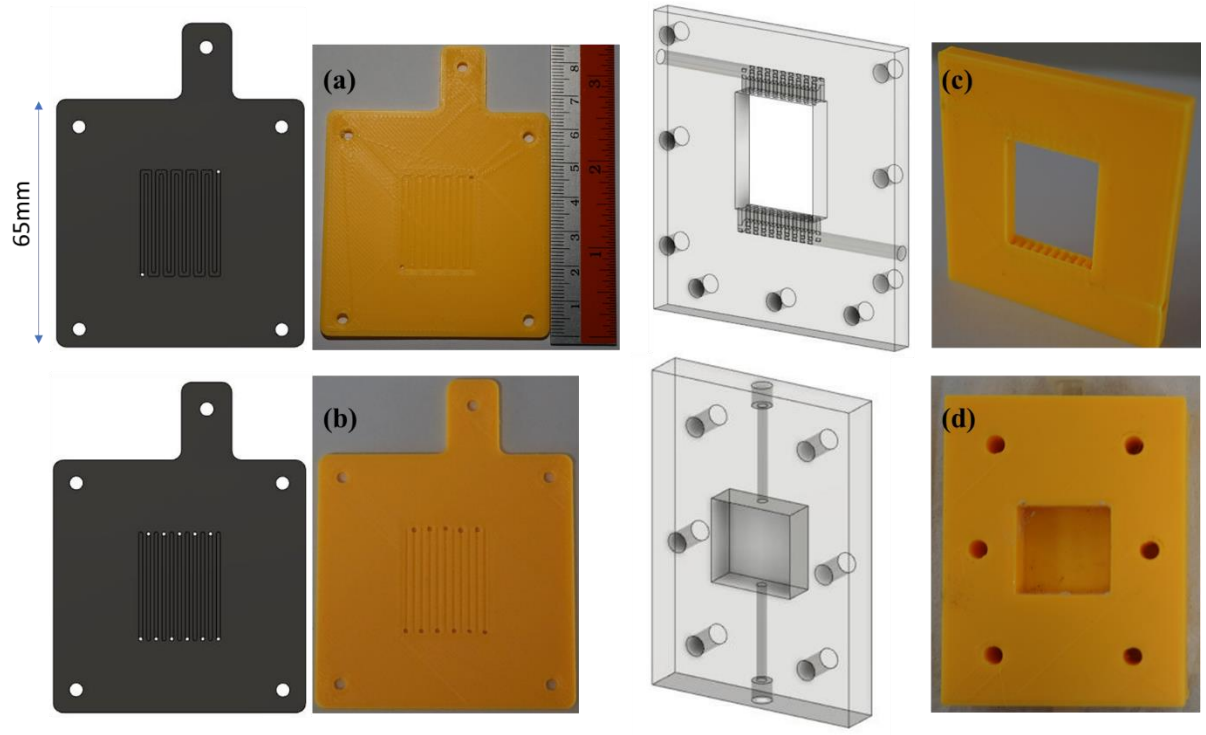

Figure 5.3. The 3D illustrations and the 3D-printed objects. (a) Flow-by configuration (Serpentine). (b) Flow-by configuration (Interdigitated). (c) Flow-through configuration (Type 1). (d) Flow-through configuration (Type 2).

The following figure shows the examples of test cell prototype assembled with 3D printed components from Figure 5.3.

Figure 5.4. Assembled test cell prototype. (a) With flow-by configuration. (b) Type 1 flow-through configuration (c) Type 2 flow-through configuration.

To demonstrate the feasibility of 3D printing, the cell prototype (Figure 5.4c) was assembled with the 3D printed PLA end plates and the following items shown in Figure 6.5a. The AvCarb G200 soft graphite felt with a thickness of 6.5mm was used as the electrodes. A thin piece of copper plate was attached to the conductive glassy carbon (GC) plate and the combined pieces was embedded into the end plate to serve as the current collector. Thin layer Teflon gaskets were used to seal the flow frame and the membrane to prevent leakage. During cell stacking, the electrodes were compressed with a compression ratio of 20% to reduce the contact resistance between the electrode and the membrane.[7-8] Electrochemical impedence spectroscopy (EIS) was performed on the cell prototype to determine the ohmic resistance (R_Ω) contributed by the contact resistances between electrolyte and electrodes, electrolyte resistances and membrane resistance in the cell.[9] The aqueous mixed reactant system of 50 mM methylhydroquinone /9,10-anthraquinone-2,6-disulfonic acid disodium salt (AQDS) in 0.5 M H_2SO_4 were used for the preliminary studies. Based on the analysis of the EIS Nyquist plot, the test cell prototype exhibits a low ohmic resistance of 0.878 Ω (Figure 5.6).

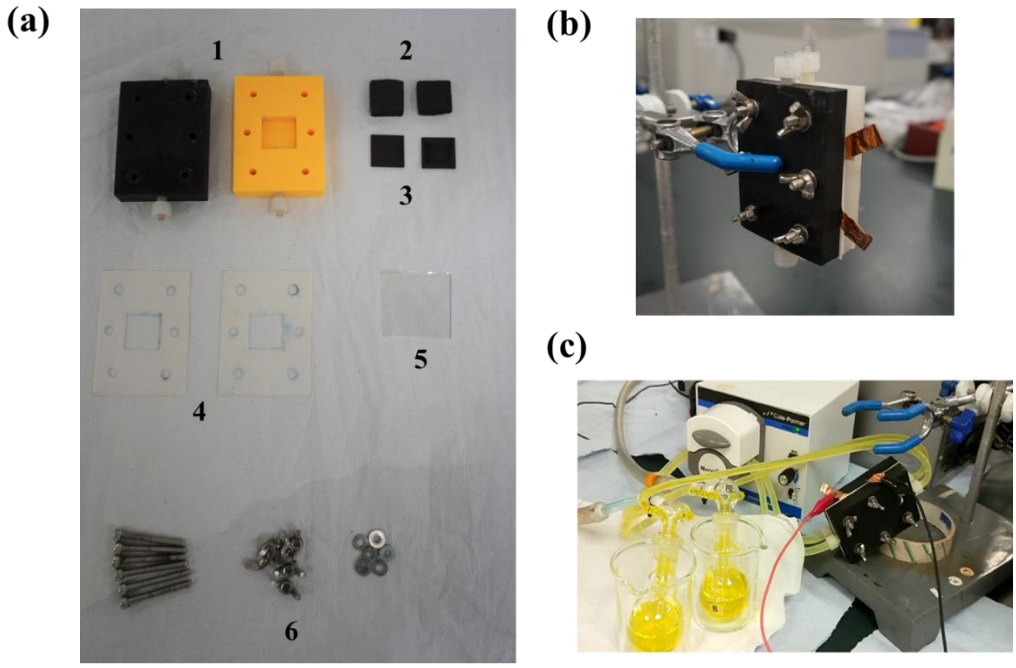

Figure 5.5. The test cell prototype in deconstructed view. (a) cell components: 1) 3D-printed end plates with type 2 flow-through configuration, 2) graphite felts, 3) glassy carbon plates, 4) teflon gaskets, 5) nafion 212 membrane and 6) screws, wing nuts and washers. (b) Assembled test cell prototype. (c) Test setup (For demonstration).

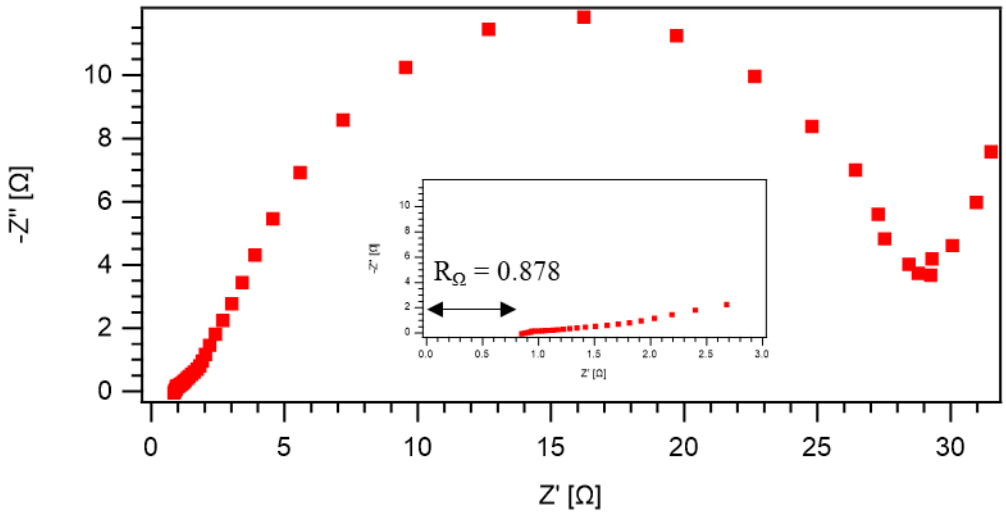

Figure 5.6. The EIS spectrum of the test cell prototype.

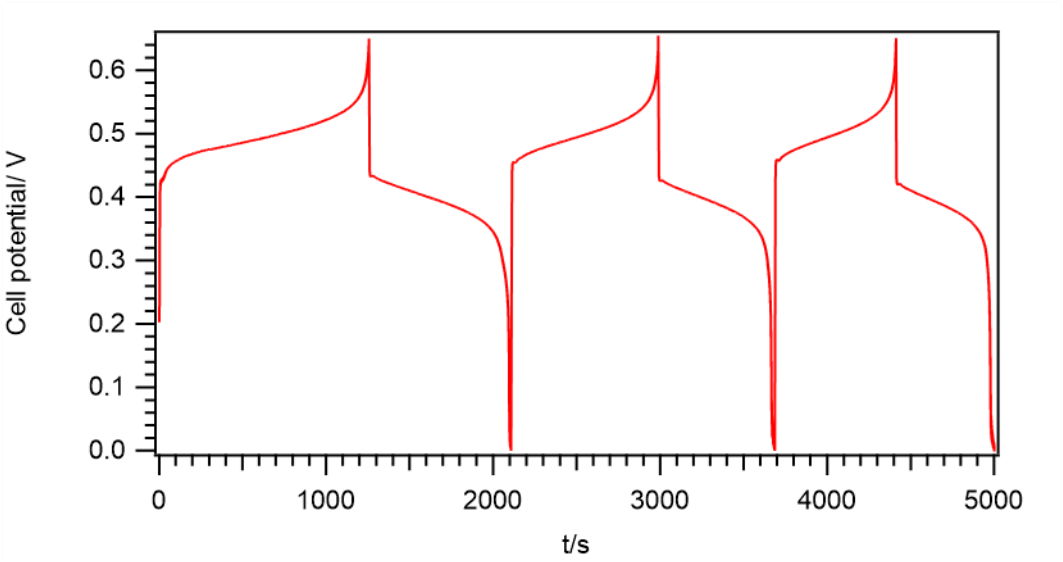

Figure 5.7. Charge-discharge cycles of 50 mM methylhydroquinone/AQDS in 0.5 M H_2SO_4 at 7.5 mA cm^{-2} between 0.65 and 0 V upper and lower potential thresholds.

The rapid prototyping and low-cost printing enable quick identification of the problems associated with the new design. For instance, the charge and discharge study performed on the test cell prototype with the 3D printed flow frame (Figure 5.3d) have experienced capacity loss in the flowing experiments. The amount of charge requires for the charging cycle is decreasing upon each successive charge-discharge cycle as shown in Figure 5.7. The loss of electrolyte was found to be due to leakage from the inlet flow port which was associated with the issue of back pressure. Since different modified version of the flow frames can be easily created by 3D-printing, appropriate adjustment to the design such as the dimension of the flow channels can be effectively implemented to rectify this issue. Nevertheless, the use of 3D printing technology to develop a functional laboratory test cell suitable for the battery testing in organic-based systems is still in the development stage. Work is presently ongoing in the laboratory to study and optimize the flow and mass transport of the 3D-printed prototype, and the search for suitable materials used in 3D-printing for organic systems that can survive prolonged electrochemical cycling.

5.3 Summary

The benefits of 3D printing technology have been illustrated by the design and fabrication process of the laboratory test cell prototype. 3D printing technology is a convenient tool which enables the fabrication of cell components with new design features that are usually difficult and expensive to manufacture with traditional manufacturing processes. In addition, 3D printed components can be easily reproduced with high level of precision. The rapid prototyping and low-cost manufacturing facilitate the identification of the problems associated with the new designs and allow quick implementation of new design improvements. Nonetheless, the state of 3D printing in the fabrication of laboratory test cells for organic-based RFB is still in its early stage as the search for compatible materials for the organic systems remains a challenge.

References

1. Eapen, D. E.; Choudhury, S. R.; Rengaswamy, R. *Appl. Surf. Sci.* **2019,** *474*, 262-268.

2. Winsberg, J.; Hagemann, T.; Janoschka, T.; Hager, M. D.; Schubert, U. S. *Angew. Chem. Int. Ed.* **2017,** *56*, 686-711.

3. Arenas, L. F.; Walsh, F. C.; de León, C. P. *ECS J. Solid State Sci. Technol.* **2015,** *4*, P3080-P3085.

4. Akuzum, B.; Alparslan, Y. C.; Robinson, N. C.; Agar, E.; Kumbur, E. C. *J. Appl. Electrochem.* **2019,** *49*, 551-561.

5. Ambrosi, A.; Webster, R. D. *Curr. Opin. Electrochem.* **2020,** *20*, 28-35.

6. Ambrosi, A.; Pumera, M. *ACS Sustainable Chem. Eng.* **2018,** *6*, 16968-16975.

7. Hsieh, C. L.; Tsai, P. H.; Hsu, N. Y.; Chen, Y. S. *Energies.* **2019,** *12*.

8. Park, S. K.; Shim, J.; Yang, J. H.; Jin, C. S.; Lee, B. S.; Lee, Y. S.; Shin, K. H.; Jeon, J. D. *Electrochim. Acta.* **2014,** *116*, 447-452.

9. Percin, K.; van der Zee, B.; Wessling, M. *ChemElectroChem.* **2020,** *7*, 2165-2172.

Chapter 6

Conclusion and Future Work

6.1 Summary

The utilization of organic molecules for energy storage applications has attracted great attention owing to the structural diversity and synthetic tunability of organic compounds. Such factors have driven the present study with the aim of developing new organic based electrolyte systems to potentially serve as all-organic batteries for RFB applications. In Chapter 3, four different organic compounds have shown suitable electrochemical properties required for practical function in organic electrolytes. Using bulk electrolysis and spectroscopic studies, the radical cation of the vitamin E analogue (VEA) exhibits an exceptional chemical stability and reversibility. In contrast, it was found that the addition of acid additives (i.e. TFA) were required to stabilize the charged form of VKA and TMB. Under acidic conditions, VKA exhibits a reversible $2e^-/2H^+$ reduction process while TMB undergoes a $2e^-/H^+$ reversible oxidation process. In the case of TCNQ, studies have revealed that the dianion, $TCNQ^{2-}$ is reactive to oxygen, while the anion radical is highly stable. To utilize the two-electron storage capacity of TCNQ, a more stringent cell design is required to eliminate the presence of oxygen.

In Chapter 3, the electrochemical performance of quinones and benzidine derivatives were evaluated. Among the derivatives, AQ and *o*-tolidine displayed good chemical reversibility and the pairing of both in half-cells provided the highest theoretical cell potential. 50 equivalents of TFA were found to be the optimum concentration to maintain a reasonably high redox potential while facilitating charge stabilization. AQ and *o*-tolidine were subjected to a mixed reactant system for further evaluation under practical conditions. The results from exhaustive electrolysis showed that the mixed reactants were chemically compatible since the charged species did not interact with the neutral counterpart. There was no sign of deterioration to the functionality of the system upon prolong storage in organic solvents, and exposure to water. The mixed reactants also displayed excellent thermal stability over the typical operating

temperature of a RFB. However, the results from the time-based UV-vis study suggests that the reduced anthraquinone (anthrahydroquinone) was prone to self-discharge in the presence of oxygen and further work is required to improve the solubility of anthraquinone in acetonitrile. Nevertheless, the studies have identified an organic electrolyte system comprised of molecules capable of two-electron redox reactions. Such qualities are useful in designing a high energy density battery system.

In Chapter 4, the effects of different additives on the reduction mechanism of VKA were examined. The result from the study suggests that the electrochemical reduction process of VKA proceeds through a "wedge-scheme" mechanism in the presence of DEM. At low DEM concentrations (< 10 mM), the electrochemical reduction of VKA exhibits features characteristic of hydrogen bonding interactions, while at high DEM concentration (>20 mM), the reduction process was accompanied by proton-coupled electron transfer (PCET). VKA was chemically modified by incorporating ethylene glycol ether side chains into the NQ core structure. The resultant molecule, VKA1, exhibited a four-fold increase in solubility from 0.5 M to 2.0 M in CH_3CN. VKA1 achieved an optimal redox potential and chemical stability with the addition of 200 equivalents of DEM. Coupled with VEA, the mixed reactant system provides a desirable experimental cell potential of 1.23 V. The mixed reactants were chemically compatibility and have shown good chemical stability under practical conditions. The studies have fulfilled the objective to develop a chemically stable organic based electrolyte system and the findings can be taken into consideration when developing an organic quinone-based RFB.

In chapter 5, 3D printing technology was incorporated into the design and fabrication process of laboratory test cell prototypes. The 3D printed flow frames and end plates can be easily produced as per design with a high level of precision. The rapid prototyping enables rapid assessment of any problems associated with new designs. However, the development of

3D-printed laboratory test cells for organic-based RFB systems is limited by material compatibility in organic solvents.

6.2 Future Outlook

The organic electrolyte system comprised of AQ and *o*-tolidine has the potential to be used for the development of high energy density battery systems due to its two-electron transfer capability. Strong acid is required to stabilize the charged form of AQ and *o*-tolidine. The redox potential of AQ is affected by the extent of protonation. The occurrence of the reduction process appears at a potential that is significantly more positive under a strong acidic environment. The use of weak acid such as acetic acid can potentially improve the redox potential of AQ while sustaining the chemical stability. However, the stability of *o*-tolidine can be compromised using weak acids in the mixed reactant system. In a previous study, Oh *et al.* chemically modified *p*-phenylenediamine by replacing the hydrogen atoms on the -NH_2 group with a methyl substituent to enhance the stability of the dication via steric protection. Such an approach can be implemented on the structure-similar *o*-tolidine to improve the chemical stability of the dication.[1] Therefore, weak acid can be used in the mixed-reactants AQ and *o*-tolidine to impart a higher overall cell potential. The solubility of AQ in CH_3CN can also be improved by incorporating ethylene glycol ether side chain into the AQ core structure.[2-3]

VEA can undergo a two-electron oxidation process. However, the product of the second oxidation step is chemically short-lived. Studies have revealed that the positive charge distribution in $VEA^{\bullet+}$ is similar to the cation of α tocopherol model compound, (CH_3)α-$TOH^{\bullet+}$ which is mainly located on the quaternary carbon in the chromanol ring with less charge delocalized in the aromatic ring.[4-5] It is possible to stabilize the dication of VEA through extending the conjugation of the system.[6-7] An effective strategy to improve the energy density

of battery system is to utilize redox couples with higher electron storage capability, therefore, this is an area that is worth exploring in the future.

The results obtained from the present studies leads to the possibility that the two organic based electrolyte systems can potentially be used for the design of an all-organic battery suited for future RFB applications.

References

1. Kim, H. S.; Lee, K. J.; Han, Y. K.; Ryu, J. H.; Oh, S. M. *J. Power Sources.* **2017,** *348*, 264-269.

2. Shimizu, A.; Takenaka, K.; Handa, N.; Nokami, T.; Itoh, T.; Yoshida, J. I. *Adv. Mater.* **2017,** *29*, 1606592.

3. Wang, W.; Xu, W.; Cosimbescu, L.; Choi, D.; Li, L.; Yang, Z. *Chem. Commun.* **2012,** *48*, 6669-6671.

4. Peng, H. M.; Choules, B. F.; Yao, W. W.; Zhang, Z.; Webster, R. D.; Gill, P. M. W. *J. Phys. Chem. B.* **2008,** *112*, 10367-10374.

5. Lee, S. B.; Lin, C. Y.; Gill, P. M. W.; Webster, R. D. *J. Org. Chem.* **2005,** *70*, 10466-10473.

6. Duan, W.; Huang, J.; Kowalski, J. A.; Shkrob, I. A.; Vijayakumar, M.; Walter, E.; Pan, B.; Yang, Z.; Milshtein, J. D.; Li, B.; Liao, C.; Zhang, Z.; Wang, W.; Liu, J.; Moore, J. S.; Brushett, F. R.; Zhang, L.; Wei, X. *ACS Energy Lett.* **2017,** *2*, 1156-1161.

7. Luo, J.; Hu, B.; Debruler, C.; Liu, T. L. *Angew. Chem. Int. Ed.* **2018,** *57*, 231-235.

Appendix

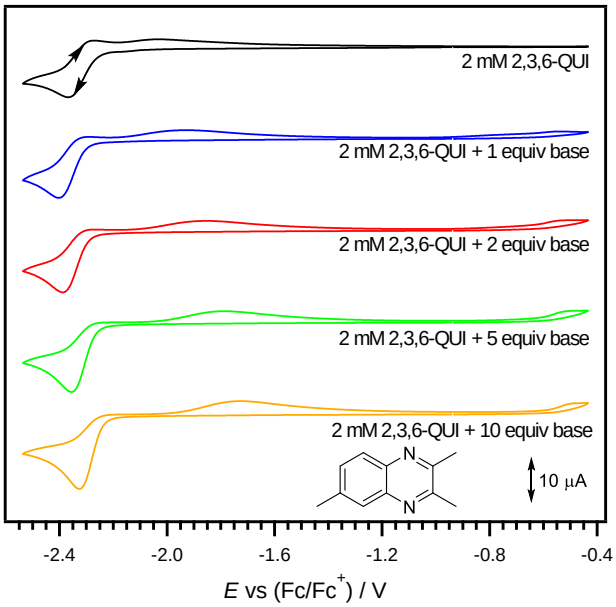

Figure A.1. Cyclic voltammograms of 2 mM 2,3,6-QUI in 0.2 M *n*Bu_4NPF_6/CH_3CN containing different equivalents *n*Bu_4NOH base, recorded using a 1-mm diameter planar GC disk electrode at 0.1 V s^{-1}.

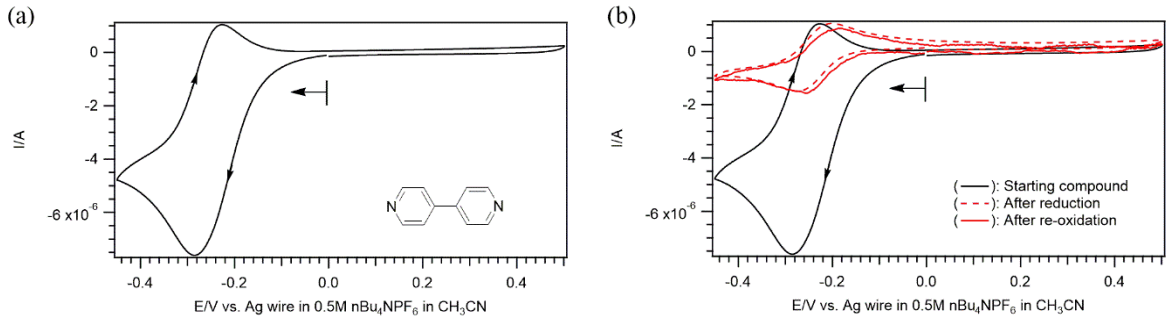

Figure A.2. Cyclic voltammograms of 1 mM 4,4-dipyridyl in 0.1 M *n*-Bu_4NPF_6/CH_3CN recorded using a 1-mm diameter planar GC disk electrode at 0.1 V s^{-1} (a) 4,4-dipyridyl, (b) 4,4-dipyridyl before and after exhaustive CPE.

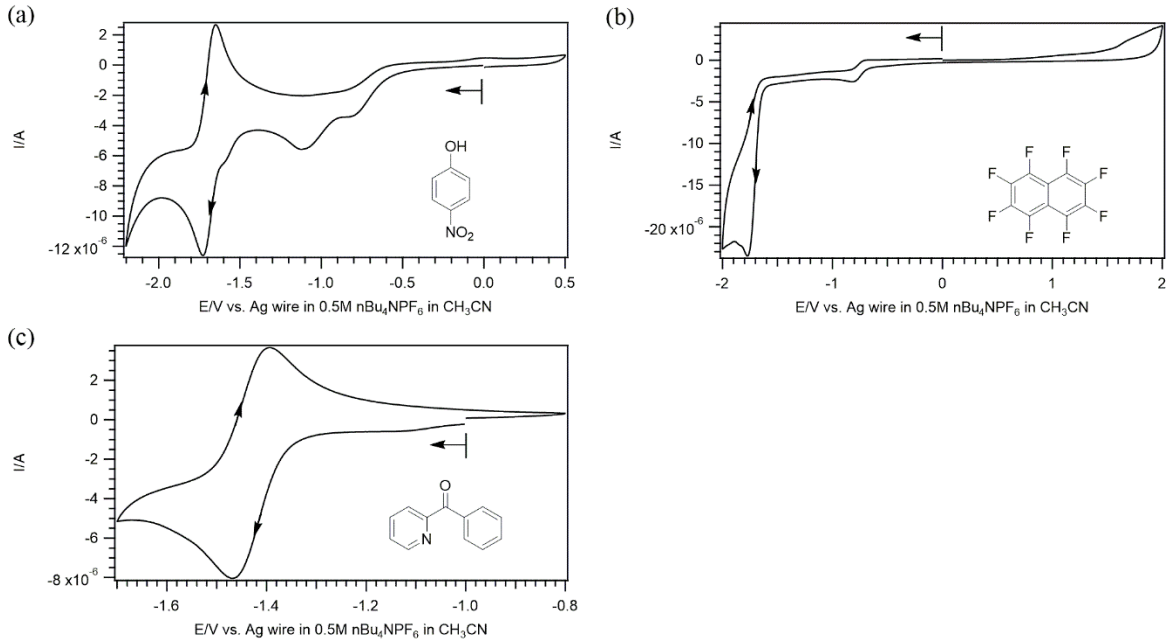

Figure A.3. Cyclic voltammograms of 1 mM (a) 4-nitrophenol, (b) OFN and (c) phenyl-2-pyridinylmethanone in 0.1 M *n*-Bu_4NPF_6/CH_3CN recorded using a 1-mm diameter planar GC disk electrode at 0.1 V s^{-1}.

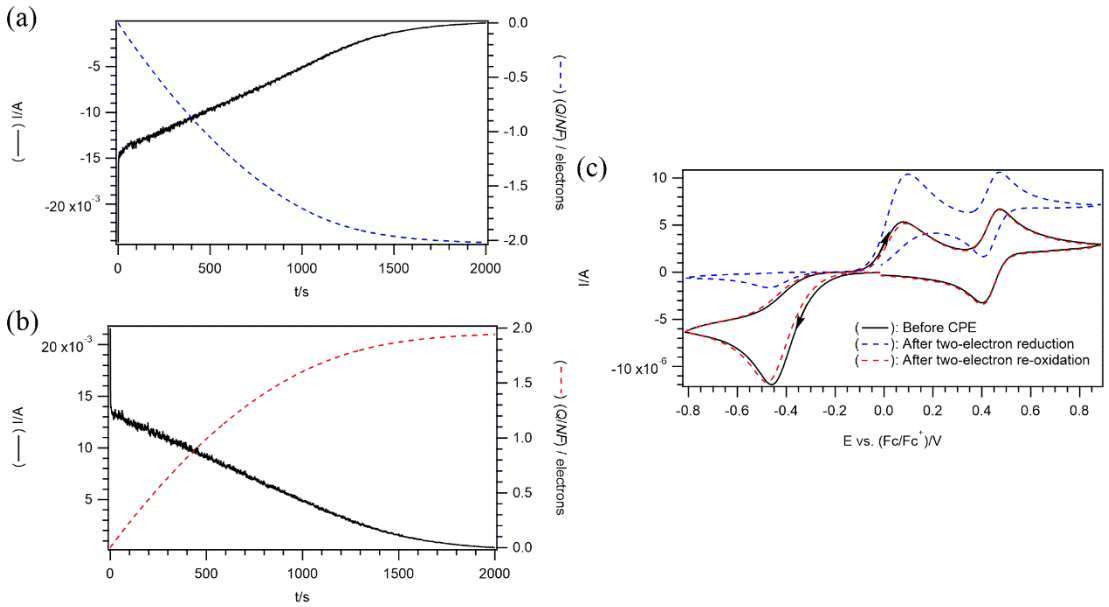

Figure A.4. Coulometric data (current against time) and CV response for the reductive electrolysis of 2 mM VKA/VEA in 0.2 M *n*-Bu_4NPF_6/CH_3CN and 50 equiv. of TFA using a 1-mm diameter planar GC disk electrode at 0.1 V s^{-1} (a) Coulometric data for the reductive CPE

at –0.62 vs (Fc/Fc$^+$)/V. (b) Coulometric data for the oxidative CPE at 0.26 vs (Fc/Fc$^+$)/V. (c) CV response before and after reductive and oxidative CPE. (Black solid line) Original voltammetric profile of VK_A (Red dashed line) After two-electron reductive CPE (Blue dashed line) After two-electron oxidative CPE back to starting material.

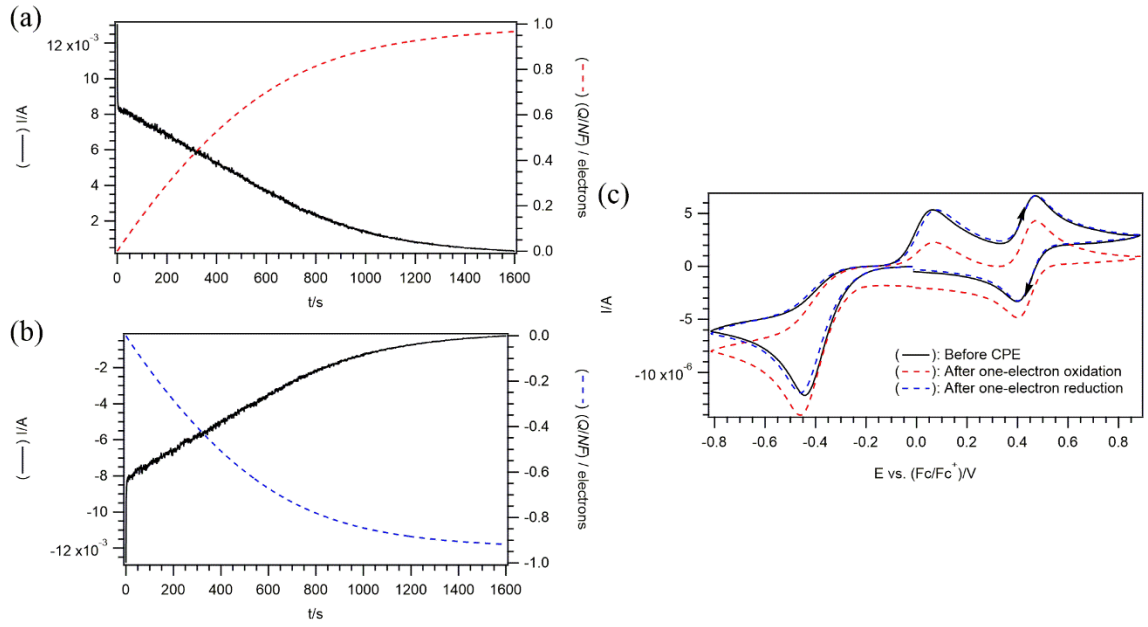

Figure A.5. Coulometric data (current against time) and CV response for the oxidative electrolysis of 2 mM VKA/VEA in 0.2 M *n*-Bu_4NPF_6/CH_3CN and 50 equiv. of TFA using a 1-mm diameter planar GC disk electrode at 0.1 V s^{-1} (a) Coulometric data for the oxidative CPE at 0.64 vs (Fc/Fc$^+$)/V. (b) Coulometric data for the reductive CPE at 0.24 vs (Fc/Fc$^+$)/V. (c) CV response before and after oxidative and reductive CPE. (Black solid line) Original voltammetric profile of VE_A (Red dashed line) After one-electron oxidative CPE (Blue dashed line) After one-electron reductive CPE back to starting material.

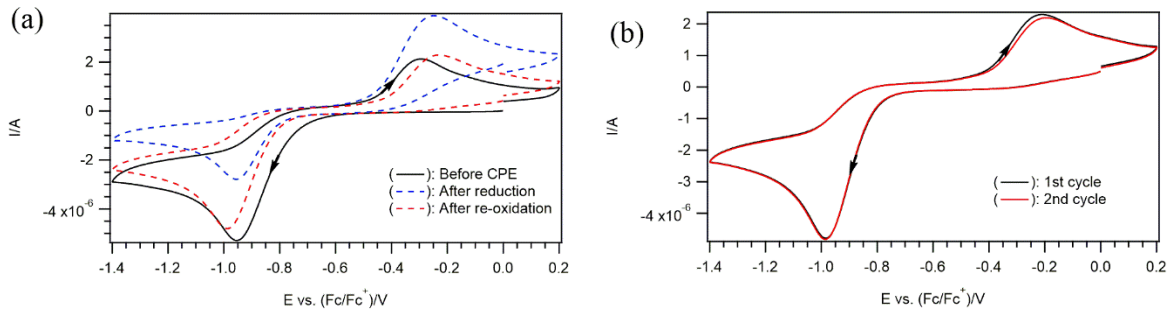

Figure A.6. CV responses for the exhaustive electrolysis of 1 mM VKA2 in 0.1 M *n*-Bu_4NPF_6/CH_3CN and 200 equiv. of DEM performed using a 1-mm diameter planar GC disk electrode at 0.1 V s^{-1} (a) CV response before and after reductive and oxidative CPE. (Black solid line) Original voltammetric profile (Red dashed line) After reductive CPE (Blue solid line) After oxidative CPE back to starting material. (b) CV response of VKA2 after exhaustive CPE for cycle 1 and 2.

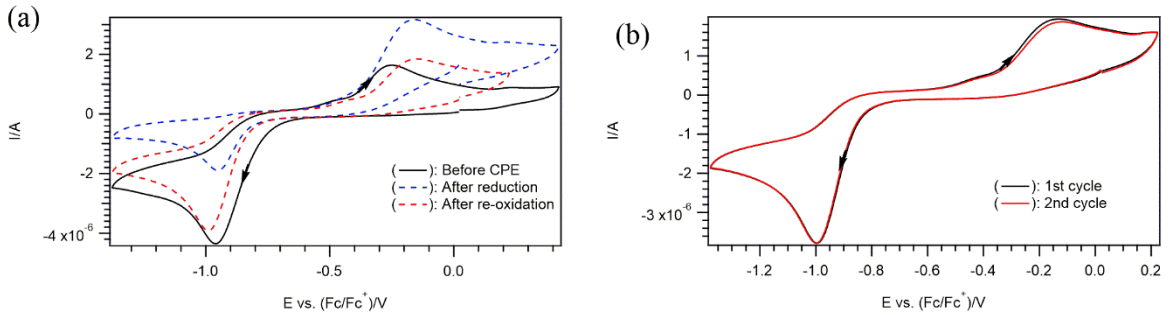

Figure A.7. CV responses for the exhaustive electrolysis of 1 mM VKA3 in 0.1 M *n*-Bu_4NPF_6/CH_3CN and 200 equiv. of DEM performed using a 1-mm diameter planar GC disk electrode at 0.1 V s^{-1} (a) CV response before and after reductive and oxidative CPE. (Black solid line) Original voltammetric profile (Red dashed line) After reductive CPE (Blue solid line) After oxidative CPE back to starting material. (b) CV response of VKA3 after exhaustive CPE for cycle 1 and 2.

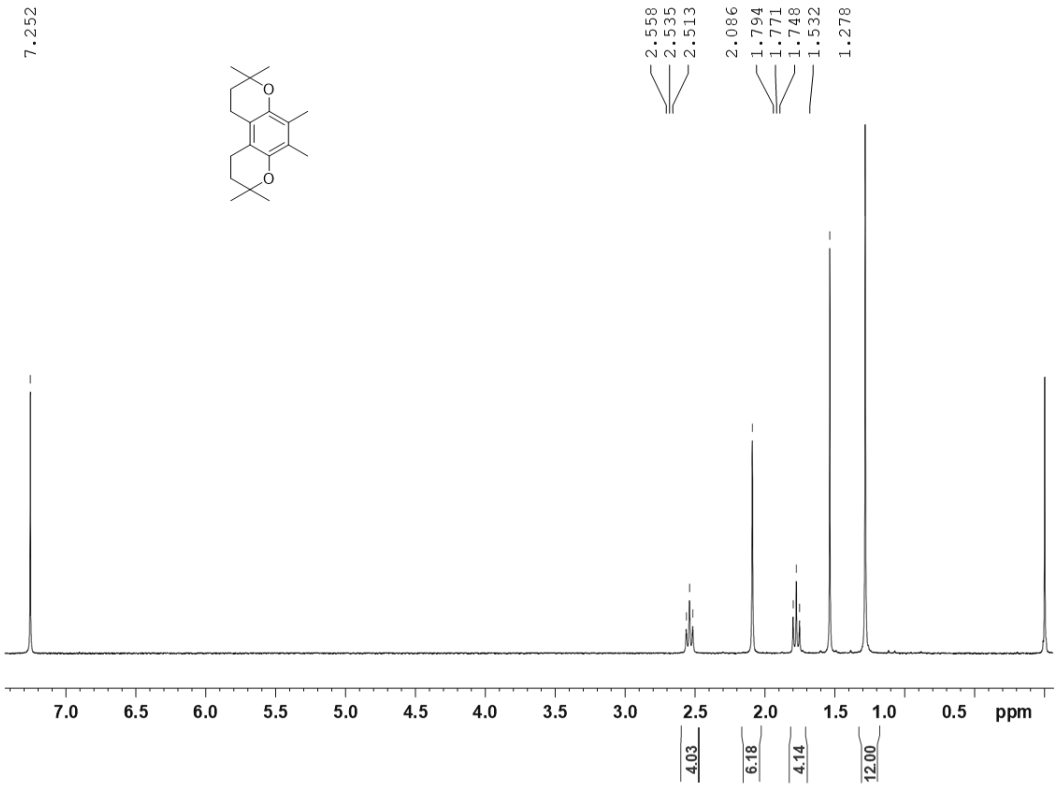

Figure A.8. The ^{1}H NMR spectrum of **VEA** in $CDCl_3$.

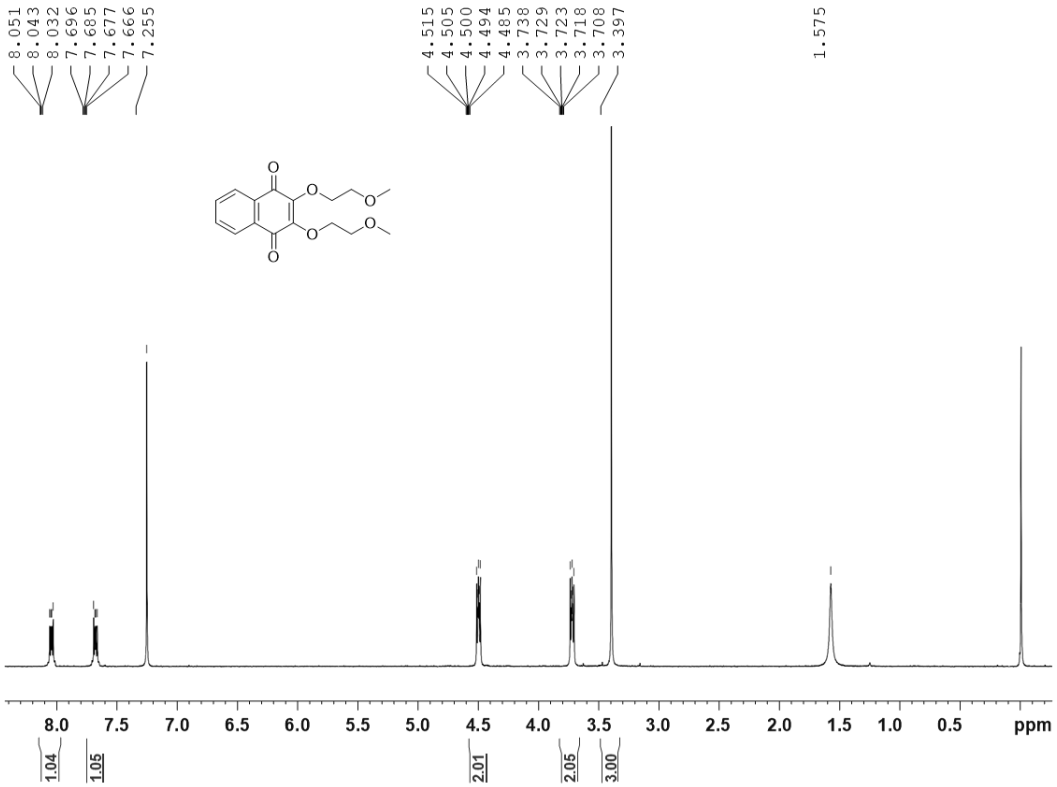

Figure A.9. The ^{1}H NMR spectrum of **VKA1** in $CDCl_3$.

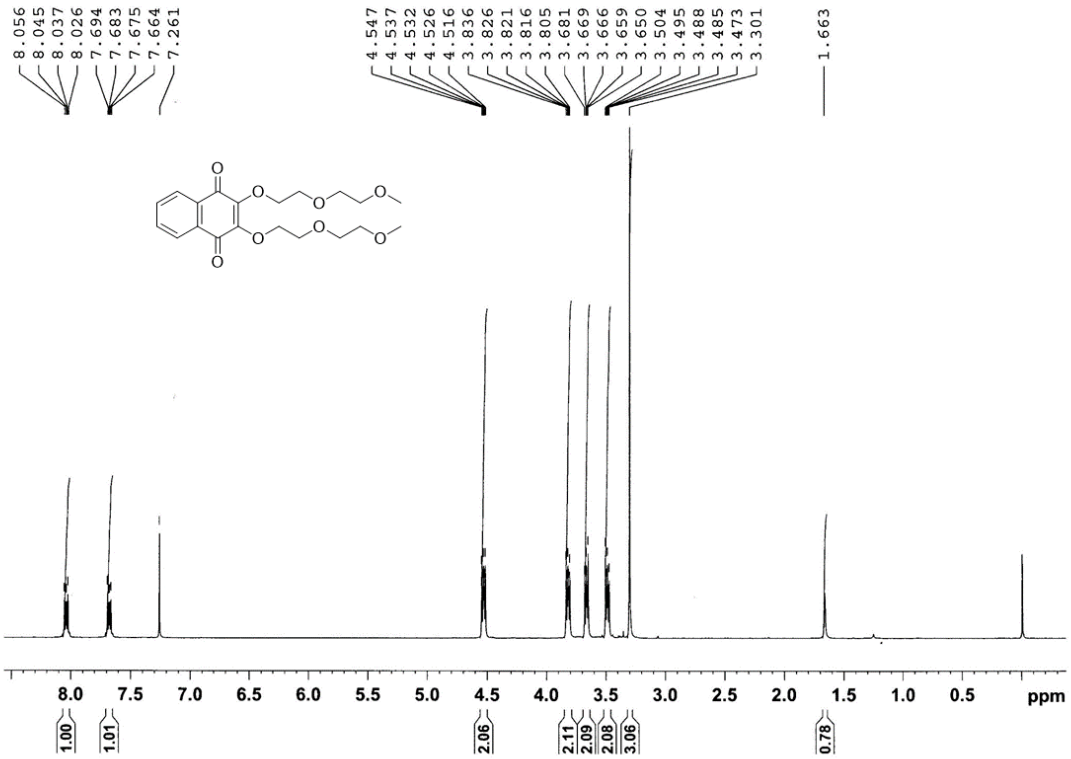

Figure A.10. The ^{1}H NMR spectrum of **VKA2** in $CDCl_3$.

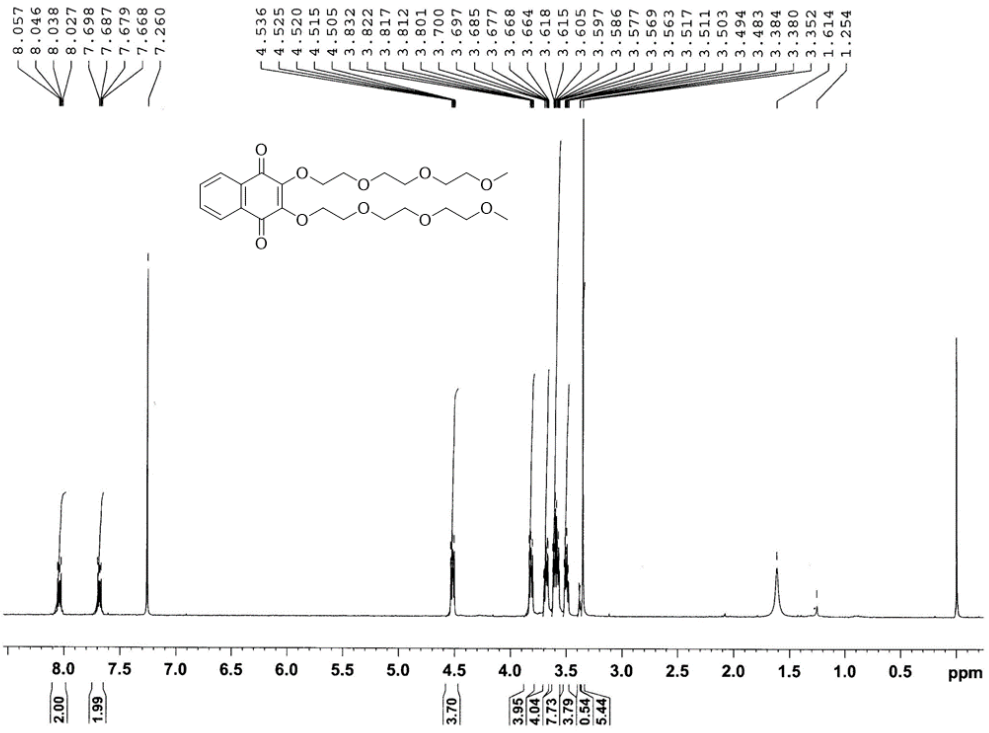

Figure A.11. The ^{1}H NMR spectrum of **VKA3** in $CDCl_3$.

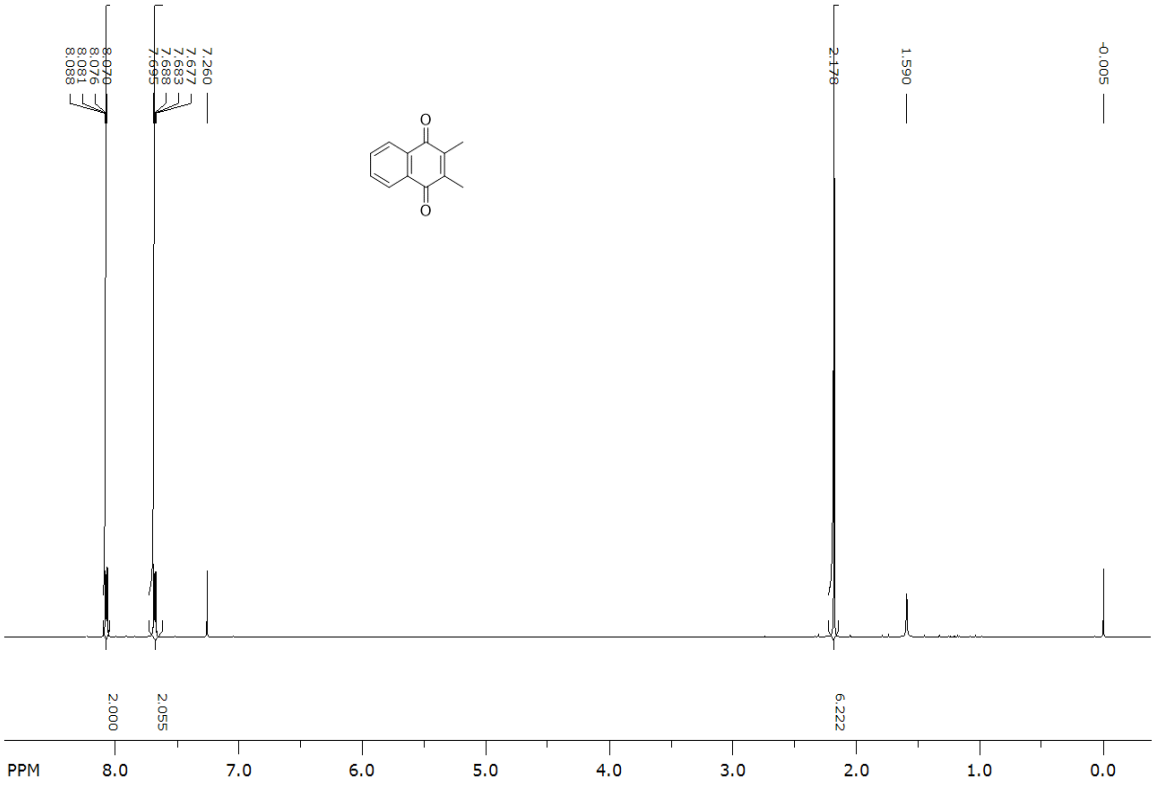

Figure A.12. The ^{1}H NMR spectrum of **VKA** in $CDCl_3$.